VOLUME 39 DECEMBER 1961 NUMBER 12

Canadian Journal of Physics

Editor: H. E. DUCKWORTH

Associate Editors:

L. G. ELLIOTT, *Atomic Energy of Canada, Ltd., Chalk River*
J. S. FOSTER, *McGill University*
G. HERZBERG, *National Research Council of Canada*
L. LEPRINCE-RINGUET, *Ecole Polytechnique, Paris*
B. W. SARGENT, *Queen's University*
G. M. VOLKOFF, *University of British Columbia*
W. H. WATSON, *University of Toronto*
G. A. WOONTON, *McGill University*

Published by THE NATIONAL RESEARCH COUNCIL

OTTAWA CANADA

CANADIAN JOURNAL OF PHYSICS

Under the authority of the Chairman of the Committee of the Privy Council on Scientific and Industrial Research, the National Research Council issues THE CANADIAN JOURNAL OF PHYSICS and five other journals devoted to the publication, in English or French, of the results of original scientific research. Matters of general policy concerning these journals are the responsibility of a joint Editorial Board consisting of: members representing the National Research Council of Canada; the Editors of the Journals; and members representing the Royal Society of Canada and four other scientific societies.

EDITORIAL BOARD

Representatives of the National Research Council

I. McT. Cowan (Chairman), *University of British Columbia*
Léo Marion, *National Research Council*
A. D. Misener, *Ontario Research Foundation*
D. L. Thomson, *McGill University*

Editors of the Journals

D. L. Bailey, *University of Toronto*
T. W. M. Cameron, *Macdonald College*
F. E. Chase, *Ontario Agricultural College*
H. E. Duckworth, *McMaster University*
Léo Marion, *National Research Council*
J. F. Morgan, *Department of National Health and Welfare, Ottawa*
J. A. F. Stevenson, *University of Western Ontario*

Representatives of the Societies

D. L. Bailey, *University of Toronto*
Royal Society of Canada
T. W. M. Cameron, *Macdonald College*
Royal Society of Canada
H. E. Duckworth, *McMaster University*
Royal Society of Canada
Canadian Association of Physicists
P. R. Gendron, *University of Ottawa*
Chemical Institute of Canada
D. J. Le Roy, *University of Toronto*
Royal Society of Canada
J. F. Morgan, *Department of National Health and Welfare, Ottawa*
Canadian Biochemical Society
R. G. E. Murray, *University of Western Ontario*
Canadian Society of Microbiologists
J. A. F. Stevenson, *University of Western Ontario*
Canadian Physiological Society

Ex officio

Léo Marion (Editor-in-Chief), *National Research Council*
J. B. Marshall (Administration and Awards), *National Research Council*

Manuscripts for publication should be submitted to Dr. H. E. Duckworth, Editor, Canadian Journal of Physics, Hamilton College, McMaster University, Hamilton, Ontario.
For instructions on preparation of copy, see **NOTES TO CONTRIBUTORS** (back cover).

Proof, correspondence concerning proof, and orders for reprints should be sent to the Manager, Editorial Office (Research Journals), Division of Administration and Awards, National Research Council, Ottawa 2, Canada.

Subscriptions, renewals, requests for single or back numbers, and all remittances should be sent to Division of Administration and Awards, National Research Council, Ottawa 2, Canada. Remittances should be made payable to the Receiver General of Canada, credit National Research Council.

The journals published, frequency of publication, and subscription prices are:

Canadian Journal of Biochemistry and Physiology	Monthly	$9.00 a year
Canadian Journal of Botany	Bimonthly	$6.00 a year
Canadian Journal of Chemistry	Monthly	$12.00 a year
Canadian Journal of Microbiology	Bimonthly	$6.00 a year
Canadian Journal of Physics	Monthly	$9.00 a year
Canadian Journal of Zoology	Bimonthly	$5.00 a year

The price of regular single numbers of all journals is $2.00.

Canadian Journal of Physics

Issued by THE NATIONAL RESEARCH COUNCIL OF CANADA

VOLUME 39 DECEMBER 1961 NUMBER 12

ON THE TEMPERATURE DEPENDENCE OF PARAMAGNETIC RESONANCE IN THE CASE OF THE ISING MODEL[1]

Y. Y. LEE[2]

ABSTRACT

The adequacy of the approximation method used by McMillan and Opechowski in their theoretical study of the temperature dependence of the paramagnetic resonance line shape function is very difficult to ascertain for the case of a typical paramagnetic crystal. For this reason the approximation method has been investigated for the very simple case of the one-dimensional Ising model. Exact expressions for the line shape function of the model are compared with expressions obtained by the approximation method mentioned above. The agreement between the two expressions is found to be very good in general, and extremely good at very low temperatures.

At sufficiently low temperatures, the paramagnetic resonance absorption is temperature dependent mainly through the Boltzmann factors which contain the energy eigenvalues of the system.

The total Hamiltonian of the paramagnetic spin system can be written as follows:

$$\mathcal{H} = \mathcal{H}^0 + \mathcal{H}' + \mathcal{H}''$$

where $\mathcal{H}^0$ is the unperturbed spin-Hamiltonian of the system which incorporates the effects of the external constant magnetic field and of the crystalline electrostatic field. The Hamiltonian $\mathcal{H}'$ describes the spin–spin interactions which include magnetic dipole–dipole interactions as well as exchange interactions. $\mathcal{H}''$ describes the effects of the high-frequency oscillating magnetic field on the system.

We shall assume that the spin–spin interactions are weak, i.e.,

$$\mathcal{H}^0 \gg \mathcal{H}'$$

and also

$$\mathcal{H}' \gg \mathcal{H}''.$$

[1]Manuscript received August 14, 1961.
Contribution from the Department of Physics, University of British Columbia, Vancouver, B.C.

[2]Present address: Department of Physics, University of Toronto, Toronto, Ont.

Thus the total Hamiltonian of the system can be written approximately as

$$\mathscr{H} = \mathscr{H}^0 + \mathscr{H}'.$$

In a theoretical study of the temperature dependence of the paramagnetic resonance line shape function, McMillan and Opechowski (1960) used the following method of approximation (first used in this connection by Pryce and Stevens 1950). Since $\mathscr{H}^0$ and $\mathscr{H}'$ commute, and $\mathscr{H}^0 \gg \mathscr{H}'$, they expanded the Boltzmann factors in the following way:

$$e^{-E_\lambda/kT} = e^{-E_\lambda^0/kT}\left[1 - \frac{E_\lambda'}{kT} + \tfrac{1}{2}\left(\frac{E_\lambda'}{kT}\right)^2 - \ldots\right] \tag{1}$$

where E_λ, E_λ^0, and E_λ' are the eigenvalues of the Hamiltonians $\mathscr{H}$, $\mathscr{H}^0$, and $\mathscr{H}'$ respectively. We shall call the approximation consisting of keeping only the first term in the square bracket "the first approximation" and so on. The adequacy of this method of approximation at low temperatures is very difficult to ascertain. In order to obtain some idea of the adequacy of the method, we have applied it to the case of a one-dimensional Ising model consisting of an arbitrary number N of identical spins arranged in a ring. We shall here call this model simply the "Ising model". Owing to the simplicity of this model, there exist only three component lines in the absorption band in contrast to the case of a typical paramagnetic crystal where the number of component lines in the absorption band is practically infinite. In the latter case we can regard it as a continuous absorption band, which is usually called a paramagnetic resonance "line".

We have calculated the exact as well as the approximate expressions for the line shape function at the three frequencies. In this note we give a summary of our results (for details of the calculation, see Lee 1961).

To calculate the general expression for the line shape function, we adopt the basic assumption of the Ising model that the exchange energy is positive for a pair of antiparallel spins and negative for a pair of parallel spins. We introduce the following notation:

N = total number of spins in the system,
$\mathbf{H}$ = external constant magnetic field,
μ = magnetic moment constant,
V_1 = number of positive spins (i.e. spins with magnetic moment vector $\boldsymbol{\mu}$ parallel to $\mathbf{H}$) in the system,
V_2 = number of negative spins (i.e. spins with magnetic moment vector $\boldsymbol{\mu}$ antiparallel to $\mathbf{H}$) in the system,
J = exchange interaction constant (positive),
S = the number of groups of negative spins in the ring, e.g.

$$\begin{array}{ccccc} & + & + & & \\ + & & & - & S = 2. \\ - & & & + & \\ & - & - & & \end{array}$$

The expression for the energy values of the system is then given by

$$E = \mu H(2V_2 - N) - (N - 4S)J. \tag{2}$$

Let us define

$$\begin{aligned} \Delta V_2 &= V_2' - V_2, \\ \Delta S &= S' - S, \\ \Delta E &= E' - E. \end{aligned}$$

Then for a transition of the type

$$\Delta V_2 = -1,$$

the Zeeman energy decreases by a fixed amount of $2\mu H$ while the exchange energy variation depends on ΔS, which can only have the following three values:

$$\Delta S = \begin{cases} -1, & \text{hence } \Delta E_{-1} = -(2\mu H + 4J); \\ 0, & \text{hence } \Delta E_0 = -2\mu H; \\ +1, & \text{hence } \Delta E_{+1} = -(2\mu H - 4J). \end{cases} \tag{3}$$

It follows that the paramagnetic resonance "line" in this case consists of only three components. Since the number of permissible transitions between any two levels is the same both ways, the transitions which belong to the type

$$\Delta V_2 = +1$$

need not be treated separately.

Now the line shape function can be defined as follows:

$$I(|\Delta E_{\Delta S}|) = \sum_{V_2, S} (e^{-E'/kT} - e^{-E/kT}) W_{\Delta S}(V_2, S) \tag{4}$$

where $W_{\Delta S}(V_2, S)$ is the number of permissible transitions for a given pair of energy levels E and E' satisfying the condition

$$E' - E = \Delta E_{\Delta S},$$

where
$$\begin{aligned} E' &= E(V_2 - 1, S + \Delta S), \\ E &= E(V_2, S), \end{aligned}$$

and $\sum_{V_2, S}$ means summation over all energy levels. It is clear from the definition (4) that the line shape function for our Ising model vanishes everywhere except at the three energy values given by (3).

The calculation of the exact expressions for the intensity function is rather complicated and tedious. However, it becomes slightly simpler if we assume that N takes the following particular form:

$$N = 4P - 1 \qquad (P = 1, 2, \ldots).$$

By so doing, we obtain the following set of expressions:

$$\begin{aligned} I(2\mu H + 4J) &= (1 - e^{-(2\mu H + 4J)/kT}) \cdot e^{N(\mu H + J)/kT} \cdot N \cdot \{1 + e^{-(2\mu H + 2J)/kT} Q_1\}, \\ I(2\mu H) &= (1 - e^{-2\mu H/kT}) \cdot e^{N(\mu H + J)/kT} \cdot 2N \cdot \{e^{-(2\mu H + 4J)/kT} Q_2\}, \\ I(|2\mu H - 4J|) &= (1 - e^{-(2\mu H - 4J)/kT}) \cdot e^{N(\mu H + J)/kT} \\ &\qquad \cdot N \cdot \{e^{-(2\mu H + 6J)/kT} Q_3 + e^{-[2(N-1)\mu H + 4J]/kT}\}, \end{aligned} \tag{5}$$

where

$$Q_1 = e^{2J/kT}\sum_{R=0}^{N-4}(e^{-2\mu H/kT})^R\sum_{r=1}^{R+1}(e^{-4J/kT})^r\binom{N-3-R}{r}\binom{R}{r-1},$$

$$(6)\qquad Q_2 = \sum_{R=0}^{N-3}(e^{-2\mu H/kT})^R\sum_{r=0}^{R}(e^{-4J/kT})^r\binom{N-3-R}{r}\binom{R}{r},$$

$$Q_3 = e^{-2J/kT}\sum_{R=1}^{N-3}(e^{-2\mu H/kT})^R\sum_{r=0}^{R-1}(e^{-4J/kT})^r\binom{N-3-R}{r}\binom{R}{r+1}.$$

These expressions are exact. We have checked them by specializing them to the case $N = 7$ and comparing the values so obtained with the values obtained for this case directly (that is, without using equations (5) and (6)).

By using a suitable generating function and assuming that N tends to infinity, we obtain the following set of asymptotically exact expressions for the Ising model:

$$\hat{I}(2\mu H+4J) = (1-e^{-(2\mu H+4J)/kT})\cdot e^{N(\mu H+J)/kT}\cdot N$$
$$\cdot(-1/\alpha)(\tfrac{1}{2})^{N-1}[(-1+e^{-2\mu H/kT}-\alpha)(1+e^{-2\mu H/kT}+\alpha)^{N-2}$$
$$-(-1+e^{-2\mu H/kT}+\alpha)(1+e^{-2\mu H/kT}-\alpha)^{N-2}],$$

$$(7)\qquad \hat{I}(2\mu H) = (1-e^{-2\mu H/kT})\cdot e^{[N(\mu H+J)-(2\mu H+4J)]/kT}\cdot 2N$$
$$\cdot(1/\alpha)(\tfrac{1}{2})^{N-2}[(1+e^{-2\mu H/kT}+\alpha)^{N-2}-(1+e^{-2\mu H/kT}-\alpha)^{N-2}],$$

$$\hat{I}(|2\mu H-4J|) = (1-e^{-(2\mu H-4J)/kT})\cdot e^{[N(\mu H+J)-(2\mu H+4J)]/kT}\cdot N$$
$$\cdot(1/\alpha)(\tfrac{1}{2})^{N-1}[(-1+e^{-2\mu H/kT}+\alpha)(1+e^{-2\mu H/kT}+\alpha)^{N-2}$$
$$-(-1+e^{-2\mu H/kT}-\alpha)(1+e^{-2\mu H/kT}-\alpha)^{N-2}],$$

where

$$\alpha = [(1-e^{-2\mu H/kT})^2+4e^{-(2\mu H+4J)/kT}]^{\frac{1}{2}}.$$

The circumflex indicates that the expressions are asymptotic.

It is obvious from (1) and (2) that the corresponding expressions in the first approximation can be obtained by simply putting J equal to zero in the expressions (7).

If we normalize the line shape function and then let T tend to zero, we obtain the same zero-temperature limit for both the exact and the first approximation line shape function as follows:

$$F_0(2\mu H+4J) = 1,$$
$$F_0(2\mu H) = 0,$$
$$F_0(|2\mu H-4J|) = 0,$$

where we use the letter F to indicate that the function is normalized, and the subscript "$_0$" indicates that the function is in the zero-temperature limit.

A graph (Fig. 1) is plotted by putting $\mu H = 20J$ for the line shape function calculated from both the asymptotically exact expressions and the corresponding first approximation expressions at various temperatures. The line

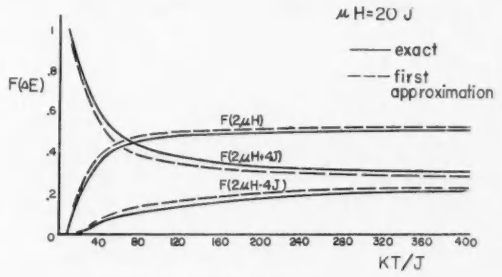

FIG. 1. Temperature dependence of the line shape function according to the asymptotically exact formula, and according to the first approximation formula.

shape function is normalized such that the sum of the values at the three frequencies equals unity.

It is seen from the graph that, in the case of the Ising model, the method of approximation used by McMillan and Opechowski is quite good in general and is extremely good at temperatures below say, $T \approx 4J/k$.

I am indebted to Prof. W. Opechowski for suggesting this problem and for his continued interest throughout the performance of this research. I also wish to thank Mr. K. Nishikawa for some valuable discussions. Finally I should like to acknowledge financial help from the National Research Council of Canada.

REFERENCES

ISING, E. 1925. Z. Physik, **31**, 253.
LEE, Y. Y. 1961. M.Sc. Thesis, University of British Columbia, Vancouver, B.C.
MCMILLAN, M. and OPECHOWSKI, W. 1960. Can. J. Phys. **38**, 1168.
PRYCE, M. H. L. and STEVENS, K. W. H. 1950. Proc. Phys. Soc. A, **63**, 36.

THE ABSORPTION SPECTRUM OF BO_2[1]

J. W. C. JOHNS

ABSTRACT

The boron flame bands have been observed in absorption during the flash photolysis of mixtures of boron trichloride and oxygen. Detailed analysis of the spectrum has shown that the bands arise from two electronic transitions in the linear symmetric molecule BO_2, $B\,^2\Sigma_u^+$–$X\,^2\Pi_g$ and $A\,^2\Pi_u$–$X\,^2\Pi_g$. The main molecular constants, in cm^{-1} except for r_0, are summarized below:

$B\,^2\Sigma_u^+$	$T_0 = 24507.9_9$	$\nu_2 = 505$
	$B_0 = 0.3250$	$r_0 = 1.273$ Å
$A\,^2\Pi_u$	$T_0 = 18291.5_9$	$\nu_1 = 994$
	$B_0 = 0.3115$	$\nu_2 = 484$
	$r_0 = 1.302$ Å	$\nu_3 = 2357$
	$A_0 = -101.3$	
$X\,^2\Pi_g$	$B_0 = 0.3292$	$\nu_1 = 1070$
	$r_0 = 1.265$ Å	$\nu_2 = 464$
	$A_0 = -148.6$	$\nu_3 = 1322.$

Both $^2\Pi$ states show the Renner effect. In the ground state the Renner parameter, $\epsilon\omega_2$, was found to be -92.2, whereas in the first excited state it is much smaller, $-13.1\ cm^{-1}$.

1. INTRODUCTION

The green coloration of flames containing boron has been familiar to chemists for many years and the 'boric acid fluctuation bands' were measured as long ago as 1873 by Salet. The bands have usually been assigned to the molecule B_2O_3. Until recently the bands were thought to be completely diffuse, but observations by Kaskan, MacKenzie, and Millikan (1961) and Soulen (1955) have indicated that there is a large amount of complicated fine structure. It was felt that the complexity of the bands might be due, in part at least, to the high temperature of the sources used hitherto. In the present work it has been found that the bands can be observed conveniently in absorption, at approximately room temperature, during the flash photolysis of mixtures of boron trichloride and oxygen. Sufficient fine structure has been resolved to enable many of the bands to be analyzed completely.

It has been shown that the bands arise from two electronic transitions in the linear symmetric molecule BO_2, $A\,^2\Pi_u$–$X\,^2\Pi_g$ and $B\,^2\Sigma_u^+$–$X\,^2\Pi_g$, analogous to the two well-known transitions in the isoelectronic molecule CO_2^+. Both $^2\Pi$ states show the Renner effect and it has been found possible to test some of the theoretical predictions of Pople (1960) and Hougen (1961).

2. EXPERIMENTAL

The spectrum was observed during the flash photolysis of BCl_3:O_2 mixtures using an apparatus similar to that described by Claesson and Lindqvist (1957).

[1]Manuscript received August 28, 1961.
Contribution from the Division of Pure Physics, National Research Council, Ottawa, Canada.
Issued as N.R.C. No. 6546.

The 2-meter absorption tube was fitted with multiple reflection mirrors of the type described by White (1942). The mirrors were coated with silver and silica or aluminum and silica according to the spectral region, and up to 20 traversals of the tube were used.

The two photolysis lamps, each 1 meter long, were connected in series; 11,000 joules were discharged through them in about 30 μsec. The continuous background was supplied by a Lyman flash source, viewed sideways on, in which 225 joules were discharged in about 15 μsec. The time interval between the two flashes was controlled by a Dumont Type 326 time delay generator which permitted delays from 5 μsec to 10 msec to be used. The maximum intensity of absorption occurred when the time interval between the two flashes was about 100 μsec, and the absorption cell was filled with about 5 mm of a 1:1 mixture of BCl_3 and O_2 which was changed for every flash.

The spectrum which falls in the region 3800 Å to 6800 Å was photographed in the second order of a 21-ft grating spectrograph. A survey of the spectral region from 2600 Å to 9000 Å revealed no further absorption which could be attributed to BO_2. No boron monoxide bands were found, but bands due to chlorine monoxide were observed near 3000 Å (Durie and Ramsay 1958). Eastman Kodak IO, ID, and hypersensitized IN plates were used. Satisfactory exposures were obtained with 60 to 100 flashes. Iron lines, emitted by a hollow cathode source, were used as wavelength standards. The wavelengths, which were taken from the M.I.T. Tables (Harrison 1939), were corrected for vacuum by means of the tables of Edlén (1953). The relative accuracy of measurement of strong unblended lines was estimated to be about ± 0.02 cm^{-1}.

3. DESCRIPTION OF THE SPECTRUM

The long wavelength end of the spectrum consists of groups of absorption bands, degraded to the red, at 5450 Å, 5180 Å, 4930 Å, and 4500 Å, which correspond to the maxima of the 'boric acid fluctuation bands' (Pearse and Gaydon 1950). The two strongest groups are shown in Fig. 1. Bands corresponding to the fluctuation maxima at 5800 Å, 6200 Å, and 6380 Å were also observed, but in emission, as fluorescence excited by the photolysis flash.

Most of the bands occur in pairs, separated by about 45 cm^{-1}, and are single-headed having only P and R branches. In some of the bands a distinct staggering of the rotational structure can be observed, which implies the absence of alternate rotational levels. The appearance of the bands is thus consistent with their interpretation as a $^2\Pi$–$^2\Pi$ transition of a linear symmetric molecule in which all off-center atoms have zero nuclear spin.

Weak bands observed to the violet of each strong band, with an intensity ratio of about 1:4, have been interpreted as being due to the presence of ^{10}B in natural abundance. Furthermore, the presence of only two isotopic species shows that the molecule can contain only one boron atom, which, since the molecule is symmetric, must lie on the center of symmetry. The method of production of the spectrum indicated that BCl_2 and BO_2 were the most likely molecular species; in BO_2 alone will alternate levels be missing since oxygen has zero nuclear spin.

Towards the short wave end of the spectrum, at about 4070 Å, an isolated group of bands shows a doublet structure where the separation is about 150 cm^{-1}. This group, reproduced in Fig. 2, is remarkably similar to the 2900-Å system of CO_2^+ observed by Bueso-Sanllehi (1941), and which is known to be a transition of the type $^2\Sigma_u^+$–$^2\Pi_g$.

The spectrum was thus shown to consist of two electronic transitions in linear symmetric BO_2: (i) $A\ ^2\Pi_u$–$X\ ^2\Pi_g$ (hereafter referred to as the A system) in which there is an appreciable change in B value resulting in extensive vibrational structure, and (ii) $B\ ^2\Sigma_u^+$–$X\ ^2\Pi_g$ (hereafter referred to as the B system) in which $B' \simeq B''$ so that only one isolated group of bands is observed. These conclusions were confirmed by detailed rotational analysis of many of the bands.

4. THE RENNER EFFECT

When the bending vibration of a linear triatomic molecule is excited, the angular momentum, $lh/2\pi$, associated with this vibration interacts with the electronic orbital angular momentum, $\Lambda h/2\pi$, to give a total angular momentum along the internuclear axis, $Kh/2\pi$, in a way first discussed by Renner (1934). Pople (1960) has extended the results obtained by Renner to include spin–orbit interaction and has derived expressions for the vibronic energy levels. These expressions have been included here in a form thought to be more convenient for practical spectroscopists:

$$E^{+}_{v_2,K,\pm\frac{1}{2}} = \omega_2(v_2+1)+r_{v_2,K}-\frac{(\epsilon\omega_2)^2}{8\omega_2}(v_2+1)\mp\frac{KA(\epsilon\omega_2)^2(v_2+1)}{8\omega_2 r_{v_2,K}},$$

$$E^{-}_{v_2,K,\pm\frac{1}{2}} = \omega_2(v_2+1)-r_{v_2,K}-\frac{(\epsilon\omega_2)^2}{8\omega_2}(v_2+1)\pm\frac{KA(\epsilon\omega_2)^2(v_2+1)}{8\omega_2 r_{v_2,K}}, \tag{1}$$

$$r_{v_2,K} = \tfrac{1}{2}\sqrt{[A^2+(\epsilon\omega_2)^2\{(v_2+1)^2-K^2\}]}, \tag{2}$$

where $\epsilon\omega_2$ is the Renner parameter and $K = |\Lambda+l|$. The pattern of energy levels formed is shown in a qualitative manner in Fig. 3, assuming the electronic state to be $^2\Pi_g$.

It has been found convenient to designate vibronic levels in the following manner: v_1, v_2^l, v_3 followed by the vibronic symmetry in parentheses, e.g. $02^20(^2\Pi_{3/2})$. This is different from the notation proposed by Dixon (1960*a*), who wrote v_1, v_2^K, v_3. His method does not, however, distinguish between the pairs of states in which $K \leqslant v_2-1$. It should be pointed out that l is a good quantum number only when the Renner effect is small compared with spin–orbit interaction, which is the case in the $A\ ^2\Pi_u$ state of BO_2.

5. VIBRATIONAL ANALYSES

5.1. The B System

Only two vibrational transitions have been observed in the B system, 000–000 and 010–010. The latter, because of the Renner effect and spin–orbit interaction in the lower state, is split into four subbands as indicated in Fig. 2.

PLATE I

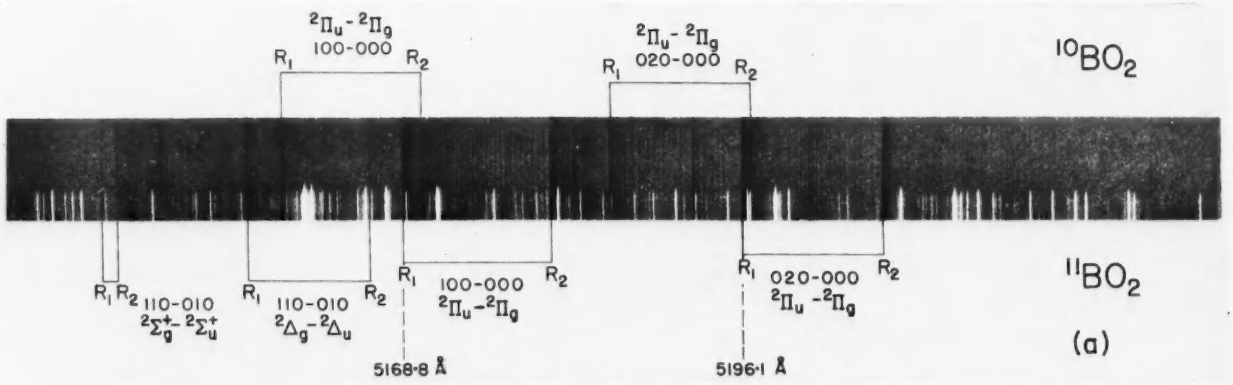

FIG. 1*a*.

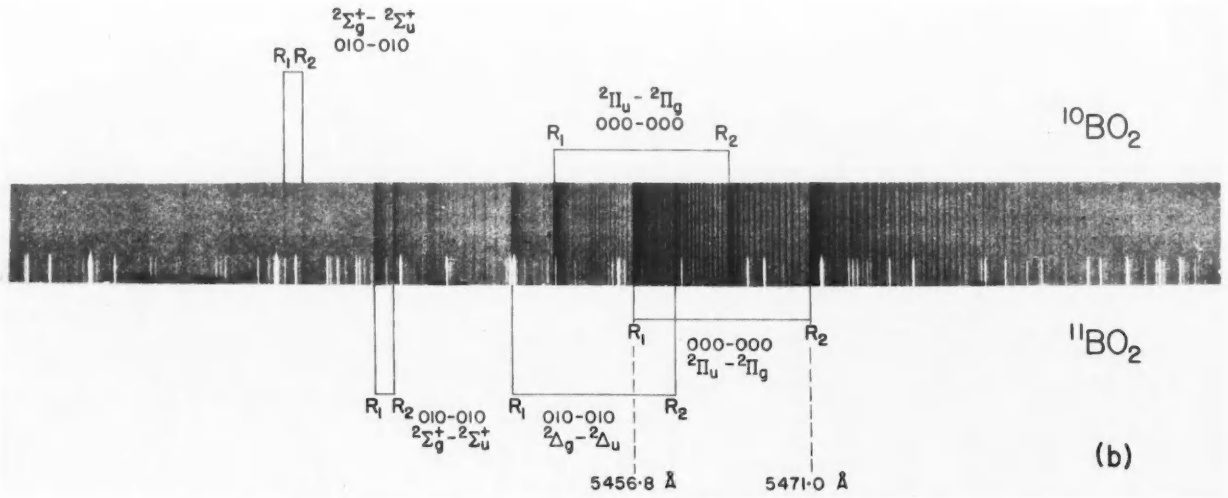

FIGS. 1*a* and 1*b*. The two strongest band groups of the $A\ ^2\Pi_u$–$X\ ^2\Pi_g$ system of BO_2.

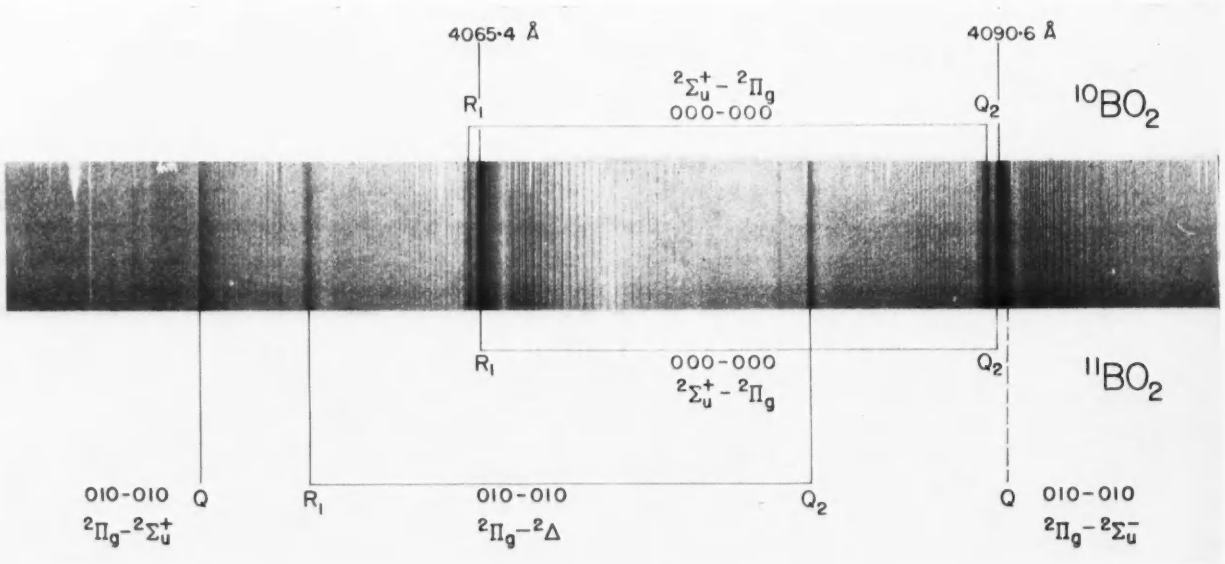

FIG. 2. The $B\,{}^2\Sigma_u^+ - X\,{}^2\Pi_g$ system of BO_2.

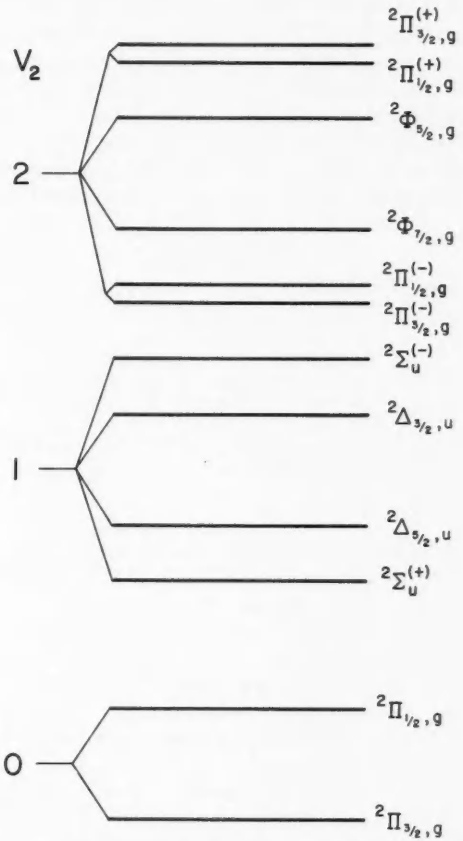

FIG. 3. The pattern of vibronic energy levels formed when the bending vibration of a linear symmetric molecule in a $^2\Pi_g$ electronic state is excited. Note: For $^2\Sigma$ vibronic levels ($\pm$) denotes the symmetry of the levels with which they correlate as A tends to zero. For other ($K \neq 0$) levels ($\pm$) merely refers to the order in which they occur.

5.2. The A System

(a) The Upper State

The 5450-Å band group was readily shown to contain the 000–000 transition since it was the longest wavelength group in the absorption spectrum. This conclusion was confirmed by the rotational analysis of the 100–000, 000–000, and 000–100 bands as described in Section 6.2. The appearance of the individual bands shows BO_2 to be linear (see Section 3), so that, with an appreciable change in internuclear distance, progressions in the symmetric stretching frequencies, ν_1, should be prominent. In particular, the absorption spectrum should consist of a single progression in the upper state stretching frequency.

Each $^2\Pi$–$^2\Pi$ band is expected to have four heads, two strong ones for $^{11}BO_2$ and two weaker ones for $^{10}BO_2$. This is indeed found to be so with the 5450-Å group, which contains two strong heads, and was assigned as an essentially single transition. However, the 5180-Å group, which contains four strong heads, was assigned to two transitions (see Fig. 1).

These facts were readily explained on the basis of a Fermi resonance between levels of the type v_1,v_2,v_3 and $(v_1-1),(v_2+2),v_3$. However, the situation is complicated in this case by the Renner effect. Figure 4 shows the $^2\Pi(K = |\Lambda+l|$

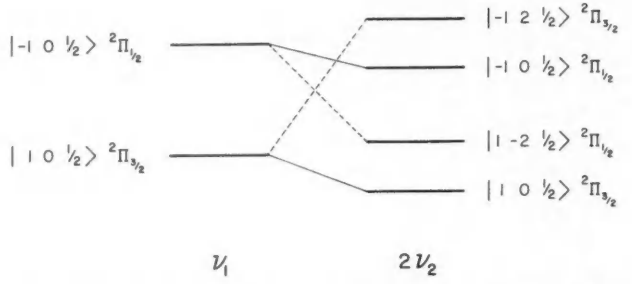

FIG. 4. Schematic representation of the interaction between ν_1 and $2\nu_2$ in a $^2\Pi$ electronic state. For simplicity only wave functions with $\Sigma = +\frac{1}{2}$ have been included.

$= 1$) levels in the diad ν_1 and $2\nu_2$. In this diagram appropriate wave functions, written in the Dirac ket notation, $|\Lambda,l,\Sigma\rangle$, have been included. Qualitatively one would expect states with identical quantum numbers to interact strongly, and these have been connected with solid lines; whereas states with identical values of $P = |\Lambda+l+\Sigma|$ but different l would be expected to interact only weakly, and these have been connected with broken lines. Six transitions are allowed by the selection rule $\Delta P = 0$ between such a diad and the ground state. Of these, four, involving $2\nu_2$, will be weak because of the Franck–Condon principle. However, two of these transitions can 'borrow' intensity from ν_1 since they mix readily with it as shown above. Figure 5 is an energy level diagram of the transition between the diad (100; 020) and the ground state in which the strong transitions are shown in heavy full lines. Figure 6 is a similar diagram for the triad (120; 200; 040). For clarity the $^2\Pi$ states have been grouped in pairs, $^2\Pi^{(+)}$ and $^2\Pi^{(-)}$, after Pople (1960). However, as has been discussed by Hougen (1961), it would seem better in some cases, such as when the Renner effect is small, to pair the states according to the value of l. At least five band groups have been observed. Since the resonance between levels of the type v_1,v_2,v_3 and $(v_1-1),(v_2+1),v_3$ is close, the structure of these groups becomes very complicated so that only tentative assignments have been made beyond the group at 5180 Å.

A comparatively strong isolated band at about 4345 Å has been assigned to the transition 002–000. The analysis showed that the upper level of this band lies at 4712 cm^{-1} above 000 in $A\ ^2\Pi_u$, and that $B''_{000}-B' = 0.0047$ cm^{-1}

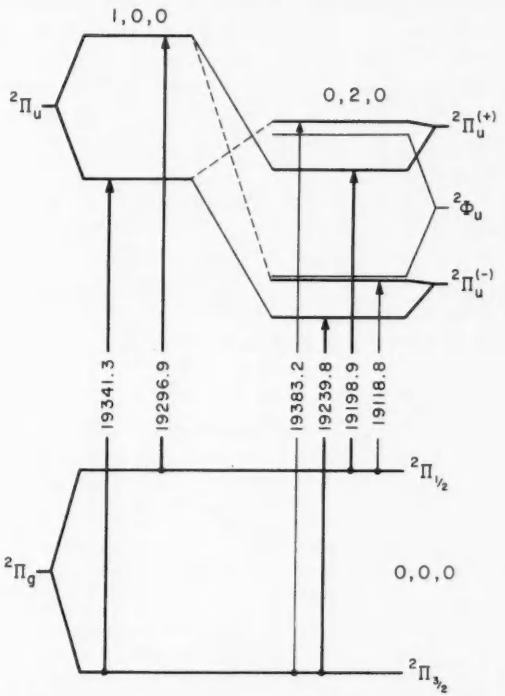

FIG. 5. Energy level diagram of the transitions 100–000 and 020–000. Strong transitions have been indicated with heavy full lines.

(see Section 6). The assignment thus gives $\frac{1}{2}(2\nu_3) = 2357$ cm^{-1} and $\frac{1}{2}(2\alpha_3) = 0.0023$ cm^{-1}. Both these values are close to the corresponding constants in CO_2 where $\omega_3 = 2396$ cm^{-1} and $\alpha_3 = 0.0029$ cm^{-1}.

When even quanta of the bending vibration are excited, four $^2\Pi$ sublevels are formed. Figures 5 and 6 show that the pairs involved in the strong transitions are separated, in the absence of resonance, by $\nu(^2\Pi^{(+)}) - \nu(^2\Pi^{(-)}) = 2r_{v_2,K}$, which is given as a function of v_2 in equation (2). The separation of the strong band heads is thus a function of v_2 and can be shown to be equal to

$$A'' - \sqrt{[(A')^2 + (\epsilon'\omega_2')^2\{(v_2+1)^2 - 1\}]}.$$

Values of this expression have been calculated for values of v_2 up to 6 using the constants listed in Table X and are compared with head–head separations observed in a number of progressions of BO_2 bands in Table I. The agreement between observed and calculated values is, on the whole, good, and the differences may be accounted for by Fermi resonance.

Vibration frequencies in the isotopic molecule $^{10}BO_2$ have also proved useful in making vibrational assignments. For the two non-totally symmetric

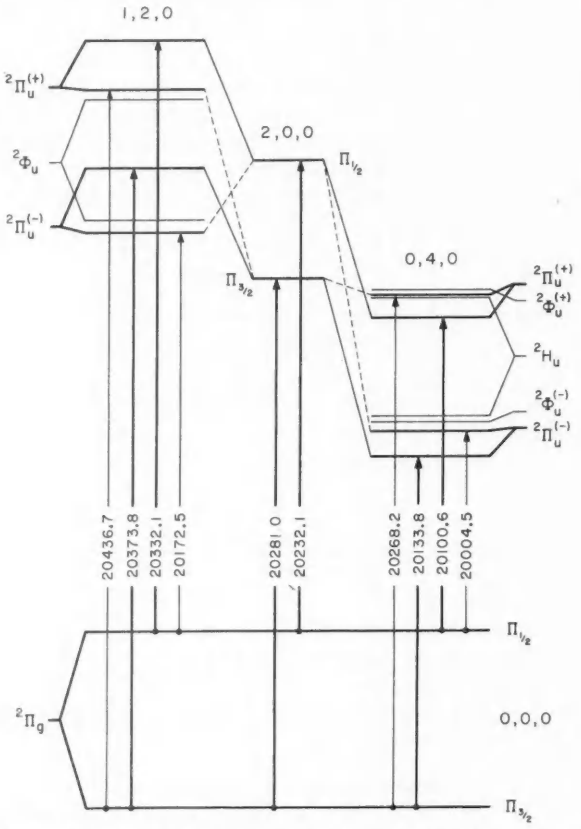

FIG. 6. Energy level diagram of the transitions 120–000, 200–000, and 040–000. Strong transitions have been indicated with heavy full lines.

TABLE I

R_1–R_2 head–head separations in system A

		Obs.			
v_2	Calc.	$0,v_2,0$	$1,v_2,0$	$2,v_2,0$	$0,v_2,2$*
0	47.3	47.1	44.1	48.9	45.4
2	40.8	40.9	41.7	41.0	34.7
4	28.7	33.2	35.0	28.2	29.7
6	12.6		16.1	13.5	

*The identification of this progression is somewhat doubtful since it could be assigned as v_1,0,2 by consideration of the isotope effect. However, A' is not expected to vary greatly with changes in v_1.

vibrations, ν_2 and ν_3, the ratio of the isotopic frequencies is calculated to be 1.0363 if anharmonic terms and effects of Fermi resonance are ignored. There

should be no isotopic shifts in the ν_1 frequencies. In general, it was found that the ratio of ν_1 frequencies was greater than unity whereas the ratio of ν_2 frequencies was less than 1.0363, as would be expected if there was any mixing of the levels concerned. Only one vibrational level, $2\nu_3$, seemed unaffected by any resonance. For this level the ratio of the isotopic frequencies was found to be 1.035, in good agreement with the theoretical value.

(b) Hot Bands

A number of 'hot' bands have been observed arising from levels as high as $02^20(^2\Pi^{(-)})$ at about 825 cm^{-1} above the ground state. The observation of the two bands $01^10(\kappa^2\Sigma^{(-)})$–$01^10(\mu^2\Sigma^{(+)})$ and $01^10(\mu^2\Sigma^{(+)})$–$01^10(\mu^2\Sigma^{(+)})$ gave directly the difference $2r_{v_2,K}$ for the 010 level of $A\ ^2\Pi_u$, thus making it possible to obtain a good value of $\epsilon\omega_2$ from equation (2). Unfortunately all bands involving $01^10(\kappa^2\Sigma^{(-)})$ in $X\ ^2\Pi_g$ were heavily overlapped and it was not possible to measure the position of this level.

(c) Fluorescence Bands

The strongest features of the emission spectrum obtained in this work have been assigned unambiguously as shown in the Deslandres Table II below.

TABLE II

Deslandres table of emission bands of BO_2

100	R_1	19341.3*				17219.4
	R_2	19296.9*				17142.3
		1020.7				1020.6
		1023.4				1023.5
000	R_1	18320.6*	1056.4	17264.2	1065.4	16198.8
	R_2	18273.5*	1076.0	17197.5	1078.7	16118.8
v_1',v_2',v_3' / v_1'',v_2'',v_3''		000		100		200

*Observed in absorption only.

Examination of Table II shows that the head–head separation and thus A'' is dependent on v_1''. A similar effect has been noted by Dixon (1960*b*) in the spectrum of NCO. The reason became obvious when it was found that the $^2\Pi^{(+)}$ sublevel of 020 was predicted to lie between the two components of 100 thus forcing them apart. Indeed a weak band can plausibly be assigned to one of the transitions 000–020 ($^2\Pi^{(+)}$).

A weak fluorescence band at about 6377 Å corresponds to the strongest of a group of four bands in the emission spectrum as observed by Soulen (1955). These bands have been assigned to the 000–002 transition in the two isotopic molecules. This gives the unusually low value of 1322 cm^{-1} for $\frac{1}{2}(2\nu_3'')$, bearing in mind that $\nu_1'' = 1070$. The ratio of these two frequencies should be 1.98:1 on the assumption of simple valence forces. However, there is strong evidence in favor of this assignment:

(i) the isotopic ratio was found to be 1.037;

(ii) the high intensity of the absorption band 002–000 was made plausible by the large change in ν_3 between the two states;

(iii) with both non-totally symmetric vibration frequencies known in each state of the A system (ν_1 can be ignored since there is no isotopic shift for this vibration), it was possible to calculate the isotope shift of the 000–000 band. With

$$\nu_2'' = 464 \quad \nu_2' = 484 \qquad \text{and} \qquad \frac{\nu(^{10}BO_2)}{\nu(^{11}BO_2)} = 1.0363,$$
$$\nu_3'' = 1322 \quad \nu_3' = 2357$$

the frequency difference, 000–000($^{10}BO_2$)–000–000($^{11}BO_2$), was calculated to be 19.5 cm^{-1} in good agreement with the experimental value of 21.5 cm^{-1}.

Kaskan and Millikan (1961) have observed the infrared emission from trimethyl borate flames and have found a band at about 1350 cm^{-1} which they attributed to the ν_3 vibration of BO_2. This is in excellent agreement with the value predicted in this work. White (1961) has also observed what appears to be the same band in a matrix isolation experiment at about 1282 cm^{-1}.

5.3. Determination of Constants

The wavelengths and frequencies of the band heads are listed in Table III together with the earlier measurements of Soulen (1955). Vibrational assignments are also included in this table. Figure 7 is an energy level diagram illustrating the observed transitions in the A system.

TABLE III

Band heads of the system $A\ ^2\Pi_u$–$X\ ^2\Pi_g$ of BO_2

λ_{air},[a] Å	Present work ν_{vac}, cm^{-1}	Soulen ν_{vac}, cm^{-1}	I	Isotope	Branch	Upper level	Lower level
6429.4		15549		10	R_2	$00^00\ ^2\Pi$	$00^02\ ^2\Pi$
6408.7		15599		10	R_1	$00^00\ ^2\Pi$	$00^02\ ^2\Pi$
6401.0		15618					
6396.0		15630		11	R_2	$00^00\ ^2\Pi$	$00^02\ ^2\Pi$
6389.9		15645					
6376.61	15678.0	15676	0	11	R_1	$00^00\ ^2\Pi$	$00^02\ ^2\Pi$
6360.5		15717					
6352.1		15738					
6349.2		15746					
6344.1		15758					
6341.2		15766					
6331.5		15790					
6327.1		15801					
6320.0		15818					
6312.0		15838					
6202.2	16118.8		2	11	R_2	$00^00\ ^2\Pi$	$20^00\ ^2\Pi$
6190.24	16150.0	16149	1	10	R_2	$00^00\ ^2\Pi$	$20^00\ ^2\Pi$
6179.0		16179					
6171.59	16198.8	16196	2	11	R_1	$00^00\ ^2\Pi$	$20^00\ ^2\Pi$
6168.4		16207					
6159.77	16229.9		1	10	R_1	$00^00\ ^2\Pi$	$20^00\ ^2\Pi$
6153.47	16246.5	16244	1				
6023.2		16598					
6017.5		16614					
6005.7		16646					
6001.8		16657					
5991.6		16685					
5980.8		16716					
5970.3		16745					
5831.90	17142.3	17142	3	11	R_2	$10^00\ ^2\Pi$	$20^00\ ^2\Pi$
5813.19	17197.5	17197	5	11	R_2	$00^00\ ^2\Pi$	$10^00\ ^2\Pi$

TABLE III (*Continued*)

λ_{air},[a] Å	Present work ν_{vac}, cm^{-1}	Soulen ν_{vac}, cm^{-1}	I	Isotope	Branch	Upper level	Lower level
5809.30	17209	17211	0				
5805.79	17219.4	17219	3	11	R_1	10^00 $^2\Pi$	20^00 $^2\Pi$
5801.6		17232					
5797.7		17245					
5790.72	17264.2	17264	5	11	R_1	00^00 $^2\Pi$	10^00 $^2\Pi$
5785.40	17280.1		1	10	R_1	00^00 $^2\Pi$	10^00 $^2\Pi$
5782.32	17289.3	17289	0	11	R_1	01^10 $^2\Delta$	11^10 $^2\Delta$
5767.38	17334.1		1	11	R_2	01^10 $^2\Sigma^{(+)}$	11^10 $^2\Sigma^{(+)}$
5766.48	17336.8	17336	1	11	R_1	01^10 $^2\Sigma^{(+)}$	11^10 $^2\Sigma^{(+)}$
5764.7	17342		0				
5503.14	18166.4		0				
5476.3		18255					
5472.4		18268					
5470.89	18273.5	18272	10	11	R_2	00^00 $^2\Pi$	00^00 $^2\Pi$
5468.2		18282		11	R_1	10^00 $^2\Pi$	10^00 $^2\Pi$
5464.48	18294.9	18294	5	10	R_2	00^00 $^2\Pi$	00^00 $^2\Pi$
5460.12	18309.5	18310	4	11	R_2	01^10 $^2\Delta$	01^10 $^2\Delta$
5456.82	18320.6	18321	10	11	R_1	00^00 $^2\Pi$	00^00 $^2\Pi$
5453.42	18332.0	18332	3	10	R_2	01^10 $^2\Delta$	01^10 $^2\Delta$
5450.40	18342.2	18345	7	10	R_1	00^00 $^2\Pi$	00^00 $^2\Pi$
5447.07	18353.4	18352	6	11	R_1	01^10 $^2\Delta$	01^10 $^2\Delta$
5440.43	18375.8	18376	5	10	R_1	01^10 $^2\Delta$	01^10 $^2\Delta$
5437.53	18385.6		6	11	R_2	01^10 $^2\Sigma^{(+)}$	01^10 $^2\Sigma^{(+)}$
5435.99	18390.8	18389	6	11	R_1	01^10 $^2\Sigma^{(+)}$	01^10 $^2\Sigma^{(+)}$
5430.26	18410.2		4	10	R_2	01^10 $^2\Sigma^{(+)}$	01^10 $^2\Sigma^{(+)}$
5428.73	18415.4		4	10	R_1	01^10 $^2\Sigma^{(+)}$	01^10 $^2\Sigma^{(+)}$
5424.37	18430.2	18429	2				
5420.72	18442.6	18442	4	11		02^20 $^2\Pi$	02^20 $^2\Pi$
5412.86	18469.4	18469	2	10		02^20 $^2\Pi$	02^20 $^2\Pi$
5407.24	18488.6		2	11	$^QR_{12}$	01^10 $^2\Sigma^{(-)}$	01^10 $^2\Sigma^{(+)}$
5406.33	18491.7	18491	2				
5403.79	18500.4		2	11	$^SR_{21}$	01^10 $^2\Sigma^{(-)}$	01^10 $^2\Sigma^{(+)}$
5399.99	18513.4		2	10	$^QR_{12}$	01^10 $^2\Sigma^{(-)}$	01^10 $^2\Sigma^{(+)}$
5384.17	18567.8		2				
5228.97	19118.9		4	11	R_2	02^20 $^2\Pi$	00^00 $^2\Pi$
5214.2		19173					
5207.18	19198.9	19197	8	11	R_2	02^20 $^2\Pi$	00^00 $^2\Pi$
5201.49	19219.9	19221	4				
5198.26	19237.2		6	10	R_2	02^20 $^2\Pi$	00^00 $^2\Pi$
5196.11	19239.8	19238	8	11	R_1	02^20 $^2\Pi$	00^00 $^2\Pi$
5192.14	19254.5	19255	4				
5185.52	19279.1	19278	6	10	R_1	02^20 $^2\Pi$	00^00 $^2\Pi$
5183.51	19286.6		4		R_2	03^30 $^2\Sigma^{(+)}$	01^10 $^2\Sigma^{(+)}$
5182.54	19290.2		4		R_1	03^30 $^2\Sigma^{(+)}$	01^10 $^2\Sigma^{(+)}$
5180.74	19296.9	19297	8	11	R_2	10^00 $^2\Pi$	00^00 $^2\Pi$
5170.31	19335.8		5	10	R_2	10^00 $^2\Pi$	00^00 $^2\Pi$
5168.84	19341.3	19342	8	11	R_1	10^00 $^2\Pi$	00^00 $^2\Pi$
5166.09	19351.6		4	11	R_2	11^10 $^2\Delta$	01^10 $^2\Delta$
5159.10	19377.8		6	10	R_1	10^00 $^2\Pi$	00^00 $^2\Pi$
5157.66	19383.2		4	11	R_1	02^20 $^2\Pi$	00^00 $^2\Pi$
5156.28	19388.4		5	11	R_1	11^10 $^2\Delta$	01^10 $^2\Delta$
5149.38	19414.4	19406	4				
5147.6		19421					
5145.89	19427.6	19428	5	11	R_2	11^10 $^2\Sigma^{(+)}$	01^10 $^2\Sigma^{(+)}$
5144.61	19432.4		5	11	R_1	11^10 $^2\Sigma^{(+)}$	01^10 $^2\Sigma^{(+)}$
5140.5		19448					
5138.13	19456.9		0				
5136.5		19463					
5134.33	19471.3		2	10	R_2	11^10 $^2\Sigma^{(+)}$	01^10 $^2\Sigma^{(+)}$
5133.12	19475.9	19472	2	10	R_1	11^10 $^2\Sigma^{(+)}$	01^10 $^2\Sigma^{(+)}$
5127.72	19496.4	19498	2	11		12^20 $^2\Pi$	02^20 $^2\Pi$
5125.2		19506					

TABLE III (*Continued*)

λ_{air},[a] Å	Present work ν_{vac}, cm^{-1}	Soulen ν_{vac}, cm^{-1}	I	Isotope	Branch	Upper level	Lower level
5118.66	19530.9		0	11	$^{Q}R_{12}$	$11^{1}0$ $^{2}\Sigma^{(-)}$	$01^{1}0$ $^{2}\Sigma^{(+)}$
5115.49	19543.0		0	10		$12^{2}0$ $^{2}\Pi$	$02^{2}0$ $^{2}\Pi$
5112.6		19554					
5110.09	19563.7						
4997.49	20004.5		2	11	R_2	$04^{2}0$ $^{2}\Pi$	$00^{0}0$ $^{2}\Pi$
4992.49	20024.5		1				
4973.59	20100.6		5	11	R_2	$04^{0}0$ $^{2}\Pi$	$00^{0}0$ $^{2}\Pi$
4965.38	20133.8		5	11	R_1	$04^{0}0$ $^{2}\Pi$	$00^{0}0$ $^{2}\Pi$
4964.52	20137.3		2				
4959.38	20158.2		2	10	R_2	$04^{0}0$ $^{2}\Pi$	$00^{0}0$ $^{2}\Pi$
4955.86	20172.5		4	11	R_2	$12^{2}0$ $^{2}\Pi$	$00^{0}0$ $^{2}\Pi$
4951.05	20192.1		2	10	R_1	$04^{0}0$ $^{2}\Pi$	$00^{0}0$ $^{2}\Pi$
4941.26	20232.1		7	11	R_2	$20^{0}0$ $^{2}\Pi$	$00^{0}0$ $^{2}\Pi$
4933.92	20262.2		4	10	R_2	$20^{0}0$ $^{2}\Pi$	$00^{0}0$ $^{2}\Pi$
4932.46	20268.2		2	11	R_1	$04^{2}0$ $^{2}\Pi$	$00^{0}0$ $^{2}\Pi$
4929.34	20281.0		7	11	R_1	$20^{0}0$ $^{2}\Pi$	$00^{0}0$ $^{2}\Pi$
4921.59	20313.0		4	10	R_1	$20^{0}0$ $^{2}\Pi$	$00^{0}0$ $^{2}\Pi$
4916.96	20332.1		6	11	R_2	$12^{0}0$ $^{2}\Pi$	$00^{0}0$ $^{2}\Pi$
4913.96	20344.5		1				
4906.89	20373.8		7	11	R_1	$12^{0}0$ $^{2}\Pi$	$00^{0}0$ $^{2}\Pi$
4902.87	20390.5		1	10	R_2	$12^{0}0$ $^{2}\Pi$	$00^{0}0$ $^{2}\Pi$
4901.05	20398.1		1				
4899.97	20402.6		1	11	R_2	$21^{1}0$ $^{2}\Delta$	$01^{1}0$ $^{2}\Delta$
4892.12	20435.3		2	10	R_1	$12^{0}0$ $^{2}\Pi$	$00^{0}0$ $^{2}\Pi$
4891.79	20436.7		2	11	R_1	$12^{2}0$ $^{2}\Pi$	$00^{0}0$ $^{2}\Pi$
4891.60	20437.5		2	11	R_1	$21^{1}0$ $^{2}\Delta$	$01^{1}0$ $^{2}\Delta$
4882.07	20477.4		2	11	R_2	$21^{1}0$ $^{2}\Sigma^{(+)}$	$01^{1}0$ $^{2}\Sigma^{(+)}$
4881.05	20481.7		2	11	R_1	$21^{1}0$ $^{2}\Sigma^{(+)}$	$01^{1}0$ $^{2}\Sigma^{(+)}$
4734.78	21144.4		3				
4727.30	21147.8		3	11	R_2	$14^{0}0$ $^{2}\Pi$	$00^{0}0$ $^{2}\Pi$
4719.49	21182.8		4	11	R_1	$14^{0}0$ $^{2}\Pi$	$00^{0}0$ $^{2}\Pi$
4704.19	21251.7		2				
4700.71	21267.4		2	10	R_1	$14^{0}0$ $^{2}\Pi$	$00^{0}0$ $^{2}\Pi$
4694.85	21294.0		2	11	R_2	$22^{0}0$ $^{2}\Pi$	$00^{0}0$ $^{2}\Pi$
4694.08	21297.5		2				
4685.82	21335.0		1	11	R_1	$22^{0}0$ $^{2}\Pi$	$00^{0}0$ $^{2}\Pi$
4666.85	21421.7		1				
4666.27	21424.4		1				
4506.07	22186.1		1	11	R_2	$16^{0}0$ $^{2}\Pi$	$00^{0}0$ $^{2}\Pi$
4503.00	22201.2		1	11	R_1	$16^{0}0$ $^{2}\Pi$	$00^{0}0$ $^{2}\Pi$
4502.51	22203.6		1	11	R_2	$24^{0}0$ $^{2}\Pi$	$00^{0}0$ $^{2}\Pi$
4496.80	22231.8		1	11	R_1	$24^{0}0$ $^{2}\Pi$	$00^{0}0$ $^{2}\Pi$
4486.22	22284.2		1				
4477.30	22328.6		1	10	R_1	$24^{0}0$ $^{2}\Pi$	$00^{0}0$ $^{2}\Pi$
4349.04	22987.1		7	11	R_2	$00^{0}2$ $^{2}\Pi$	$00^{0}0$ $^{2}\Pi$
4348.06	22992.3		1	11	R_2	$01^{1}2$ $^{2}\Delta$	$01^{1}0$ $^{2}\Delta$
4340.47	23032.5		7	11	R_1	$00^{0}2$ $^{2}\Pi$	$00^{0}0$ $^{2}\Pi$
4340.02	23034.9		2	11	R_1	$01^{1}2$ $^{2}\Delta$	$01^{1}0$ $^{2}\Delta$
4335.39	23059.5		2	11	R_2	$01^{1}2$ $^{2}\Sigma^{(+)}$	$01^{1}0$ $^{2}\Sigma^{(+)}$
4335.01	23061.5		2	11	R_1	$01^{1}2$ $^{2}\Sigma^{(+)}$	$01^{1}0$ $^{2}\Sigma^{(+)}$
4314.23	23172.6		3	10	R_2	$00^{0}2$ $^{2}\Pi$	$00^{0}0$ $^{2}\Pi$
4305.89	23217.5		4	10	R_1	$00^{0}2$ $^{2}\Pi$	$00^{0}0$ $^{2}\Pi$
4305.14	23221.5		1	11	R_2	$26^{0}0$ $^{2}\Pi$	$00^{0}0$ $^{2}\Pi$
4302.64	23235.0		2	11	R_1	$26^{0}0$ $^{2}\Pi$	$00^{0}0$ $^{2}\Pi$
4168.88	23980.5		4	11	R_2	$02^{0}2$ $^{2}\Pi$	$00^{0}0$ $^{2}\Pi$
4162.89	24015.0		5	11	R_1	$02^{0}2$ $^{2}\Pi$	$00^{0}0$ $^{2}\Pi$
4135.10	24176.4		2	10	R_2	$02^{0}2$ $^{2}\Pi$	$00^{0}0$ $^{2}\Pi$
4129.29	24211.4		2	10	R_1	$02^{0}2$ $^{2}\Pi$	$00^{0}0$ $^{2}\Pi$
4002.17	24979.4		2	11	R_2	$04^{0}2$ $^{2}\Pi$	$00^{0}0$ $^{2}\Pi$
3997.41	25009.1		3	11	R_1	$04^{0}2$ $^{2}\Pi$	$00^{0}0$ $^{2}\Pi$
3964.82	25214.7		1	10	R_1	$04^{0}2$ $^{2}\Pi$	$00^{0}0$ $^{2}\Pi$

TABLE III (*Concluded*)

λ_{air},[a] Å	Present work ν_{vac}, cm^{-1}	Soulen ν_{vac}, cm^{-1}	I	Isotope	Branch	Upper level	Lower level
Band heads of the system $B\ ^2\Sigma_u^+$–$X\ ^2\Pi_g$ of BO_2							
4090.70	24438.8		10	11	Q_2	$00^00\ ^2\Sigma^+$	$00^00\ ^2\Pi$
4090.60	24439.4			11	$^QR_{12}$	$00^00\ ^2\Sigma^+$	$00^00\ ^2\Pi$
4090.07	24442.6		5	10	Q_2	$00^00\ ^2\Sigma^+$	$00^00\ ^2\Pi$
4089.92	24443.5			10	$^QR_{12}$	$00^00\ ^2\Sigma^+$	$00^00\ ^2\Pi$
4081.53	24493.7		5	11	$Q_2+^QR_{12}$	$01^10\ ^2\Pi$	$01^10\ ^2\Delta$
4081.48	24494.0			11			
4080.08	24502.4		2				
4065.53	24590.1		10	11	R_1	$00^00\ ^2\Sigma^+$	$00^00\ ^2\Pi$
4065.39	24590.9			11	$^RQ_{21}$	$00^00\ ^2\Sigma^+$	$00^00\ ^2\Pi$
4065.06	24592.9		5	10	R_1	$00^00\ ^2\Sigma^+$	$00^00\ ^2\Pi$
4064.95	24593.6			10	$^RQ_{21}$	$00^00\ ^2\Sigma^+$	$00^00\ ^2\Pi$
4057.16	24640.8		5	11	$R+^RQ_{21}$	$01^10\ ^2\Pi$	$01^10\ ^2\Delta$
4051.86	24673.1		6	11	Q_1	$01^10\ ^2\Pi$	$01^10\ ^2\Sigma^{(+)}$

NOTES: [a]Where two frequencies are listed the wavelength corresponds to that measured in this work.
The figures 10 and 11 in the column headed Isotope refer to the molecules $^{10}BO_2$ and $^{11}BO_2$ respectively.
The intensities are visual estimates taken from the photographic plates.

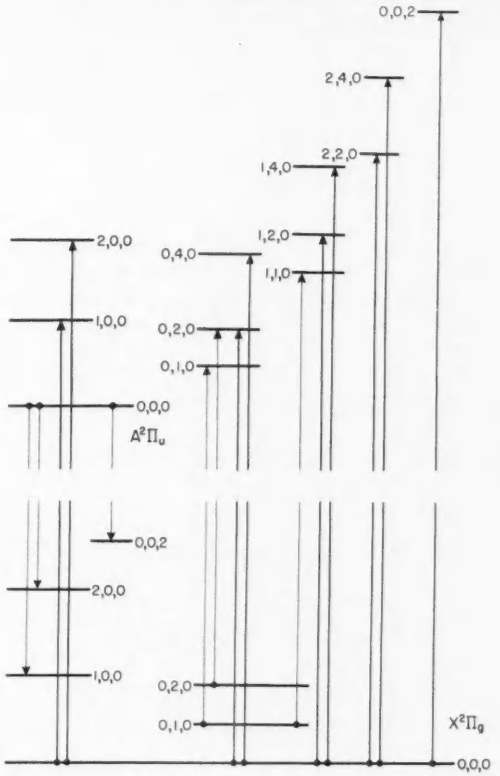

FIG. 7. The observed transitions in the A system of BO_2. Spin orbit and Renner interactions have been omitted in this diagram.

The preceding discussion has shown that very few vibronic levels in BO_2 are entirely unaffected by Fermi resonance. The Renner effect in $A\ ^2\Pi_u$ is of such a magnitude that levels of the type $02^00(^2\Pi_u)$ and $02^20(^2\Pi_u)$ are nearly degenerate in the absence of resonance. If it is assumed, as has been indicated previously, that levels such as $02^20(^2\Pi_u)$ are little affected by the resonance, it is possible to estimate the magnitude of the shifts produced by the Fermi interaction and to make appropriate corrections. If this is done the following frequencies, in cm^{-1}, result:

$$\begin{array}{lrr} A\ ^2\Pi_u & \nu_1 = 994 & 2\nu_2 = 947 \\ & 2\nu_1 = 1986 & 4\nu_2 = 1831 \\ & \nu_1+2\nu_2 = 2007 & 2\nu_3 = 4714. \end{array}$$

For the ground state, $X\ ^2\Pi_g$, the best value of ν_1 seems to be about 1070; ν_2 can be obtained from the 010–010 band of system A and the estimated frequency in the upper state and is found to be 464.

The Renner parameters, $\epsilon\omega_2$, for states A and X were determined by fitting the 010–010 subbands of systems A and B to equations (1).

In the B system the only band other than 000–000 to be observed was 010–010 from which, together with the known value of ν_2'', ν_2' was found to be 505. This frequency, together with the small isotope shift in the 000–000 band of about 3 cm^{-1}, allows ν_3' to be estimated at about 1410.

6. ROTATIONAL ANALYSIS

6.1. Rotational Energy Levels

Hougen (1961) has shown that if third-order corrections and a small constant term are ignored, the rotational energies of $^2\Pi$ vibronic levels with $v_2 = 0$ can be expressed by the equations of Hill and Van Vleck (1928). These equations have been used in this work. Hougen has further shown that the rotational energies of the pair, μ and κ, of $^2\Sigma$ levels (μ and κ are convenient symbols to distinguish these two levels, and by definition $\kappa(^2\Sigma)$ lies above $\mu(^2\Sigma)$) formed for odd values of v_2 can be represented by:

$$\begin{array}{ll} \kappa(^2\Sigma) & \begin{cases} F_1^{\kappa}(N) = r_{v_2,K}+\frac{1}{2}\gamma_v^{\kappa}+B_{\text{eff}}^{\kappa}N(N+1)+\frac{1}{2}\gamma_v^{\kappa}N, \\ F_2^{\kappa}(N) = r_{v_2,K}+\frac{1}{2}\gamma_v^{\kappa}+B_{\text{eff}}^{\kappa}N(N+1)-\frac{1}{2}\gamma_v^{\kappa}(N+1), \end{cases} \\ \mu(^2\Sigma) & \begin{cases} F_1^{\mu}(N) = -r_{v_2,K}+\frac{1}{2}\gamma_v^{\mu}+B_{\text{eff}}^{\mu}N(N+1)+\frac{1}{2}\gamma_v^{\mu}N, \\ F_2^{\mu}(N) = -r_{v_2,K}+\frac{1}{2}\gamma_v^{\mu}+B_{\text{eff}}^{\mu}N(N+1)-\frac{1}{2}\gamma_v^{\mu}(N+1), \end{cases} \end{array} \tag{3}$$

where

$$B_{\text{eff}} = B_v[1\pm BA^2/(2r_{v_2,K})^2] \tag{4}$$

and

$$\gamma_v = 2B_v[1-|(v_2+1)\epsilon\omega_2/2r_{v_2,K}|\pm BA^2/(2r_{v_2,K})^2]. \tag{5}$$

Here the + sign in $\pm$ refers to $\kappa(^2\Sigma)$ and the − sign to $\mu(^2\Sigma)$. $2r_{v_2,K}$ is the separation of the two $^2\Sigma$ states and is given by equation (2). The equations (3) show that the $^2\Sigma$ vibronic levels can be treated as if they were $^2\Sigma$ levels of a

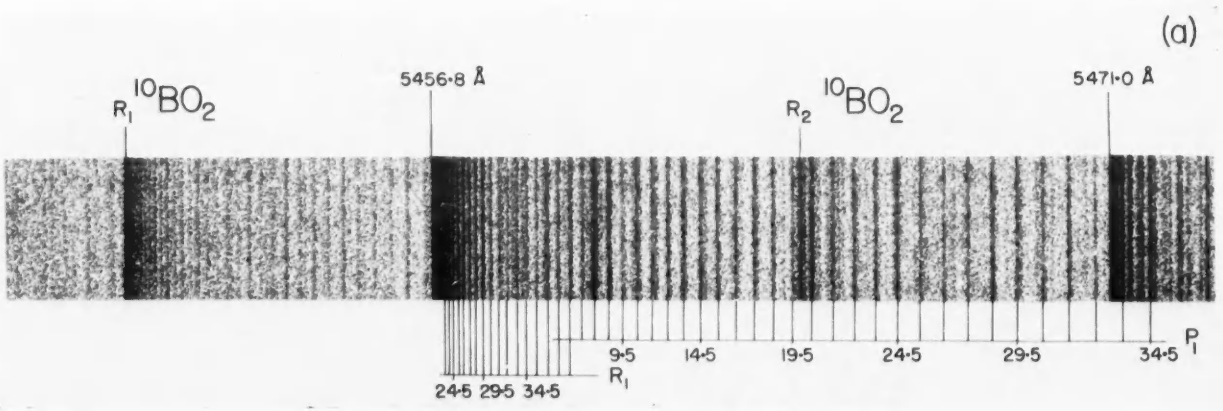

FIG. 8*a*. The 000–000 band of the A system. The $^2\Pi_{3/2}$–$^2\Pi_{3/2}$ subband.

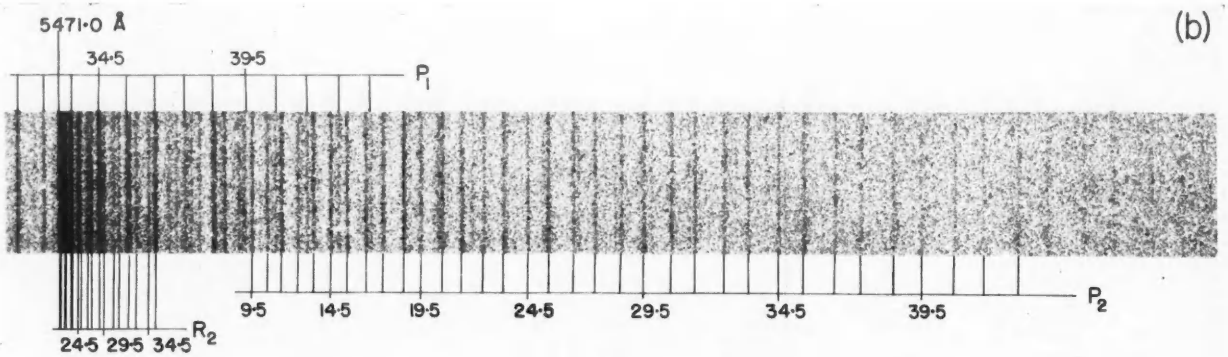

FIG. 8*b*. The 000–000 band of the A system. The $^2\Pi_{1/2}$–$^2\Pi_{1/2}$ subband.

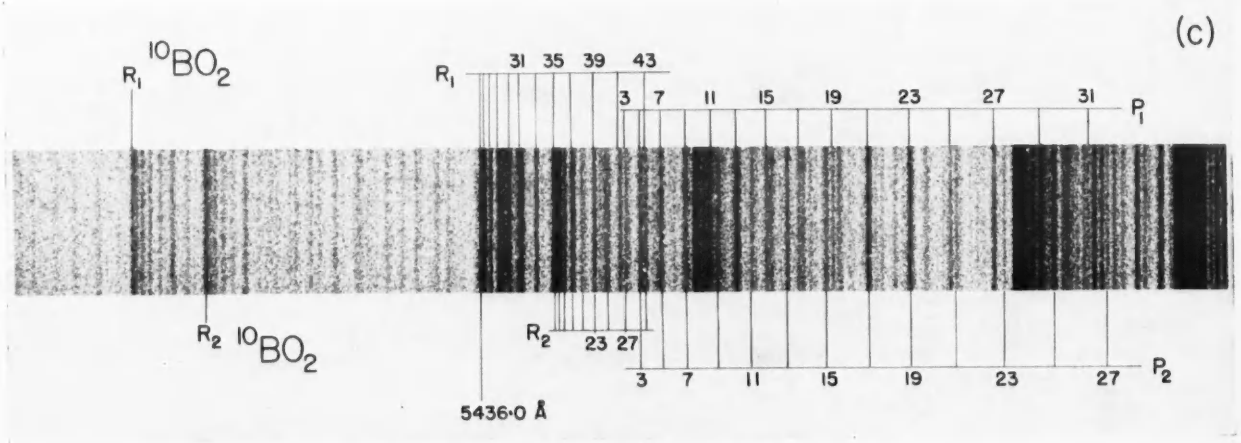

FIG. 8c. The 01^10–01^10 $^2\Sigma^{(+)}$–$^2\Sigma^{(+)}$ subband of the A system.

diatomic molecule in which γ, the spin-doubling constant, can be as large as $2B$, but is always positive.

Vibronic levels with $K \neq 0$ or 1 will not be dealt with here since no such bands were found sufficiently free from overlapping structure to permit rotational analysis.

6.2. The B System

The 000–000 band is of the type $^2\Sigma_u^+$–$^2\Pi_g$ and an energy level diagram of such a transition has been given by Bueso-Sanllehi (1941). In all, 12 branches are expected of which eight proved to be comparatively free from overlapping. Standard methods were used in the analysis and determination of constants (see, for example, Jevons 1932 and Herzberg 1950). The line frequencies together with the rotational assignments are given in Table IV and the derived constants in Table V.

6.3. System A. $^2\Pi_u$–$^2\Pi_g$ Vibronic Bands

Several $^2\Pi_u$–$^2\Pi_g$ bands were sufficiently free from overlapping structure to permit complete analyses to be made. Each band consists of eight branches; however, due to the absence of alternate rotational levels and the relatively large change in spin–orbit coupling constant ($\Delta A \simeq 47$ cm^{-1}), each band is separated into two subbands, which appear to have only single P and R branches. Some of the branches are staggered. Figure 8*a* shows the 000–000 $^2\Pi_{3/2}$–$^2\Pi_{3/2}$ subband. Figure 8*b* shows the 000–000 $^2\Pi_{1/2}$–$^2\Pi_{1/2}$ subband in which the branches are staggered. The analysis was straightforward and its correctness was confirmed by comparison of combination differences obtained from these bands and from the 000–000 band of system B. In addition to absorption bands having the ground state as their lower level, one emission band, 000–100, was analyzed. The line frequencies, together with the rotational assignments, are given in Table VI. Constants for the upper state of the 000–000 band of system A were determined by adding appropriate ground state term values to the line frequencies and fitting the resulting upper state terms to the equations of Hill and Van Vleck (1928). The constants for the remaining levels were obtained by taking differences between bands having a common lower state (or common upper state) as described by Herzberg (1950). The constants obtained in this way are set out in Table VII.

6.4. Systems A and B. 'Hot' Absorption Bands

Characteristic double-headed bands, which can be seen clearly in Fig. 1 and in more detail in Fig. 8*c*, were observed to the violet of each band group in system A. These bands have double the line spacing associated with the $^2\Pi$–$^2\Pi$ bands and have proved to be of the type $^2\Sigma$–$^2\Sigma$.

It has been indicated in Section 4 that, when one quantum of the bending vibration is excited in a linear symmetric triatomic molecule in a $^2\Pi_g$ electronic state, three sublevels are formed, $^2\Sigma_u^{(+)}$, $^2\Sigma_u^{(-)}$, and $^2\Delta_u$. The strongest 'hot' bands must have the lower of the $^2\Sigma$ states as their initial level. Rotational analysis has shown that only odd values of N are present in this level, proving it to be $^2\Sigma_u^{(+)}$ rather than $^2\Sigma_u^{(-)}$ (Herzberg 1945, p. 16). Thus $\epsilon\omega_2$, the Renner parameter, is negative ($\epsilon\omega_2$ is defined as positive or negative as $\nu(\Sigma^+)$–$\nu(\Sigma^-)$ is positive or negative).

TABLE IV

The 00⁰0–00⁰0 band of the $B\,^2\Sigma_u^+$–$X\,^2\Pi_g$ system

$J+\frac{1}{2}$	${}^sR_{21}$	R_1	${}^RQ_{21}$	Q_1	${}^QP_{21}$	P_1	R_2	${}^QR_{12}$	Q_2	${}^PQ_{12}$	P_2	${}^OP_{12}$
1								24434.08*	24434.08*			
2	24585.58*			24582.24*	24582.24					24433.06*	24433.06*	
3		24583.84*	24583.84*					34.79*	34.79*			24430.78*
4	87.31*			81.60*	81.60*					32.36*	32.36*	
5		84.47*	84.47*			24578.58*		35.23*	35.23*			29.12*
6				80.85*	80.85*					31.61*	31.61*	
7		85.05*	85.05*			76.73*		35.76*	35.76*			27.37*
8				80.16*	80.16*					30.78*	30.78*	
9		85.58*	85.58*			74.61		36.27*	36.27*			25.32*
10				79.40*	79.40*					30.01*	30.01*	
11		86.04*	86.04*			72.45*		36.72*	36.72*			23.17*
12	94.63			78.58*	78.58*		24445.19*			29.12*	29.12*	
13		86.52*	86.52*			70.37*						20.95*
14	96.44			77.79	77.63		46.91			28.24	28.11	
15		86.90*	86.90*			68.24*						18.72
16	98.16			76.88	76.73*		48.52			27.37*	27.20	
17		87.67*	87.31*			66.03*						16.60*
18	99.89			76.11	75.83		50.12			26.34	26.18	
19		88.07*	87.67*			63.98*						14.45*
20	24601.52			75.23	74.83		51.68			25.32*	25.10	
21		88.43*	88.07*			61.75*						11.95
22	03.19			74.34	73.97		53.20			24.30	23.92	
23		88.76*	88.43*			59.54						09.55*
24	04.81			73.34	72.99		54.64			23.17*	22.89	
25		89.17*	88.76*			57.24						07.16
26	06.39			72.45*	72.02		56.09			22.09	21.68	

TABLE IV (*Concluded*)

$J+\frac{1}{2}$	$^{S}R_{21}$	R_1	$^{R}Q_{21}$	Q_1	$^{Q}P_{21}$	P_1	R_2	$^{Q}R_{12}$	Q_2	$^{P}Q_{12}$	P_2	$^{O}P_{12}$
27			24589.17*			24554.97						24404.73
28	24607.93			24571.36	24570.95		24457.47			24420.95*	24420.45	
29						52.67						02.30
30	09.51			70.37*	69.86		58.86			19.71	19.23	
31						50.34						24399.77
32	10.99			69.28	68.74		60.13		24438.78[h]	18.48	17.94	
33						47.95						97.21
34	12.48			68.24*	67.64		61.39	24439.37[h]		17.17	16.60*	
35						45.54						94.66
36	13.89			67.09	66.64		62.65			15.87	15.29	
37						43.11						91.96
38	15.29			66.03*	65.29		63.86			14.45*	13.91	
39						40.68						89.35
40	16.65			64.76			65.09			13.07	12.42	
41												
42	18.05			63.98*			66.18				10.95	
43		24590.94[h]	90.08[h]			35.69						
44	19.43			62.89							09.55*	
45						33.15						
46	20.76			61.75*								
47						30.59						
48	22.05											
49						28.04						
50	23.23											
51						25.35						

*Denotes blended line.
[h]Denotes band head.

TABLE V

Constants obtained from the 000–000 band of the B system

The upper $B\,^2\Sigma_u^+$ state	
$B_{000} = 0.3250 \pm 0.0003$	$D \simeq 1.3 \times 10^{-7}$*
$\nu_{000} = 24507.9_9$	$\gamma = 0.0158$
The lower $X\,^2\Pi_g$ state	
$B_{000} = 0.3292 \pm 0.0003$	$D \simeq 1.3 \times 10^{-7}$*
$A = -148.5_8$	$p = 0.006_5$†

*Calculated with $D = 4B^3/\omega_1^2$, $\omega_1 \simeq 1070$.
†The width of the Λ-doublets is given by $\Delta\nu = p(J+\frac{1}{2})$.

TABLE VI

The $A\,^2\Pi_u$–$X\,^2\Pi_g$ system

$J+\frac{1}{2}$	R_{1a}	R_{1b}	P_{1a}	P_{1b}	R_{2a}	R_{2b}	P_{2a}	P_{2b}
				00°0–00°0				
1					18268.88*			
2		18316.70*				18269.46*		18266.94
3	18317.25*		18313.49*		69.84*			
4		17.74*		18312.76*		70.50*		65.46*
5	18.20*		11.98*		70.84*		18264.68	
6		18.61*		11.14*		71.40*		63.88*
7	18.98*		10.29*		71.57*		62.86*	
8		19.32*		09.43*		72.24*		62.11
9	19.64*		08.46*		72.24*		61.13	
10		19.92*		07.52*		72.79*		60.20
11	20.12*		06.49*		72.79*		59.18	
12				05.43*		73.19*		58.16
13			04.35*		73.19*		57.02	
14				03.25*		73.47*		55.96
15			02.03*		73.47*		54.75*	
16				00.86				53.63
17	20.58[h]		18299.61		73.47*	h	52.32	
18				18298.33				51.14
19			97.04				49.70*	
20				95.67		73.47*		48.50
21			94.34*		73.19*		47.02	
22		20.12*		92.87		73.19		45.69
23	19.92*		91.39		72.79*		44.14	
24		19.64*		89.89*		72.79		42.78
25	19.32*		88.37		72.24*		41.13	
26		18.98*		86.76		72.24		39.70
27	18.61*		85.16		71.57*		37.94	
28		18.20*		83.50		71.40		36.46
29	17.74*		81.82*		70.84*		34.64	
30		17.25*		80.08		70.50*		33.11
31	16.70*		78.30		69.84*		31.20	
32		16.10		76.49		69.46*		29.59
33	15.52		74.66		68.75		27.56	
34		14.88		72.79		68.24		25.91
35	14.19		70.84*		67.39		23.83	
36		13.49*		68.88		66.94*		22.08
37	12.76*		66.94		66.01		19.94	
38		11.98*		64.85		65.46		18.17
39	11.14*		62.86		64.46		15.87	
40		10.29*		60.80		63.88		14.04
41	09.43*		58.56				11.70	
42		08.46*		56.39				09.78
43	07.52*		54.17				07.38	
44		06.49*		51.95				05.38
45	05.43*		49.70				02.87	
46		04.35*		47.24				00.81
47	03.25*		44.95				18198.25	
48		02.03*		42.60				

TABLE VI (*Continued*)

$J+\frac{1}{2}$	R_{1a}	R_{1b}	P_{1a}	P_{1b}	R_{2a}	R_{2b}	P_{2a}	P_{2b}
				00°0–10°0				
2		17259.95*						
3	17260.56*							
4		60.99*						
5	61.55*							
6		61.85*		17254.37				
7	62.34*		17253.65				17186.93	
8		62.65*		52.72				17186.00
9	63.07*		51.84				85.07	
10		63.23*		50.94				84.14
11							83.16	
12				48.84				82.12
13			47.82				80.99	
14				46.68				79.96
15			45.57		17197.41[h]		78.73	
16		64.18[h]				17197.41[h]		77.63
17	64.18[h]		43.17				76.37	
18				41.98				75.22
19			40.69				73.80	
20				39.39				72.63
21			38.02				71.18	
22				36.70				69.90
23			35.22		97.08*		68.38	
24				33.82		97.08*		67.01
25	63.23*		32.26		96.47*		65.39	
26		63.07*		30.82		96.47*		
27	62.65*		29.19		95.98		62.32	
28		62.34*		27.66				60.84
29	61.85*		25.94		95.19		59.07	
30		61.55*		24.38		94.84		57.59
31	60.99*		22.61		94.33			
32		60.56*		20.94		93.92		
33	59.95*		19.16		93.33			
34		59.44		17.41		92.76		
35					92.15			
36						91.57		
37					90.74			
38						90.33		
				02°0–00°0				
8				19228.42				19186.58
9			19227.50				19185.64	
10				26.52				84.72
11			25.53				83.69	
12				24.47				82.86*
13			23.44				81.59	
14				22.27				80.53
15			21.17				79.33	
16				19.97				78.25
17	19239.80		18.80				76.89	
18				17.67				75.79
19			16.23				74.43	
20				14.90				73.20
21			13.55		19197.98*		71.80	
22				12.17		19197.98*		70.43
23			10.71				68.93	
24		19239.18		09.27		97.49		67.50
25	38.78		07.72		97.31		65.96	
26				06.28		97.04		64.52
27	38.05		04.56		96.58		62.87	
28				03.06		96.29*		61.28
29	37.50		01.29		95.86		59.60	
30		37.16*				95.45		58.05
31	36.34		19197.98		94.95		56.16	
32		36.04		19196.29*		94.47*		54.55
33	35.35		94.47*		93.89		52.73	

TABLE VI (*Continued*)

$J+\frac{1}{2}$	R_{1a}	R_{1b}	P_{1a}	P_{1b}	R_{2a}	R_{2b}	P_{2a}	P_{2b}
34		19234.87		19192.70*		19193.36		19150.94
35	19234.06		19190.71*		19192.70*		19149.00	
36		33.56		89.00		92.01		47.23
37			86.75*		91.39		45.21	
38				84.99		90.71*		43.28
39			82.86*		89.96		41.28	
40				80.98				39.27
41					88.32		37.18	
42						87.42		35.08
43					86.75*		32.93	
44								30.75
45							28.55	
46								26.26
47							23.89	
48								21.66
49							19.30	
50								16.77
51							14.61	
52								11.93
				10⁰0–00⁰0				
6				19331.96				
7			19331.08					
8				30.20				19285.55
9			29.24				19284.67	
10				28.24				83.81
11			27.27				82.63	
12				26.22				81.68
13			25.15				80.54	
14				24.03				
15			22.80				78.28	
16		19341.31[h]						77.05
17	19341.31[h]		20.39				75.74	
18				19.06				74.60
19			17.75		19296.93*		73.19	
20				16.34		19296.93*		71.94
21			15.01		96.65*		70.37*	
22				13.57		96.65*		69.14
23			12.10		96.18*		67.72	
24				10.56		96.18*		66.20
25	40.10		09.06		95.55*		64.52	
26		39.68		07.43		95.55*		63.11
27	39.30		05.84		94.92*		61.32	
28		38.86		04.15		94.92*		59.83
29	38.41		02.50		94.00*		58.04	
30		37.88		00.71		94.00*		56.40
31	37.42							
32		36.78				92.76		52.87
33	36.10				91.94		52.87	
34						91.52		49.20
35							49.20	
36						90.22		
37					89.17			
38						88.59		
39					87.52			
				04⁰0–00⁰0				
6				20124.13				
7			20123.14					
8				22.46				
9			21.31					
10				20.40				
11			19.36					
12				18.45				

TABLE VI (*Continued*)

$J+\frac{1}{2}$	R_{1a}	R_{1b}	P_{1a}	P_{1b}	R_{2a}	R_{2b}	P_{2a}	P_{2b}
13			20117.31					
14				20116.32				
15			15.13					
16		20133.76[h]		13.91		20100.56[h]		
17	20133.76[h]		12.66		20100.56[h]			
18				11.54				
19			10.21					
20				08.98				
21			07.56					
22				06.34				
23			04.70					
24		33.49		03.47				
25	32.91*		01.80					
26		32.91*		00.56*				
27	32.25*							
28		32.25*						
29	31.51*							
30		31.51*						
31	30.62*							
32		30.62*						
33	29.64*							
34		29.64*						
35	28.49*							
36		28.49*						
37	27.22*							
38		27.22*						
39	25.76*							
40		25.76*						
				$2^{0}0-0^{0}0$				
9							20219.88	
10								20218.96
11							17.92	
12								16.94
13							15.77	
14								14.77
15							13.52	
16		20281.02[h]				20232.09[h]		12.37
17	20281.02[h]				20232.09[h]		11.23	
18								09.82
19							08.41	
20								07.06
21							05.70	
22								04.36
23							02.82	
24								01.47
25							20199.65	
26								20198.29
27							96.64	
				$1^{2}0-0^{0}0$				
8				20362.68				
9			20361.78					
10				60.64				
11			59.83					
12				58.60				
13			57.56					
14				56.40				
15			55.38					
16		20373.75[h]		54.04		20332.14[h]		
17	20373.75[h]		52.87		20332.14[h]			
18				51.51				
19			50.24					

TABLE VI (*Concluded*)

$J+\frac{1}{2}$	R_{1a}	R_{1b}	P_{1a}	P_{1b}	R_{2a}	R_{2b}	P_{2a}	P_{2b}
20				20349.83				
21			20347.52					
22				46.04				
23			44.51					
24				43.09				
25								
26								
27								
28								
29								
30		20370.54						
31	20370.02							
32		69.49						
33	69.07							
34		68.28						
35	67.73							
				$00^{0}2-00^{0}0$				
2		23029.77*						
3	23030.28*		23026.61*					
4		30.72*		23025.83*				
5	31.09*		25.00*					
6		31.46*		24.16*				
7	31.85*		23.23*					
8				22.27*				
9			21.25*				22975.68	
10				20.17*				22974.66
11			19.09*				73.48	
12		32.49[h]		17.93*		22987.11[h]		72.44
13	32.49[h]		16.72*		22987.11[h]		71.14	
14				15.48				70.03
15			14.20				68.62	
16				12.86				67.43
17			11.46				65.94	
18				10.05				64.63
19	31.85*		08.56				63.01	
20		31.46*		07.04				61.65
21	31.09*		05.48		85.60*		59.96	
22		30.72*		03.86		85.60*		58.50*
23	30.28*		02.20		84.89*		56.62	
24		29.77*		00.49		84.89*		55.18
25	29.23		22998.70		83.84*		53.22	
26		28.65		22996.92		83.84*		51.66
27	28.02		95.08		82.75		49.75	
28		27.34		93.18		82.27		48.01
29	26.61*		91.22		81.24		45.72	
30		25.83*		89.21		80.78		44.03
31	25.00*		87.11*				41.74	
32		24.16*		85.02		79.23		39.92
33	23.23*		82.89				37.48	
34		22.27*		80.78*		77.51		35.65
35	21.25*		78.56*		76.22*		33.20	
36		20.17*		76.22*		75.41		31.19
37	19.09*		73.92*		73.92		28.74	
38		17.93*		71.58*		73.22		26.56
39	16.72*		69.16*		71.58*		23.84	
40		15.18		66.64*		70.88		21.75
41	13.72		64.17*		69.16*			
42		12.26				68.27		
43	10.76		58.50*		66.64*			
44		09.28				65.44		
45	07.68				63.60			
46		06.00				62.49		
47	04.29							

*Denotes blended line.
[h]Denotes band head.

TABLE VII

Constants obtained from $^2\Pi_u$–$^2\Pi_g$ bands of system A

$B_{000} = 0.3106 \pm 0.0003$ $\quad D \simeq 1.2 \times 10^{-7}$*
$A = -101.3_0$ $\quad p = 0.014_6$
$\nu_{000} = 18291.5$

$A\,^2\Pi_u$	$^2\Pi_{3/2}$	$^2\Pi_{1/2}$
$B_{000} - B_{100}$	0.0001_7	0.0002_7
ν_1	1020.7_9	1023.5_5
$B_{000} - B_{200}$	—	0.0003_1
$2\nu_1$	—	1958.7_9
$B_{000} - B_{020}$	-0.0008_0	-0.0005_8
$2\nu_2$	918.9_7	924.5_7
$B_{000} - B_{040}$	-0.0013_7	—
$4\nu_2$	1812.7_8	—
$B_{000} - B_{002}$	0.0046_5	0.0047_0
$2\nu_3$	4713.0_7	4714.8_5
$X\,^2\Pi_g$		
$B_{000} - B_{100}$	0.0015	0.00067
ν_1	1056.7_4	1076.1_5

*Calculated with $D = 4B^3/\omega_1^2$.

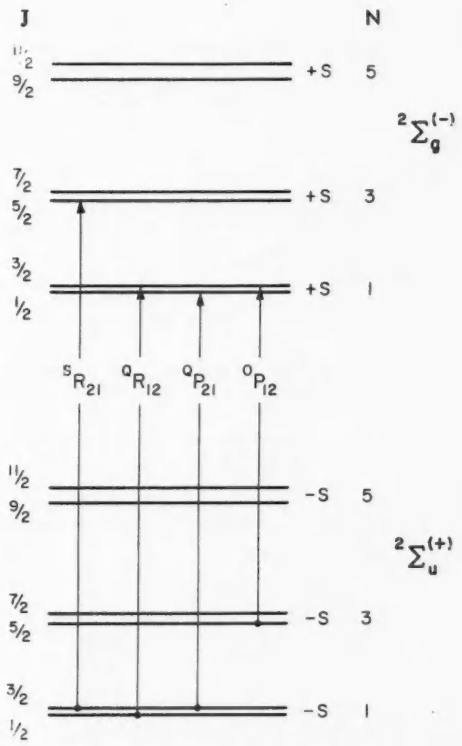

FIG. 9. Energy level diagram of a $^2\Sigma_g^{(-)}$–$^2\Sigma_u^{(+)}$ transition showing the formation of the first line of each of the four 'satellite' branches.

TABLE VIII
Hot bands

	$0,1^1,0$–$0,1^1,0$ $^2\Sigma_g^{(+)} \leftarrow {}^2\Sigma_u^{(+)}$				$0,1^1,0$–$0,1^1,0$ $^2\Sigma_g^{(-)} \leftarrow {}^2\Sigma_u^{(+)}$				$1,1^1,0$–$0,1^1,0$ $^2\Sigma_g^{(+)} \leftarrow {}^2\Sigma_u^{(+)}$				$0,1^1,0$–$0,1^1,0$ $^2\Pi_g$ (case b) $\leftarrow {}^2\Sigma_u^{(+)}$					
N	R_1	P_1	R_2	P_2	${}^SR_{21}$	${}^QP_{21}$	${}^QR_{12}$	${}^OP_{12}$	R_1	P_1	R_2	P_2	R_1	R_2	Q_1	Q_2	P_1	P_2
1	18384.39*																	
2																		
3	85.61*												24674.55				24669.84*	
4																		
5	86.95*	18379.65			18492.85				19428.73	19421.52			76.01				68.65*	
6																		
7	87.87	78.19		18376.51*	94.29				29.77	20.06		19418.41	77.14	24678.16*			67.33*	
8																		
9	88.87*	76.51	18385.39	74.21	95.55	18482.96		18477.58	30.67	18.41		16.25	78.16*	79.90*			65.86*	24667.33*
10																		
11	89.55*	74.84	85.61*	71.84	96.65	81.48		75.10	31.18	16.57	19427.60[h]	13.93	79.07	80.71			64.32*	65.86*
12																		
13	90.13	72.89	85.61*	69.34	97.63	80.06		72.38*	31.86	14.55	27.60[h]	11.27	79.90*	81.59			62.56*	64.32*
14																		
15	90.59*	70.78	85.39*	66.60	98.50	78.38	18487.76	69.34		12.52		08.61		82.71	24670.19		60.58*	62.80*
16																		
17		68.52	84.98	63.68*	99.21*	76.56	87.23	66.15	32.35[h]	10.23		05.79		84.04*	69.84*		58.85	
18																		
19	90.77[h]	66.15	84.39*	60.76*		74.59	86.47	62.91		07.79	26.53	02.68		85.16	69.19*		56.79	59.72
20																		
21		63.68*	83.74	57.52		72.38	85.62	59.57*		05.20	25.90	19399.57*	83.00*	86.11	68.65*		54.94*	58.24

TABLE VIII (*Concluded*)

	$0,1^1,0$–$0,1^1,0$ $^2\Sigma_g^{(+)} \leftarrow {}^2\Sigma_u^{(+)}$				$0,1^1,0$–$0,1^1,0$ $^2\Sigma_g^{(-)} \leftarrow {}^2\Sigma_u^{(+)}$				$1,1^1,0$–$0,1^1,0$ $^2\Sigma_g^{(+)} \leftarrow {}^2\Sigma_u^{(+)}$				$0,1^1,0$–$0,1^1,0$ $^2\Sigma_g$ (case b) $\leftarrow {}^2\Sigma_u^{(+)}$					
N	R_1	P_1	R_2	P_2	$^sR_{21}$	$^QP_{21}$	$^QR_{12}$	$^OP_{12}$	R_1	P_1	R_2	P_2	R_1	R_2	Q_1	Q_2	P_1	P_2
22																		
23	18390.59*	18360.76*	18382.80*	18354.19		18470.26	18484.59	18456.02		19402.50	19425.01	19396.38*		24686.99	24667.97*		24653.06*	24656.49
24																		
25	90.13*	57.94	81.92	50.73		67.84	83.43	52.38		19399.57*	24.00*	92.92	24684.04*	87.80	67.33*		51.13*	54.76
26																		
27	89.55*	54.90	80.63	46.90		65.32	82.12	48.57		96.38*	22.88	89.18		88.69	66.65*			53.06*
28																		
29	88.87*	51.62	79.26	43.23	18500.11	62.54	80.69	44.62	19430.39	93.15	21.52			89.49	65.86*			51.13*
30																		
31	88.02	48.35			18499.77	59.57	79.09		29.49	89.86	20.06*				65.16	24669.84*		
32																		
33	86.95*	44.90			99.21*	56.53	77.42		28.49		18.41*				64.32*	69.19*		
34																		
35					98.64	53.47	75.44								63.38	68.65*		
36																		
37	84.39*				97.91	50.44	73.39								62.56*	67.97*		
38																		
39	82.80*														61.60	67.33*		
40																		
41															60.58*	66.65*		
42																		
43															59.72	65.86*		

*Denotes blended line.
[b]Denotes band head.

In all, four subbands having $01^10(\mu^2\Sigma_u^{(+)})$ as their common lower state were analyzed. The upper states were $01^10(^2\Pi_g)$ in the $B\,^2\Sigma_u^+$ electronic state and $01^10(\mu^2\Sigma_g^{(+)})$, $11^10(\mu^2\Sigma_g^{(+)})$, and $01^10(\kappa^2\Sigma_g^{(-)})$ in the $A\,^2\Pi_u$ electronic state. The last was observed in a transition which can be regarded as $^2\Sigma^{(-)}$–$^2\Sigma^{(+)}$ and as such would normally be rigorously forbidden. However, as Pople (1960) has pointed out, the symmetry of these states has been reduced so that their classification as $^2\Sigma^+$ or $^2\Sigma^-$ is no longer precise, particularly if the spin is strongly coupled to the internuclear axis, and there is a tendency towards the formation of $^2\Sigma_{1/2}$ (case *a*) states. Transitions such as that mentioned above then become allowed. An energy level diagram of this type of transition is given in Fig. 9, which shows the formation of the first line in each of the four 'satellite' branches.

In the electronic state $B\,^2\Sigma_u^+$, it was assumed that the energy levels of $01^10(^2\Pi_g)$ could be expressed adequately by:

$$\begin{aligned} F_1(N) &= B[N(N+1)-K^2]+\tfrac{1}{2}\gamma N\pm\tfrac{1}{2}qN(N+1), \\ F_2(N) &= B[N(N+1)-K^2]-\tfrac{1}{2}\gamma(N+1)\pm\tfrac{1}{2}qN(N+1). \end{aligned} \tag{6}$$

These formulae describe the energy levels of a pure case (*b*) $^2\Pi$ state ($A = 0$) with terms in γ included (see Herzberg 1950, p. 232). The $01^10(^2\Pi_g)$ state is electronically $^2\Sigma_u^+$ and thus might be expected to belong to Hund's case (*b*). The line frequencies and rotational assignments are given in Table VIII and the constants are collected in Table IX.

TABLE IX

Constants obtained from the 'hot' absorption bands

Electronic state	$B\,^2\Sigma_u^+$	$A\,^2\Pi_u$	$A\,^2\Pi_u$	$A\,^2\Pi_u$	$X\,^2\Pi_g$
Vibronic state	$01^10(^2\Pi_g)$	$01^10(^2\Sigma_g^{(+)})$	$01^10(^2\Sigma_g^{(-)})$	$11^10(^2\Sigma_g^{(+)})$	$01^10(^2\Sigma_u^{(+)})$
B^*	0.325_1	0.3108_1	0.3124_8	0.3107_1	0.3307_5
γ	0.016	0.474	0.444	0.454	0.163
q	0.000_3	—	—	—	—
T	$24672.9+a$	18382.8_8+a	18487.5_1+a	19424.7_8+a	a†

*The relative accuracy of these B values is indicated by the number of figures quoted but the absolute accuracy is probably not better than ± 0.001.

†The direct observation of the height of this level is prevented because of the operation of the $g \leftrightarrow u$, $g \leftrightarrow g$, $u \leftrightarrow u$ selection rules.

It was difficult to obtain good values of γ from the data since the quantities easily measured with precision are either $(\gamma'-\gamma'')$ or $(\gamma'+\gamma'')$ depending on the type of band. The values quoted were obtained by assuming the value for $01^10(^2\Pi_g)$ to be identical with that of 000 in $B\,^2\Sigma_u^+$. It was noted that the *l*-type doubling constant for $01^10(^2\Pi_g)$, $q = 0.000_3$, was in reasonable agreement with that calculated from the formulae of de Heer and Nielsen (1952) and Nielsen (1950) which give $q = 0.0006$.

$$\begin{aligned} q_0 &= 2B^2/\omega_2[1+4\omega_2^2/(\omega_3^2-\omega_2)], \\ q &= \tfrac{1}{2}q_0(v_2+1). \end{aligned} \tag{7}$$

The main molecular constants for the observed states of BO_2 are collected in Table X.

TABLE X

Summary of the main molecular constants of BO_2

	$B\ ^2\Sigma_u^+$	
$T_{000} = 24507.9_9$	$\nu_1 = ?$	
$B_{000} = 0.3250 \pm 0.0003$	$\nu_2 = 505$	
$r_{000} = 1.2733 \pm 0.0006$ Å	$\nu_3 \simeq (1410)^*$	
	$A\ ^2\Pi_u$	
$T_{000} = 18291.5_9$	$\alpha_1 = +0.0002$	$\omega_1 = 994$
$B_{000} = 0.3106 \pm 0.0003$	$\alpha_2 = -0.0003$	$\omega_2 = 502$
$r_{000} = 1.3025 \pm 0.0006$ Å	$\alpha_3 = +0.0023$	$\frac{1}{2}(2\nu_3) = 2357$
$x_{11} \simeq 0$		
$x_{22} \simeq -7$	$\epsilon\omega_2 = -13.1$	
$x_{12} \simeq 16$	$A_{000} = -101.3_0$	
	$X\ ^2\Pi_g$	
$B_{000} = 0.3292$	$\nu_1 = 1070$	
$r_{000} = 1.2653 \pm 0.0006$ Å	$\nu_2 = 464$	
$\epsilon\omega_2 \simeq -92.2$	$\frac{1}{2}(2\nu_3) = 1322$	
$A_{000} = -148.5_8$		

NOTE: Unless otherwise stated all constants are in cm^{-1}.
*Estimated from the isotopic shift of the 003–000 band.

7. DISCUSSION

7.1. Electron Configuration

The electron configurations of the low-lying states of BO_2 are given below:

$$\ldots\ldots (\sigma_g)^2\ (\sigma_u)^2\ (\pi_u)^4\ (\pi_g)^3 \ldots\ldots X\ ^2\Pi_g \text{ (inv.)},$$

$$\ldots\ldots (\sigma_g)^2\ (\sigma_u)^2\ (\pi_u)^3\ (\pi_g)^4 \ldots\ldots A\ ^2\Pi_u \text{ (inv.)},$$

$$\ldots\ldots (\sigma_g)^2\ (\sigma_u)\ \ (\pi_u)^4\ (\pi_g)^4 \ldots\ldots B\ ^2\Sigma_u^+.$$

These three states give rise to the two transitions observed in this work. These are the same two transitions that have been observed by Bueso-Sanllehi (1941) and Mrozowski (1941, 1942, 1947) in the isoelectronic molecule CO_2^+.

When the molecule is bent, the ground state is split into two levels which may be written:

$$\ldots\ldots (a_1)^2\ (b_2)^2\ (b_1)^2\ (a_1)^2\ (a_2)^2\ (b_2)\ \ \ldots {}^2B_2$$

$$\ldots\ldots (a_1)^2\ (b_2)^2\ (b_1)^2\ (a_1)^2\ (a_2)\ (b_2)^2\ \ \ldots {}^2A_2.$$

$^2A_2$ correlates with $^2\Sigma_u^{(-)}$ in the linear molecule with odd quanta of the bending vibration excited and $^2B_2$ correlates with $^2\Sigma^{(+)}$ (see Mulliken 1941). Walsh (1953) has predicted $^2A_2$ to lie above $^2B_2$ in accord with the order of the $^2\Sigma$ states found in the 01^10 level of the ground state of BO_2 where $^2\Sigma^{(-)}$ was found to lie above $^2\Sigma^{(+)}$. Similar arguments are also found to hold for the first excited state of BO_2, $A\ ^2\Pi_u$.

7.2. The Products of Dissociation

It is reasonable to suppose that the ground states of BO_2 and CO_2^+ dissociate into $O(^3P)$ and the appropriate diatomic molecule in its ground electronic state. A similar situation holds for CO_2 except that the oxygen must be in its ^1D state to give the known $^1\Sigma_g^+$ ground state. These dissociative processes can be summarized as follows:

$$CO_2(^1\Sigma_g^+) \rightarrow CO(^1\Sigma^+)+O(^1D)$$

$$r = 1.163 \qquad r = 1.131 \qquad \Delta r = +0.032$$

$$CO_2^+(^2\Pi_g) \rightarrow CO^+(^2\Sigma^+)+O(^3P)$$

$$r = 1.176 \qquad r = 1.118 \qquad \Delta r = +0.058$$

$$BO_2(^2\Pi_g) \rightarrow BO(^2\Sigma^+)+O(^3P)$$

$$r = 1.265 \qquad r = 1.208 \qquad \Delta r = +0.057.$$

In each case the oxygen—boron or oxygen—carbon bond shortens as one oxygen atom is removed. Linnett and Hoare (1949) have correlated such changes of bond length with the sign and magnitude of the ratio of the two bond stretching force constants, k_{12}/k_1. These constants, for the ground states of CO_2 and BO_2, are given below.

	k_1 ($\times 10^5$ dynes/cm)	k_{12}
CO_2 ($X\ ^1\Sigma_g^+$)*	15.5	1.3
BO_2 ($X\ ^2\Pi_g$)	7.3	3.2

*Taken from Herzberg (1945), p. 187.

The large value of k_{12} in BO_2 is reasonable in view of the large change in the bond length as one oxygen atom is removed. It is interesting to note a similar change in bond length in CO_2^+ which would indicate k_{12} to be large and positive. This would require ν_3 to be low, about 1500 cm^{-1}, contrary to the tentative value of 2305 cm^{-1} suggested by Mrozowski (1947).

In the $A\ ^2\Pi_u$ state of BO_2, it was found that $k_1 = 11.5$ and $k_{12} = -2.5\times 10^5$ dynes/cm. The negative value of k_{12} would be expected if dissociation is assumed to take place in the following manner:

$$BO_2(A\ ^2\Pi_u) \rightarrow BO(A\ ^2\Pi_i)+O(^3P)$$

$$r = 1.303 \qquad r = 1.359 \qquad \Delta r = -0.056$$

where the boron–oxygen distance increases as one oxygen atom is removed. These dissociation products lie at about 23900 cm^{-1} above the lowest products. With ν_{000} for the A–X transition at 18300 cm^{-1} this would imply that the dissociation energy of the upper state is greater than that of the ground state. In this transition, $\nu_3' > \nu_3''$ so that the upper state dissociation energy might be expected to be the greater. It should be pointed out that similar arguments would hold if $A\ ^2\Pi_u$ dissociated to the next excited state of BO which has a similar bond length to the A state. No estimate, based on the spectrum, is possible at present of the dissociation energy of BO_2. Figure 10 shows the various possible low-lying dissociation products together with the observed molecular levels and tentative correlations.

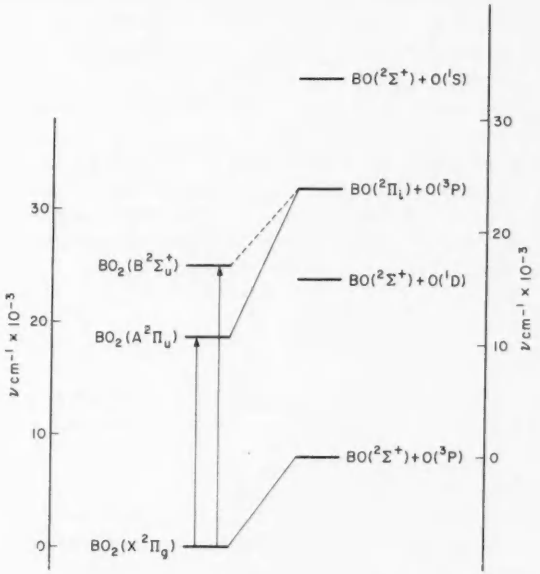

FIG. 10. Tentative correlation of the molecular states of BO_2 with the products of dissociation.

7.3. The Renner Effect

(a) Vibrational Energies

It has not been possible to test the equations (1) to any great extent. However, the Renner parameters listed in Table X were evaluated by fitting the 01^10–01^10 bands of system A and B to equations (1). The calculated subband origins are compared with those experimentally observed in Table XI.

TABLE XI

	Obs.	Calc.
System B	01^10–01^10	(ν_0 = 24548.9)
$^2\Pi_g$–$^2\Sigma_u^{(+)}$	24673.0	24672.1
$^2\Pi_g$–$^2\Delta_{5/2,u}$	24636.3	24637.7
$^2\Pi_g$–$^2\Delta_{3/2,u}$	24489.8	24489.1
$^2\Pi_g$–$^2\Sigma_u^{(-)}$	—	24435.3
System A	01^10–01^10	(ν_0 = 18311.7)
$^2\Sigma_g^{(-)}$–$^2\Sigma_u^{(+)}$	18487.5	18487.2
$^2\Sigma_g^{(+)}$–$^2\Sigma_u^{(+)}$	18382.9	18382.6
$^2\Delta_{5/2,g}$–$^2\Delta_{5/2,u}$	18348.0	18349.9
$^2\Delta_{3/2,g}$–$^2\Delta_{3/2,u}$	18304.0	18302.5
$^2\Sigma_g^{(-)}$–$^2\Sigma_u^{(-)}$	—	18250.2
	02^20–02^20	
$^2\Pi_{1/2,u}$–$^2\Pi_{1/2,g}$	18442.6	18489.4

The last value, for 02^20–02^20, is probably as good as can be expected considering that the anharmonicity of the lower state has not been taken into account. The observed values given in Table XI are subband origins obtained either from rotational analyses or from band heads, with an estimated head-to-origin correction applied, except in the case of the 02^20–02^20 band where the measurement is of the head.

It may be noted that the $^2\Delta$ sublevel in $X\,^2\Pi_g$ shows a measured splitting of 146.5 cm^{-1} as opposed to 148.6 (the value for the 000 level) required by Pople's equations which assume A, the spin–orbit coupling constant, to remain the same for all values of v and K. Hougen has extended the calculation to third order and has shown that

$$A_{eff} = A\left[1-\frac{\epsilon^2}{8}K(K+1)\right]. \tag{8}$$

If 148.6 cm^{-1} is put equal to A_{eff} for the 000 ($K = 1$) level, A is found to be 150.0_8 and for Δ ($K = 2$) levels $A_{eff} = 145.6$, in good agreement with the value found.

(b) Rotational Energies

The rotational energies of four $^2\Sigma$ vibronic levels have been studied in detail. In particular, values of γ, the ρ-type doubling constant, have been determined and are compared with those calculated from equation (5) in Table XII.

TABLE XII

	Obs.	Calc.	γ (obs.)	γ (calc.)
	$A\,^2\Pi_u$			
$B_{eff}(\kappa^2\Sigma)$–$B_{eff}(\mu^2\Sigma)$	+0.00167	+0.00175		
$11^10(\mu^2\Sigma)$			0.454	0.465
$01^10(\kappa^2\Sigma)$			0.444	0.469
$01^10(\mu^2\Sigma)$			0.474	0.465
	$X\,^2\Pi_g$			
$01^10(\mu^2\Sigma)$			0.163	0.143

In 01^10 of $A\,^2\Pi_u$ both $\kappa(^2\Sigma)$ and $\mu(^2\Sigma)$ have been observed. Although the absolute values of B_{eff} which have been obtained are not of high accuracy, the quantity $B_{eff}\,\kappa(^2\Sigma)$–$B_{eff}\,\mu(^2\Sigma)$ has been determined with some precision and is compared with the value calculated from equation (4) in Table XII. In all cases the agreement between observed and calculated values is good.

7.4. Comparison of BO_2 with CO_2^+

The molecular constants of BO_2 and CO_2^+ are remarkably similar as Table XIII shows, although most of the constants of CO_2^+ are some 15% higher than those of BO_2. However, the whole spectrum of CO_2^+ is shifted about 10,000 cm^{-1} to higher frequencies.

An interesting point in both BO_2 and CO_2^+ is the close similarity of γ in the $B\,^2\Sigma_u^+$ state and p in the $A\,^2\Pi_u$ state. This suggests that perhaps Van

TABLE XIII

Comparison of constants of BO_2 and CO_2^+

	BO_2	CO_2^+
	$B\ ^2\Sigma_u^+$	
T_0	24508.0	34597.9
B_0	0.3250	0.3784
γ	0.016	0.019
	$A\ ^2\Pi_u$	
T_0	18291.6	28500.5
B_0	0.3106	0.3493
A_0	−101.3	−95.5
$\epsilon\omega_2$	−13.1	
p	0.015	0.015*
ν_1	994	1131
	$X\ ^2\Pi_g$	
B_0	0.3292	0.3804
A_0	−148.6	−159.5
$\epsilon\omega_2$	−92.2	−93†
ν_1	1070	1280

*This value is twice that quoted by Mrozowski (1941), who defined the width of the A-type doublets as $\Delta\nu = 2p(J+\frac{1}{2})$ whereas in the present work the width has been defined as $\Delta\nu = p(J+\frac{1}{2})$ after Mulliken and Christy (1931).

†The Renner parameter in the ground state of CO_2^+ has been estimated from the published frequencies of Bueso-Sanllehi (1941) by assigning the 010–010 band of the B system in the same way that the corresponding band of BO_2 was assigned in the present work.

Vleck's case of 'pure precession' might hold between these states. If this is so, Mulliken and Christy (1931) have shown that

$$p = \gamma = 2AB_v l(l+1)/\nu(\Pi\Sigma),$$

which with $l = 1$ and using the constants of either molecule gives $p = \gamma = +0.02$ cm^{-1} which is very close to, but a little higher than, the experimental values. The situation is analogous to that of OH in which there is the same change in electron configuration between the $^2\Pi$ and $^2\Sigma$ states, and in which the calculated constants, p and γ, are also somewhat greater than those observed (see Mulliken and Christy 1931).

It appears likely that the analysis of the CO_2^+ spectrum could be extended in view of the present knowledge of the Renner effect and by comparison with BO_2.

8. CONCLUSION

The detailed analysis of the 'boric acid fluctuation bands' has shown that they arise from two electronic transitions in the linear symmetric molecule BO_2. Two of the electronic states involved are $^2\Pi$ and thus show the Renner effect together with spin–orbit interaction. In the ground state the Renner effect is large and comparable with the spin–orbit interaction whereas in the first excited state the Renner effect is small compared with spin–orbit interaction. In both states it has been shown that the vibronic and rotational energies are in accord with the theoretical predictions of Pople (1960) and Hougen (1961).

ACKNOWLEDGMENTS

The author wishes to record his gratitude to Dr. J. T. Hougen for many stimulating discussions during the course of this work and to Drs. G. Herzberg, A. E. Douglas, and D. A. Ramsay for critical discussion of the manuscript.

REFERENCES

BUESO-SANLLEHI, F. 1941. Phys. Rev. **60**, 556.
CLAESSON, S. and LINDQVIST, L. 1957. Arkiv Kemi, **11**, 535.
DIXON, R. N. 1960*a*. Phil. Trans. Roy. Soc. A, **252**, 165.
——— 1960*b*. Can. J. Phys. **32**, 10.
DURIE, R. A. and RAMSAY, D. A. 1958. Can. J. Phys. **36**, 35.
EDLÉN, B. 1953. J. Opt. Soc. Am. **43**, 339.
HARRISON, G. R. 1939. M.I.T. wavelength tables (John Wiley and Sons, Inc., New York).
DE HEER, J. and NIELSEN, H. H. 1952. J. Chem. Phys. **20**, 101.
HERZBERG, G. 1945. Infrared and Raman spectra (D. Van Nostrand Company, New York).
——— 1950. Spectra of diatomic molecules (D. Van Nostrand Company, New York).
HILL, E. L. and VAN VLECK, J. H. 1928. Phys. Rev. **32**, 250.
HOUGEN, J. T. 1961. J. Chem. Phys. In press.
JEVONS, W. 1932. Report on the band spectra of diatomic molecules. Physical Society, London.
KASKAN, W. E., MACKENZIE, J. D., and MILLIKAN, R. C. 1961. J. Chem. Phys. **34**, 570.
KASKAN, W. E. and MILLIKAN, R. C. 1961. Eighth Symposium (International) on Combustion (Williams and Wilkins Co., Baltimore). In press.
LINNETT, J. W. and HOARE, M. F. 1949. Trans. Faraday Soc. **45**, 844.
MROZOWSKI, S. 1941. Phys. Rev. **60**, 730.
——— 1942. Phys. Rev. **62**, 270.
——— 1947. Phys. Rev. **72**, 682, 691.
MULLIKEN, R. S. 1941. Phys. Rev. **59**, 873.
MULLIKEN, R. S. and CHRISTY, A. 1931. Phys. Rev. **38**, 87.
NIELSEN, H. H. 1950. Phys. Rev. **77**, 132.
PEARSE, R. W. B. and GAYDON, A. G. 1950. The identification of molecular spectra (John Wiley and Sons, Inc., New York).
POPLE, J. A. 1960. Mol. Phys. **3**, 16.
RENNER, R. 1934. Z. Physik, **92**, 172.
SALET, G. 1873. Ann. chim. et phys. Ser. **4**, **28**, 5.
SOULEN, J. R. 1955. Ph.D. Thesis, University of Wisconsin, University Microfilms, Ann Arbor, Michigan.
WALSH, A. D. 1953. J. Chem. Soc. 2266.
WHITE, D. 1961. Private communication.
WHITE, J. U. 1942. J. Opt. Soc. Am. **32**, 285.

THE RAMAN EFFECT IN GASEOUS HYDROGEN AT HIGH PRESSURES[1]

A. D. MAY,[2] V. DEGEN, J. C. STRYLAND, AND H. L. WELSH

ABSTRACT

The Raman spectrum of hydrogen as a pure gas and in mixtures with helium and argon was studied in the pressure range 100 to 2000 atmospheres at room temperature. Frequency shifts and half-widths of the vibrational Q_1 lines and the rotational $S_0(0)$ and $S_0(1)$ lines were measured at a series of gas densities with a high-dispersion grating spectrograph. The perturbations in ω_0 and B_0 are represented as power series in the density with linear and quadratic terms. The linear term for $\Delta\omega_0$ is positive for H_2–He, slightly negative for H_2, and more negative for H_2–A. These results are discussed in terms of an anharmonic oscillator model for the H_2 molecule, a polarizability model for the dispersion forces, and the classical pair distribution function. The rotational lines show additional perturbations which are not accounted for in this treatment.

INTRODUCTION

The study of changes in frequency, intensity, and shape of rotation–vibration bands of molecules in the transition from the free molecule to the dense phases is, at first sight, a promising way of studying intermolecular forces. Unfortunately, the situation is very complex from the theoretical point of view and interpretation of the experimental data is difficult. Solid parahydrogen seems to be the only case in which the rotational and vibrational frequency perturbations have been more or less completely interpreted by a detailed theoretical examination of the effects of intermolecular forces (Van Kranendonk 1959, 1960). Although much experimental work has been done on the frequency shifts of the bands of a solute molecule in different solvents, discussions of these data have centered mainly around the Kirkwood–Bauer–Magat relation or modifications of this (cf., for example, Pullin 1960). This relation, which follows from a consideration of the interaction of a dipole molecule with a continuous dielectric medium, takes into account only one aspect of the vibrational perturbation; it neglects entirely the effect of the dispersion forces, for example. Although the behavior of complex solute molecules in complex solvents has interest from the chemical point of view, it may be some time before a theory of solvent effects is developed to explain the phenomena observed. It would seem, therefore, to be the experimentalist's first duty to present the theorist with accurate data on many simple systems; a meaningful theory of the effect of molecular interactions on molecular spectra might then be gradually built up.

A detailed interpretation of any effect of intermolecular forces requires, of course, a knowledge of the molecular distribution function. This function is usually known for the crystal state and can be accurately approximated to in

[1]Manuscript received August 30, 1961.
Contribution from the McLennan Laboratory, University of Toronto, Toronto, Ontario. This research was supported in part by a grant from the National Research Council of Canada.
[2]Holder of a scholarship from the National Research Council of Canada, 1957–1959.

the gaseous state at low and medium pressures. The crystal and the gas at not too high pressures are thus more suitable for study than the liquid. Moreover, the compressed gas allows the phenomenon to be investigated over a range of density and temperature. The case of induced infrared absorption may be cited as an example; in this case experiments on the compressed gas and on the solid delineated many features of the phenomenon and, particularly in the case of hydrogen, encouraged detailed theoretical investigations.

Much of the experimental data on spectroscopic effects of intermolecular forces is complicated by the fact that perturbations of the molecular rotation and of the molecular vibration are superimposed and cannot be easily separated. Thus, as the density of a compressed gas is increased, the rotational lines are broadened and finally overlap so that a rotation–vibration band becomes continuous with one or more broad maxima. At very high densities, as in a liquid, the shape of the band is presumably a superposition of transitions involving both the perturbed vibrational and the hindered rotational motions. In such a case the vibrational frequency is usually taken to be the frequency of the main maximum of the band; however, the latter is often ill-defined and may not in fact correspond to the vibrational frequency at all.

In one case, that of isotropic Raman scattering, it appears that the vibrational perturbation is effectively separated from the rotational perturbation. It has been noted that the Q branches of totally symmetric vibrations, which are due mainly to isotropic Raman scattering, are often just as sharp for the liquid as for the corresponding gas; lines due to anisotropic scattering, on the other hand, show considerable broadening (Crawford, Welsh, and Harrold 1952). These observations can be understood in a general way from the selection rules for the Raman effect. The permitted changes in the rotational quantum numbers J and M are 0, ± 1, ± 2, independently, with certain restrictions when symmetry is present in the molecular configuration (Placzek 1934). For isotropic scattering the selection rule is $\Delta J = \Delta M = 0$, whereas for anisotropic scattering at least one of the quantum numbers must change. If the effect of the intermolecular force field can be considered in a first approximation as a removal of the M degeneracy of the rotational levels, the splitting of the levels would be a function of J but not of the vibrational quantum number, v, provided the rotation–vibration interaction is small. It is clear then from the selection rule, $\Delta J = \Delta M = 0$, that rotational perturbations will not in the first approximation affect the frequencies of isotropic transitions. It can therefore be concluded that any shift or broadening of isotropic transitions which is observed can be interpreted directly as a vibrational perturbation. For anisotropic Raman transitions, on the other hand, rotational and vibrational perturbations are always superimposed; this is also true for infrared transitions for which the general dipole selection rules are $\Delta J = 0$, ± 1, and $\Delta M = 0$, ± 1, independently, but $\Delta M = 0$ not allowed for $\Delta J = 0$.

From these considerations it appeared that the systematic investigation of Raman spectra of compressed gases might yield results of sufficient importance to compensate for the anticipated experimental difficulties. The totally symmetric Raman bands of some simple non-polar molecules were chosen for

the first experiments with a view to elucidating the effect of the dispersion forces on the vibrational frequencies. Since the hydrogen molecule has proved itself in other cases to be most amenable for the interpretation of intermolecular force effects, a series of experiments with pure hydrogen and hydrogen – foreign gas mixtures was carried out. The results of these experiments are discussed in this communication.

EXPERIMENTAL

In the Raman tube for high pressure gases developed for this investigation the compressed gas was contained *inside* a steel cell and *outside* a thick-walled pyrex tube sealed mechanically at its ends to the steel cell. The gas was irradiated by a water-cooled mercury lamp passing through the bore (1 cm in diameter) of the pyrex tube; the light scattered by the gas was observed through a silica window sealed to the steel cell. The Raman tube was used for many experiments in the pressure range 100 to 2000 atm with only occasional breakages due to deterioration of the seal between the pyrex tube and the steel cell. Details of the construction have been given by Stryland and May (1960).

The gas to be studied was compressed into the Raman tube by a mercury column gas compressor. The pressures were measured on a Bourdon tube gauge and the gas densities determined from PVT data available in the literature. Density ratios for the gas mixtures were determined by the method described by Hare and Welsh (1958). Linear interpolation, according to the mixture ratio, between the isothermals of the two gases involved gave a working isothermal for the gas mixture. All the experiments were carried out near room temperature.

The spectra were photographed on Kodak 103*a*-O plates with a grating spectrograph of high light-gathering power. This instrument, which employs a 5 in.$\times$10 in. grating in a Littrow mounting with an off-axis paraboloidal mirror, gives a reciprocal linear dispersion of 6.0 cm^{-1} per mm at 4358 Å; the aperture ratio is $f/12.5$.

Frequency determinations were made from iron arc lines superimposed on the Raman spectrograms. The wavelengths of the iron lines as determined from the M.I.T. Wavelength Tables were converted to vacuum frequencies using Edlén's formula (1953). The values 24,705.350 cm^{-1} and 22,938.133 cm^{-1} were used for the vacuum frequencies of Hg 4046.5630 Å and 4358.3277 Å respectively (Burns, Adams, and Longwell 1950). The frequencies of the maxima of the Raman lines were determined from density traces of the spectrograms obtained with a Leeds and Northrup microphotometer. Although spectral slit widths in the range 0.3–1.0 cm^{-1} were used, the reproducibility of measurements from different spectrograms showed that the precision of the frequency determinations was in most cases of the order of 0.03 cm^{-1}. However, in the case of the vibrational band of pure hydrogen, which was studied before all the technical difficulties were solved, the accuracy is of the order of 0.1 cm^{-1}.

Intensity profiles of the Raman lines were measured with the aid of intensity

calibration curves obtained by replacing the usual slit of a high dispersion glass spectrograph by a stepped slit illuminated by a source of continuous radiation. The intensity calibrations were photographed on the same plate and with the same exposure times as the Raman spectra.

Experiments were carried out with pure hydrogen and hydrogen–helium and hydrogen–argon mixtures with total pressures in the range 100 to 2000 atm. A summary of the lines observed and of the experimental conditions is given in Table I. Because of line broadening the exposure times for a given line were

TABLE I

Summary of the experiments on the Raman spectrum of H_2 at high pressures

Gas	Mixture ratio	H_2 lines recorded	Spectral slit width (cm^{-1})	Exposure time (hours)
H_2	—	$Q_1(J)(J = 0,1,2,3)$	0.75	12
		$S_0(0)$, $S_0(1)$	0.3	2
H_2–A	1:3.66	$Q_1(1)$	1.0	20
		$S_0(0)$, $S_0(1)$	0.6	6
H_2–He	1:3.84	$Q_1(1)$	1.0	25
		$S_0(0)$, $S_0(1)$	0.5	7

independent of the gas density. The mixture ratios used (1:4) were not as large as desirable for a quantitative interpretation of the results; even so, only the strongest vibrational line, $Q_1(1)$, could be recorded with reasonable exposure times for the mixtures.

THE VIBRATIONAL BAND

Four Q_1 branch lines of the fundamental band of hydrogen, excited by Hg 4047, were recorded for a series of densities of the pure gas in the interval of relative densities ρ/ρ_0 from 100 to 800, where ρ_0 is the density at N.T.P. The measured frequencies and half-widths are given in Table II and are

TABLE II

The fundamental vibrational Raman frequencies of compressed H_2

Pressure (atm)	Relative density ρ/ρ_0	$Q_1(0)$ (cm^{-1})	$Q_1(1)$ (cm^{-1})	$Q_1(2)$ (cm^{-1})	$Q_1(3)$ (cm^{-1})	Half-width (cm^{-1})
1	1	4161.134*	4155.201*	4143.387*	4125.832*	—
148	123	4161.0_2	4154.9_8	4143.3_2	4125.7_8	0.2_7
265	209	4160.7_3	4154.6_3	4143.1_3	4125.6_2	0.4_6
495	346	4160.8_9	4154.6_5	4143.3_0	4125.7_0	0.5_7
970	543	4161.6_7	4155.1_5	4144.3_1	4126.9_3	1.1_9
1455	686	4162.9_3	4156.1_1	4145.5_2	4128.3_9	1.3_4
1940	802	—	4157.1_0	4146.8_0	—	1.4_1

*Stoicheff (1957).

plotted as a function of the density in Fig. 1; the frequencies for 1 atm pressure are those measured by Stoicheff (1957). It is interesting to note that the frequencies of the four lines behave in approximately the same way, decreasing at first and then increasing with increasing density of the gas. This similarity

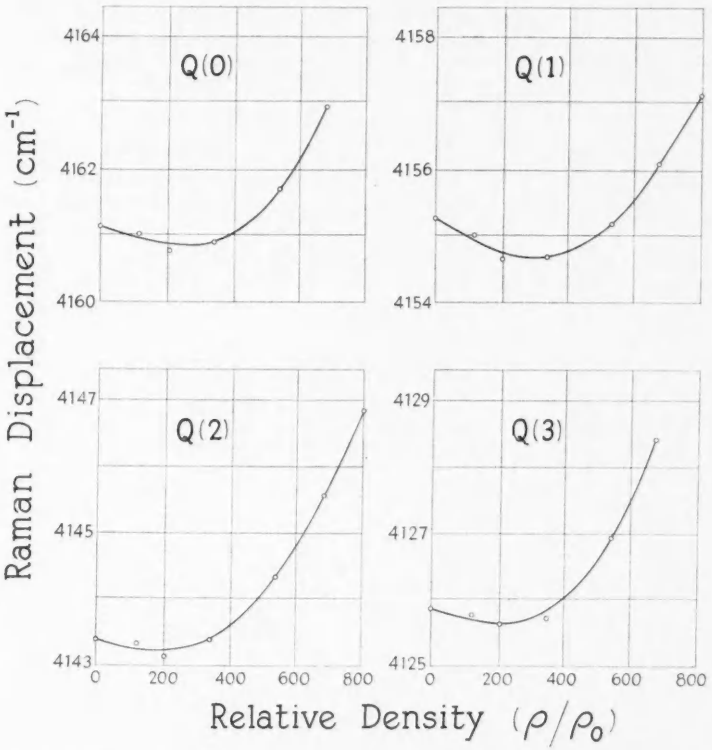

FIG. 1. Raman frequencies of the fundamental vibration lines of hydrogen as a function of the gas density.

in behavior indicates that the observed perturbation is due primarily to a change in vibration frequency as expected from the discussion in the Introduction. The highest relative density reached, 802, approaches the densities of the liquid and solid, which are 860 and 970 respectively. The Raman spectra of the condensed phases show a *lowering* of the vibrational frequency by about 10 cm^{-1} (Allin, Feldman, and Welsh 1956; Bhatnagar, Allin, and Welsh 1962). Extrapolation of the curves in Fig. 1 shows that the gas at comparable densities at room temperature would show an *increase* of approximately 8 cm^{-1} in the vibrational frequency. It is therefore evident that the perturbation of the vibrational frequency is not simply a density effect but must also depend on the molecular distribution.

The experimental data for the $Q_1(1)$ line of hydrogen in compressed H_2–He and H_2–A mixtures are given in Table III, and the frequencies are plotted as a function of the total relative density of the mixtures in Fig. 2. The curve for the H_2–A mixture is of the same general form as for pure hydrogen but the

TABLE III

The $Q_1(1)$ line of H_2 in H_2–He and H_2–A mixtures

Total pressure (atm)	Total density ρ/ρ_0	$Q_1(1)$ (cm^{-1})	Half-width (cm^{-1})
	Hydrogen–helium		
204	166	4156.48	0.2_8
362	282	4157.49	0.4_4
522	377	4158.59	0.7_3
772	519	4160.31	0.8_1
956	605	4161.50	—
1052	647	4162.14	1.6_5
1538	827	4164.84	1.7_5
1926	950	4167.03	3.0_4
	Hydrogen–argon		
265	241	4153.17	—
408	336	4152.79	1.0_6
632	440	4152.68	1.5_2
970	541	5152.83	2.7_6
1555	650	4154.48	4.1_5
1940	698	4155.39	5.0_4

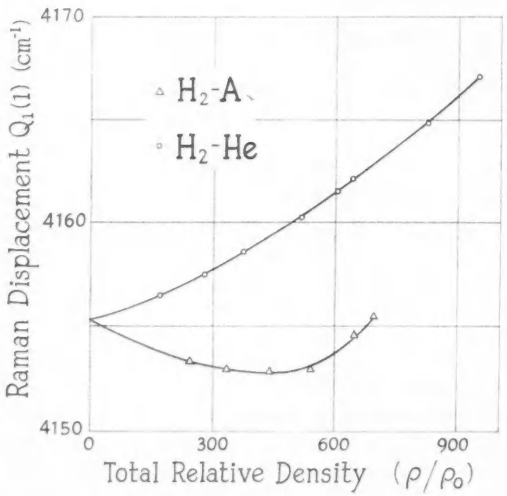

FIG. 2. Raman frequency of the $Q_1(1)$ line of hydrogen in H_2–He and H_2–A mixtures as a function of the total density of the gas mixture.

frequency shift remains negative over most of the density range; for the H_2–He mixture, on the other hand, the shift increases monotonically over the whole range. Pure hydrogen thus exhibits a behavior intermediate between the H_2–He and H_2–A mixtures.

For a quantitative analysis of the vibrational perturbation we introduce the frequency shift, $\Delta Q_1(J)$, defined as the difference between the frequency at

a given density, ρ/ρ_0, and the corresponding frequency at 1 atmosphere as measured by Stoicheff (1957). We shall represent $\Delta Q_1(J)$ as a power series in the density:

$$\Delta Q_1(J) = a(\rho/\rho_0)+b(\rho/\rho_0)^2+ \ldots . \tag{1}$$

The graph of $\Delta Q_1/(\rho/\rho_0)$ vs. ρ/ρ_0 in Fig. 3 shows straight lines for all cases except the $Q_1(1)$ line of the H_2–A mixture. The shifts will therefore be represented by the first two terms of the power series, the values of a and b being

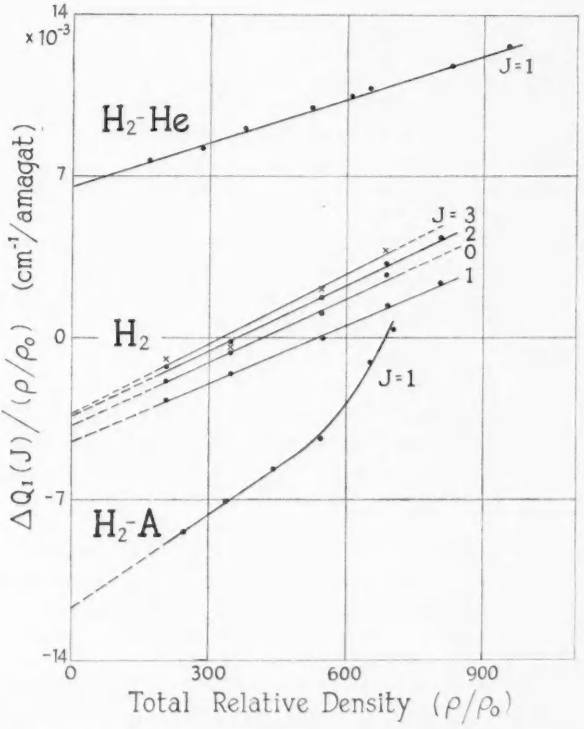

FIG. 3. Plot of $\Delta Q_1(J)/(\rho/\rho_0)$ vs. the total density in pure hydrogen and in H_2–He and H_2–A mixtures.

obtained from the intercepts and slopes of the straight lines. The H_2–A mixture requires in addition a cubic term to represent the data adequately at the highest densities. The values of a and b are summarized in Table IV.

The coefficient, a, of the linear term is positive for H_2–He, negative for pure H_2, and considerably more negative for H_2–A; this order is also the order of increasing Van der Waals forces. On the other hand, the coefficients, b, of the quadratic term are positive in all three cases. It will be noted that both

TABLE IV

Density dependence of the vibrational perturbation, $\Delta Q_1(J) = a(\rho/\rho_0)+b(\rho/\rho_0)^2$

Gas	J value	a (cm^{-1}/unit density)	b (cm^{-1}/unit density^2)
H_2	0	-3.70×10^{-3}	$+8.9\times10^{-6}$
	1	-4.45×10^{-3}	$+8.4\times10^{-6}$
	2	-3.40×10^{-3}	$+9.6\times10^{-6}$
	3	-3.30×10^{-3}	$+10.0\times10^{-6}$
H_2–He	1	$+6.60\times10^{-3}$	$+6.2\times10^{-6}$
H_2–A	1	-11.70×10^{-3}	$+13.7\times10^{-6}$

coefficients vary somewhat for the four Q_1 lines observed in pure hydrogen, and the small scatter of the points in Fig. 3 indicates that the differences are not due to experimental error. The implication is that the shifts are mainly due to vibrational perturbation with only a small dependence on the state of rotation of the molecule. It may be significant that the magnitudes of the coefficients for the four Q_1 lines are in the same order as the populations of the rotational states.

We shall now indicate how the vibrational shifts can be related to the intermolecular interaction. The mutual potential energy of a given hydrogen molecule and a perturbing molecule j will be assumed to be spherically symmetric and of the Lennard–Jones (6–12) form,

$$V_j = A/R_j^{12} - B/R_j^6, \tag{2}$$

where A and B are positive constants and R_j is the intermolecular distance. Both A and B must be considered to be functions of the internuclear separation, r, of the hydrogen molecule, so that there is an additional restoring force contributing to the vibrational motion of the hydrogen molecule given by

$$F_j = -(\partial V_j/\partial r) = -(1/R_j^{12})(\partial A/\partial r)+(1/R_j^6)(\partial B/\partial r). \tag{3}$$

The total contribution to the restoring force for a hydrogen molecule surrounded by a gas of perturbing molecules is

$$F = \sum_j F_j, \tag{4}$$

where the summation is taken over all the molecules of the gas.

To obtain the effect of the force F on the vibration and rotational constants of the hydrogen molecule, it is necessary to assume a potential function for the free molecule; for the present discussion we shall assume the simple anharmonic form

$$V = f(r-r_e)^2 - g(r-r_e)^3 \tag{5}$$

where r_e is the equilibrium distance. A short calculation shows that the changes introduced in the more important molecular constants by the perturbing force F are:

$$\Delta r_e = F/2f, \tag{6a}$$

$$\Delta B_e = -B_e F/f r_e, \tag{6b}$$

$$\Delta \omega_e = -3\omega_e g F/4f^2, \tag{6c}$$

$$\Delta x_e \omega_e = \Delta \alpha_e = 0.* \tag{6d}$$

It may then be shown that the frequency shifts of the Q_1 lines are to a good approximation given by

$$\Delta Q_1 = -3F(2x_e\omega_e/15hcf)^{1/2}. \tag{7}$$

The main difficulty arises of course in the calculation of F. In principle, there are two steps involved: (*a*) selection of a model for the pair potential (equation (2)) which will allow the calculation of $\partial A/\partial r$ and $\partial B/\partial r$ in terms of known molecular constants, and (*b*) statistical summation of the F_j over all perturbing molecules (equation (4)).

(*a*) The attractive part of the pair potential can be represented in the present cases by London's approximate formula for the dispersion forces.

$$V_j^{\text{disp}} = -\frac{3}{2}\frac{EE_j}{E+E_j}\frac{\alpha\alpha_j}{R_j^6}, \tag{8}$$

where the α's are the molecular polarizabilities and the E's the ionization potentials. To a first approximation the value of $\partial B/\partial r$ is given by

$$\frac{\partial B}{\partial r} = B\left(\frac{\alpha'}{\alpha} + \frac{E'E_j}{E(E+E_j)}\right) \tag{9a}$$

for a hydrogen – foreign gas pair, or

$$\frac{\partial B}{\partial r} = B\left(\frac{\alpha'}{\alpha} + \frac{E'}{2E}\right) \tag{9b}$$

for an H_2–H_2 pair. The rate of change of polarizability, $\alpha' \equiv \partial\alpha/\partial r$ is accurately known for hydrogen from the experiments of Crawford and MacDonald (1958). The value of $E' \equiv \partial E/\partial r$, as estimated by the method of Van Kranendonk (1959), is -4.6×10^8 ev per cm. Unfortunately, there does not appear to exist at present any adequate representation of the repulsive part of the intermolecular potential which would permit the calculation of $\partial A/\partial r$; we will therefore neglect this term in equation (3) for the moment.

(*b*) The statistical summation requires a knowledge of the appropriate molecular distribution function, which in this case is the pair correlation function, $g(R_j)$. As shown by de Boer (1949), the function $g(R_j)$ for a gas can be developed as a power series in the density,

$$g(R_j) = g_0(R_j) + L(\rho/\rho_0)g_1(R_j) + \ldots, \tag{10}$$

where L is Loschmidt's number. Classically the first term of this expansion is given by $g_0(R_j) = \exp(-V_j/kT)$, where k is the Boltzmann constant, T the

*The notation follows that of Herzberg (1950).

absolute temperature, and V_j is the average of the intermolecular potential (2) over the intramolecular motions. The latter will be represented by the Lennard–Jones potential

$$V_j = 4\epsilon\left[\left(\frac{\sigma}{R_j}\right)^{12} - \left(\frac{\sigma}{R_j}\right)^{6}\right]. \tag{11}$$

The constants, ϵ and σ, are available in the literature for hydrogen, helium, and argon; for H_2–He and H_2–A, the formulae $\epsilon_{12} = \sqrt{\epsilon_1\epsilon_2}$ and $\sigma_{12} = (1/2)(\sigma_1+\sigma_2)$ will be used, but it should be emphasized that these relations are only approximate. We shall use $B = 4\epsilon\sigma^6$ in calculating $\partial B/\partial r$ in equations (9*a*) and (9*b*).

Standard statistical methods show that for gas densities which are not too high

$$\sum_j F_j = 4\pi L(\rho/\rho_0)\int_0^\infty g_0(R)FR^2dR.$$

Hence we have finally

$$F = 4\pi L(\rho/\rho_0)\frac{\partial B}{\partial r}\int_0^\infty \exp\left\{-4\epsilon\left[\left(\frac{\sigma}{R}\right)^{12} - \left(\frac{\sigma}{R}\right)^{6}\right]\Big/ kT\right\}R^{-4}dR, \tag{12}$$

and ΔQ_1 can be evaluated from equation (7).

It is clear from the above equations that ΔQ_1 is proportional to the numerical density. Thus, the calculation gives that part of the linear coefficient a in equation (2), which arises from the dispersion forces; we will designate this as a_{disp}(calc.). In calculating a_{disp}(calc.) for the gas mixtures, F was taken to be the mean of the values for the two types of perturbing molecules, weighted according to the mixture ratio. The repulsive intermolecular potential would also give rise to a linear term, a_{rep}, in ΔQ_1 which we are unable to calculate; we can, however, determine this from the experimental data using the equation

$$a_{\text{exptl}} = a_{\text{disp}}(\text{calc.}) - a_{\text{rep}}.$$

The values of a_{exptl}, a_{disp}(calc.), and a_{rep} for the $Q_1(1)$ line of hydrogen are given in Table V.

TABLE V

Values of the constant a in the equation $\Delta Q_1(1) = a(\rho/\rho_0)+b(\rho/\rho_0)^2$

Gas	a_{exptl} (cm^{-1}/unit density)	a_{disp} (calc.) (cm^{-1}/unit density)	a_{rep} (cm^{-1}/unit density)
H_2	-4.45×10^{-3}	-14.8×10^{-3}	10.4×10^{-3}
H_2–He	6.60×10^{-3}	-7.46×10^{-3}	14.1×10^{-3}
H_2–A	-11.70×10^{-3}	-29.7×10^{-3}	18.0×10^{-3}

The value of a_{disp}(calc.) is negative in all cases, and increasingly negative as the dispersion forces increase. The value of a_{rep} is always positive and of the same order of magnitude for the three cases, as might be expected since the overlap interaction giving rise to the repulsive force is probably not greatly

different in the three cases. The fact that the frequency shift for H_2–He is always positive indicates that in this case the effect of the repulsive forces is greater than that of the attractive forces.

At lower temperatures one would expect a_{rep} to be smaller than at room temperature since small intermolecular distances occur less frequently; the frequency shifts should therefore become more negative at lower temperatures. The present equipment does not allow the temperature to be lowered conveniently so that this point cannot be tested. However, the comparatively large negative shift for solid hydrogen (Bhatnagar *et al.* 1962) is in qualitative agreement with this conclusion; in solid hydrogen the molecules are fixed on the crystal lattice at intermolecular distances for which the attractive forces are greatly predominant.

The simple theory given here for vibrational perturbation by Van der Waals forces thus seems to be adequate as far as it has been developed. The coefficient b of the quadratic term in the density might be calculated by taking into account the second term in the pair correlation function. The most important lack in the theory at the moment is, however, a method of calculating $\partial A/\partial r_1$, that is, the dependence of the repulsive potential on the internuclear distance in the hydrogen molecule.

THE ROTATIONAL BAND

Two members, $S_0(0)$ and $S_0(1)$, of the rotational band excited by Hg 4358 were recorded at various densities. The frequencies of the maxima and the half-widths of these lines are collected in Table VI; the frequency shifts are

TABLE VI

Frequencies and half-widths of the rotational Raman lines of hydrogen

Pressure (atm)	Total density ρ/ρ_0	Frequency (cm^{-1})		Half-width (cm^{-1})	
		$S_0(0)$	$S_0(1)$	$S_0(0)$	$S_0(1)$
		Hydrogen			
1	1	354.381*	587.055*	—	—
136	113	354.41	587.09	0.4_2	0.5_7
245	196	354.39	587.05	0.5_8	0.8_6
270	211	354.41	587.09	0.5_9	1.2_6
525	358	354.48	587.17	1.0_3	1.4_9
968	542	354.62	587.43	1.7_3	2.6_2
1458	686	354.70	587.66	1.9_1	3.2_3
1938	801	354.82	587.85	2.4_4	3.6_5
		Hydrogen–helium			
136	116	354.45	587.13	0.1_0	0.2_3
204	167	354.46	587.22	0.1_8	0.2_8
306	240	354.59	587.32	0.4_1	0.5_5
508	371	354.71	587.48	0.6_9	0.9_0
1052	648	355.14	587.97	1.2_3	1.5_8
1440	790	355.22	588.34	1.3_2	1.7_7
1926	950	355.52	588.91	1.7_7	2.4_2
		Hydrogen–argon			
408	336	354.45	586.89	—	0.7_2
715	467	354.48	586.88	—	1.1_9
970	541	—	586.91	—	1.0_6
1457	636	354.60	587.07	—	1.7_2
1940	698	354.72	587.32	—	2.1_0

*Stoicheff (1957).

plotted as a function of the total relative density of the gas in Figs. 4 and 5. The pressure shifts are in general much smaller than for the vibrational lines and the scatter of the points about the mean curves is correspondingly greater.

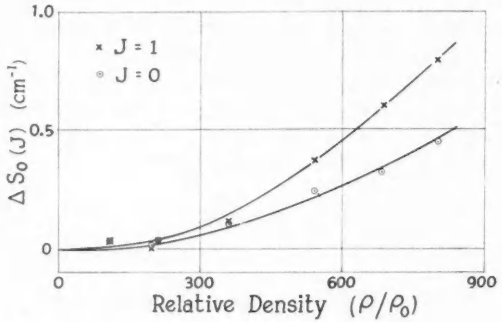

FIG. 4. Frequency shifts of the $S_0(0)$ and $S_0(1)$ lines of hydrogen as a function of the gas density.

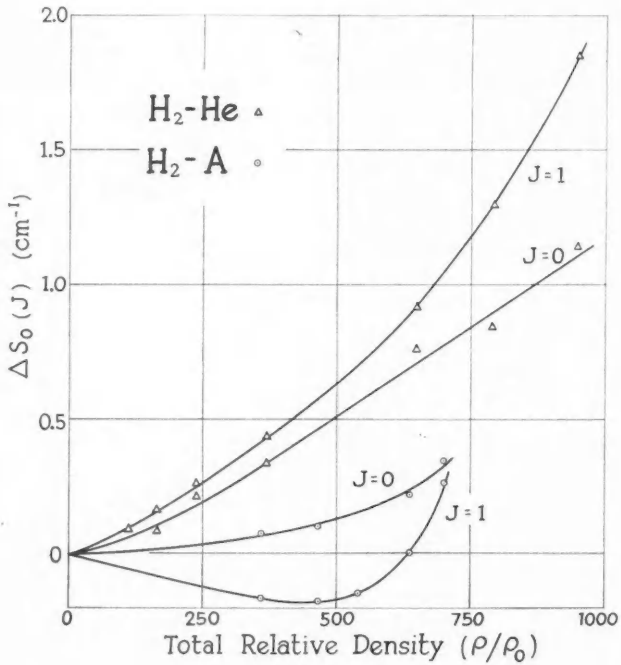

FIG. 5. Frequency shifts of the $S_0(0)$ and $S_0(1)$ lines of hydrogen in H_2–He and H_2–A as a function of the total gas density.

From graphs similar to Fig. 3 the shifts of the rotational lines were represented as power series in the total density,

$$\Delta S_0(J) = c_J(\rho/\rho_0)+d_J(\rho/\rho_0)^2, \qquad (J = 0,1). \tag{13}$$

The values of the coefficients are given in Table VII; these are much less

TABLE VII

Density dependence of the rotational perturbation, $\Delta S_0(J) = c_J(\rho/\rho_0)+d_J(\rho/\rho_0)^2$

Gas	c_0	c_1	d_0	d_1	c_1/c_0	d_1/d_0
H_2	~0	~0	7.1×10^{-7}	12×10^{-7}	—	1.73
H_2–He	4.6×10^{-4}	7.2×10^{-4}	8.9×10^{-7}	12×10^{-7}	1.57	1.43
H_2–A	-1.1×10^{-4}	-13×10^{-4}	7.8×10^{-7}	22×10^{-7}	12	2.8

accurate than in the vibrational case, particularly for H_2–A where the shifts are very small. For pure hydrogen the linear term in the expansion is practically zero; the shifts here are therefore proportional to the square of the density. For H_2 and H_2–He the ratios of the coefficients, c_1/c_0 and d_1/d_0, are not greatly different from the value 10/6 = 1.67, the ratio of the Raman displacements, $\sim 6\,B_0$ and $\sim 10\,B_0$; it can therefore be concluded that in these cases the pressure shifts arise for the most part from a perturbation of the rotational constant B_0. For H_2–A the relation does not hold and the situation is clearly more complex.

The probable origin of the frequency shift of the $S_0(0)$ and $S_0(1)$ lines of H_2 and H_2–He in a perturbation of B_0 can also be seen from the graphs of Fig. 6 where ΔB_0 ($= \Delta S_0(0)/6$ for $S_0(0)$ and $\Delta S_0(1)/10$ for $S_0(1)$) is plotted

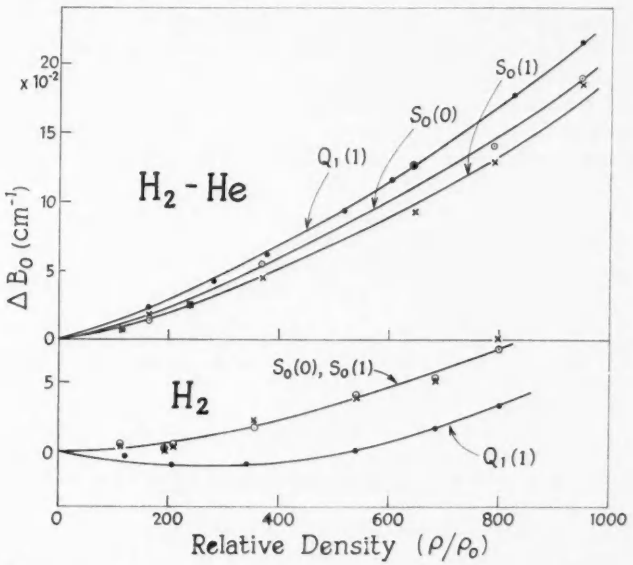

FIG. 6. Variation of B_0, as calculated from the $S_0(0)$, $S_0(1)$, and $Q_1(1)$ lines, as a function of the total gas density.

against the density. The graphs are identical for pure hydrogen and very close together for the H_2–He mixture.

Equation (6*b*) shows that the presence of the additional restoring force F leads to a perturbation of B_e. If the rotational frequency shift actually arises from F, the values of ΔQ_1 and ΔB_e should be related according to the equation

$$\Delta B_e = \Delta Q_1 \times \frac{B_e}{3r_e}\left(\frac{15hc}{2x_e\omega_e f}\right)^{\frac{1}{2}} = 0.0182 \times \Delta Q_1, \tag{15}$$

obtained by eliminating F from equations (6*b*) and (7). The variation of B with density obtained in this way from the Q_1 frequency shifts is also plotted in Fig. 6. For the H_2–He mixture the graph derived from $Q_1(1)$ shows fair agreement with the graphs derived from $S_0(0)$ and $S_0(1)$, and one is tempted to conclude that all the perturbations in the spectrum can be correlated through the force F; however, the discussion of the half-widths below shows that this conclusion is not justified. For pure hydrogen it is clear that the perturbation in B_e cannot be accounted for by the force F alone.

THE LINE WIDTHS

All the Raman lines observed showed symmetrical broadening in the high pressure gas. The intensity profiles of both the vibrational and the rotational lines were found to be well represented by Lorentz (dispersion) line shapes. The intrinsic half-widths of the broadened lines were obtained by subtracting the instrumental slit widths from the half-widths of the intensity profiles; the values obtained are given in the last columns of Tables II, III, and VI. At the highest pressures the half-widths did not exceed a few cm^{-1}. For pure hydrogen the half-widths of the four Q_1 lines did not appear to vary appreciably with J; Table II therefore gives average values for the four lines. The intensity measurements for the $S_0(0)$ line of H_2–A were considered too inaccurate for the determination of meaningful half-widths.

For H_2 and H_2–He the half-widths are approximately proportional to the total gas density. In these cases it is therefore possible to define broadening coefficients; these are given in Table VIII.

TABLE VIII

Broadening coefficients for the Raman lines of hydrogen

Line	Broadening coefficient (cm^{-1} per unit density)	Line	Broadening coefficient (cm^{-1} per unit density)
	Hydrogen		Hydrogen–helium
$S_0(0)$	3.0×10^{-3}	$S_0(0)$	1.8×10^{-3}
$S_0(1)$	4.6×10^{-3}	$S_0(1)$	2.5×10^{-3}
Q_1	1.9×10^{-3}	$Q_1(1)$	2.6×10^{-3}

If our hypothesis is correct that the perturbation of the Q_1 lines is caused by vibrational perturbation alone, then the intensity profiles of the Q_1 lines must represent the statistical distribution of the perturbation of the vibrational frequency throughout the gas. The half-widths could presumably be calculated

by statistical methods, but this will not be attempted here. If the half-widths of the S_0 lines are also due to the perturbing force F, they should of course be related to the half-widths of the Q_1 lines by equations immediately derivable from equation (15): $\delta S_0(0) = 6\times0.0182\times\delta Q_1$ and $\delta S_0(1) = 10\times0.0182\times\delta Q_1$. Broadening coefficients for the S_0 lines derived in this way are of the order of 1/10th of those actually observed. There is thus no doubt that the anisotropic scattering, even in the H_2–H_2 case, undergoes perturbations which are not present for the isotropic scattering; the arguments developed in the Introduction seem therefore to have a general validity.

The present research was intended to explore the potentialities of high resolution Raman spectroscopy of compressed gases in studying the effects of intermolecular forces on the vibration and rotation of molecules. The results indicate that, in simple systems at least, the method offers the possibility of a penetrating analysis of the physical mechanisms involved. Some suggestions can be made as to the directions which further experimental work might take. Since the linear terms in the expansions of the perturbations as power series in the density are the easiest to discuss theoretically, these should be determined as accurately as possible by experiments in the low and medium density ranges. Because of the importance of the molecular distribution in the interpretation of the results, provision should be made for observing the Raman spectra at various temperatures. It is anticipated that the recently developed optical maser can be used to eliminate some of the technical difficulties in the Raman spectroscopy of compressed gases.

REFERENCES

ALLIN, E. J., FELDMAN, T., and WELSH, H. L. 1956. J. Chem. Phys. **24**, 1116.
BHATNAGAR, S., ALLIN, E. J., and WELSH, H. L. 1962. Can. J. Phys. In press.
BURNS, K., ADAMS, K. B., and LONGWELL, J. 1950. J. Opt. Soc. Am. **40**, 339.
CRAWFORD, M. F. and MACDONALD, R. E. 1958. Can. J. Phys. **36**, 1022.
CRAWFORD, M. F., WELSH, H. L., and HARROLD, J. H. 1952. Can. J. Phys. **30**, 81.
DE BOER, J. 1949. Repts. Progr. in Phys. **12**, 305.
EDLÉN, B. 1953. J. Opt. Soc. Am. **43**, 339.
HARE, W. F. J. and WELSH, H. L. 1958. Can. J. Phys. **36**, 88.
HERZBERG, G. 1950. Spectra of diatomic molecules (Van Nostrand Co. Inc., New York).
PLACZEK, G. 1934. Handbuck der Radiologie VI(2) (Akademische Verlagsgesellschaft m.b.H, Leipzig).
PULLIN, A. D. E. 1960. Spectrochim. Acta, **16**, 12.
STOICHEFF, B. P. 1957. Can. J. Phys. **35**, 730.
STRYLAND, J. C. and MAY, A. D. 1960. J. Sci. Instr. **31**, 414.
VAN KRANENDONK, J. 1959. Physica, **25**, 1080.
——— 1960. Can. J. Phys. **38**, 240.

THERMAL NEUTRON CROSS SECTIONS AND RESONANCE INTEGRALS OF THE REACTIONS $O^{17}(n,\alpha)C^{14}$, $Ar^{36}(n,\alpha)S^{33}$, AND $N^{14}(n,p)C^{14}$ [1]

G. C. Hanna, D. B. Primeau, and P. R. Tunnicliffe

ABSTRACT

The thermal neutron cross sections of the exothermic reactions $O^{17}(n,\alpha)C^{14}$, $Ar^{36}(n,\alpha)S^{33}$, and $N^{14}(n,p)C^{14}$ have been measured, relative to the activation cross section of gold, by using a pulse ionization chamber technique. The results obtained are 0.235 ± 0.005 barn, 5.52 ± 0.11 millibarns, and 1.83 ± 0.03 barns respectively. All the reactions were shown to have the same cadmium ratio as the $B^{10}(n,\alpha)Li^7$ reaction with accuracies of $\pm10\%$, $\pm40\%$, and $\pm3\%$ respectively. The O^{17} result shows that capture in this nuclide contributes significantly to neutron absorption in heavy water.

I. INTRODUCTION

The thermal neutron cross section of the reaction $O^{17}(n,\alpha)C^{14}$ has been measured as 0.46 ± 0.11 barn by May and Hincks (1947), and more recently as 0.25 ± 0.15 barn (Hughes and Schwartz 1957). These results show that this reaction is of some importance in the neutron absorption of heavy water. It would, for natural abundance, contribute 10 to 20% of the absorption in pure D_2O, and records at Chalk River show that heavy water can be enriched several times in O^{17} depending on the preparation process (Lewis 1957). A large resonance integral would further increase its importance. The work reported here was undertaken to determine the cross section accurately and to obtain a value for the resonance integral.

The reaction $Ar^{36}(n,\alpha)S^{33}$ was also observed and its cross section determined. The $N^{14}(n,p)C^{14}$ reaction was observed in subsidiary investigations and its cross section was also measured.

The reactions were induced in the filling gas of a large gridded ionization chamber of known sensitive length, by a well-collimated neutron beam from the NRX reactor of intensity about 5×10^7 neutrons/second. The chamber was filled with argon – carbon dioxide or argon–nitrogen mixtures of known composition, and several samples of carbon dioxide with different O^{17} contents were used. The reaction rate was determined by sorting the output pulses of the chamber with a pulse-height analyzer and counting the pulses in the appropriate peak.

The neutron beam intensity was determined from the counting rate in a fission chamber containing a thin uniform deposit of U^{233} which intercepted the whole beam area. The U^{233} fission chamber was calibrated by activating uniform gold foils in the beam. After an activation of several hours, during which the total number of fission counts was determined, the foils were compared with accurately calibrated Au^{198} standards in a 4π γ-counter. In

[1]Manuscript received September 18, 1961.
Contribution from Atomic Energy of Canada Limited, Chalk River, Ontario.
Issued as A.E.C.L. No. 1378.

some of the earlier measurements the fission chamber was not used; the O^{17} counts in the main chamber were recorded during the activation of gold foils.

An auxiliary fission chamber, inserted in a neighboring hole in the reactor shield, was used as a beam monitor.

A cadmium filter, which could be inserted in the beam, enabled the cadmium ratios of the reactions in the main chamber to be compared with that of the U^{233} fission chamber. The U^{233} cadmium ratio was subsequently compared with that of a BF_3 counter placed in the beam, so that the cadmium ratios could be related to that of a $1/v$ detector.

Some fast neutron reactions, due to unmoderated fission neutrons from the reactor core, were observed.

A preliminary account of this work was given at the Third Symposium on Nuclear and Radiochemistry at Chalk River in September, 1960.

II. EXPERIMENTAL APPARATUS

1. General Arrangement

The design of the experimental equipment was a compromise between counting rate and resolution from a continuum of background pulses mainly due to unmoderated fast neutrons from the reactor. The major difficulty in resolving the reactions from this background arose when attempting to detect epithermal neutron events, which required the minimum achievable spread in the pulse-height distribution peaks.

The general arrangement is shown in Fig. 1. The neutron beam was formed by a tapered collimator made of pure magnesium and inserted in a 10 cm

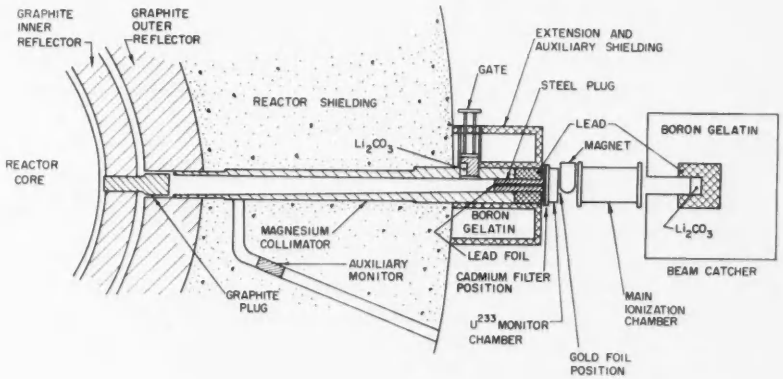

FIG. 1. General arrangement of the apparatus.

diameter hole through the reactor shield. The neutrons originated from the face of the removable graphite plug in the reflector. The length of this plug affected the epithermal to thermal neutron ratio, but also (which was more important) governed the epithermal to fast neutron ratio. Most of the measure-

ments were made with a 60 cm long plug which gave an optimum value for this latter ratio, the resultant beam having a cadmium ratio of about 1000 for a $1/v$ detector and a flux of about 4×10^7 n/cm^2 sec. The addition of lead to the face of the plug did not appreciably reduce the loss in resolution in the main chamber due to γ-rays in the beam.

A removable steel plug, about 45 cm long, was fitted to the exit of the collimator to control the beam diameter. The apparatus was designed to use a neutron beam up to 4 cm in diameter but the beam diameters used in practice were 1.3 cm or less. The extension of the collimator beyond the reactor shield was necessary to avoid other equipment; it also provided a convenient arrangement for a shutter to close off the beam.

The beam passed first through the U^{233} fission chamber, then between the poles of a permanent magnet (a 10,000 Mc/s magnetron magnet, field $\sim$2200 gauss), through the main ionization chamber, and finally into a beam catcher where the thermal neutrons were absorbed in lithium carbonate without capture γ-rays being produced. A lead cup surrounding the lithium carbonate block absorbed the beam γ-rays, and the assembly was located at the base of a re-entrant hole in a barrel filled with an aqueous solution of borax and boric acid. This solution, which absorbed the fast neutrons, was jelled with agar to prevent spills.

The 0.5 mm thick lead foil, mounted over the inner end of the exit aperture, and the magnet reduced the number of charged particles entering the ionization chamber and degrading the resolution by contributing to the noise.

The U^{233} chamber was bolted to the collimator to maintain its alignment; the main chamber was supported by antivibration mounts on adjustable brackets.

The auxiliary monitor was inserted in a secondary 5 cm diameter hole originally provided for the remote insertion of isotope samples for irradiation in the reflector (the NRX self-serve arrangement). The monitor chiefly responded to neutrons scattered from the collimator wall and streaming down the hole.

2. Main Chamber

The main chamber, a gridded parallel-plate ionization chamber, is illustrated in Figs. 2 and 3. It was designed to accept a 4 cm diameter neutron beam traversing the grid-cathode space, and the electrode structure was made large enough that no reaction products from the beam area would leave the sides of the collecting volume. The total volume was about 11 liters. Duralumin windows, 0.007 cm thick, cemented in the end plates of the container, allowed the neutron beam to enter and leave with minimum scattering. Except for the windows, the chamber was wrapped in 0.04 cm thick cadmium sheet to absorb stray thermal neutrons.

The electrode structure (Fig. 3) was designed to give a well-defined sensitive length of about 27 cm. The field-shaping electrodes, 0.0025 cm diameter tungsten wire, were used to ensure that the equipotential surfaces were parallel over the area of the collecting electrode. Twice-scale models of the

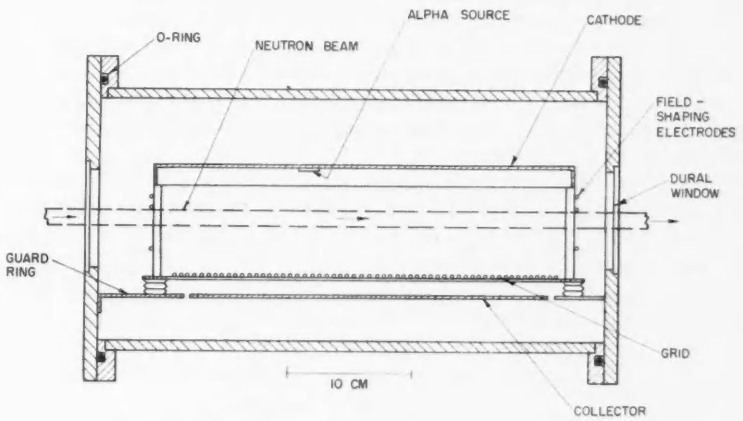

FIG. 2. Longitudinal cross section of the main ionization chamber.

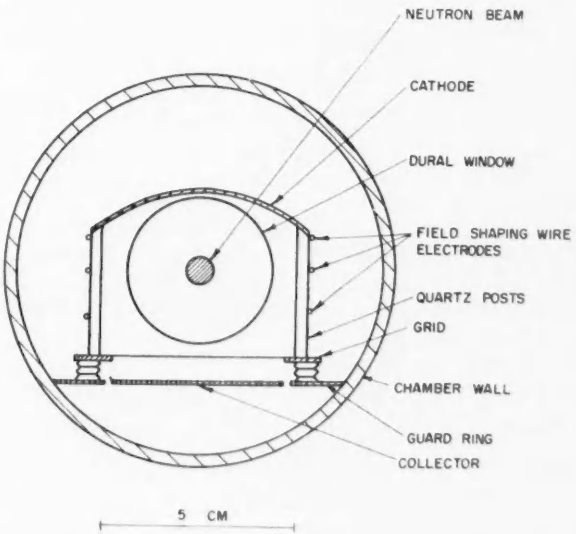

FIG. 3. Transverse cross section of the main ionization chamber.

electrodes were drawn with conducting ink on conducting paper.* The appropriate voltages were supplied to the model and the equipotentials mapped with a voltage probe. The positions and voltages of the field-shaping electrodes were adjusted until it was judged that the sensitive length was defined to within a millimeter, and that there would be no loss of ions from the sides of the required sensitive volume. The arrangement and voltages finally used are illustrated in Fig. 4.

The grid was made of 0.009 cm diameter stainless steel wires spaced 0.16 cm apart on a rectangular aluminum frame. It was necessary to insert a stiffening bar parallel to the wires across the middle of the frame to prevent sag of the wires; this essentially divided the chamber into two halves, because the loss of ionization collected on the bar removed the pulse from the main peak of the distribution.

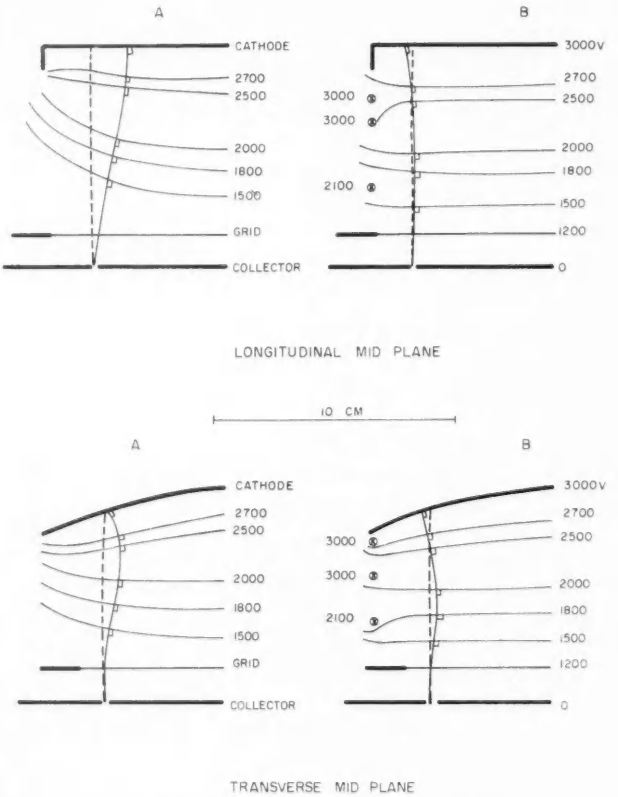

FIG. 4. Equipotentials obtained from the conducting paper model, A, without, and B with, field-shaping electrodes.

*Manufactured by Sunshine Scientific Instruments, Philadelphia.

The effective length of the chamber, i.e. the length yielding pulses unaffected by loss of ionizing track over the ends and therefore in the main peak, was calculated by subtracting from the physical length of the collecting electrode, 270 mm, the width of the stiffening bar (3.5 mm), and four "end-effects", each equal to one quarter of the estimated range of the reaction products in the chamber filling (~1 cm). Because of the finite energy resolution of the apparatus, the main peak included a contribution from the low-energy "tail" of degraded pulses, and the effective length was increased (generally by ~2 mm) to allow for this effect. This correction was obtained from the observed amplitude of the tail adjacent to the peak. This amplitude agreed satisfactorily with a rough calculated value; an accurate calculation was not possible because of lack of knowledge of the specific ionization along the tracks of the heavy recoil atoms. The corrected effective length was generally about 259 mm.

The grid shielding inefficiency was about 3.5% and the loss in resolution due to track-orientation effects was not significant for the ~1 cm long tracks of the neutron-induced reactions.

The resolution of the chamber was controlled by a combination of electronic noise and "noise" from γ-rays in the neutron beam. The latter contribution was minimized by using amplifier time constants as short as possible, consistent with the rise-time limitations of the chamber. At these time constants, 1 μsec for both smoothing and slipping, and with the relatively high capacity of the chamber (about 40 pf), the electronic noise was mainly anode-current shot noise in the first tube. Various tubes and arrangements of the first stage of the preamplifier were investigated: the most satisfactory was the E83F used in the circuit of Cottini *et al.* (1956), the adjustable plate current providing a convenient arrangement for optimizing the conditions of a particular measurement.

Some reduction in noise was obtained by adding a second smoothing time constant of 1.7 μsec. Under these conditions and with 8.5-ma anode current in the first tube, the electronic noise gave a resolution of about 40 kev (full width at half maximum); with the 1.3 cm diameter beam passing through the chamber it was 65 kev.

The resolution of the chamber could have been improved, at the expense of counting rate, by reducing its size (to reduce the capacity and the γ-ray noise), and by reducing the beam intensity. With lower beam intensities the amplifier time constants could have been increased; this would have improved the circuit noise but increased the contribution from acoustic vibrations.

A small (~200 c.p.m.) sample of U^{233} attached to the inner surface of the cathode provided an approximate energy calibration. For measurements involving these longer-range alpha particles the amplifier time constants had to be increased (to $\geqslant 5$ μsec) to avoid rise-time effects; such measurements were only made with the neutron beam shut off. In the later stages of the investigation the energy calibration was not required and the U^{233} sample was removed in order to reduce background.

3. U^{233} Fission Chamber

The U^{233} fission chamber (Fig. 5) was a gridded parallel-plate chamber having circular symmetry about the neutron beam axis. It was designed to

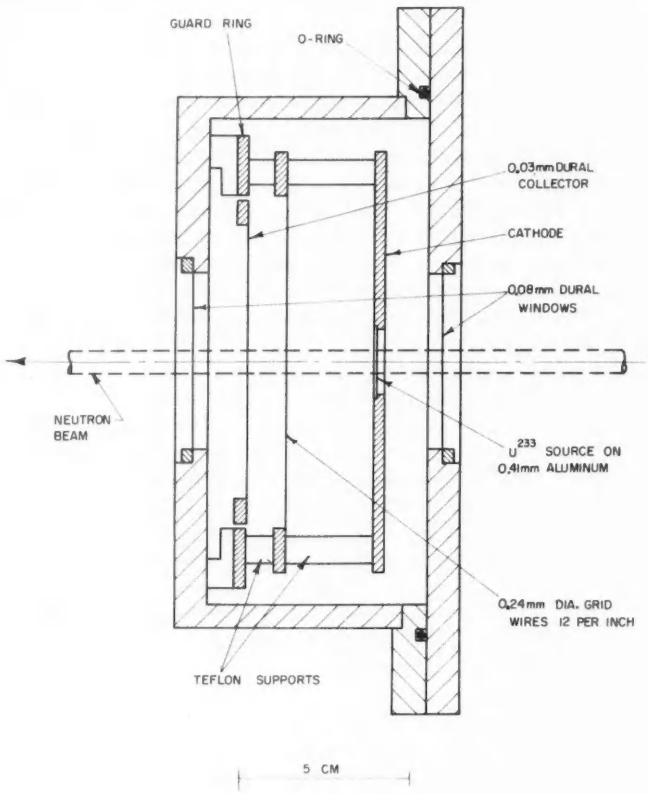

FIG. 5. Cross section of the U^{233} fission chamber.

introduce a minimum amount of scattering material into the beam. With a filling of 1 atm pressure of argon containing 5% carbon dioxide, the fission fragments from the U^{233} sample were stopped well within the collecting volume of the chamber. Connections to the electrodes were made through copper-glass seals, and voltages of 3 and 1.2 kv were applied to the cathode and grid respectively. The uniform U^{233} sample, about 2.5 $\mu g/cm^2$, was prepared by the method described by Bigham *et al.* (1958).

A typical fission pulse-height distribution from the chamber is shown in Fig. 6. The scaler discrimination bias was set just below the lower peak as shown. Deterioration of the filling caused a slow drift downwards of the distribution and it was necessary to refill the chamber periodically. Frequent pulse-height distributions enabled corrections to be made for loss of sensitivity; these were never more than 0.5%.

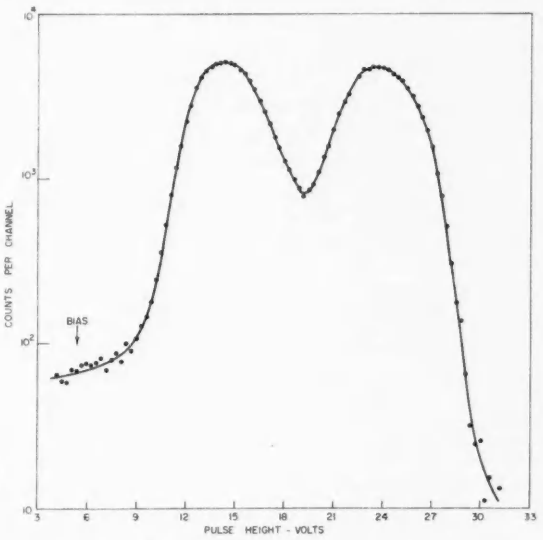

FIG. 6. Pulse-height distribution from the U^{233} fission chamber.

4. The Auxiliary Monitor Chamber

The auxiliary monitor was a "parallel-plate" fission chamber of the type described by McKenzie (1959). It contained about 70 μg of natural uranium. Its pulse-height distribution, illustrated in Fig. 7, had a satisfactory minimum to set the discriminator bias in, and did not change appreciably during the measurements.

5. Electronic Equipment

Standard Chalk River electronic equipment was used. Preamplifiers for the main and U^{233} chambers were mounted directly on the chambers; the preamplifier for the auxiliary monitor was located at the surface of the reactor shield and connected to the chamber by a length of low-capacity cable. Two scalers in parallel were used for each counting function to verify their correct operation. A 100-channel analyzer was used to record pulse-height distributions. The overflow from the top channel of the analyzer was counted so that the number of pulses recorded by the analyzer could be checked against a scaler. No important discrepancies were observed except under fault conditions.

III. GAS-PREPARATION AND FILLING OF THE MAIN CHAMBER

During the course of the experiments the main chamber was filled at various times with argon – carbon dioxide and argon–nitrogen mixtures and in one case with a krypton – carbon dioxide mixture. Natural carbon dioxide and carbon dioxide containing oxygen enriched to two different concentrations of

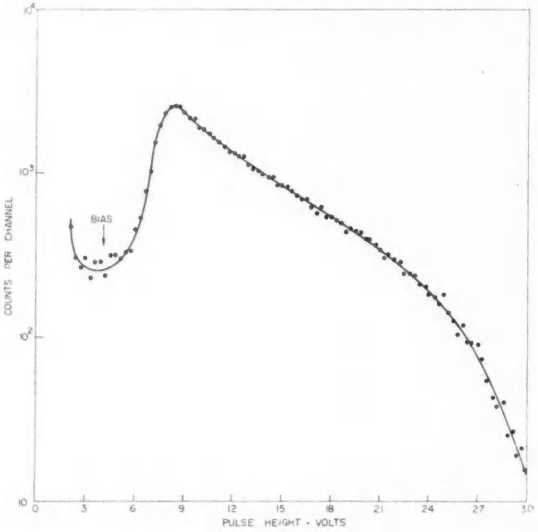

FIG. 7. Pulse-height distribution from the auxiliary monitor.

O^{17} were used. In general, the gases were purified by freezing in a liquid nitrogen trap, pumping on the condensate, and then allowing the trap to warm up slowly. The first portion of gas evolved was discarded and the subsequent portion admitted to the chamber. Sufficient condensate was employed to leave a residue which was also discarded. All the enriched carbon dioxide available was used, however; it was purified in the manner described later. The nitrogen ("bone-dry" grade) was found to be satisfactory without purification.

After a thorough evacuation of the chamber the minor constituent of the filling (carbon dioxide or nitrogen) was admitted first. When the desired pressure was reached, the condensate reservoir was closed off by a valve (and cooled) and sufficient time allowed for the vacuum-system manifold to reach a constant pressure. The ambient temperature was then noted and the pressure measured by either a calibrated McLeod gauge or a simple mercury manometer, the heights being read accurately with a cathetometer. The chamber valve was then closed and the vacuum system pumped down. Purified argon (or krypton) was then admitted to the system and the chamber valve opened after the manifold pressure exceeded the pressure of the minor component, thus ensuring that no gas was lost from the chamber. The final chamber pressure was usually a few centimeters of mercury above atmospheric pressure.

The enriched carbon dioxide was prepared by equilibrating natural carbon dioxide with water enriched in O^{17} (and O^{18}). Two samples of water (primarily prepared as O^{18} enriched material) were obtained, one from the Radiochemical Centre in the United Kingdom containing $\sim 0.7\%$ O^{17}, and the other from the Weizmann Institute, Israel, containing $\sim 2\%$ O^{17}. About one liter of carbon

dioxide was equilibrated with 10 ml of water and gave 10-fold and 60-fold O^{17}-enriched samples respectively. The water was inserted into the exchange vessel (previously filled with dry nitrogen), pumped on for about one minute to outgas it, frozen with liquid nitrogen into a cold finger, and then pumped to a good vacuum. Dry carbon dioxide was then admitted and the vessel gently rolled, for a period of about two hours in the case of the first sample. For the second sample this period was increased to two days, which gave a much closer approach to equilibrium. The water was then frozen with a dry-ice acetone mixture and the carbon dioxide transferred into a flask by freezing into a cold finger with liquid nitrogen. After pumping on the frozen carbon dioxide the liquid nitrogen was replaced by a dry-ice acetone mixture. Dry carbon dioxide was slowly evolved overnight and then transferred to a storage flask.

After the counting rate measurements the enriched carbon dioxide was recovered by slow evacuation of the chamber through a coil of copper tubing immersed in liquid nitrogen, which retained the carbon dioxide but not the argon. The pump and chamber were then closed off by a valve and the carbon dioxide transferred to a storage flask by freezing into a cold finger while the coil was allowed to warm up. Samples of the enriched material were taken for mass analysis during both filling and recovery. The samples were sealed in break-seal flasks whose content was subsequently analyzed for O^{17} content by mass spectroscopy.

IV. THE NEUTRON FLUX AND THE CALIBRATION OF THE U^{233} FISSION CHAMBER

The intensity of the neutron beam (i.e. the flux integrated over the beam area) was determined in a manner similar to that described by Bigham *et al.* (1958). Gold foils, 1.9 cm diameter (larger than the beam diameter of 0.6 cm to 1.3 cm), were irradiated in the beam for several hours. The induced Au^{198} activity was subsequently determined in a 4π γ-scintillation counter by comparison with absolute Au^{198} standards, which were thin samples of high specific activity material on thin plastic backings. Their absolute disintegration rates had been determined in the A.E.C.L. Radioisotope Standardization Section by the 4π $\beta-\gamma$ coincidence method described by Campion (1959).

The gold foils were all punched from the same 0.0025 cm thick sheet of high-purity gold. The dimensions and weights of the sheet and of the individual foils were accurately determined and it was concluded that the foil was very uniform in thickness. The mass per unit area obtained from the individual foils was 45.143 ± 0.033 mg/cm^2.

During the irradiation of the gold foils the counts from the U^{233} and auxiliary monitors were recorded; the main chamber, filled with an enriched carbon dioxide – argon mixture, was also operated and the pulses recorded on the pulse-height analyzer. The effective bias points on the pulse-height distributions from the monitor chamber were determined (with a signal generator) just before the irradiation.

Two sets of flux determinations were carried out in each of which four gold irradiations were made. For each set three freshly determined Au^{198} standards

were available, of approximate strengths 3×10^3, 8×10^3, and 1.6×10^4 d.p.s., determined with an accuracy of 0.2%. On each occasion the sensitivity of the 4π γ-counter deduced from the different standards was the same within counting statistics ($\sim$0.4%).

The first set was done without the U^{233} fission chamber and variations of $\pm4\%$ in the sensitivity of the auxiliary monitor were noted in the four irradiations. Such variations were subsequently found to be correlated with transient changes in the reactor operation; its sensitivity was constant to within $\sim1\%$ when reactor conditions were stable. However, the relation between gold activity and counting rate in the main chamber was not significantly affected by changes in reactor operation and these data were included in the determination of the O^{17} cross section.

The second set of gold irradiations was used to calibrate the newly constructed U^{233} fission chamber which was used in all subsequent work. The consistency of the calibration is illustrated by the results of four successive measurements with different gold foils from which the ratios of the fission chamber counts to Au^{198} c.p.m. were 8.023, 8.033, 7.994, and 7.990, giving a mean of 8.013 ± 0.010.

These measurements were made with a 0.8 cm diameter neutron beam. Auxiliary measurements, in which the beam diameter was varied from 0.6 cm to 1.3 cm, showed that the relation between the U^{233} chamber and main chamber counting rates was independent of beam diameter to within a statistical accuracy of about 0.5%; it was concluded that non-uniformities of the U^{233} sample did not introduce any appreciable uncertainties in relative flux determinations.

The average thermal flux in the main chamber was obtained from the gold activations using a 2200 m/sec gold cross section of 98.8 ± 0.3 barns (Hughes and Schwartz 1958) and a decay constant of 0.010705 hr^{-1} (Bell and Yaffe 1954). Corrections were made for:

(*a*) the epithermal contributions to the gold activity and U^{233} fission rate, which were obtained from measurements with an 0.076 cm cadmium filter in the beam, about 1% and 0.5% respectively;

(*b*) the effective temperature of the neutron beam, about 120° C (Bigham 1958), which gave *g*-values of 1.011 and 1.001 for gold and U^{233} respectively (Westcott 1960);

(*c*) attenuation in the gold foil (for measurements without the foil), $\sim$0.7%;

(*d*) excess activation of the gold due to self-scattered neutrons; a scattering cross section of 9 barns (Hughes and Schwartz 1958) gave a correction of 0.3%;

(*e*) scattering of neutrons from the beam by air and by the window of the main chamber, about 0.3%; and

(*f*) γ-ray self-shielding of the gold foils during the Au^{198} counting (Bigham *et al.* 1958), about 0.5%.

The calibration factor obtained for the U^{233} chamber was 2.917×10^5 neutrons passing through the sensitive volume of the main chamber per U^{233} chamber count.

V. RESULTS

1. Identification of Reactions

Preliminary measurements on natural carbon dioxide – argon mixtures showed two peaks in the pulse-height distribution at about 1.75 and 1.91 Mev. These values include a correction for grid inefficiency effects, but were derived, by comparison with U^{233} alpha-particle pulses, on the assumption that ionization is proportional to energy.

The lower peak was assigned to the carbon dioxide component by varying the carbon dioxide content from 10% to zero (when 1% nitrogen was used to give a filling with satisfactory electron drift velocities). The upper peak was assigned to the argon component by using a krypton – carbon dioxide mixture, in which only the lower peak was observed. The reactions were shown to be due to thermal neutrons by inserting the cadmium absorber into the beam.

The two peaks were assigned to the reactions $O^{17}(n,\alpha)C^{14}$ and $Ar^{36}(n,\alpha)S^{33}$, for which Everling *et al.* (1961) give reaction energies of 1.819 and 2.002 Mev respectively. The discrepancies with the present approximate measurements are considered not unreasonable because of ionization-defect effects which are not known for the short-range recoil products. The Ar^{36} reaction is the only one energetically possible in argon (it could not be assigned to an impurity since different samples of argon gave consistent results). Measurements with the enriched carbon dioxide confirmed the O^{17} assignment.

A strong peak from the argon–nitrogen filling at 0.62 Mev was assigned to the $N^{14}(n,p)C^{14}$ reaction (reaction energy 0.627 Mev). This peak was never completely absent in the argon – carbon dioxide fillings but it could be reasonably explained by a nitrogen impurity of partial pressure 60 ± 30 microns.

2. Thermal Cross Section for $O^{17}(n,\alpha)C^{14}$

The $O^{17}(n,\alpha)C^{14}$ cross section was obtained from data taken with six different fillings of the chamber. For the first five, the O^{17} isotopic abundance was about 0.3%, the carbon dioxide pressure being varied, and for the sixth it was 2%. Typical pulse-height distributions from the two types of filling taken with a 0.6 cm diameter neutron beam are shown in Figs. 8 and 9. Other data with better statistical accuracy obtained with a 1.3 cm diameter beam had a somewhat poorer resolution because of the greater γ-ray "noise". Each of these distributions has been corrected for epicadmium background, which was measured in a subsequent run and normalized to the same integrated beam intensity with the aid of the auxiliary monitor. In spite of its dependence on changes in reactor operation this instrument was adequate for this purpose.

For reasons of cheapness, availability, and superior electron-collecting properties, argon (rather than, for example, krypton) was used throughout as the main constituent of the chamber filling. The O^{17} peak was therefore always accompanied by a smaller but incompletely resolved Ar^{36} peak. It was decided not to rely on peak-shape fitting to resolve the two peaks, but rather to determine the Ar^{36} contribution from runs in which the O^{17} peak was absent (Section V. 3).

After correction for epicadmium effects, the high-energy side of the distribution fell to zero within the statistical accuracy; the low-energy side did

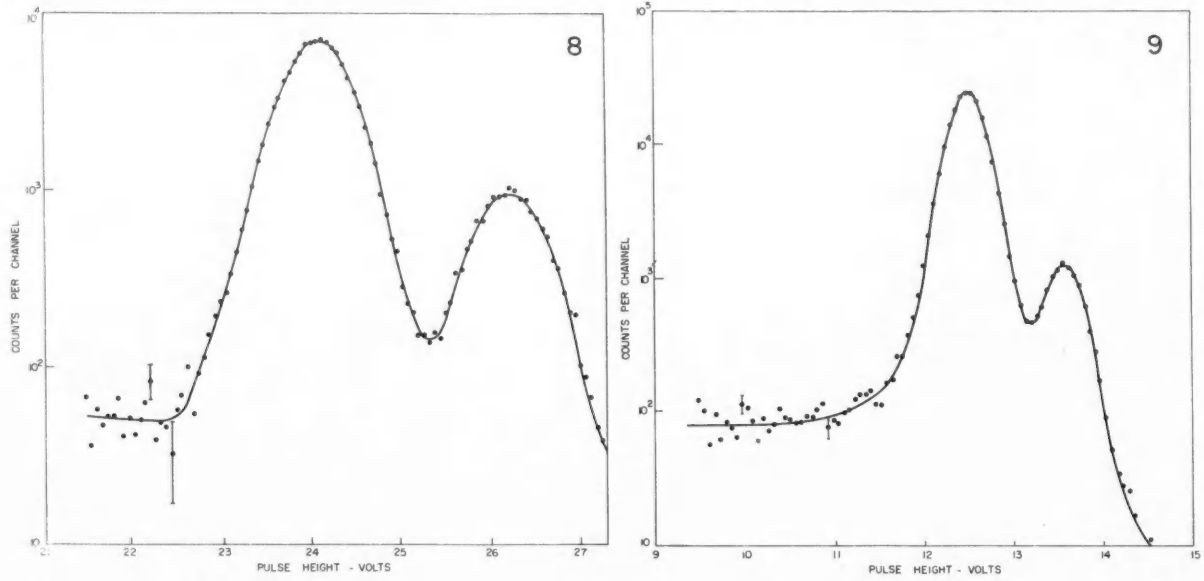

FIG. 8. Pulse-height distribution with an argon – carbon dioxide filling in the main chamber (O^{17} abundance 0.3%, carbon dioxide pressure 6 cm Hg) showing the $O^{17}(n,\alpha)C^{14}$ and $Ar^{36}(n,\alpha)S^{33}$ peaks. The contribution from epicadmium neutrons has been subtracted.
FIG. 9. As in Fig. 8, but O^{17} abundance 2%, and carbon dioxide pressure 3 cm Hg.

not because of the "tail" due to end-effects. The total counts in the two peaks were taken from the point where the distribution rose above the low-energy tail. Between 5 and 10 runs were taken with each filling, with 25,000 to 50,000 counts per run. In general the results for a given filling were consistent and the over-all statistical accuracy was a small fraction of one per cent. The epicadmium corrected Ar^{36} contribution over this energy range was then subtracted from this total. This contribution was obtained from the argon–nitrogen data by normalizing to the same argon pressure and the same number of U^{233} monitor counts. The resulting O^{17} intensity included a contribution from its own low-energy tail; this was evaluated by extrapolating the observed tail and was expressed as a correction to the effective length of the chamber as already outlined in Section II. 2.

Table I summarizes the results from the six fillings of argon–enriched carbon dioxide mixtures. The cross sections were calculated from the mean of the mass spectrometer analyses of samples taken before and after the counting.

TABLE I

$O^{17}(n,\alpha)C^{14}$ cross section

Chamber filling (mm Hg)		O^{17} abundance (atom %)		Relative weight	Thermal neutron cross section (barns)
Ar	CO_2	Before	After		
734	43.4	0.3238	0.3206	1†	0.245
695	60.1	0.3726	—*	1‡	0.227
677	109.6	—*	0.3345	1‡	0.239
658	109.0	0.3435	0.3357	2	0.235
719	61.7	0.3368	0.3196	2	0.232
755	30.0	2.091	2.002	2	0.234
				Mean	0.235±0.002

*Sample lost.
†No U^{233} monitor.
‡Only one mass spectrometer analysis.

The differences between the mass analyses appear to be real, since they were given with uncertainty errors of ±0.5%. It is not known whether the isotopic degradation resulted from a deterioration while in the chamber, from handling and sampling procedures, or from both; only for the last filling was there clear evidence of deterioration during the counting rate measurements.

The final result, 0.235±0.002 barn, is the weighted mean of the individual results, the error being the standard deviation of the mean. The counting rate ratio Ar^{36}/O^{17} varied between 0.2 (first filling) and 0.05 (last filling) so that the ~3% uncertainty in the Ar^{36} contribution is not important. Errors in the evaluation of the corrected effective length of the chamber are believed to be less than ±0.5% and may also be neglected. More serious are the uncertainties in the actual O^{17} content of the gas in the chamber during the measurements. These introduce an uncertainty of about ±1.5% into the mean. Other minor errors combine to give an over-all uncertainty of about ±2%, i.e. ±0.005 barn.

3. Thermal Cross Section for $Ar^{36}(n,\alpha)S^{33}$

The Ar^{36} peak observed in the argon – 1.1% nitrogen filling, after correction for epicadmium background, is shown in Fig. 10. It will be observed that the high-energy side of the peak did not fall to zero; this behavior was apparently peculiar to this filling and is possibly associated with the presence of an intense low-energy peak due to the $N^{14}(n,p)C^{14}$ reaction. However, it was not properly investigated since its effect on the analysis of the Ar^{36} peak intensity was not serious.

For the purpose of obtaining the Ar^{36} contribution to the O^{17} distributions of the previous section, the counts were merely summed over the appropriate energy interval (and then suitably normalized), no correction being made for the high-energy tail. A back extrapolation of this tail over the whole energy region would give an intensity about 2% of that of the Ar^{36} peak.

The cross section for the $Ar^{36}(n,\alpha)S^{33}$ reaction was obtained by summing only over the Ar^{36} peak and correcting for the contribution of the low-energy tail to the main peak in the usual way. As a check, the argon cross section was also measured by analyzing the data from two chamber fillings containing low percentages of natural carbon dioxide (1.9% and 0.5%). As shown in Fig. 11, a typical epicadmium corrected pulse-height distribution from the 1.9% filling, the argon peak could be separated without appreciable error.

The cross sections obtained from these three fillings, via the calibrated U^{233} monitor, are shown in Table II. The error of the mean deduced from the

TABLE II

$Ar^{36}(n,\alpha)S^{33}$ cross section

Filling (cm/Hg)	Thermal cross section (millibarns)
75.5 Ar + 0.9 N_2	5.53
73.1 Ar + 0.4 natural CO_2	5.54
74.2 Ar + 1.4 natural CO_2	5.48
	Mean 5.52±0.03

observed dispersion is only ±0.03, but a consideration of the accuracy of the various corrections suggests that the final result is probably accurate to about ±2%.

4. Thermal Cross Section for $N^{14}(n,p)C^{14}$

The $N^{14}(n,p)C^{14}$ reaction cross section was determined from the data obtained with the argon – 1.1% nitrogen filling. Figure 12 shows the pulse-height distribution, corrected for epicadmium effects, in this energy region.

It will be noted that there is a "shoulder" on the low-energy tail about 150 kev below the main peak which is attributed to the effect of the grid-stiffening bar. If the instrumental resolution were perfect, and if the specific

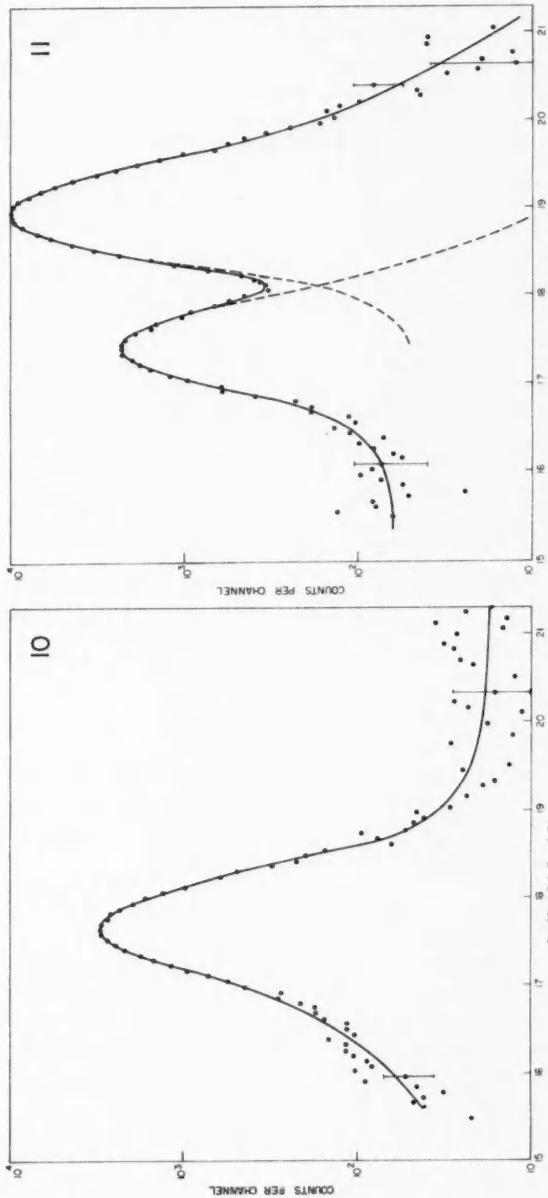

FIG. 10. As in Fig. 8, but with an argon – 1.1% nitrogen filling showing the $Ar^{36}(n,\alpha)S^{33}$ peak.
FIG. 11. As in Fig. 8, but with a 1.9% natural carbon dioxide filling.

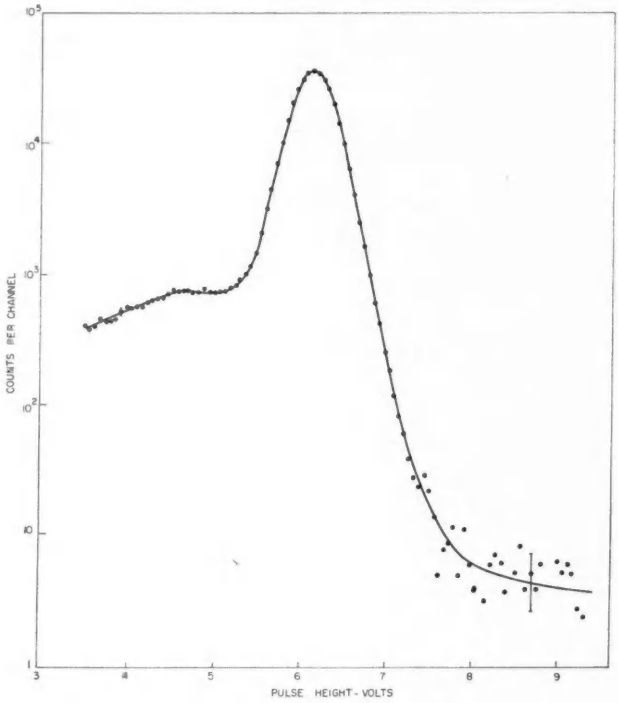

FIG. 12. As in Fig. 10, but showing the $N^{14}(n,p)C^{14}$ peak.

ionization were constant along the whole track, there would be a discontinuous step at a distance below the main peak corresponding to a loss of range equal to the width of the bar. This step is smeared out by the variation of specific ionization and the finite energy resolution; no quantitative estimates have been made, but the identification of this observed shoulder with the expected step is considered to be correct. The shoulder of the Ar^{36} and O^{17} reactions was not seen since it lay below the energy region examined.

The ordinary low-energy tail correction is rather more serious in this reaction than the others because the instrumental resolution represents a greater fraction of the total energy and therefore a larger fraction of the low-energy tail lies within the main peak. In addition, a small allowance ($\sim$0.1%) was made for a continuum of background pulses from higher-energy reactions. A correction of 60 ± 30 microns to the nominal nitrogen pressure was made for impurity in the argon. A correction of about 2% for resolving time losses in the pulse-height analyzer was also necessary in this case. The result obtained was 1.83 ± 0.03 barns. The error was due mainly to uncertainties (due to tail corrections) in the effective length of the chamber; the statistical errors and the errors in the gold calibration were small contributions.

5. Epithermal Cross Sections

The epithermal component of the neutron beam was not expected to be of the dE/E form (Bigham and Pearce 1961; Bigham and Tunnicliffe 1961) since it was derived from the reflector of the reactor and was therefore deficient in high-energy neutrons. Consequently, being of an unknown form, it could not be used to determine a resonance integral. However, it was considered satisfactory to verify the expectation that the cadmium ratios of the reactions studied were the same as for the $1/v$ reaction $B^{10}(n,\alpha)Li^7$.

For convenience the U^{233} fission chamber was used as an intermediary. It was calibrated in a subsidiary experiment in which a small BF_3 counter was placed in the beam (in place of the main ionization chamber). The relative cadmium ratios of this counter and the fission chamber were determined, with a precision of about 1%, for each of the graphite plugs used at the bottom of the beam hole.

Pulse-height distributions with the cadmium filter in the beam were then taken from the main chamber over long periods, the counts from the fission chamber also being recorded. The $O^{17}(n,\alpha)C^{14}$ reaction was investigated by using the filling containing the 60-fold enriched carbon dioxide (the 10-fold enriched material did not give a peak resolved from the background). The argon – 0.5% carbon dioxide filling was used to investigate the argon reaction, and the argon–nitrogen filling for the nitrogen reaction. Pulse-height distributions for these three reactions are shown in Figs. 13, 14, and 15 respectively.

The epicadmium $N^{14}(n,p)C^{14}$ peak was well resolved from the continuum of background, and the reaction rate was determined by adding the pulses

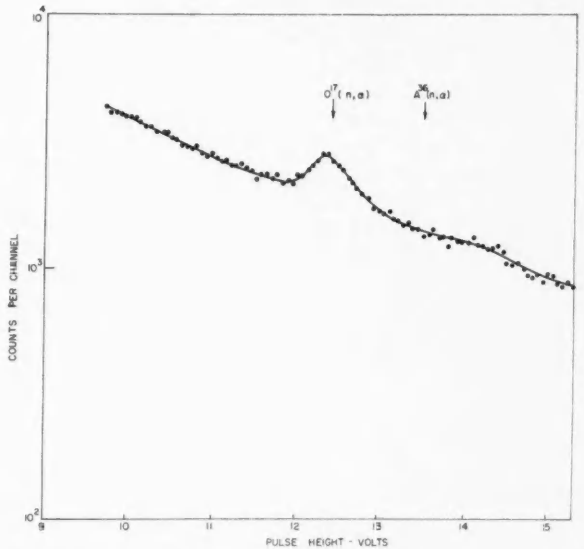

FIG. 13. Epicadmium pulse-height distribution for the $O^{17}(n,\alpha)C^{14}$ reaction with the same argon – carbon dioxide filling as in Fig. 9.

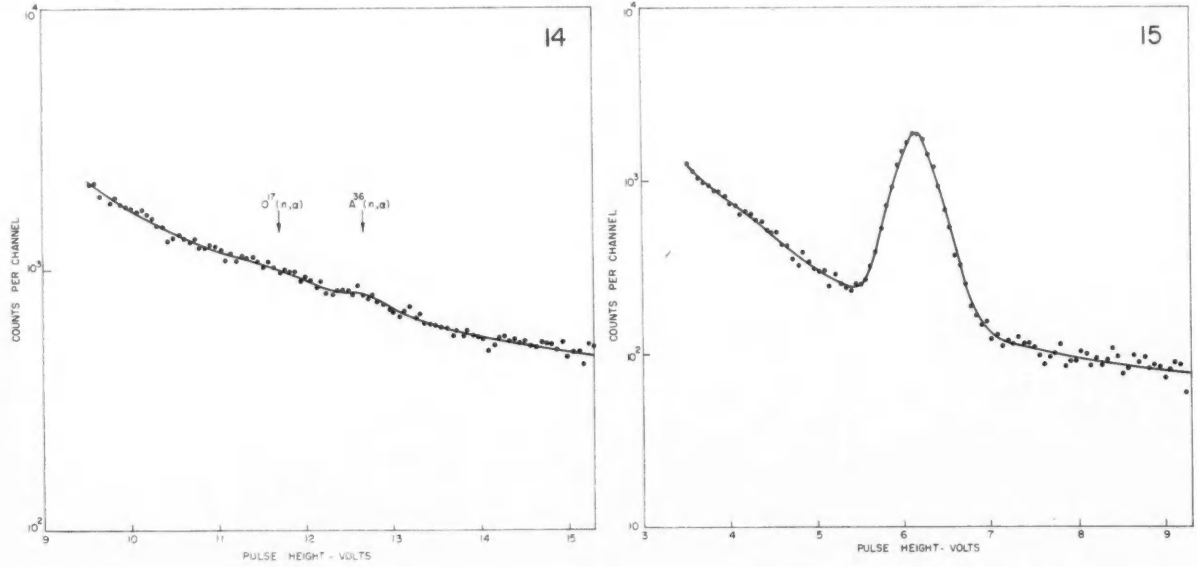

FIG. 14. Epicadmium pulse-height distribution for the $Ar^{36}(n,\alpha)S^{33}$ reaction with an argon – 0.5% natural carbon dioxide filling. The curve has been drawn to show a reaction peak of the intensity indicated by the analytical procedure described in the text.
FIG. 15. Epicadmium pulse-height distribution for the $N^{14}(n,p)C^{14}$ reaction with the argon – 1.1% nitrogen filling.

recorded in the peak and subtracting a background obtained by smoothly joining the distribution on either side of the peak, allowing for a low-energy tail as observed in the thermal neutron irradiations (Fig. 12). The result obtained for the ratio of cadmium ratios $N^{14}(n,p)/B^{10}(n,\alpha)$ was 0.97 ± 0.03, where the error is due to comparable contributions from statistics, and uncertainties in the background and low-energy tail corrections, and in the relative cadmium ratio B^{10}/U^{233}.

Because of the much higher background a different procedure was used for the O^{17} and Ar^{36} reactions. By bracketing a long epicadmium run by short open-beam runs the position and shape of the reaction peak was accurately determined. The epicadmium counting data was then summed over an energy region $\pm\delta$ from the center of the peak, and from this total was subtracted the sum of the counts recorded in the energy intervals -2δ to $-\delta$ and δ to 2δ. With the assumption that the background is a linear function of energy over this range, this difference contains no background contribution, and represents a fraction of the total peak area that can be calculated from the open-beam data. The error introduced by a finite curvature in the background increases as δ^3, and the accuracy of the assumption that it was linear was tested by varying δ from 1/3 to 2/3 times the full width at half maximum. It was shown that the O^{17} peak observed under cadmium was not due to stray thermal neutrons by placing a paraffin wax plug in the epicadmium beam; the peak disappeared. The results obtained for the ratios of cadmium ratios $O^{17}(n,\alpha)/B^{10}(n,\alpha)$ and $Ar^{36}(n,\alpha)/B^{10}(n,\alpha)$ were 0.97 ± 0.10 and 1.1 ± 0.4 respectively.

6. Fast Neutron Reactions

A number of other peaks were observed in the pulse distributions from the main chamber which were not removed by the cadmium; they could, however, be removed by inserting a paraffin plug in the beam and were attributed to fast neutron reactions caused by unmoderated fission neutrons. With a continuum of neutron energies, resonances in a fast neutron reaction give rise to peaks in the pulse-height spectrum at energies corresponding to the difference between the reaction threshold energy and the resonance energy.

No detailed investigations were made, but it was possible to assign a peak at 2.8 Mev observed with argon – carbon dioxide fillings to a close group of resonances near 5-Mev neutron energy in the reaction $O^{16}(n,\alpha)C^{13}$, which is endothermic by 2.2 Mev. Resonances between 4 and 4.4 Mev in this reaction were responsible for a broader "bump" in the pulse-height distribution near 2 Mev. A vestige of the high-energy side of this bump can be seen in Fig. 13; it was observed more clearly with fillings where the O^{16} abundance was 10 times, and the carbon dioxide pressure twice, that of Fig. 13. Several fast neutron peaks were observed with the argon–nitrogen filling, which could readily be ascribed to resonances in the $N^{14}(n,p)C^{14}$ reaction.

VI. DISCUSSION AND CONCLUSIONS

The thermal neutron cross sections obtained were

$O^{17}(n,\alpha)C^{14}$	0.235 ± 0.005 barn,
$Ar^{36}(n,\alpha)S^{33}$	5.52 ± 0.11 millibarns,
$N^{14}(n,p)C^{14}$	1.83 ± 0.03 barns,

based on a Au^{197} activation cross section of 98.8 barns for 2200 m/sec neutrons. It is expected, from general considerations of level widths and spacings, that these reactions should have a $1/v$ dependence on neutron velocity, and this is supported by the cadmium ratio measurements. Further, Batchelor and Flowers (1949) have shown that the $N^{14}(n,p)$ reaction has a $1/v$ dependence between 0.02 ev and 0.1 ev within $\pm 4\%$. Consequently these measured values are also the 2200 m/sec values.

The cross section for the $N^{14}(n,p)C^{14}$ reaction has been measured for thermal neutrons by Batchelor and Flowers (1949) and Coon and Nobles (1949), in each case by comparison with the $B^{10}(n,\alpha)Li^7$ cross section. Correcting their results to a value of 755 barns for the boron cross section gives values of 1.72 ± 0.04 and 1.89 ± 0.05 barns; the latter (Coon and Nobles) value is in better agreement with the present measurement.

The reaction $Ar^{36}(n,\alpha)S^{33}$ has not previously been reported with thermal neutrons. The (n,γ) cross section has been measured as 6.5 ± 1 barns by McMurtrie and Crawford (1950), and the (n,α) cross section is expected to be much smaller because of the small ratio of α energy to barrier height; the barrier penetration term is very sensitive to the value assumed for the nuclear radius, but it is probably about 10^{-7}.

The cross section obtained for the $O^{17}(n,\alpha)C^{14}$ reaction is rather smaller than suggested by the earlier values of 0.46 ± 0.11 barn (May and Hincks 1947) and 0.25 ± 0.15 barn reported by Hughes and Schwartz (1957). It contributes only about 7% to the calculated total absorption cross section of pure D_2O when the O^{17}/O^{16} ratio is the same as in natural oxygen. However, it is of some interest to consider the possible magnitude of the $O^{17}(n,\gamma)O^{18}$ cross section.

Since the ground state of O^{17} has spin 5/2 and positive parity (the available information on the nuclear states involved is summarized by Ajzenberg-Selove and Lauritsen (1959)), the capture of a thermal (s-wave) neutron can produce 2+ and 3+ states. A 2+ state is expected to decay rapidly by α-particle emission to the (0+) ground state of C^{14}, and in fact there is a 2+ state at 8.229 Mev, i.e. 160 kev above the excitation energy produced by neutron capture, with an α-particle width of 1.3 ± 0.8 kev. Because of the decreased barrier penetration probability this width is expected to be reduced to about 0.75 kev at the neutron-capture excitation energy. This is still very much larger than the expected gamma-ray width, so that $\sigma(n,\gamma)$ for this 2+ state is negligible (and is confidently expected to be negligible for any other 2+ state).

If it is assumed that this state is solely responsible for the observed (n,α) cross section, its neutron width can be calculated directly from the Breit-Wigner formula. For a single resonance at E_r (see Vogt 1959, esp. pp. 239, 240)

$$\sigma(n,\alpha) = \pi\lambda\!\!\!^{-2}\frac{2J+1}{2(2I+1)}\frac{\Gamma_n\Gamma_\alpha}{(E_r+\Delta-E_c)^2+\Gamma^2/4}$$

where $I(=5/2)$ and $J(=2)$ are the initial and final spins, and Γ_n, Γ_α, and Γ are the neutron, α-particle, and total widths at the excitation energy E_c produced by the capture of a thermal neutron. $\Gamma(\sim\Gamma_\alpha)$ may be neglected in

comparison with $E_r - E_c (= 160$ kev), as may the level shift Δ, which is of the order of 2 kev.

This gives $\Gamma_n = 0.6$ ev, which is substantially less than the expected value of ~ 10 ev (see below), so that there is no need to postulate a contribution from any other level to account for the observed (n,α) cross section.

In contrast to this behavior the formation of a 3+ state would not lead to α-particle emission, since there is no state of odd parity or non-zero spin available in C^{14}, but to gamma-ray emission instead. There are apparently no negative parity states in O^{18} below 4 Mev at least, so that the energy of any $E1$ γ-ray would be less than 4 Mev. A 6-Mev $M1$ transition to the first excited (2+) state would also be possible. The single-particle widths (Wilkinson 1960) are <30 ev and 4 ev for these $E1$ and $M1$ transitions respectively. How much they would be hindered in practice is quite uncertain, but a value of Γ_γ equal to 1 ev is probably correct within an order of magnitude for either transition.

The experimentally observed values of reduced widths for nucleon emission have been collected by Vogt (1959); the data of his Fig. 3 indicate that Γ_n at 0.025 ev should be within an order of magnitude of 10 ev.

With $\Gamma_\gamma = 1$ ev and $\Gamma_n = 10$ ev a value of $\sigma(n,\gamma) > 0.23$ barn (i.e. $> \sigma(n,\alpha)$) would result if a 3+ level lay within 25 kev of the neutron capture excitation energy, or within 250 kev if the estimates of Γ_γ and Γ_n are both increased by an order of magnitude. There is no information on such states in this energy region, which has been studied only by the α-particle bombardment of C^{14}, but the separation of 3+ states would be expected on general grounds to be in the region of 1 Mev. It therefore appears that the possibility of an (n,γ) cross section greater than the observed (n,α) cross section cannot be neglected.

ACKNOWLEDGMENTS

We are indebted to M. Lounsbury and R. W. Jones for mass analyses of the carbon dioxide samples, to R. O. Kelly, who developed the method of preparing O^{17}-enriched carbon dioxide and supplied the 10-fold enriched material, to Janet Merritt and J. G. V. Taylor for the Au^{198} standards, and to Erich Vogt for helpful discussions, especially on the theory of level shift and the occurrence of 3+ states in O^{18}.

REFERENCES

AJZENBERG-SELOVE, F. and LAURITSEN, T. 1959. Nuclear Phys. **11**, 1.
BATCHELOR, R. and FLOWERS, B. H. 1949. AERE N/R 370.
BELL, R. E. and YAFFE, L. 1954. Can. J. Phys. **32**, 416.
BIGHAM, C. B. 1958. Private communication.
BIGHAM, C. B., HANNA, G. C., TUNNICLIFFE, P. R., CAMPION, P. J., LOUNSBURY, M., and MACKENZIE, D. R. 1958. Proc. 2nd International Conference on Peaceful Uses of Atomic Energy, **16**, 125.
BIGHAM, C. B. and PEARCE, R. M. 1961. CRRP-1006.
BIGHAM, C. B. and TUNNICLIFFE, P. R. 1961. CRRP-985A.
CAMPION, P. J. 1959. Intern. J. Appl. Radiation and Isotopes, **4**, 232.
COON, J. H. and NOBLES, R. A. 1949. Phys. Rev. **75**, 1358.
COTTINI, C., GATTI, E., GIANNELLI, G., and ROZZI, G. 1956. Nuovo Cimento, **3**, 473.
EVERLING, F., KOENIG, L. A., MATTAUCH, J. H. E., and WAPSTRA, A. H. 1961. 1960 Nuclear Data Tables, Part I, U.S. Govt. Printing Office.

HUGHES, D. J. and SCHWARTZ, R. B. 1957. BNL-325, Supplement No. 1.
——— 1958. BNL-325, Second Edition.
LEWIS, W. B. 1957. Private communication.
MAY, A. N. and HINCKS, E. P. 1947. Can. J. Research, **A25**, 77.
MCKENZIE, J. M. 1959. Nucleonics, **17** (1), 60.
MCMURTRIE, G. E. and CRAWFORD, D. P. 1950. Phys. Rev. **77**, 840.
VOGT, E. 1959. Nuclear reactions, Vol. I, *edited by* P. M. Endt and M. Demeur (North-Holland Publishing Company, Amsterdam), Chap. V.
WESTCOTT, C. H. 1960. CRRP-960.
WILKINSON, D. H. 1960. Nuclear spectroscopy, Part B, *edited by* F. Ajzenberg-Selove (Academic Press), Chap. V(F).

STEREO-PROJECTION SYSTEMS FOR AURORAL HEIGHT MEASUREMENTS[1]

G. G. SHEPHERD, K. V. PAULSON, AND J. A. NILSON[2]

ABSTRACT

In the past, auroral heights have been obtained analytically from parallactic photographs. Even though much of the calculation can be replaced with graphical aids, the method is still slow, and somewhat indirect. This paper discusses two stereo-projection systems from which auroral heights can be scaled directly. These and other methods are compared and discussed.

1. INTRODUCTION

A great many height measurements of aurora over Norway have been made by Störmer (1955) and others (Harang 1951). These number in the thousands and therefore have given reliable statistical data. By comparison, the number of height measurements made in North America is relatively small. Those made by Currie (1934, 1955), Fuller (1935), Alty and Wilson (1934), and McEwen and Montalbetti (1958) are in general agreement with the Norwegian results. Hence, it is generally considered that there is little need for establishing extensive auroral height measurement programs in North America. But if further statistical studies are not required, and even this is not certain, height measurements have considerable value when made in conjunction with other observations. Examples of this are for spectroscopic observation (Shepherd and Hunten 1955), rocket firings through aurora (McEwen and Montalbetti 1958), and auroral radar observations (Currie, Forsyth, and Vawter 1953). In problems of this type, one may wish to use rapid sequence cameras, and large numbers of photographs may be obtained in a single evening's observing. Hence, even here, one is faced with the reduction of large amounts of data.

The usual method of measurement was developed mainly by Störmer (1955) and consists of simultaneous photography from two stations situated about 40 kilometers apart. The reduction of the photographs combines hand calculation with graphical techniques. One advantage of the method is that very simple instrumentation can be used. However, the reduction is very time consuming, and 1 hour or more may be required for a pair of photographs. As will be seen, other criticisms may be made of the method. These factors are rather discouraging to anyone considering making such measurements as part of an auroral investigation.

About twenty-five years ago, Chapman (1934) suggested an entirely different method of analysis in which the auroral height and distance would be scaled from a model of the auroral situation. As far as the authors are aware, the

[1]Manuscript received August 18, 1961.
Contribution from the Institute of Upper Atmospheric Physics, University of Saskatchewan, Saskatoon, Saskatchewan.
[2]Present address: Department of Electrical Engineering, Imperial College, London.

method has not been tried previously.* This may have been because of the lack of interest in statistical studies. The application of such a method would make possible the other types of programs previously mentioned.

In this paper, the conventional method is reviewed briefly, followed by a description of two projection systems. A true stereoscopic method is also discussed. Finally, some suggestions for non-photographic methods are given.

2. THE CONVENTIONAL METHOD

The conventional method consists of photographing roughly the same parts of the sky from two different stations. It requires an operator for each camera and either a radio or telephone communication system. The time is recorded along with the names of some stars in the photograph, but no readings of camera position are taken. For the earlier work, the shutters were also manually controlled, but it is much better to have them operated by synchronized timing units (McEwen and Montalbetti 1958) or to have one operator control both shutters using remote control. The latter method has been used at Saskatoon using resonant relays in conjunction with the radio communication system. This ensures that the exposure times are of the same length and taken precisely at the same time. This is very important when the aurora is in motion. The camera positions are found later from the photographs using the stars. This is the first disadvantage of the method. With the short focus lenses used, aurora can be photographed with exposures so brief that only stars of second magnitude or brighter are recorded. With longer exposures, fainter stars are recorded, but it is sometimes necessary to spend considerable time identifying them. Figure 1(*a*) indicates the geometry of the situation where the two stations are separated by a distance *g*. Parallel rays from a star (S) are shown, and

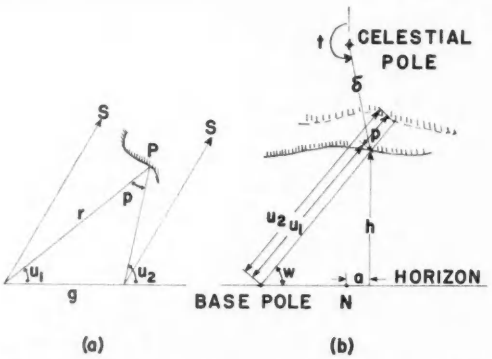

FIG. 1. (*a*) Camera arrangement, showing parallactic displacement (p) of auroral point (P) with respect to a star (S).

(*b*) The same situation as 1(*a*) but viewed along the base axis. The plane of parallactic displacement appears as a line. t and δ are hour angle and declination respectively and h and a are altitude and azimuth respectively.

*After the completion of the work reported here it was noted that Manring, Bedinger, and Petit (1959) had used a projection method for determining the height of an artificial sodium cloud.

P is a point on an auroral form. Rays joining P with the two stations make angles u_1 and u_2 with the line joining the stations (called the base-axis). The angle p is the parallactic displacement, and is given by $p = u_2 - u_1$. The range (r) of P from the main station is given by $r = g \sin u_2 / \sin p$. It is clear that u_1 and u_2 are colatitude angles in a spherical co-ordinate system with the base-axis as its axis. The longitudinal angle is called w, and is shown in Fig. 1(b), where the plane of parallactic displacement is viewed edge on. Figure 1(b) is obtained in the analysis from tracings of the two projected photographs which are superimposed with the stars in each one in coincidence. The auroral forms are then observed to be displaced as indicated. The hour angle (t) and declination (δ) of three stars in the tracings are obtained, and converted to altitude (h) and azimuth (a) using standard transformation equations or graphical methods. The altitude and azimuth of each auroral point is next found by interpolation. Conversion is also made to the (u,w) system, giving p for each auroral point and thus r. Knowing h and a, the height and distance of each point can then be found. A second disadvantage of the method, apart from the labor involved, is now apparent. The entire analysis is based on pencilled lines which have been drawn in the early stages to represent the edges of auroral forms. This representation is often extremely difficult to make. The errors involved depend not only on the diffuseness of the aurora but also on the perpendicularity of the displacement direction to the auroral edge. This latter quantity is usually not known until the later stages of analysis and long after the contours have been chosen and drawn.

3. A TWO-DIMENSIONAL STEREO-PROJECTION SYSTEM

If the parallactic displacement could be measured directly from the photographs without the intervention of line drawings, one of the above objections would be removed. In the following projection system, two projectors are placed side by side, containing the pair of auroral negatives. They are projected on a movable screen, and the parallactic angle is determined from the position of the screen.

Figure 2(a) represents the geometry for the cameras, and is the same as in Fig. 1(a). Parallel rays from a star (S) pass through lenses L_1 and L_2 of focal lengths f_c. The displacements between the images of the stars and the auroral points on the two films are given by x_1 and x_2. Figure 2(b) represents the projection geometry. The projection lenses L_1' and L_2' of focal lengths f_p are separated by a distance g'. The star images are arranged to coincide on a screen at a distance s, and the auroral images then coincide on a screen at a distance d.

Since x_1 and x_2 are the same in both Figs. 2(a) and 2(b), it follows that $p_1 = (f_p/f_c)p_1'$ and $p_2 = (f_p/f_c)p_2'$. Since the angles p and ϕ are small, usually less than 5°, one may use $\sin p = \tan p = p$ and the same for ϕ. Thus, from Fig. 2(b), it follows that $p_1' + \phi = g_1'/d$; $p_2' + \phi = g_2'/d$; and $\phi = g'/2s$. Substituting in $p = p_1 + p_2$, it follows that

$$p = (f_p/f_c)(p_1' + p_2') = \frac{f_p g'}{f_c}\left[\frac{1}{d} - \frac{1}{s}\right].$$

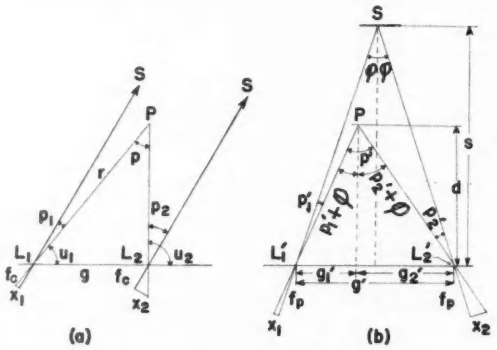

FIG. 2. (*a*) Camera arrangement as in 1(*a*), showing displacements x_1 and x_2 on the film. (*b*) Projection arrangement for the two-dimensional projection system.

Substituting into the range equation, $r = g \sin u_2/\sin p$, one obtains

$$r = \frac{g \sin u_2}{g'} \frac{f_c}{f_p}\left[\frac{sd}{s-d}\right].$$

For a given arrangement, all quantities are constant except d and u_2. Thus, $r = Cd \sin u_2/(s-d)$, where C is a constant.

This system is two-dimensional in that only the range is scaled, and the position in space must be calculated using the altitude and azimuth as before. Unfortunately, this means that u_2, h, and a must still be found by the conventional method. Nevertheless, the projection system solves the most critical part of the problem, that of measuring the parallactic displacement. Setting a screen at the place where two projected auroral forms coincide is a much more direct and objective process than that of tracing outlines of auroral forms and later measuring the distance between them. A scale can be provided for the moving screen, giving the range directly.

An apparatus based on the above ideas was constructed at Saskatoon just prior to the I.G.Y., and in preliminary tests it appeared satisfactory. It was then sent to Fort Churchill for use (McEwen and Montalbetti 1958). It turned out that with the unusually large parallactic angles used there, the projectors would defocus seriously between s and d. The focus cannot be changed because of the change of magnification. As will be seen, a solution exists to this problem, but it was not followed up at that time. Since the equation derived above was for small angles, it would probably not have been valid in any case. When the problem was considered again, it was felt that a three-dimensional system would be much better.

4. A THREE-DIMENSIONAL STEREO-PROJECTION SYSTEM

The three-dimensional system is essentially what was proposed by Chapman (1934) and is an attempt to scale the auroral situation to a laboratory model. In such a scaling, some difficulties become immediately apparent.

In the two-dimensional system just described, a particular transformation relates the camera space to the projection space because the stars are located at a finite distance. In a true model, the stars in projection space must be located at infinity, and rays corresponding to the same star proceeding from the two projectors must be parallel. The projection and camera arrangements are shown superimposed in Fig. 3(*a*). The parallactic angles in the two spaces are related by $p' = (f_c/f_p)p$ and so the parallactic triangles in the two spaces

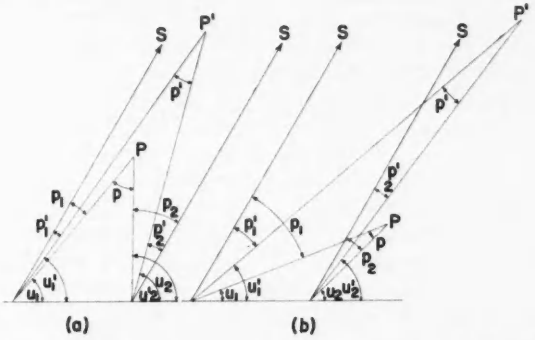

FIG. 3. Camera and three-dimensional projection arrangement superimposed; (*a*) reference star and auroral point adjacent, (*b*) reference star and auroral point widely separated.

differ in appearance as shown. Since the three angles in the parallactic triangle must still add up to 180°, this means that the u angles are also altered; that is, a space distortion takes place. It is true that this is not important when p is small, since the difference $p'-p$ does not affect the u angles appreciably in Fig. 3(*a*). However, when the aurora and stars are in rather different directions as in Fig. 3(*b*), the error is serious, even for small values of p. Here, $p = p_1-p_2$, and so p_1 and p_2 can be large even for small values of p with the distortion becoming serious, as illustrated in Fig. 3(*b*). The stars chosen here are arbitrary, of course, and one could in principle choose new reference stars near the auroral point in question. This amounts to reorienting the projectors for each auroral point. One way to avoid this is to use lenses of the same focal length in the projector and the camera. This is an ideal solution as now all angles are unchanged in going from camera to projection space.

A further problem related to scaling is that of focus. In the camera space, both the aurora and stars are at infinity as far as focus is concerned, even though the aurora is at a finite distance for the parallactic measurements. In projection space the stars are at infinity, and the aurora is close at hand so that both cannot be in focus simultaneously. The focus cannot be changed during measurements as this affects the magnification. This can be solved by stopping down the projection lenses. One further problem remains. In order to preserve angles in the transformation, the film-to-lens distances rather than the focal lengths must be the same for camera and projector. Thus, in order to project the aurora at a finite distance, the projector focal length should be

slightly less than that of the camera. This rules out the possibility of using the same lens for both purposes to eliminate lens distortion. A 100-watt zirconium arc lamp giving a spot 1.5 mm in diameter with a brightness of 33,000 candles/in^2 is now available commercially. This should permit the use of a very low aperture projector or perhaps even a pinhole projector. One could then have a projector with continuously variable magnification and infinite depth of field. This would solve all of these problems.

One of the mechanically complicated aspects of Chapman's suggestion was the artificial celestial sphere for orienting the projectors. Besides the mechanical complication, this method is subject to the objection that it relies on the use of stars. A system which operates without reference to stars could be made by mounting the cameras on accurate altitude–azimuth mounts and recording their position at the time of exposure. Duplicate mounts could be used for the projectors. Such mounts, and the recording, are greatly simplified if a detent mechanism is used, giving adjustment in steps rather than continuously. Jacka and Ballantyne (1955) describe a photo-theodolite mount in which 2° steps are used with a reproducibility of 1 minute of arc. One added feature of such mounts is that electrical control could be incorporated, allowing the operator at the main station to operate the second camera by remote control, or having the two cameras follow a sequence determined by a programming unit.

In order to test these ideas, the simplified arrangement shown in Fig. 4 was constructed. The projectors (A) were pivoted on a rotatable table (C), along a

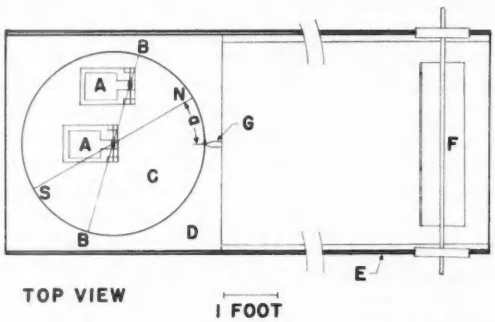

FIG. 4. Schematic top view of the mechanical arrangement of the three-dimensional projection system.

line B—B representing the base-axis, having the correct azimuth with respect to N–S for the two stations in question. The azimuth of the photographs is set at a pointer (G). With the screen (F) movable horizontally along tracks (E) and vertically as well, the whole sky can be covered. For each auroral point, the screen is positioned for best coincidence. The height and distance are then measured with a ruler.

Some results obtained with this projection system are shown in Fig. 5. The edges of auroral forms are represented by the solid line, and the measured

points are indicated. Beside each point, the horizontal distance and height respectively are given in kilometers. The open circles were measured by the conventional method and the solid circles by the stereo-projection system. The agreement is satisfactory and in fact the contribution from the conventional method to the error may be as great as that from the projection system. The reproducibility of the projection system was found to be within 1 km for a height of 145 km. This includes the error only in repositioning the screen and not the projectors.

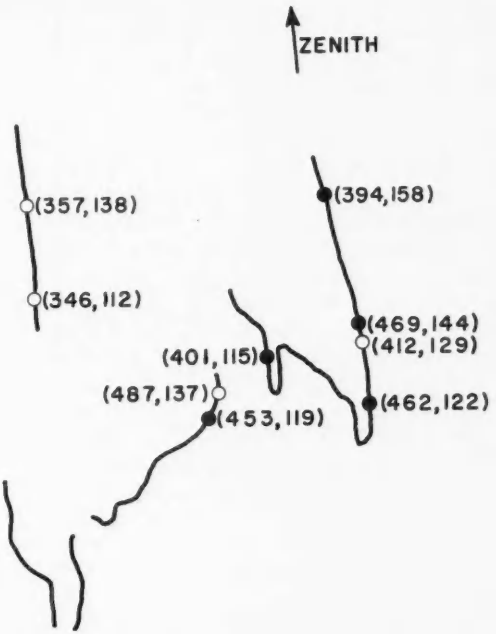

FIG. 5. Comparison of height measurements made by conventional (open circles) and projection (solid circles) methods. The solid line indicates the edges of the auroral form.

The results of the analysis of a ray in another photograph are shown in Fig. 6 as a plot of height (H) vs. distance (D). Again open circles indicate the conventional method and solid circles the mechanical method. Both sides of the ray were measured and plotted on the same graph. A straight line having the inclination of the magnetic lines at this latitude is drawn through the points and is reasonably consistent with them. The large apparent scatter results from the magnified scales. Actually, no point deviates more than 4 kilometers from the line and the average deviation of all points is 2 kilometers. In addition, one cannot be certain that the points should lie on a straight line.

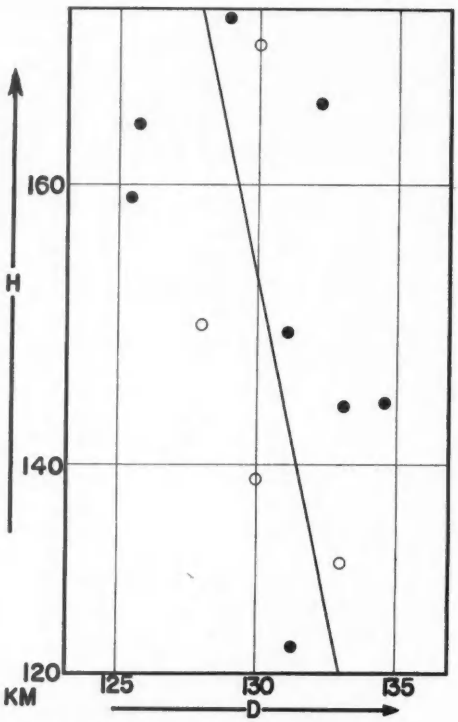

FIG. 6. Graph of height (H) versus distance (D) for an auroral ray measured by the conventional (open circles) and projection (solid circles) methods. The straight line has the inclination of the geomagnetic field.

5. A TRUE STEREOSCOPIC SYSTEM

Although the above method of locating the auroral points by superposition of two images on a moving screen seems satisfactory, this makes no use of the stereoscopic acuity of the human observer. This ability is used almost exclusively in photogrammetry and should be applicable to the auroral problem. The advantages of the stereoscopic effect are first that the whole aurora can be seen positioned in space at once, and second that very small parallactic angles can be detected. Finally, a moving screen is not required, as fiducial marks can be projected to appear at any distance. An attempt was made to produce a stereoscopic effect with the three-dimensional system using polaroid filters in the projectors and in eyeglasses. One expected to see the aurora extending in projection space, both in front of and behind the screen, but no such sensation was experienced. The same negative result was obtained using a stereocomparator, and cannot be attributed entirely to the inexperience of the observers, as an experienced photogrammetrist had no better success. Although the problem was not explored very fully, the following suggestions are offered.

There are important differences between the problems of auroral height measurement and contouring by aerial photography. First of all, an aerial survey requires three known ground points. Absolute parallaxes are not measured but only relative parallaxes with respect to the known points. This is not possible with aurora where absolute parallaxes must be measured against the stars. For this reason, the parallactic angles used for aurora are often larger than those which the eyes will tolerate. It should still be possible to use the stereoscopic method to study the variation of position within an auroral form, but there are two further problems. The first is that the plane of parallactic displacement must pass through the eyes of the observer. This means that the pictures must be properly oriented, and so it may happen that an arc, for example, may be viewed sideways. This is a little disturbing to the viewer but should not make a measurement impossible. Secondly, the auroral photographs lack the detail of aerial photographs. To produce a stereoscopic effect, the eyes must know which point in photograph No. 2 corresponds to a given point in photograph No. 1. This is often not possible with aurora. It should be noted that this same information need not be known for the positioning of the screen in the projection system described, since it is provided by the geometry of the projector arrangement. This diffuse quality is not always the fault of the aurora, which may have extensive detail, but of the long exposures (5–10 seconds) usually used. By reducing exposure times to 1 second or less, it is possible that pictures with sufficient detail for stereoscopic fusion could be obtained. Because of the value of the stereoscopic method it would be premature to discard it. In addition to the advantages outlined above it should give a better conception of the volume extent of aurora than do the other methods.

6. OTHER METHODS

Any serious consideration of auroral height finding should not stop with photographic methods. For example, the use of two narrow beam photoelectric photometers, scanning in the plane of parallactic displacement, could be considered. Although only a small portion of the sky would be studied at one time, this does result in simpler reduction methods. It has the further advantage that one would be matching entire intensity profiles, rather than just the positions of edges of forms. This should give additional information on the vertical extent of aurora, not readily available by photographic methods. Intensity vs. the angle u could be displayed for the two stations on a double beam oscilloscope, as the information is being obtained. By shifting one of the traces to bring the two into coincidence, the parallactic angle would be indicated directly. An analog computer could be constructed to complete the calculation and thus provide instantaneous heights. This information would be of great value to other observers, particularly in spectroscopy, indicating desirable auroral forms at which to direct instruments. The use of narrow band interference filters would allow also the study of height variation of different spectral features.

An extension of the above method would be to replace the photographic cameras by television cameras. These and similar ideas should all be considered as the techniques and the funds become available.

7. DISCUSSION

Two stereo-projection systems have been described. The first, referred to as two-dimensional, allows the range of aurora to be measured mechanically by the projection system. The height and distance still must be found by conventional methods. The second system, a three-dimensional one, produces an accurately scaled model of the aurora in the laboratory, from which distance and height can be derived directly. In both methods, one adjusts a movable screen to bring two projected auroral forms into coincidence. Use of the stereoscopic ability of the observer should provide a better method of doing this, but this was not found to be the case. Further work on the stereoscopic viewing of aurora should be carried out. It is concluded that a properly designed camera and projection system, while rather complicated technically, could yield auroral heights very quickly and accurately.

The use of photoelectric scanning for auroral height measurements is suggested. While only a limited part of the sky is covered at any one time, the heights could be produced immediately for use by other observers.

ACKNOWLEDGMENTS

The authors wish to thank Dr. B. W. Currie and Dr. D. M. Hunten for their advice and encouragement throughout this project. Mr. D. J. McEwen made some measurements with the two-dimensional system. Mr. W. B. McCoy of the Department of Civil Engineering, University of Saskatchewan, made a stereocomparator available.

REFERENCES

ALTY, T. and WILSON, F. J. 1934. Nature, **133**, 687.
CHAPMAN, S. 1934. Terrestrial Magnetism and Atmospheric Elec. **39**, 299.
CURRIE, B. W. 1934. Terrestrial Magnetism and Atmospheric Elec. **39**, 293.
——— 1955. Can. J. Phys. **33**, 773.
CURRIE, B. W., FORSYTH, P. A., and VAWTER, F. E. 1953. J. Geophys. Research, **58**, 179.
FULLER, V. B. 1935. Terrestrial Magnetism and Atmospheric Elec. **40**, 269.
HARANG, L. 1951. The aurorae (Chapman and Hall).
JACKA, F. and BALLANTYNE, H. 1955. Interim Reports on the Australian Natl. Antarctic Research Expt. No. 11.
MANRING, E., BEDINGER, J. F., and PETIT, H. B. 1959. J. Geophys. Research, **64**, 587.
MCEWEN, D. J. and MONTALBETTI, R. 1958. Can. J. Phys. **36**, 1593.
SHEPHERD, G. G. and HUNTEN, D. M. 1955. J. Atmospheric and Terrest. Phys. **6**, 328.
STÖRMER, C. 1955. The polar aurora (Clarendon Press, Oxford).

THE DECAY OF Er^{171} [1]

A. ARTNA[2] AND M. W. JOHNS

ABSTRACT

The decay of Er^{171} has been studied with a magnetic beta-ray spectrometer at a resolution of 0.5%. The energies and intensities of 30 transitions in Tm^{171} have been established. The energies (Mev) and intensities (%) are as follows: 0.086 (~0.1), 0.1117 (68.8), 0.1166 (6.05), 0.1240 (20.5), 0.1664 (0.65), 0.2104 (0.67), 0.2364 (0.57), 0.2770 (0.74), 0.2956 (28.7), 0.3082 (64.4), 0.3712 (~0.4), 0.4040 (0.03), 0.4189 (0.09), 0.5437 (0.04), 0.5571 (0.08), 0.5727 (0.07), 0.6061 (0.10), 0.6187 (0.13), 0.6703 (0.30), 0.6753 (0.39), 0.7321 (0.18), 0.738 (0.06), 0.7835 (0.31), 0.7962 (0.80), 0.842 (0.04), 0.869 (0.06), 0.882 (0.07), 0.906 (0.88), 0.9105 (0.25), 0.962 (0.11). These transitions are interpreted in terms of 12 levels whose energies and spins are: 0 (1/2+), 0.0051 (3/2+), 0.1167 (5/2+), 0.1291 (7/2+), 0.4251 (7/2−), 0.5915 (9/2−), 0.6355 (7/2+), 0.675 (3/2+), 0.737 (5/2+), 0.912 (5/2+), 0.963 (5/2+), 0.997 (7/2+). The decay energy of Er^{171} is 1.490±0.002 Mev.

INTRODUCTION

The decay of 7.5-hour Er^{171} has been investigated by a number of workers (Nuclear Data Sheets 1959). The two most complete studies are those reported by Cranston, Bunker, and Starner (1956, 1958) and by Hatch and Boehm (1957). The former authors carried out an exhaustive series of coincidence experiments using scintillation detectors while the latter provided precise crystal spectrometer energy measurements of the stronger gamma rays. As a result of these investigations, the positions of levels *A* to *E* in the decay scheme of Fig. 9 have been well established, and levels corresponding to those labelled *G*, *H*, *I*, *J*, and *L* have been proposed. Inasmuch as many of the gamma rays involved in transitions from the latter levels were unresolved in the earlier work, it was decided to reexamine these transitions with a Siegbahn-type double-focussing beta-ray spectrometer operating at a resolution of 0.5% in momentum.

These experiments have revealed the presence of a number of additional transitions and have made necessary some additions to the decay scheme proposed by Cranston *et al.* (1958).

EXPERIMENTAL METHOD AND SOURCE PREPARATION

The general features of the spectrometer have been described elsewhere (Johns *et al.* 1953, 1954). In the present work the detectors were anthracene crystals of thickness 0.2 cm for electrons below 300 kev and of thickness 0.4 cm for electrons with higher energies. Both gave 100% detection efficiency until the crystal surface became seriously pitted by sublimation in the vacuum.

With beta sources of area 2.5×0.5 cm^2 and a detector width of 0.4 cm, the instrumental resolution was 0.5%. The converters for external conversion

[1]Manuscript received August 31, 1961.
Contribution from the Department of Physics, McMaster University, Hamilton, Ontario.
[2]Present address: Nuclear Data Project, National Academy of Sciences, National Research Council, 2100 Constitution Avenue N.W., Washington, D.C.

measurements were gold or uranium foils of suitable thickness (0.4 to 4.2 mg/cm² gold and 1.4 to 6.6 mg/cm² uranium) and of area 3.0×0.75 cm². By appropriate choice of the radiator, the resolution in external conversion measurements was maintained below 1%.

The gamma-ray sources consisted of 450 mg of natural erbium oxide sealed in quartz capsules about 4 mm in diameter and 2.5 cm long. These were irradiated for about 10 hours at a flux of 1.5×10^{13} neutrons sec^{-1} cm^{-2} in the McMaster reactor.

The beta sources were prepared from erbium oxide enriched to 87.3% in Er^{170}. The radioactive oxide was dissolved in concentrated HNO_3, evaporated to dryness under a heat lamp, and then redissolved in acetone. The solution in acetone was sprayed on an aluminum-coated mylar source backing by the ion ejection technique (Parker *et al.* 1960).

THE EXTERNAL AND INTERNAL CONVERSION SPECTRA

Inasmuch as it was impossible to scan the entire external conversion spectrum with any one source, the strong K-conversion peak of the 0.308-Mev transition was measured in each of the 45 sources studied and used for normalization. Figure 1 presents a composite of the entire gamma-ray spectrum,

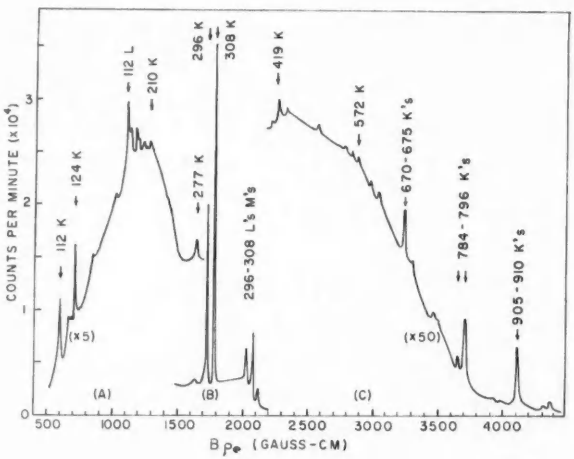

FIG. 1. The external conversion spectrum. (A) with a 0.40 mg/cm² Au radiator; (B) with a 1.55 mg/cm² Au radiator; and (C) with a 4.20 mg/cm² Au radiator. Only the more prominent peaks are labelled.

showing the strong transitions below 0.308 Mev and the very weak gamma rays above this energy. Figures 2, 3, and 4 present details of the more interesting portions of this spectrum as obtained in individual runs.

Figure 2 presents evidence for previously unreported gamma rays of energy 0.1664 Mev and 0.2770 Mev in addition to two other weak lines at 0.2104

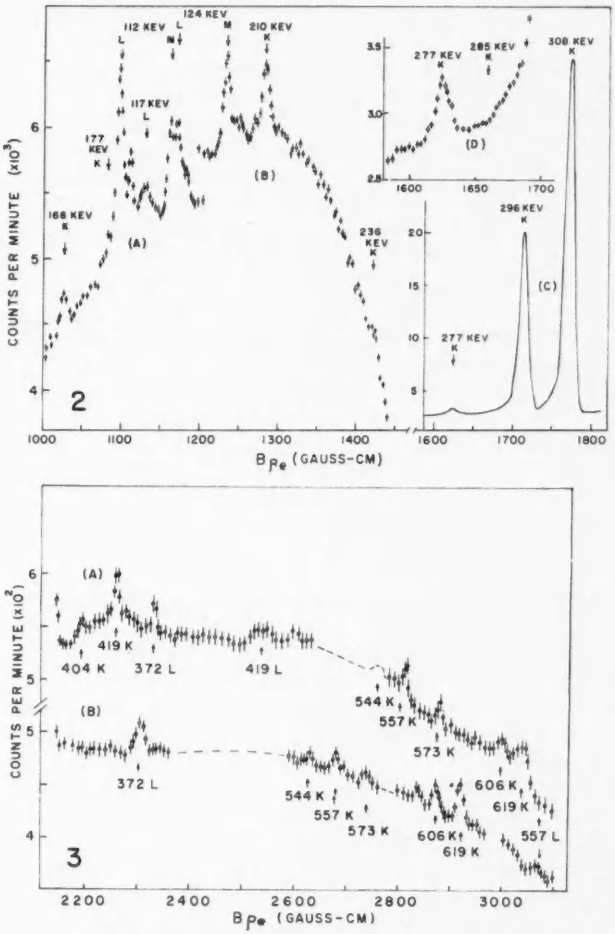

FIG. 2. The external conversion spectrum. (A) with a 0.40 mg/cm² Au radiator; (B), (C), and (D) with a 1.55 mg/cm² Au radiator. The positions of the previously reported gamma rays of energies 0.177 and 0.285 Mev not found in this work are indicated.

FIG. 3. The external conversion spectrum. (A) with a 4.20 mg/cm² Au radiator, and (B) with a 2.60 mg/cm² U radiator.

and 0.2364 Mev both of which had been observed by other workers. There is no evidence for either the 0.177-Mev transition reported by Keller and Cork (1951) or the 0.2849-Mev gamma ray reported by Cranston *et al.* (1956) and by Hatch and Boehm (1957).

Figure 3, which shows the photoelectron spectrum in gold and uranium for gamma rays from 0.4 to 0.62 Mev, reveals the presence of six new gamma

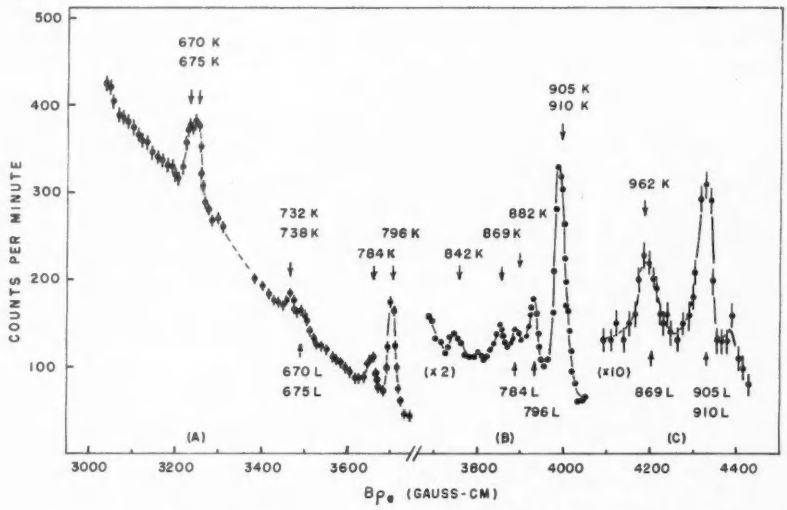

FIG. 4. The external conversion spectrum. (A) with a 4.20 mg/cm Au² radiator; (B) with a 4.40 mg/cm² U radiator, and (C) with a 6.60 mg/cm² U radiator.

rays and confirms the existence of the 0.419-Mev transition originally reported by Keller and Cork (1951). This line was not found by Cranston *et al.* (1958), who set an upper limit on its intensity just above the measured intensity of the present work. Figure 4 presents evidence for the existence of 12 gamma rays. The portions of the spectrum shown in Figs. 3 and 4 are characterized by the presence of doublets, some with an energy difference of 5 kev and others with an energy difference of 12 kev. These figures thus confirm the doublet structure proposed by Cranston *et al.* (1958) and provide accurate energy measurements of the individual gamma rays unresolved in earlier work.

It should be pointed out that the entire external conversion spectrum was recorded with both gold and uranium radiators, and that each spectrum was measured at least twice with each converter so that the spectra presented here represent a small fraction of those actually used in energy and intensity determinations.

The spectrometer was calibrated for momentum measurements using external conversion peaks from the gamma rays of Au^{198}, Ir^{192}, and Co^{60}. In addition, it was possible to use the internal standards provided by the precise energy measurements of Hatch and Boehm (1957) of the stronger lines in the Er^{171} spectrum.

The spectrometer was calibrated for intensity measurements using the gamma-ray cascades present in Co^{60}, Sc^{46}, In^{114}, and Hf^{180m}. The measured peak heights were fitted to the semiempirical formula discussed by Johns and Nablo (1954), using the more recent data on ionization potentials determined by Chen and Warshaw (1951). Sufficient cross-checking was done so

that the converter efficiency, i.e. the number of photons per count recorded, was known as a function of energy for each radiator used, for energies from 0.2 to 1.3 Mev. For energies below 0.2 Mev, the intensity calibration involved a dangerous extrapolation of the semiempirical relations. It was found possible to calculate the gamma-ray intensities of the three transitions at 0.1117, 0.1166, and 0.1240 Mev from the decay scheme and to use these to establish the low-energy end of the semiempirical efficiency curve (Artna 1961). It is believed that the accuracy of the intensity measurements is limited chiefly by uncertainties in the peak heights.

The internal conversion spectrum below 0.4 Mev is presented in Figs. 5 and 6. All of the transitions seen in external conversion reveal their presence. In addition, Fig. 5 shows evidence for a weak 0.086-Mev transition. The K peak of the 0.1664-Mev transition, clearly seen in external conversion, falls under the 0.1166-Mev L peaks. Since both the 0.1166- and 0.1240-Mev transitions are $E2$, it is possible to use the profile of the 0.1240-Mev L peaks to analyze the 0.1166-Mev peaks. When this is done, it appears that part of the 0.1166-Mev L_3 peak is really due to the 0.1664-Mev K-conversion line. The 0.236- and 0.371-Mev K-conversion lines are much more clearly defined than their external conversion counterparts. In the latter, the 0.371-Mev K peak is masked by the 0.296-Mev M peaks in gold and is mixed up with the 0.277-Mev L peaks in uranium. Again there is no evidence for conversion

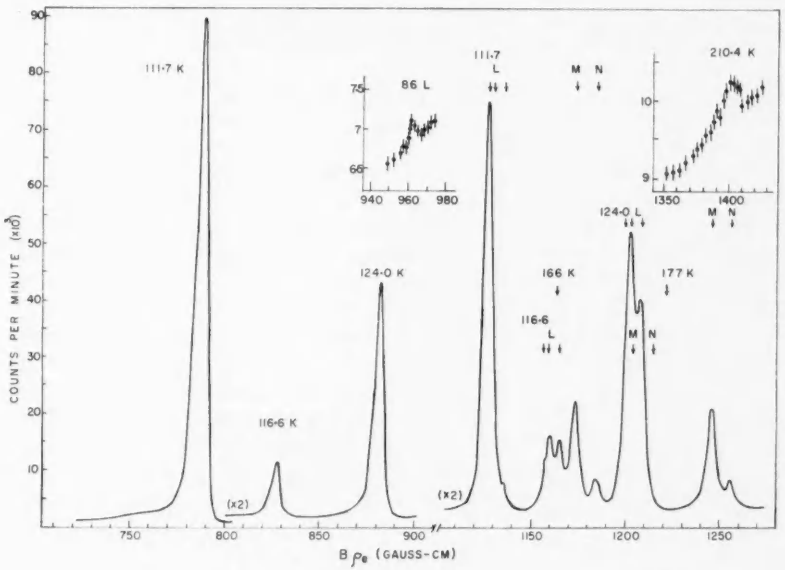

FIG. 5. Internal conversion spectrum showing the K, L, and M peaks of the low-energy transitions. The two inserts show the 0.086-Mev L peak and the 0.2104-Mev K peak respectively. The expected position for a 0.177-Mev K peak is shown.

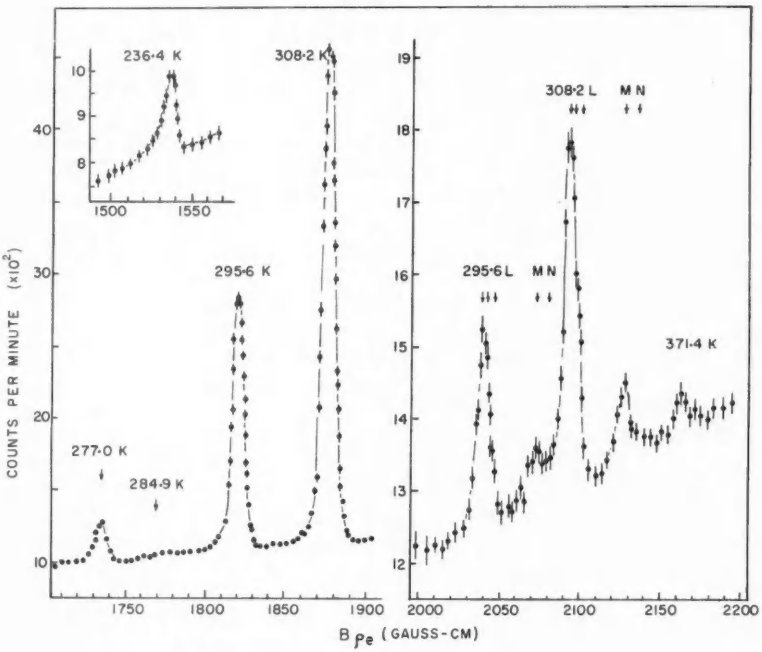

FIG. 6. Internal conversion spectrum. The expected position for a 0.2849-Mev K peak is shown.

lines corresponding to the previously reported transitions of energies 0.177 or 0.2849 Mev.

The beta spectra from two different sources were subjected to Fermi analysis. The analysis for one of these is presented in Fig. 7. For each of these sources, the intensity of the 0.308-Mev K-conversion line was carefully measured.

In order to relate the beta- and gamma-ray intensity scales, the K-conversion coefficients of the 0.296- and 0.308-Mev transitions were measured directly by comparing the number of K-conversion electrons with the gamma-ray intensity from the same source. For this experiment an extremely strong beta source was prepared with dimensions 0.5×2.5 cm² and thickness ~ 500 μg/cm². The number of conversion electrons was measured directly and then the source was covered with a gold radiator and the external conversion peak height determined. Under these circumstances

$$\alpha_K = k(N_{ce}/N_{pe} \times f)$$

where f is the known converter efficiency for the photon energy being studied and k is a geometric factor. The value of k was determined by repeating the experiment with a Au^{198} source of the same dimensions placed in the same geometry, using the value 0.028 for α_K of the 0.4118-Mev transition of Au^{198}

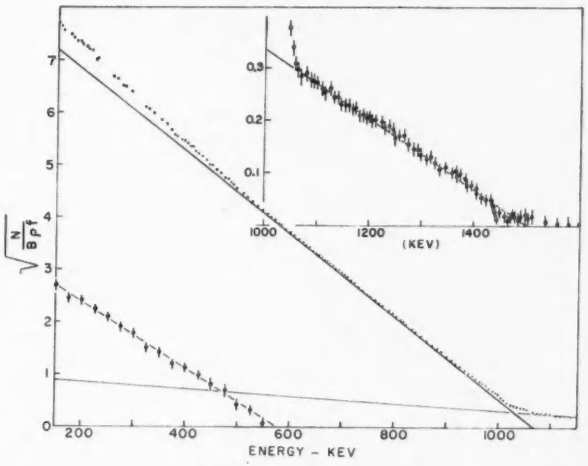

FIG. 7. Fermi analysis of the beta-spectrum. The insert shows the high-energy end of the spectrum on an enlarged scale.

(Wapstra *et al.* 1958). Figure 8 presents the peaks from which one such determination was made. The effects of source thickness in the Er^{171} beta source are evident but not serious enough to make the analysis difficult.

EXPERIMENTAL RESULTS

(a) The Beta Spectrum

Fermi analysis of the beta spectrum revealed three groups with the following end-points and intensities: 1.492±0.007 Mev (2.3±0.2%), 1.065±0.002 Mev (90±1%), and 0.575 Mev (8±1%). It is clear from the decay scheme and the work of Cranston *et al.* (1958) that the first and third groups are complex. Inasmuch as the high energy component is weak, the total disintegration energy can be more reliably determined by adding the end-point of the dominant beta-group to the energies of the succeeding gamma rays. The value so obtained is 1.490±0.002 Mev.

(b) The Absolute Intensity of the 0.308-Mev Gamma Ray

The K-conversion probability of the 0.308-Mev transition was found to be 1.06±0.04% by comparing the area of the K-conversion line with the total area of the beta spectrum. The values of α_K for the 0.308- and 0.296-Mev transitions were found to be 0.0169±0.0008 and 0.0200±0.001 respectively, each result being the average of five determinations. The absolute intensity of the 0.308-Mev gamma ray is then 63.1±3.6%.

(c) Summary of Data Concerning Transitions

All the information obtained concerning the transitions is summarized in Tables I and II. The former presents the results for the low-energy transitions while the latter tabulates the less complete information concerning the high-energy radiations.

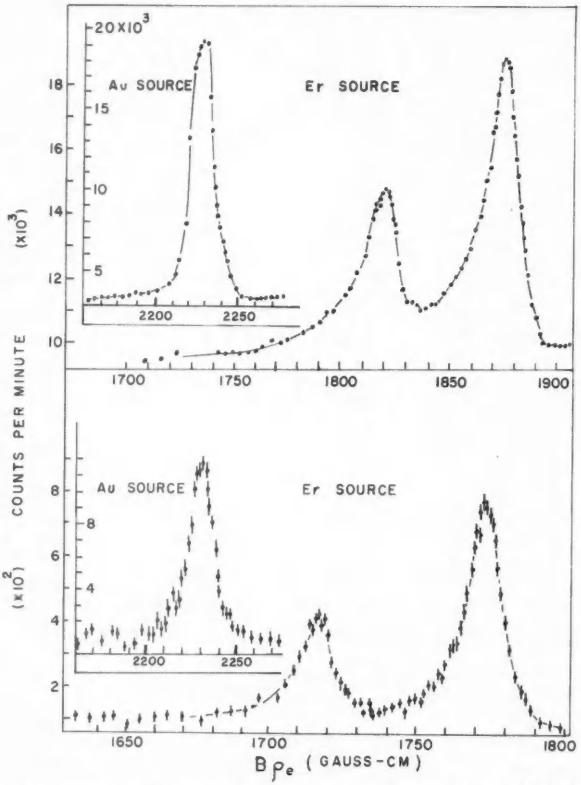

FIG. 8. Upper graph: *K*-shell internal conversion peaks of the 0.412-Mev transition of Au^{198} and the 0.296- and 0.308-Mev transitions of Er^{171}. Lower graph: *K*-shell external conversion peaks in a 2.0 mg/cm² Au radiator for the 0.412-Mev transition of Au^{198} and the 0.296- and 0.308-Mev transitions of Er^{171}.

In Table I the first column gives the energies of the transitions as measured in this study. The errors quoted are the standard deviations of a mean determined from at least five independent peak measurements. The second column gives the values found by Hatch and Boehm. The third presents the gamma-ray intensities, partly obtained from external conversion data and partly calculated from other information. The uncertainties shown on these intensities refer to the relative values and do not allow for systematic errors introduced by the normalization process.

The intensity of the 0.371-Mev transition is very uncertain since it was obtained by subtracting the estimated 0.277-Mev *L*-peak height from the composite "371-*K*+277-*L*" peak in uranium.

The next three columns give the internal conversion intensities. Again the error denotes the uncertainty in the actual relative measurement. In this case

TABLE I

Low-energy transitions in Tm^{171}

Photon energies (Mev)			Conversion electron intensities (%)			Conversion coefficients			Multi-pole character	Tran-sition intensity (%)	Position in decay scheme
Present work	Hatch and Boehm	Photon intensity (%)	N_K	N_L	N_M	α_K	α_L	K/L			
	0.00506									91*	$B \rightarrow A$
	0.00124									8.7*	$D \rightarrow C$
0.086				0.009±0.003						~0.1	$L \rightarrow J$
0.1117±0.0002	0.11163	25.2*	36.1 ±1.0	5.8 ±0.6	1.66 ±0.2	1.44	0.23	6.2	$M1$	68.8*	$C \rightarrow B$
0.1166±0.0002	0.11669	2.34†	1.60 ±0.2	1.67 ±0.2	0.44 ±0.05	0.68	0.72	0.96	$E2$	6.05†	$C \rightarrow A$
0.1240±0.0002	0.12403	8.7†	5.1 ±0.5	5.0 ±0.5	1.67 ±0.2	0.59	0.58	1.02	$E2$	20.5†	$D \rightarrow B$
0.1664±0.0003		0.56±0.13	0.08 ±0.04			0.14			$E2$	0.65	$F \rightarrow E$
0.2104±0.0003	0.21062	0.63±0.06	0.036±0.007			0.057			$E1$	0.67	$G \rightarrow E$
0.2364±0.0007		0.51±0.13	0.057±0.002			0.11			$M1+E2$	0.57	$J \rightarrow H$
0.2770±0.0002		0.65±0.05	0.09 ±0.01	<0.015		0.14	<0.02	>6	$M1$	0.74	$J \rightarrow G$
0.2956±0.0002	0.29597	28.0 ±0.6	0.56 ±0.02	0.071±0.005	0.019±0.002	0.020	0.0025	7.9	$E1$	28.7	$E \rightarrow D$
0.3082±0.0002	0.30837	63.1 ±3.6	1.06 ±0.04	0.144±0.007	0.033±0.007	0.0169	0.0023	7.4	$E1$	64.4	$E \rightarrow C$
0.3712±0.0005		~0.4	0.02 ±0.01	0.010±0.005	0.006±0.003	~0.05	~0.02	~2		~0.4	$K \rightarrow F$

*Calculated from the decay scheme.

†Calculated from the internal conversion data.

TABLE II

High-energy gamma rays

Energy (Mev)	Intensity (%)	Position in decay scheme
0.4040±0.008	0.03±0.013	$L \rightarrow F$
0.4189±0.0004	0.09±0.013	$E \rightarrow B$
0.5437±0.0010	0.04±0.02	$H \rightarrow D$
0.5571±0.0010	0.08±0.02	$H \rightarrow C$
0.5727±0.0005	0.07±0.02	$L \rightarrow E$
0.6061±0.0010	0.10±0.01	$I \rightarrow D$
0.6187±0.0010	0.13±0.03	$I \rightarrow C$
0.6703±0.0005	0.30±0.06	$H \rightarrow B$
0.6753±0.0005	0.39±0.06	$H \rightarrow A$
0.7321±0.0005	0.18±0.06	$I \rightarrow B$
0.738 ±0.002	0.06*	$I \rightarrow A$
0.7835±0.0005	0.31±0.03	$J \rightarrow D$
0.7962±0.0006	0.80±0.04	$J \rightarrow C$
0.842 ±0.002	0.04±0.02	$K \rightarrow C$
0.869 ±0.002	0.06±0.01	$L \rightarrow D$
0.882 ±0.002	0.07±0.01	$L \rightarrow C$
0.906 ±0.001	0.88±0.13	$J \rightarrow B$
0.9105±0.0010	0.25±0.06	$J \rightarrow A$
0.962 ±0.002	0.11±0.05	$K \rightarrow A$

*This line is somewhat doubtful.

the scale was defined by the direct measurement of the 0.308-Mev K-conversion probability. As previously pointed out, the 0.1166-Mev L lines are superimposed on the 0.1664-Mev K-conversion line and so the uncertainty in the intensity measurement for the latter is very large. Although the 0.277-Mev L lines were not observed, an upper limit could be established for their intensity. Columns 7, 8, and 9 present the conversion coefficients derived from the gamma-ray and internal conversion probabilities. It should be noted that, although the value of α_K quoted here for the 0.296-Mev transition has been calculated in the same manner as all the other conversion coefficients in this table, the value presented is in very good agreement with the directly measured value.

The next column gives the probable multipolarity for each transition, based on the conversion coefficients and ratios, while the last two columns present the total transition intensities and the position of each transition in the decay scheme.

The $E2$ assignments for the 0.1166- and 0.1240-Mev gamma rays have been made on the basis of their K/L and $L_1:L_2:L_3$ ratios. If one accepts the pure $E2$ character of these two radiations, one can use the theoretical conversion coefficients to compute the photon intensities and the total intensities of the 0.1166- and 0.1240-Mev transitions. When this has been done, the intensity balance from the decay scheme yields the transition probabilities given in Table I for the 0.00506-, 0.0124-, and 0.1117-Mev radiations. The photon intensity of 25% for the latter transition then follows by subtraction. The values of α_K and α_L for this transition, deduced from the measured values of N_K and N_L and the computed value of the photon intensity, are in reasonable agreement with the $M1$ character deduced from its K/L and $L_1:L_2:L_3$ ratios.

Table I lists a gamma ray of energy 0.1664 Mev not previously reported and omits the 0.1764-Mev transition reported by Keller and Cork (1951) and observed in the gamma–gamma coincidence spectrum by Cranston *et al.* (1958). No evidence for the 0.1764-Mev transition was found in either the external or internal conversion spectra (see Figs. 2 and 6). These experiments set an upper limit of 0.2% on the intensity of this transition.

Table I also lists a transition of energy 0.2770 Mev which has not been previously recorded. The energy of this line corresponds closely to a prominent transition in 2.36-hr Dy^{165} which might be expected to show immediately after irradiation. However, since the 0.2770-Mev transition observed in this work decayed with the 7.5-hr half-life characteristic of Er^{171} and was found in both the external and internal conversion spectra, there can be no doubt that it belongs to the decay of Er^{171}. No trace of the 0.2849-Mev transition was found in either internal or external conversion. From its absence one can set an upper limit of 0.06% on its intensity (see Figs. 2 and 6). This limit is compatible with the value of $\sim$0.06% for the intensity of this transition found by Hatch and Boehm (private communication).

Table II, which presents the experimental results for gamma rays of energy greater than 0.4 Mev, reveals the presence of a large number of doublets, with either the 5-kev energy separation of levels *A* and *B* or the 12-kev separation of levels *C* and *D*. The energies quoted represent in all cases the average of at least two determinations, one from external conversion in gold and the other from external conversion in uranium. It is quite possible that the transitions of energies 0.842 and 0.962 Mev are also doublets, but they were too weak to make possible an analysis of their peak profiles. The final column indicates the position of each transition in the decay scheme.

THE DECAY SCHEME

The decay scheme based on the energy and intensity measurements and the multipole assignments of this work is presented in Fig. 9. All of the 30 gamma rays observed may be fitted in as transitions between the sequence of the 12 energy states, denoted by letters *A* to *L* in the figure. In addition, the scheme shows the positions of four transitions not seen in the present work. The levels *A*, *B*, *C*, and *D* form the ground state rotational band, which has been well documented by previous workers (Johansson 1957; Hatch and Boehm 1957; and Cranston *et al.* 1958) and will be accepted without further justification. Similarly, the existence of the 2.6-μsec metastable level *E* at 0.4251 Mev is well established and needs no further consideration.

The 5- and 12-kev doublets of Table II serve uniquely to establish five levels (*H*, *I*, *J*, *K*, and *L*), with all but one of these (level *L*) being supported by two pairs of gamma rays. Although the doublet character of the two weak transitions of energies 0.962 and 0.842 Mev deexciting level *K* has not been established, the energy difference between these strongly suggests that they both are transitions to the ground state rotational band.

Level *F* is based on two cascading gamma-ray pairs: 0.1664+0.3712 = 0.5376 and 0.1664+0.4040 = 0.5704 Mev. These energy sums are to be compared with 0.538 and 0.572 Mev, the energy differences of levels *E* and *K* and *E*

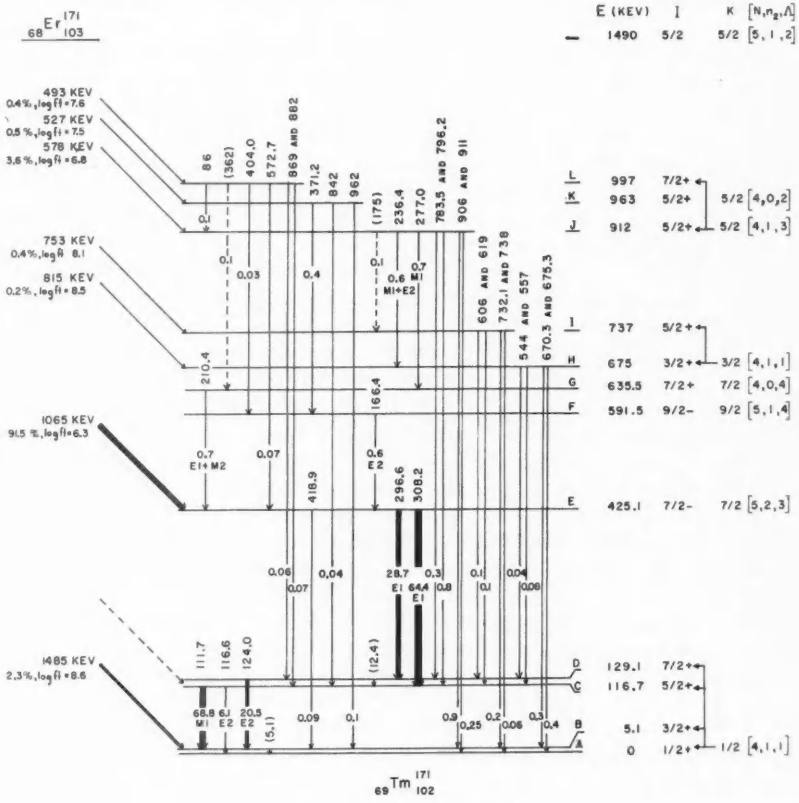

FIG. 9. The decay scheme of Er^{171}.

and L respectively. Similarly, level G is established by the energy sum $0.2104+0.2770 = 0.4874$, which agrees with the 0.487-Mev separation of levels E and J.

The beta–gamma intensity balance is excellent except for the beta group of energy 0.575 Mev which has a somewhat larger intensity than that required by the observed gamma-ray intensities. The latter are regarded as more accurate and have been used in the decay scheme, except for the 2.3% beta group feeding the ground state. The intensity balance for transitions between the levels in Tm^{171} is excellent.

Since Cranston *et al.* have already carried out an exhaustive series of gamma–gamma coincidence experiments on the decay of Er^{171}, it seems appropriate to subject this decay scheme to the test of their coincidence results. In general, the present work supports their conclusions: the nature of the transitions below E, the existence of a large number of 5- and 12-kev

doublets, and the positions of the 0.236- and 0.086-Mev transitions in the decay scheme. However, in order to satisfy the energy measurements of the present work, it has been necessary to shift the positions of levels *G*, *H*, *I*, *J*, and *L* downward by about 10 kev and at the same time to add the two new levels *F* and *K* to the decay scheme. The present decay scheme satisfies the coincidence results of Cranston *et al.* (1958) if one is permitted to reinterpret one of their coincidence experiments.

Cranston *et al.* found the 0.210-Mev transition to be in coincidence with gamma rays of energy 0.285 and 0.372 Mev which they interpreted as transitions between levels *J* and *G* and *L* and *G* respectively. This interpretation is quite incompatible with the energy measurements of the present work, since the *J*–*G* and *L*–*G* separations are now 0.277 and 0.362 Mev respectively. The 0.277-Mev separation corresponds to the relatively strong 0.277-Mev gamma ray observed in the present work and suggests strongly that the peak they have labelled 0.285 Mev in their coincidence spectrum (Fig. 5 of their paper) corresponds in reality to a 0.277-Mev transition. If this recalibration is accepted, their 0.372-Mev peak would have an energy of 0.362 Mev and, on their evidence, should have an intensity roughly one-sixth of that of the 0.277-Mev radiation. A 0.362-Mev transition of intensity 0.1% would have been missed in the present experiments. On this interpretation, Cranston *et al.* produce evidence for a 0.362-Mev transition of intensity ~0.1% between levels *L* and *G*, and the 0.371-Mev gamma ray of intensity 0.4% is a previously unreported radiation which falls naturally in place as a transition between levels *K* and *F*.

Two more of their coincidence experiments should be mentioned. (1) The coincidence peak at 0.177 Mev observed when gating in the interval 0.65–0.75 Mev is probably caused by a weak 0.175-Mev transition between levels *J* and *I* which was not observed in the present work. (2) In the beta–gamma coincidence experiments, the peak attributed to the 0.177-Mev transition may have been largely due to the 0.1664-Mev radiation, which is about six times as intense as the 0.177-Mev gamma ray.

DESCRIPTION OF THE ENERGY LEVELS IN Tm^{171}

A detailed discussion of the levels of Tm^{171} in terms of the Nilsson model has been given by Cranston *et al.* (1958). The new data presented here makes it possible to extend this discussion, although the conclusions reached by the earlier workers concerning all the levels found by them remain unaltered.

The description of levels *A*, *B*, *C*, and *D* as rotational states based on the Nilsson 1/2+ [4,1,1]* level (Mottelson and Nilsson 1959) and the identification of level *E* as a hole state associated with the 7/2− [5,2,3] Nilsson level have been well documented. Likewise the spin of Er^{171} has been found experimentally to be 5/2 (Cabezas 1960) and is presumably to be associated with the 5/2− [5,1,2] Nilsson level.

Since level *F* feeds level *E* by means of an *E*2 transition, it also must have negative parity, and the fact that it is not fed directly in beta decay suggests

*The quantum numbers in this description are, in order, $\Omega\pi[N,n_z,\Lambda]$.

that its spin is 9/2 or 11/2. The second choice is hard to reconcile with the pattern of gamma rays feeding this level. If its spin is 9/2, one can only explain the absence of transitions to level D by assuming that its K value is high enough to seriously retard transitions to the $K = 1/2$ ground state band.

Two possible descriptions of this level suggest themselves. It might be described as the 9/2− member of the rotational band based on level E. There are three objections to this choice. In the first place, the E–F level spacing of 0.166 Mev is much larger than the spacing of 0.110 Mev predicted from the moment of inertia in the ground state band. In the second place, the ratio of the intensities of the transitions $L \rightarrow E$ and $L \rightarrow F$ do not agree with those expected from transitions from a (7/2, 7/2)* level to the (7/2, 7/2) and (9/2, 7/2) members of the same band. Finally, if levels E and F belong to the same band, one would expect the unobserved transition $K \rightarrow E$ to have an intensity of about seven times that of $K \rightarrow F$ (i.e. an absolute intensity of ~3%). Alternatively level F may be associated with the 9/2− [5,1,4] state in the Nilsson diagram. This description also presents a difficulty since this level should fall somewhat above the 7/2+ [4,0,4] level which has been associated with level G (see below). Hatch *et al.* (1956) have pointed out that the 9/2− level falls below the 7/2+ level when one reaches Lu^{177}, but one would not expect this to happen in this nuclide. Nevertheless, this choice seems to be preferable to the assignment of this level as a rotational level.

Level G deexcites to level E by means of an $E1$ transition of energy 0.210 Mev. Hence, it must have positive parity and a spin of 5/2, 7/2, or 9/2. The absence of transitions to the ground state band strongly suggests that its K value is $\geqslant 5/2$. The first positive parity Nilsson state above the ground state is 7/2+ [4,0,4] and it seems to be the logical choice for this level.

Levels H, I, J, K, and L are all deexcited by transitions to the ground state band. This suggests that for these levels $K \leqslant 5/2$. One can calculate the relative reduced transition probabilities from a given level $I_i K_i$ to the four members of the ground state band, (1/2, 1/2), (3/2, 1/2), (5/2, 1/2), and (7/2, 1/2) (Alaga 1957), without knowledge of the intrinsic wave functions of any of the states. Table III presents the results of such a calculation for a number of levels which may be expected to appear. It also shows the relative reduced transition probabilities, as determined by the present experiments, for transitions between levels H, I, J, K, and L and levels A, B, C, and D. These experimental transition probabilities have rather large errors associated with them but nevertheless may be used as a guide in assigning spins.

Since transitions from both levels H and I are observed to all four members of the ground state band, it is clear that their spins must be either 3/2 or 5/2. An inspection of Table III shows that the reduced transition probabilities given for level H correspond closely to those given for a (3/2, 3/2) state if one assumes the transitions to be predominantly $M1$ with a small $E2$ admixture. Similarly the reduced transition probabilities for level I correspond closely to those given for a (5/2, 3/2) state deexciting by $M1+E2$ transitions. Moreover, the H–I level separation of 0.063 Mev corresponds closely

*These quantum numbers refer to (I, K).

TABLE III

$B(L, I_i \rightarrow I_f)$ values for transitions to the $K = 1/2$ band

			$I_f K_f$			
I_i	K_i	L	1/2 1/2	3/2 1/2	5/2 1/2	7/2 1/2
			Theoretical values			
3/2	3/2	$M1$	0.50	0.40	0.10	—
		$E2$	0.10	0.39	0.40	0.11
5/2	3/2	$M1$	—	0.40	0.45	0.14
		$E2$	0.27	0.019	0.17	0.38
5/2	5/2	$M1$	—	—	—	—
		$E2$	0.33	0.38	0.21	0.06
7/2	5/2	$M1$	—	—	—	—
		$E2$	—	0.21	0.38	0.29
Level			A	B	C	D
			Experimental values (relative)			
H		$M1$	0.4	0.3	0.15	0.07
		$E2$	0.4	0.3	0.22	0.11
I		$M1$	0.06	0.18	0.23	0.18
		$E2$	0.06	0.18	0.35	0.27
J		$M1$	0.25	0.9	1.3	0.45
		$E2$	0.25	0.9	1.7	0.6
K		$M1$	0.1		0.11	
		$E2$	0.1		0.14	
L		$M1$	—		0.11	0.09
		$E2$	—		0.14	0.12

to that expected for the 3/2–5/2 separation with a moment of inertia equal to that of Tm^{171} in the ground state. The same conclusion is reached by examining the relative intensities of the 0.236- and 0.175-Mev transitions feeding these levels from level J. On the assumption that both gamma rays are predominantly $M1$, the theory predicts an intensity ratio of 5.7 as compared with an experimental value of ~ 6. When one looks at the Nilsson levels, the natural choice seems to be the excitation of a hole in the 3/2+ [4,1,1] state. Thus the levels H and I are described as the 3/2+ and 5/2+ members of the 3/2+ [4,1,1] band.

Level J again feeds all four members of the ground state band and therefore has $I = 3/2$ or $5/2$. It also feeds levels G, H, and I with $M1$ or $M1+E2$ transitions so that its spin is certainly $5/2$. Reference to Table III shows that the intensity pattern for transitions to levels A, B, C, D do not fit the $(5/2, 5/2)$ assignment very well. The A,B doublet is very poorly resolved here and so the relative intensities within the doublet are subject to considerable uncertainty; however, it is hard to ignore the fact that the transitions to levels C and D are about three times too strong as compared with transitions to levels A and B.

Level L appears to be the second member of the rotational band based on level J. The L–J energy separation of 0.086 Mev is in good agreement with the 0.083-Mev spacing predicted from the ground state band. Moreover, the pattern of transition intensities from this level to the ground state band fits a $(7/2, 5/2)$ assignment. The spin of level K is probably 5/2+. This

assignment is consistent with the intensity of the beta group feeding this level and the pattern of transitions to the ground state band. The intensities of the transitions deexciting this level are too uncertain to make much use of them.

There are two suitable Nilsson orbitals, the 5/2+ [4,0,2] particle state, and the 5/2+ [4,1,3] hole state, available with about the correct excitation energy for use in describing levels *J*, *K*, and *L*. On the decay scheme, levels *J* and *L* have been arbitrarily associated with the [4,0,2] particle state and *K* with the [4,1,3] hole state; it is more likely that all three levels involve a mixing of the wave functions of both states.

While the above description of the levels is satisfactory in that it uses all of the predicted Nilsson levels in the expected energy region, it also demands a liberal use of the available hole states. An alternative to the use of the lower lying hole states, 3/2+ [4,1,1] and 5/2+ [4,1,3], is to consider levels *H* and *J* as due to the 3/2 and 5/2 gamma-vibration levels based on the ground state 1/2+ [4,1,1] level; and levels *I* and *L* as rotational states based on each of these gamma-vibration levels. Unfortunately, there does not seem to be any way of deciding between these two possibilities on the basis of the present data.

ACKNOWLEDGMENTS

The authors would like to thank Dr. Bunker and Dr. Boehm for their helpful suggestions and comments. They are indebted to Miss Anne Staveley for her assistance with the source preparation and with the recording of the data. One of the authors (AA) wishes to acknowledge the generosity of the Shell Oil Company in providing a graduate fellowship. Financial support for this work was provided by the National Research Council of Canada.

REFERENCES

ALAGA, G. 1957. Nuclear Phys. **4**, 625.
ARTNA, A. 1961. Ph.D. Thesis, McMaster University.
CABEZAS, A. Y. 1960. UCRL Report No. 9346.
CHEN, J. J. L. and WARSHAW, S. D. 1951. Phys. Rev. **84**, 355.
CRANSTON, F. P., BUNKER, M. E., MIZE, J. P., and STARNER, J. W. 1956. Bull. Am. Phys. Soc. **1**, 389.
CRANSTON, F. P., JR., BUNKER, M. E., and STARNER, J. W. 1958. Phys. Rev. **110**, 1427.
HATCH, E. N. and BOEHM, F. 1957. Phys. Rev. **108**, 113.
HATCH, E. N., BOEHM, F., MARMIER, P., and DUMOND, J. W. M. 1956. Phys. Rev. **104**, 745.
JOHANSSON, S. A. E. 1957. Phys. Rev. **105**, 189.
JOHNS, M. W. and NABLO, S. V. 1954. Phys. Rev. **96**, 1599.
JOHNS, M. W., WATERMAN, H., MACASKILL, D., and COX, C. D. 1953. Can. J. Phys. **31**, 225.
KELLER, H. B. and CORK, J. M. 1951. Phys. Rev. **84**, 1079.
MOTTELSON, B. R. and NILSSON, S. G. 1959. Danske Math. Fys. Skrifter, **1**, No. 8.
NUCLEAR DATA SHEETS. 1959. National Academy of Sciences, National Research Council, Washington, D.C.
PARKER, W., DECROËS, M., and SEVIER, K., JR. 1960. Nucl. Instr. and Methods, **7**, 22.
WAPSTRA, A. H., NIJCH, G. J., SALOMONS-GROBBEN, N., and ORNSTEIN, L. TH. M. 1958. Nuclear Phys. **9**, 538.

COMPRESSIBILITY OF LIQUID He^4 [1]

M. H. Edwards and W. C. Woodbury

ABSTRACT

The refractive index n, density ρ, and isothermal compressibility $k_T = (1/\rho)\times(\partial\rho/\partial P)_T$ of liquid He^4 have been measured along isotherms between the saturated vapor pressure and 4.5 atmospheres at 3.0°, 3.5°, 4.0°, 4.5°, and 5.0° K. The liquid was compressed in an optical cell 9.58 cm long in a Jamin interferometer. Changes in density were inferred through the Lorenz–Lorentz equation from refractive index changes measured with a photomultiplier fringe recorder. One fringe corresponds to a change in refractive index of $(5.699\pm0.003)\times10^{-6}$ in this apparatus. Densities range between 0.0995 g cm^{-3} at 5.0° K at the saturated vapor pressure and 0.1501 g cm^{-3} at 3.0° K and 4.5 atmospheres pressure. Compressibilities range between 65×10^{-8} cm^2 $dyne^{-1}$ at 5.0° K at the saturated vapor pressure and 1.16×10^{-8} cm^2 $dyne^{-1}$ at 3.0° K and 4.5 atmospheres pressure. The limiting liquid structure factors for zero-angle X-ray scattering and for coherent scattering of slow neutrons have been calculated from these density and compressibility measurements. In addition, the ratio of heat capacities has been calculated at 3.0°, 3.5°, and 4.0° K where other measurements of the velocity of first sound are available.

INTRODUCTION

A study of the refractive index of He^4 (Edwards 1956, 1957, 1958) has been extended to give further information on the liquid density. The refractive index n, the density ρ, and the isothermal compressibility $k_T = (1/\rho)(\partial\rho/\partial P)_T$ of liquid He^4 have now been measured along isotherms between the saturated vapor pressure (SVP) and 4.5 atmospheres at 3.0°, 3.5°, 4.0°, 4.5°, and 5.0° K. The complete absence of "dead space" corrections makes this optical method particularly attractive at temperatures and pressures where the gas in the connecting tubing is a large correction for direct pycnometric methods. The liquid density has not previously been measured above 4.2° K at any pressure above the SVP, nor has the liquid compressibility been determined directly at any temperature or pressure.

A knowledge of the isothermal compressibility of the liquid is needed for the interpretation of the scattering of X rays through small angles, and the coherent scattering of slow neutrons, since such scattering is attributable to liquid density fluctuations. Furthermore, the liquid compressibility is a most important factor in the electrostriction calculations involved in the analysis of the movement of ions in liquid helium (Atkins 1959; de Boer and 't Hooft 1961).

2. INSTRUMENTATION

The liquid was contained and compressed in an optical cell 9.58 cm long in a special optical cryostat mounted on a Jamin interferometer (Edwards 1956, 1957, 1958). A shift of one fringe in this apparatus implies a refractive index

[1]Manuscript received June 8, 1961.
Contribution from the Department of Physics, Royal Military College, Kingston, Ontario. Supported in part by the Defence Research Board of Canada under Grant No. 9510-10, Project D44-95-10-10.

change of $(5.699\pm0.003)\times10^{-6}$. Pressures in the optical cell and in the helium bath were determined with Wallace and Tiernan absolute and differential mercury manometers and Wallace and Tiernan precision dial manometers.

The interferometer was modified so that the interference fringes could be watched visually and recorded photoelectrically at the same time. The normal viewing telescope of the Jamin interferometer was altered as follows. A cylindrical lens was used for the eyepiece lens of the Jamin telescope to give magnification perpendicular to the fringe pattern only. Then a Bausch and Lomb eyepiece camera viewing head was attached to the telescope, and a 1P21 photomultiplier tube mounted in a lighttight box behind a slit in the focal plane of the camera. The camera viewing head contains a beam splitter which sends about 10% of the light to the viewing eyepiece while 90% falls on the photomultiplier slit. This slit allows light from about a quarter of one fringe to fall on the photomultiplier tube. The photomultiplier output was recorded on a 10-mv Varian G10 recorder with a 1-second full-scale balancing time. The noise level and drift of the over-all system rarely exceeded about 0.1 of a fringe, corresponding to 5.7×10^{-7} in refractive index.

Temperatures inside the copper-walled optical cell were taken to be equal to the bath temperatures just outside the cell. These temperatures were determined from the pressure at the surface of the bath (on the 1958 scale of temperatures, T_{58}) (Brickwedde *et al.* 1960) plus a hydrostatic correction due to the depth of liquid over the cell. A separate experiment with a vapor pressure thermometer outside the cell showed that this procedure correctly accounts for the increase of bath temperature with bath depth to within about 10^{-4}° K, in this metal cryostat. Temperatures outside the cell were monitored with a carbon resistance thermometer also. In fact, the temperatures inside the cell may have been higher than the temperatures outside the cell. Using the optical cell itself as a vapor pressure thermometer led to the conclusion that when the cell was only partially filled at the SVP, the surface of the liquid in the cell may have been hotter than the bath temperatures outside by up to 4 mdeg at 5.0°, 8 mdeg at 4.5°, 13 mdeg at 4.0°, 20 mdeg at 3.5°, 23 medg at 3.0°, 20 mdeg at 2.5°, 8 mdeg at 2.2°, and 1 mdeg below the λ-temperature. These apparent differences may be due to a thin layer of warmer liquid at the upper surface of the liquid helium I, when the cell is only partially filled. Such a layer would vanish below the λ-point and at higher pressures. As we could not increase these apparent differences reproducibly by increasing the radiant heat input to the cell, we did *not* apply a correction for this possible systematic error in temperature. When isotherms were performed, the temperatures were stabilized by controlling the pumping speed to the bath with a Greiner Manostat No. 8, and (or) by manual settings of two Edwards type LB1A needle valves, as well as by varying the power input supplied to the bottom of the bath by an electric heater. This procedure prevented the temperature of the cell from drifting more than ±0.5 mdeg during any run.

3. ANALYSIS

The refractive index, n, of liquid helium or helium vapor is related to the density, ρ, by the Lorenz–Lorentz law,

$$\frac{n^2-1}{n^2+2} = \frac{4\pi}{3M}(N_0\alpha) \tag{3.1}$$

through the molar polarizability $(N_0\alpha)$. The single important assumption in the following analysis is that this molar polarizability is independent of density or temperature. The evidence on which we base this assumption is as follows. Edwards (1957) showed that, for saturated helium vapor, $(N_0\alpha)$ is constant from 1.5° K to 4.2° K and equal to (0.1245 ± 0.0005) cm^3 mole^{-1} for $\lambda = 5462.27$ Å. He also calculated that, for helium gas at N.T.P., $(N_0\alpha)$ is (0.1246 ± 0.0002) cm^3 mole^{-1} for $\lambda = 5462.27$ Å, from the data of Cuthbertson and Cuthbertson (1910, 1932). Edwards (1958) measured $(N_0\alpha) = (0.12454\pm 0.00021)$ cm^3 mole^{-1} for liquid He^4 for $\lambda = 5462.27$ Å at 3.7° K and showed $(N_0\alpha)$ was independent of temperature from 1.6° K to 4.2° K for liquid He^4 along the SVP curve. In what follows, we assume that this last value of $(N_0\alpha)$ is correct at higher temperatures and pressures as well. Consequently, refractive index measurements may be considered as measurements of the vapor or liquid density ρ, through

$$\rho = (7.67523\pm0.0077)\ (n^2-1)\ (n^2+2)^{-1}, \tag{3.2}$$

and the isothermal compressibility, k_T, of the liquid, through

$$k_T = 6n(n^2-1)^{-1}(n^2+2)^{-1}(\partial n/\partial P)_T. \tag{3.3}$$

The numerical factor for equation (3.2), and its uncertainty, come from a combination of Kerr's (1957) absolute value of the density of liquid He^4 at 3.7° K and Edwards' (1958) absolute value of the refractive index of liquid He^4 at 3.7° K. Equation (3.3) follows by differentiation of equation (3.1), assuming that $(N_0\alpha)$ is independent of temperature and pressure.

Once the density and isothermal compressibility are known, γ, the ratio of heat capacities, may be calculated for the liquid using

$$\gamma = \rho u_1^2 k_T \tag{3.4}$$

where u_1 is the velocity of first, or ordinary, sound.

Conventional theories of X-ray scattering by liquids (Zernicke and Prins 1927; and Brillouin 1922) predict that in the limit of zero-angle scattering, and not too near the critical temperature, the liquid structure factor is given by

$$\mathscr{L}_0 = N_0 k M^{-1} \rho k_T T \tag{3.5}$$

where N_0 is Avogadro's number, k is Boltzmann's constant, M is the molecular weight, ρ is the density, k_T is the isothermal compressibility, and T is the absolute temperature. Goldstein (1951*a*, *b*) has obtained the same result and has shown that equation (3.5) holds also for the coherent scattering of slow neutrons with vanishing momentum change, for atoms with zero spin nuclei. Furthermore, Goldstein and Sommers (1956) and Egelstaff and London (1957) have given expressions for various slow neutron scattering cross sections which involve the quantity $\mathscr{L}_0$ also.

4. EXPERIMENTAL RESULTS AND DISCUSSION

At five temperatures, 3.000°, 3.500°, 4.000°, 4.500°, and 5.000° K, n–P isotherms were measured. At each steady temperature, the cell was filled to a pressure slightly over 4.5 atmospheres. Then the cell pressure was slowly decreased to the SVP at that temperature, while fringes were recorded. The pressure in the cell was marked on the fringe record as the pressure fell. Figure 1 is a photograph of a portion of the chart record of the 3.000° K isotherm. Due to a slight viscous pressure drop in the capillary tube leading to the optical cell, these recorded pressures were occasionally as much as 0.01 atmosphere lower than the actual pressures. Furthermore, as the density of the liquid helium in the cell was a pronounced function of temperature, the unavoidable slow temperature drifts of ± 0.5 mdeg during an isotherm required small corrections to be applied to the fringe numbers obtained to make them appropriate to the nominal temperature of the isotherm being taken. Thus the extreme precision to which a fringe number could be read, viz. about 0.05 of a fringe, corresponding to about 2.35×10^{-7} in refractive index, was much better than the actual accuracy of the measurements. However, small changes in n with pressure P could be measured fairly accurately and give values of the isothermal compressibility k_T. We estimate the increase of the length of the optical cell itself due to an internal pressure of 4.5 atmospheres to be only about $3.5 \times 10^{-4}\%$. The resulting correction to n, ρ, and k_T has been omitted as entirely negligible. The *absolute* values of refractive index obtained all depend on the accuracy of the one absolute value at 3.700° K, $n = (1.026{,}124 \pm 0.000{,}035)$ (Edwards 1958) and upon the accuracy of the comparison of changes from this one value. Values of n at the SVP have been determined in separate experiments (Edwards 1958; Edwards and Woodbury, to be published) for temperatures from 1.6° to 5.2° K. From these known values at the SVP the absolute value anywhere along an isotherm ending at the SVP could be determined.

The results of these measurements are given in Table I at the SVP and at intervals of 0.5 atmosphere to 4.5 atmospheres pressure. Because of limitations of space, the original data of fringe numbers versus pressure are not shown, since at 5.000° K, for example, about 950 fringes were obtained. The absolute values of the refractive index are believed to be within $\pm 4 \times 10^{-5}$, while relative values along any isotherm are probably within $\pm 5 \times 10^{-6}$. The absolute uncertainty in the liquid densities, obtained through equation (3.2), is about $\pm 0.15\%$ or roughly $\pm 2 \times 10^{-4}$ g cm^{-3}, while relative values along any isotherm are probably within $\pm 5 \times 10^{-5}$ g cm^{-3}. Figure 2 shows these isobaric densities of liquid He^4 as a function of temperature for pressures up to 4.5 atmospheres. Keesom and Keesom's smoothed 1933 values (Keesom 1942, p. 242) of the liquid density at 1.0 and 2.5 atmospheres, at 3.0°, 3.5°, and 4.0° K (after correction to the 1958 temperature scale), vary between 0.1 and 0.7% lower than the present results. Edeskuty and Sherman's (1957) values of the liquid density at 3.0° K at 1.0 and 2.0 atm are 0.06% and 0.08% lower than the present results.

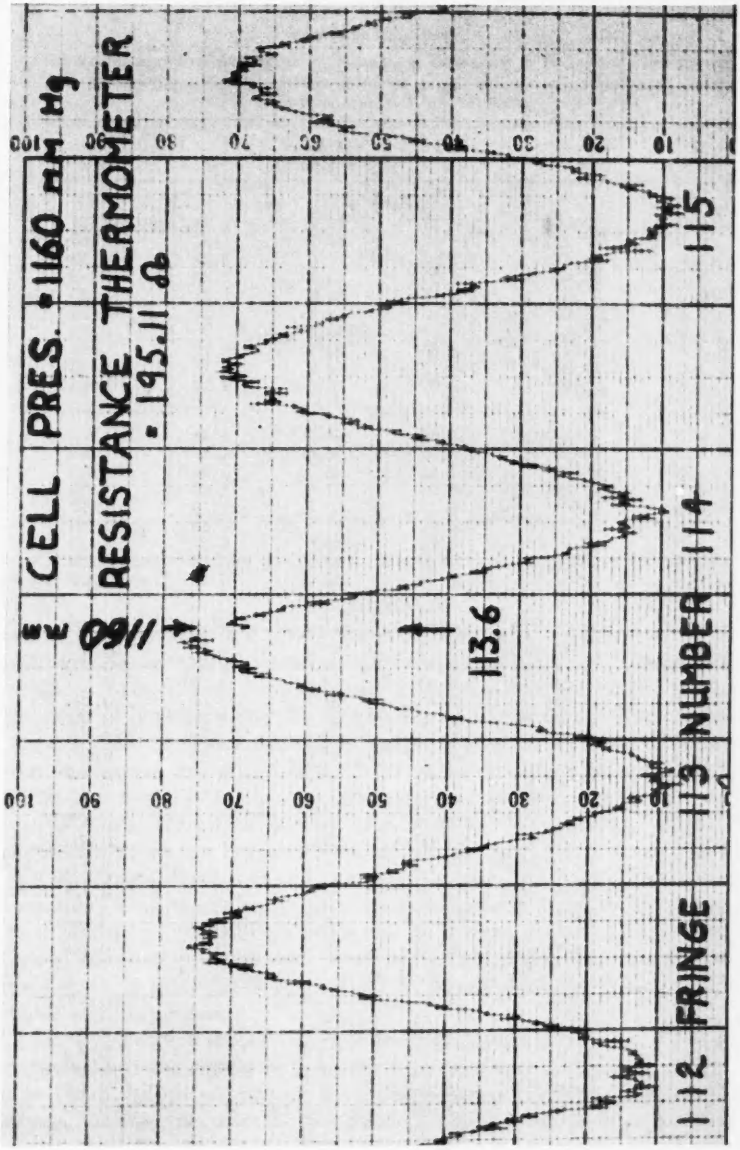

FIG. 1. A portion of the chart record of fringes obtained during the 3.000° K n–P compressibility isotherm.

TABLE I

Compressibility isotherms

(Refractive index n, at $\lambda = 5462.27$ Å, density ρ, isothermal compressibility k_T, ratio of heat capacities γ, and liquid structure factor $\mathscr{L}_0$, of liquid He^4 at even pressures for five temperatures)

P (atm)	$10^6(n-1)$	$10^3\rho$ (g cm^{-3})	$10^9 k_T$ (cm^2 dyne^{-1})	γ	$\mathscr{L}_0$
		T_{58}, 3.000° K			
SVP	27654	140.83	19.7	1.32	0.173
0.5	27792	141.52	18.7	1.27	0.165
1.0	28043	142.80	17.0	1.25	0.152
1.5	28280	144.00	15.8	1.23	0.142
2.0	28503	145.13	15.0	1.22	0.135
2.5	28716	146.20	14.2	1.21	0.129
3.0	28920	147.24	13.5	1.20	0.124
3.5	29115	148.23	12.8	1.19	0.118
4.0	29301	149.17	12.2	1.18	0.113
4.5	29480	150.07	11.6	1.17	0.108
		T_{58}, 3.500° K			
SVP	26632	135.65	25.7	1.48	0.253
0.5	26645	135.71	25.6	1.47	0.252
1.0	26980	137.41	23.2	1.44	0.231
1.5	27284	138.95	21.0	1.40	0.213
2.0	27561	140.35	19.3	1.36	0.197
2.5	27821	141.67	17.8	1.33	0.183
3.0	28067	142.92	16.6	1.31	0.172
3.5	28301	144.10	15.6	1.32	0.164
4.0	28525	145.24	15.0	1.32	0.158
		T_{58}, 4.000° K			
SVP	25223	128.50	41.4	1.92	0.442
1.0	25416	129.48	38.3	1.85	0.412
1.5	25873	131.80	32.0	1.71	0.350
2.0	26270	133.81	28.0	1.63	0.311
2.5	26626	135.61	24.8	1.57	0.280
3.0	26948	137.25	22.6	1.53	0.257
3.5	27243	138.74	20.6	1.50	0.237
4.0	27517	140.13	19.0	1.48	0.221
4.5	27774	141.43	18.0	1.47	0.212
		T_{58}, 4.500° K			
SVP	23180	118.14	81.7		0.902
1.5	23548	120.00	71.3		0.800
2.0	24289	123.76	52.7		0.610
2.5	24883	126.78	42.0		0.498
3.0	25370	129.25	35.2		0.425
3.5	25796	131.41	30.4		0.373
4.0	26168	133.29	27.0		0.336
4.5	26509	135.02	24.4		0.308
		T_{58}, 5.000° K			
SVP	19519	99.54	(650±100)		(6.72)
2.0	19951	101.74	380		4.01
2.5	21990	112.09	117		1.36
3.0	23041	117.43	73.6		0.898
3.5	23788	121.22	53.4		0.673
4.0	24391	124.28	43.9		0.567
4.5	24904	126.88	36.8		0.485

The isothermal compressibilities k_T were obtained through equation (3.3) taking values of $(\partial n/\partial P)_T$ read from large graphs of n versus P near the pressures required. For some of the k_T values second differences have been smoothed graphically. This smoothing process rarely altered any $(\partial n/\partial P)$

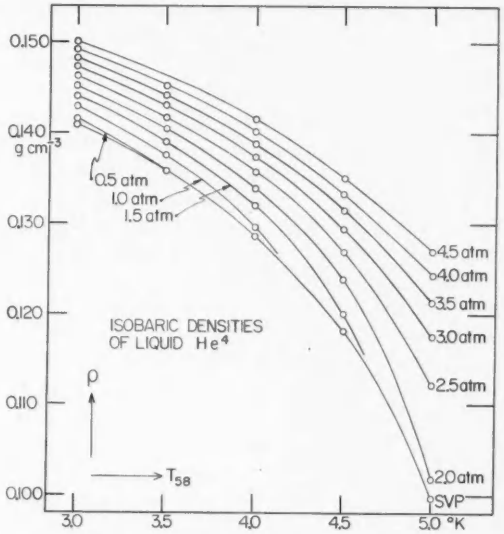

FIG. 2. Isobaric densities of liquid He^4 as a function of temperature for pressures up to 4.5 atmospheres.

value by more than 2%. We believe that the resulting uncertainty in k_T is about $\pm 3\%$, except for one point at the SVP at 5.000° K where the uncertainty is about 15%. Figure 3 shows these isothermal compressibility results as a function of pressure along the five isotherms. Keesom and Keesom (Keesom 1942, p. 243) obtained a smoothed graph of $(\partial\rho/\partial P)_T$ against T from which the isothermal compressibility of liquid helium may be obtained at 2.5 atmospheres and 3.0, 3.5, and 4.0° K to compare with the present measurements. After correction to the 1958 scale of temperatures, Keesom and Keesom's values are between 2 and 5% higher than our present results.

Table I also shows values of the ratio of heat capacities γ calculated from equation (3.4). Atkins and Stasior's (1953) smoothed values of u_1 were used, interpolating graphically where necessary. If these u_1 values are uncertain by $\pm 2\%$, then our γ values are uncertain by $\pm 5\%$. As no measurements have been made of u_1 at 4.500° K or 5.000° K, no calculation of γ was possible for those two isotherms.

Finally, Table I shows values of the liquid structure factor $\mathscr{L}_0$ calculated entirely from the results of the present measurements, using equation (3.5). The estimated uncertainty in $\mathscr{L}_0$ is the same as that for k_T, namely $\pm 3\%$, except for the one point at the SVP at 5.000° K where the uncertainty is about 15%. Gordon, Shaw, and Daunt (1954) have measured scattering of X rays down to angles of 1.5° at 4.2° K at the SVP. Their data extrapolated to zero angle gives $\mathscr{L}_0 = 0.575 \pm 0.040$.* Our results listed in Table I may be

*Due to a misprint, their paper states 0.475, but their Fig. 2 shows that 0.575 is meant for this quantity.

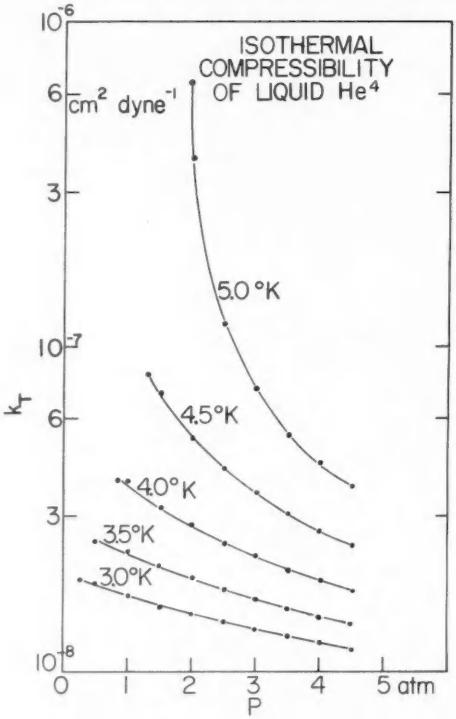

FIG. 3. Isothermal compressibility of liquid He^4 as a function of pressure along five isotherms. Along each isotherm the lowest pressure point corresponds to the saturated vapor pressure.

interpolated graphically to give a calculated $\mathscr{L}_0 = 0.58 \pm 0.02$ at 4.2° K. There is clearly excellent agreement with experiment here. Unfortunately, there is not good agreement with the calculations of $\mathscr{L}_0$ made earlier by Goldstein and Reekie (1955) and used extensively by them in their analysis of the structure of liquid He^4. At 4.2° K and the SVP, they calculated $\mathscr{L}_0 = 0.458$, which is well outside our limits of error. Tweet (1954) also calculated $\mathscr{L}_0$ at 4.16° K and the SVP and obtained approximately 0.61 ± 0.03* which agrees with our value. The earlier calculations were limited by the lack of direct measurements of the isothermal compressibilities of the liquid.

Egelstaff and London (1957) have calculated the expected zero-angle differential scattering cross section σ_s for slow neutrons scattered by liquid helium at the SVP, using, in effect,

$$\sigma_s = \left(\frac{5}{4}\right)^2 \frac{\sigma_f}{4\pi} \mathscr{L}_0 = 0.093 \mathscr{L}_0. \tag{4.1}$$

They took, σ_f, the free atom scattering cross section of helium, to be 0.75 barn (Sommers, Dash, and Goldstein 1955). At the highest temperatures

*Another unfortunate misprint in a "note added in proof" records this as 0.16.

liquid compressibilities were inferred by a considerable extrapolation of Keesom and Keesom's 1933 data. Our calculated σ_s values (obtained by multiplying our $\mathscr{L}_0$ values by 0.093) are higher than Egelstaff and London's by 6.8% at 3.0° K, 6.8% at 3.5° K, 15% at 4.0° K, 26% at 4.5° K, and 680% at 5.0° K. Egelstaff and London also measured σ_s for cold neutrons (45° K) for angles of scatter of 4.6° to 12.3° at liquid helium temperatures of 1.57° to 5.2° K. Their experimental data have been extrapolated to zero angle on plots of σ_s against $\sin^2(\theta/2)$, and are shown as lying close to their calculated σ_s values. At 3.19° K and below, these plots are nearly horizontal straight lines, and their extrapolated intercepts unambiguous. At higher temperatures, however, we believe the extrapolation, allowing for possible curvature at lower angles, could equally well pass through our calculated σ_s values.

5. CONCLUSIONS

The experiments reported here have given accurate information about the diagram of state of liquid helium in a region not covered previously. They provide the first direct measurements of the liquid compressibility. The results have been used to calculate the ratio of heat capacities γ, of liquid He^4 at 3.0, 3.5, and 4.0° K where first sound velocities u_1 are known. At 4.5° and 5.0° K, γ may also be obtained from these results when u_1 results become available. These results also permitted calculations of the limiting liquid structure factor to be made over the region covered, for zero-angle scattering of X rays and of slow neutrons.

REFERENCES

ATKINS, K. R. 1959. Phys. Rev. **116**, 1339.
ATKINS, K. R. and STASIOR, R. A. 1953. Can. J. Phys. **31**, 1156.
DE BOER, J. and 'T HOOFT, A. 1961. Proc. Seventh Intern. Conf. on Low Temperature Physics (Toronto, Ont.), p. 510.
BRICKWEDDE, F. G., VAN DIJK, H., DURIEUX, M., CLEMENT, J. R., and LOGAN, J. K. 1960. J. Research NBS, **64A**, 1.
BRILLOUIN, L. 1922. Ann. Phys. **17**, 88.
CUTHBERTSON, C. and CUTHBERTSON, M. 1910. Proc. Roy. Soc. A, **84**, 13.
——— 1932. Proc. Roy. Soc. A, **135**, 40.
EDWARDS, M. H. 1956. Can. J. Phys. **34**, 898.
——— 1957. Phys. Rev. **108**, 1243.
——— 1958. Can. J. Phys. **36**, 884.
EDESKUTY, F. J. and SHERMAN, R. H. 1957. Proc. Fifth Intern. Conf. on Low Temperature Physics and Chemistry (Madison, Wis.), p. 102.
EGELSTAFF, P. A. and LONDON, H. 1957. Proc. Roy. Soc. A, **242**, 374.
GOLDSTEIN, L. 1951*a*. Phys. Rev. **83**, 289.
——— 1951*b*. Phys. Rev. **84**, 466.
GOLDSTEIN, L. and REEKIE, J. 1955. Phys. Rev. **98**, 857.
GOLDSTEIN, L. and SOMMERS, H. S. 1956. Phys. Rev. **101**, 1235.
GORDON, W. L., SHAW, C. H., and DAUNT, J. G. 1954. Phys. Rev. **96**, 1444.
KEESOM, W. H. 1942. Helium (Elsevier, Amsterdam).
KERR, E. C. 1957. J. Chem. Phys. **26**, 511.
SOMMERS, H. S., DASH, J. G., and GOLDSTEIN, L. 1955. Phys. Rev. **97**, 855.
TWEET, A. G. 1954. Phys. Rev. **93**, 15.
ZERNICKE, F. and PRINS, J. 1927. Z. Physik, **41**, 184.

SCINTILLATION SPECTRA FROM THICK SOURCES[1]

K. G. McNeill and R. M. Green[2]

ABSTRACT

Graphs are presented showing the variation of different characteristics of scintillation spectra when the thickness of the source is altered. Correlation curves between the valley-to-peak ratio and the other characteristics enable tests to be made to decide whether or not changes such as the apparent change in resolution of a spectrum from the resolution obtained with a point source is due to the thickness of the source or to the presence of secondary gamma rays.

INTRODUCTION

In most research on radiation from radioactive sources, efforts have been made to reduce the thickness of the source itself and to minimize surrounding material, so that the radiation will be uncomplicated by scattering and absorption processes. The fewer the secondary effects, the easier is the interpretation of the resultant radiation spectrum.

In very many practical applications such complete freedom from absorption and scattering is not possible, and as a result, experiments and calculations have been carried out to find the effect of these disturbances in cases of special interest. In particular may be noted the cases of scattering by uniform material of X rays from an external source (Skarsgard 1960) and the reflection and transmission of gamma rays in a composite slab of material (Berger and Spencer 1959). There has been less work on the effects obtained with distributed gamma-ray sources, in which absorption and scattering occur in the source itself. Faust and Johnson (1949) used a Geiger counter to find the relative intensity of radiation at various points inside an extended source of Co^{60} (in the form of solution), and it is, in principle, possible to predict effects on the basis of experimental results on scattering obtained by, for example, Hine and McCall (1954) and Hayward and Hubbell (1954).

As distributed sources occur in a number of practical applications of nuclear techniques, such as analysis by photo- or neutron-activation of materials, and in physiological research using radioisotopes in the body, it was felt valuable to make a detailed study of some of the effects that do occur with an extended gamma-ray source. This paper reports the changes that occur in the scintillation counter spectra obtained from gamma-ray emitters uniformly distributed in aqueous solution as the thickness of the source is altered.

EXPERIMENTAL TECHNIQUE

In all the work to be described, a 5 in. diameter × 4 in. thick NaI(Tl) crystal was used. It was mounted on a DuMont 6364 photomultiplier tube, which was connected by conventional electronics to a 100-channel pulse-

[1]Manuscript received July 17, 1961.
Contribution from the Department of Physics, University of Toronto, Toronto 5, Ontario.
[2]Now at the Australian Atomic Energy Commission Research Establishment, Sutherland, N.S.W.

height analyzer. To hold the source solutions, a rectangular lucite box was built with dimensions 41 cm×34 cm×44 cm high, capable of holding 60 liters of aqueous solution. This box sat on a platform which could be moved 42 centimeters in a vertical direction. The crystal was mounted in a hollow lead cylinder whose axis was over the center of the lucite box, and whose height was such that with the platform in the lowest position, the vertical distance between the crystal face and the bottom of the box was 40 cm. This distance could then be reduced by the vertical movement of the box. The sources and detector were placed in a low activity room to reduce background effects. The experiment itself consisted in measuring the gamma-ray spectra produced by six individual sources (as modified by the detector system) as 10 or so successive dilutions of the solution altered the source thickness from 0 to 33 cm. The sources used and their characteristic radiations are listed in Table I. During

TABLE I

Characteristics of sources used

Source	Energy (Mev)	Other energies with relative strengths
Cr^{51}	0.32	—
Na^{22}	0.51	1.28 (50%)
Cs^{137}	0.66	—
Co^{58}	0.81	0.51 (28%) 1.62 (0.05%)
Zn^{65}	1.11	0.51 (1%)
K^{42}	1.53	—

all runs the crystal face was kept at 8 centimeters from the top surface of the liquid. For convenience, the amplification of the system was altered for runs with the different sources so that the photopeak of the main gamma ray under consideration was always in the same channel of the pulse height analyzer. Five or six runs were taken for each source thickness to reduce error. In each run approximately 8000 counts were recorded in the highest channel of the photopeak, which required approximately 5 minutes with the source strengths used. In the case of those sources which were not mono-energetic, corrections were made for the effects of the other gamma rays present.

RESULTS AND DISCUSSION

The general form of the changes that occur when self-scattering and self-absorption take place in a distributed gamma-ray source is shown in Fig. 1, in which the appearance of two spectra, from point and thick sources, have been superimposed. There is (i) an apparent broadening of the photopeak, due to small angle scattering of gamma rays in the source, (ii) a great increase in the number of pulses in lower channels, due to large angle, or to multiple, scattering in the source, and (iii) an increase in the valley-to-peak ratio, defined as the ratio N_v/N_m, where N_v is the number of counts in the lowest channel between the photopeak and the Compton edge and N_m is the number of counts in the highest channel of the photopeak.

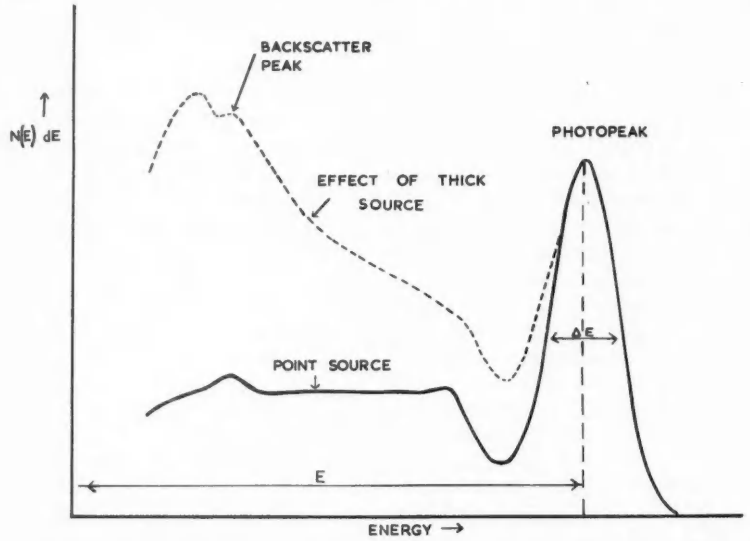

FIG. 1. Diagram to illustrate the changes that occur in the scintillation spectrum obtained from a monoenergetic gamma-ray source uniformly distributed in scattering material when the thickness of the source is increased.

The first two effects described above each create a problem in the analysis of spectra. If one is dealing with a distributed source of an unknown mixture of isotopes, the presence of a broad peak may be due to the existence of a secondary gamma line with energy slightly different from that of the main gamma ray, or it may be due simply to self-scattering. Again, the increased "low-energy" count due to scattering may mask the presence of gamma rays of low energy. Thus it is valuable to know the extent of peak broadening and the low-energy build-up as a function of source thickness. These changes are shown in graphical form in Figs. 2 and 3.

Figure 2 shows the fractional change in resolution, $(R+\Delta R)/R$, versus the thickness of the source, for six sources of energies ranging from 0.32 to 1.53 Mev. R is the point source resolution, defined by $\Delta E/E$, where ΔE is the photopeak width in Mev at half-height and E is the energy of the peak in Mev, and $(R+\Delta R)$ is the resolution at a particular source thickness. It will be seen that there is a smooth variation with thickness and with source energy. The maximum change occurs with the lowest-energy source, Cr^{51}. With a point source of this isotope the resolution is 16.3%, and with a source of depth 33 cm it is 20.0%, a change of approximately 23% as shown by the change in fractional scatter from 1.00 to 1.23. Simple calculations suggest that this is the change that may be expected on the basis of small angle scattering within the source, giving rise to gamma rays of energy slightly less in energy than the primary gamma ray.

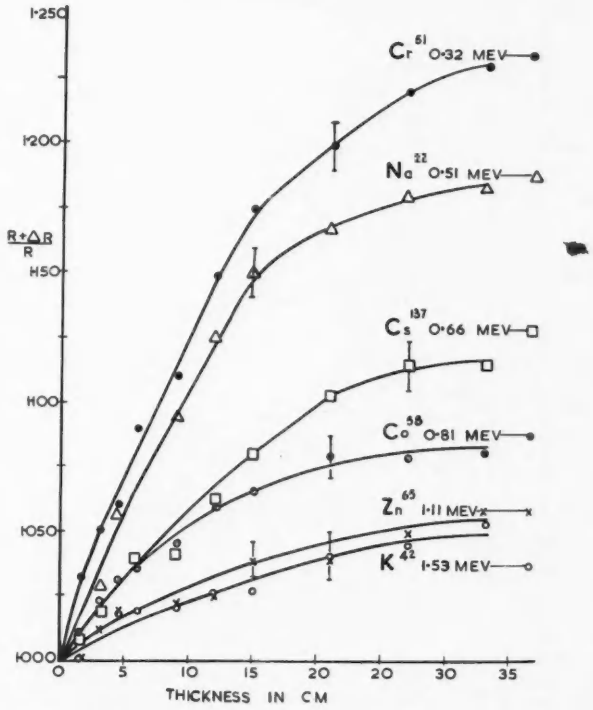

FIG. 2. The variation of the apparent resolution of the photopeak as the thickness of the source is altered. $(R+\Delta R)$ is the apparent resolution at a given thickness, and R that for a point source. Error bars are shown for representative points.

Figure 3 is a plot of the source thickness versus the fractional scatter, the latter term being defined as N_{et}/N_{ep}, where N_{et} is the total number of counts below the lowest channel in the valley between the photopeak and the Compton edge and above an energy equal to one-seventh of the gamma-ray energy, and N_{ep} is the corresponding number of counts in this region for a point source, the photopeak area being the same in both cases. The lower-energy limit was set arbitrarily to avoid troubles normally associated with the lowest channels of the pulse height analyzer; however, any other arbitrary level in the same region may be set and will give results which agree with those given here. It should be noted here that the point source values used herein are obtained by extrapolation of graphs of resolution or scatter versus source depth to zero thickness, as the thinnest sources available still had a finite thickness and were contained in glass bottles of finite thickness. Figure 3 shows that there is a smooth variation with source thickness and energy.

The only source parameter considered in the measurements described above

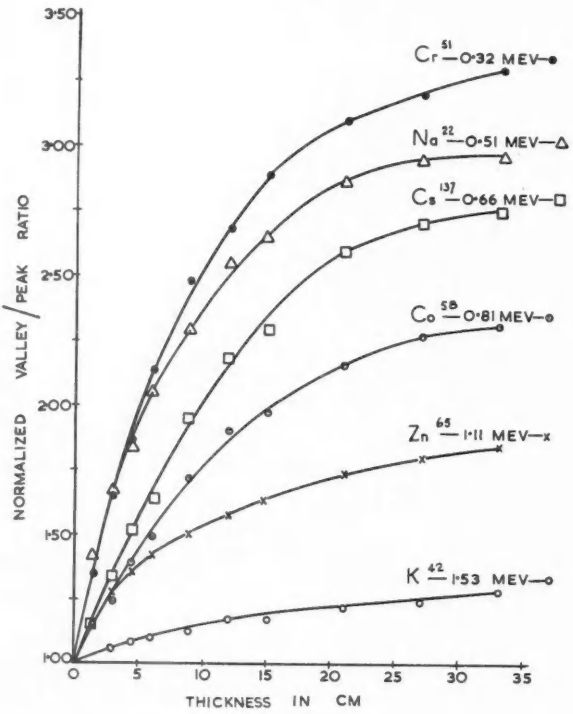

FIG. 3. Diagram to illustrate the build-up of low-energy pulses with increasing thickness of the source. The fractional scatter, a measure of the build-up, is defined in the text.

was the source thickness. However, in every case, the cross-sectional area of the source, and indeed its shape, will influence the form of the scintillation spectrum. To require a complete library of results not only for source thickness but also for all source dimensions is undesirable; it is preferable to be able to predict the fractional scatter and the fractional change in resolution from some other characteristic of the spectrum itself, thus making any reference to source dimensions or shape unnecessary.

A suitable characteristic is the valley-to-peak ratio. Figure 4 shows the normalized valley-to-peak ratio (i.e. the valley-to-peak ratio, as defined before, divided by the corresponding ratio for a point source) plotted against source thickness. This ratio is easily measured and, as is clear from the figure, shows a strong variation with thickness. The fact that the sign of the change of this characteristic of the spectrum with source thickness is the same as that of the change of fractional scatter and resolution with thickness is the reason for the adoption of the valley-to-peak ratio, rather than the perhaps more common peak-to-valley ratio.

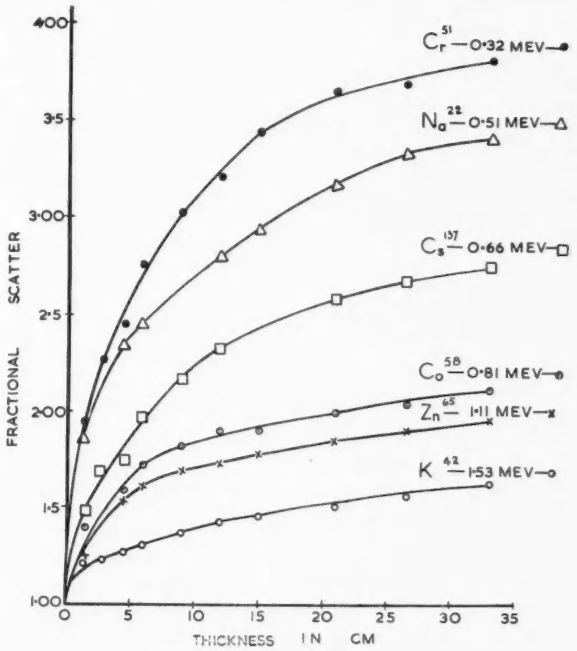

FIG. 4. Diagram to illustrate the increase with source thickness in the valley-to-peak ratio (the lowest count in any channel between the photopeak and the Compton edge divided by the highest count in the photopeak). For convenience, for all energies the ratio for a point source has been taken as unity.

Figure 5 shows the correlation between the normalized valley-to-peak ratios and the fractional change in resolution, and Fig. 6 shows the corresponding correlation with fractional scatter. The use of these curves, or of similar ones characteristic of other sizes of crystal, enables one to check spectra from thick sources to see if there are secondary gamma rays present in addition to those giving rise to the main peaks, without information about the dimensions of the source.

Although the experimental results presented here were obtained using cubical sources of activity, they are indeed applicable to other geometries. This was shown by measuring the spectra of a number of subjects, of weights ranging from 120 lb to 210 lb, who had ingested at separate times 3 μc of Na^{22} and K^{42}. With each spectrum the photopeak area, the valley-to-peak ratio, and the number of counts below the photopeak were determined. From the first two figures, a knowledge of the photofraction for monoenergetic gamma rays emitted from thin sources and the use of the fractional scatter versus valley-to-peak ratio curves presented here, it was possible to calculate the expected count below the photopeak and compare this predicted value

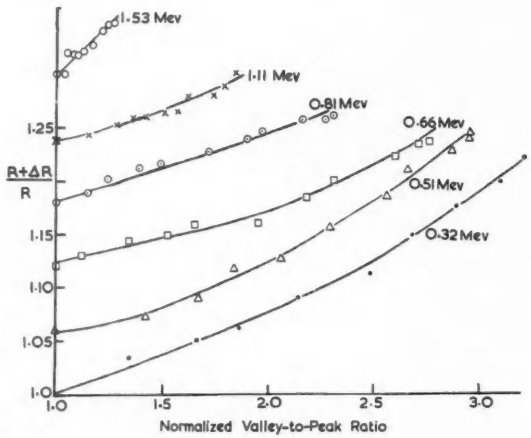

FIG. 5. Correlation curve showing the relationship between apparent resolution and valley-to-peak ratio for thick sources. Note that for convenience the axis for successive energies has been shifted by 0.06.

with that found experimentally. The results of this comparison are shown in Table II together with the fractional scatter coefficients. It is clear that the correlation curves are applicable to irregular geometries.

TABLE II

Comparison of calculated and observed low-energy count using isotopes ingested by various persons. The count was in all cases 1000 times the numbers quoted

	Case	1	2	3	4	5	6	7
Na^{22}	Calculated	174	142	141	158	180	162	
	Observed	175	141	139	159	179	162	
	Fractional scatter coefficient	3.22	2.79	2.86	3.06	3.32	3.22	
K^{42}	Calculated	145	131	133	136	158	147	130
	Observed	153	140	143	150	165	155	143
	Fractional scatter coefficient	1.86	1.69	1.71	1.76	1.98	1.91	1.72

It should be emphasized that these measurements have been made with a particular crystal and that although the trends illustrated here should be followed by any other setup, the variations found with source energy and thickness may differ in detail. In the general case it is necessary first of all to obtain, for the particular crystal assembly used, correlation curves of the type shown for a 5 in. × 4 in. crystal in the accompanying figures, using a sufficient number of different sources that accurate interpolation is possible. When the spectrum from a distributed source of a possible mixture of isotopes

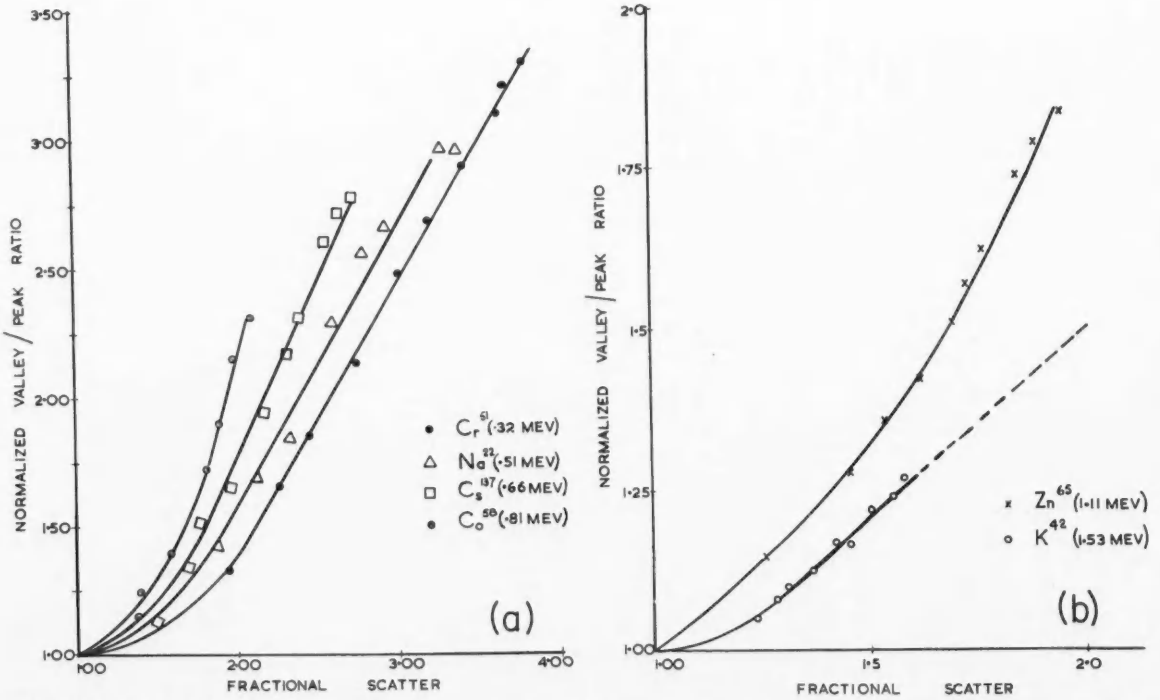

FIG. 6. (*a*) and (*b*) Correlation curves showing the relationship between fractional scatter and valley-to-peak ratio. In Fig. 6*b*, the linear extrapolation was used in the calculation of the K^{42} figures given in Table II.

is obtained, the resolution of the photopeak is checked using the valley-to-peak ratio – resolution curve (Fig. 5). Any deviation of the experimental result from the calculated value will indicate the presence of secondary gamma rays of energy near that of the most prominent one.* Then the valley-to-peak – fractional scatter curves are used to calculate the expected low-energy build-up. Comparison with the experimental value of fractional scatter will show the presence or absence of secondary gamma rays in the low-energy part of the spectrum.

Although the ideas presented here have been illustrated by graphical means, a quite simple computer programme performing the steps outlined above would permit an automatic analysis of any thick source spectrum.

ACKNOWLEDGMENTS

This work was supported by a Public Health Grant of the Department of National Health and Welfare and the Department of Health of the Government of Ontario. We should also like to express our thanks to Dr. W. H. Watson for helpful discussions.

REFERENCES

BERGER, M. J. and SPENCER, L. V. 1959. Radiation Research, **10**, 552.
FAUST, W. R. and JOHNSON, M. H. 1949. Phys. Rev. **75**, 467.
HAYWARD, E. and HUBBELL, J. H. 1954. J. Appl. Phys. **25**, 506.
HINE, G. J. and MCCALL, R. C. 1954. Nucleonics, **12**, 27.
SKARSGARD, L. D. 1960. Ph.D. Thesis, University of Toronto.

*It should be noted here that if two gamma rays of similar energy are present, both the apparent resolution and the valley-to-peak ratio will be affected. However, the change on the resolution is relatively much greater than that on the valley-to-peak ratio.

THE AUTOCORRELATION FUNCTION OF SYMMETRICALLY FOLDED GAUSSIAN NOISE[1]

T. H. SHEPERTYCKI

ABSTRACT

Noise with a uniform distribution of amplitudes and frequency of level crossings can be obtained by passing Gaussian noise through a symmetrical folder. A nonlinear device is required to do this. The input–output amplitude characteristic of this device has a positive unity slope between certain voltage (folding) levels which are symmetrical with respect to zero. The characteristic assumes a negative slope, called the folding slope, for voltages above and below the respective folding levels. The autocorrelation function of symmetrically folded noise is calculated. Curves are presented showing the power spectrum of symmetrically folded low-pass Gaussian noise for various degrees of folding and various values of folding slopes.

INTRODUCTION

Noise with an almost uniform amplitude distribution can be generated by passing Gaussian noise through a zero-memory symmetrical folding device. The input–output amplitude characteristic of this device, Fig. 1, is nonlinear

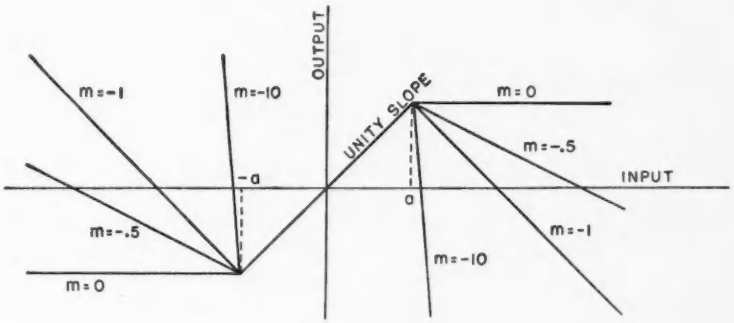

FIG. 1. Input–output amplitude characteristic of symmetrical folder.

and has a positive unity slope for a range of input voltages between two chosen voltage (folding) levels, $\pm a$, that are symmetrical with respect to zero. For input voltages above and below the folding levels the characteristic assumes a negative slope, called the folding slope, m.

The input–output amplitude characteristic of such a device can, therefore, be described by the following equations:

[1]Manuscript received May 1, 1961.
Contribution from the Division of Radio and Electrical Engineering, National Research Council, Ottawa, Canada.
Issued as N.R.C. No. 6567.

$$\begin{aligned} y &= x, && -a \leqslant x \leqslant a, \\ y &= mx+a(1-m), && x > a, \\ y &= mx-a(1-m), && x < -a, \end{aligned}$$

where y = instantaneous output voltage,
x = instantaneous input voltage,
m = slope of the folding sections, and
a = fold level.

For purposes of mathematical simplicity the fold level a is normalized in terms of the input r.m.s. noise level.

Folding devices have been described in the literature by Edson (1953) and Amo (1954). Figure 2 shows one commonly used configuration. It is of interest to note that a zero folding slope transforms the symmetrical folder into the well-known clipper.

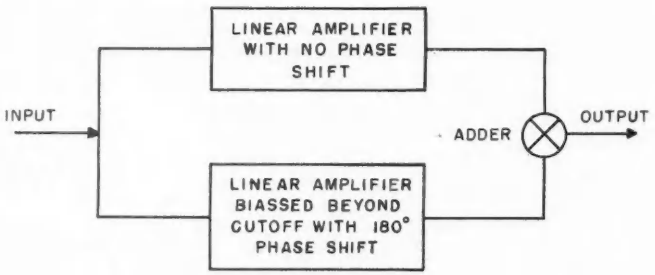

FIG. 2. One practical configuration of symmetrical folder.

Bennett (1953) has shown that noise uniformly distributed in amplitude can also be generated by passing Gaussian noise through a zero-memory device whose input–output amplitude characteristic has the form of the error-integral curve. The autocorrelation function of such noise has been given by Baum (1957). Noise generated in this manner, however, has a non-uniform distribution of the frequency of level crossings as a function of relative level. Unlike smoothly limited Gaussian noise, symmetrically folded Gaussian noise has an almost uniform distribution of the frequency of level crossings and is therefore more desirable for certain applications.

The purpose of this article is to calculate the autocorrelation function of symmetrically folded Gaussian noise. This result is then used to compute the power spectrum of symmetrically folded low-pass Gaussian noise for various degrees of folding and various values of folding slope.

DISTRIBUTION OF AMPLITUDES AND FREQUENCY OF LEVEL CROSSINGS

The amplitude distribution of Gaussian noise symmetrically folded at various amplitude levels was calculated using well-known techniques. Typical results for a unity folding slope ($m = -1$) appear in Fig. 3. It is evident that as the

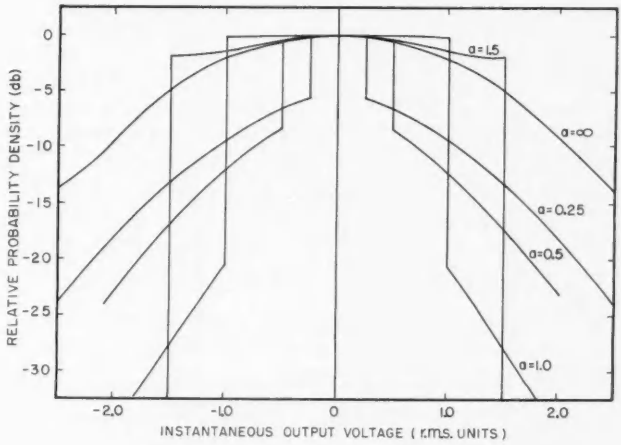

FIG. 3. Normalized amplitude and crossing rate distributions.

fold level, $\pm a$, approaches either zero or infinity the output amplitude distribution approaches the expected Gaussian shape. The intermediate fold levels, however, result in more uniformly distributed noise.

The optimum fold level will depend upon the application and will, for a unity folding slope ($m = -1$), be a compromise between an acceptable variation in the uniformity of the amplitude distribution and the percentage of time the folded waveform spends outside the fold levels. For example, noise folded at the r.m.s. level has an amplitude distribution uniform to within ± 0.08 db within the fold levels. Instantaneous voltage amplitudes in the folded waveform falling outside the fold levels occur only 0.26% of the time. By folding at greater than the r.m.s. level, or by using a shallower folding slope, these undesirable voltage amplitudes can be decreased if a greater variation from uniformity of the amplitude distribution is acceptable.

It is shown in the Appendix that the normalized distribution of the frequency of level crossings will be given by the same curves as the amplitude distribution (Fig. 3).

AUTOCORRELATION FUNCTION

Thomson (1954) has shown that for a Gaussian noise input into a nonlinear device the autocorrelation function of the output can be expressed by

$$\Phi(\tau) = \sum_{n=0}^{\infty} n! C_n^2 \phi(\tau)^n \tag{1}$$

where $\phi(\tau)$ = input autocorrelation function,

$$C_n = \frac{1}{n!\sqrt{2\pi}} \int_{-\infty}^{+\infty} f(x) \exp\left(-\frac{x^2}{2}\right) H_n(x) dx, \tag{2}$$

$f(x)$ = input–output amplitude characteristic,
$H_n(x)$ = Hermite polynomial of order n

$$= (-1)^n \exp\left(\frac{x^2}{2}\right)\frac{d^n}{dx^n}\exp\left(-\frac{x^2}{2}\right). \tag{3}$$

Performing the indicated integration in (2), for a symmetrical folding device, we obtain

$$C_n = \frac{2\exp(-a^2/2)(m-1)H_{n-2}(a)}{n!\sqrt{2\pi}} \quad \text{for } n = 3, 5, 7, 9, \text{ etc.} \tag{4}$$

and

$$C_1 = m - \frac{2(m-1)}{\sqrt{2\pi}}\int_0^a \exp\left(-\frac{x^2}{2}\right)dx. \tag{5}$$

Because of the symmetry of the folder the even order coefficients are zero; this indicates the absence of even order intermodulation products in the output as expected.

As $a \to \infty$ or $m \to +1$ (unity gain linear amplifier), the output autocorrelation function $\Phi(\tau) \to \phi(\tau)$, the input autocorrelation function.

As $a \to 0$ (linear 180° phase shifter with a gain of "m"), $\Phi(\tau) \to m^2\phi(\tau)$.

These are the expected results for the indicated boundary conditions.

An interesting property of the symmetrical folder arises when we consider the coefficient C_1 as defined by equation (5).

It is evident from this equation that, for non-zero folding slopes, C_1 will become zero at certain fold levels. In particular, for a unity folding slope C_1 becomes zero at a fold level of about 0.67455; because of the Wiener–Khinchine relationship between the autocorrelation function and the frequency spectrum, this means that the first-order intermodulation product vanishes leaving the third-order, fifth-order, etc., intermodulation products. These higher-order products, of course, generate frequency components that fall into the frequency band occupied by the input noise, as well as into their various harmonic zones.

Although the fifth-order, seventh-order, etc., intermodulation products can also vanish at certain fold levels (only the third-order intermodulation product has a non-zero value for all fold levels other than a zero or an infinite fold level) the first-order intermodulation product has the most significant effect on the output spectrum width, which, by definition, is equal to the frequency at which the power density is 10 db lower than that in the vicinity of zero frequency. Because the first- and third-order intermodulation products are the dominant ones in the expression for the power spectrum of symmetrically folded noise, the output spectrum width should, to a first approximation, become a maximum at the fold level at which C_1 vanishes. That this is so is evident from Fig. 5.

The fold levels at which the higher-order intermodulation products vanish can be obtained from a table of the zeros of the Hermitian polynomials published by Smith (1936).

SPECTRUM OF SYMMETRICALLY FOLDED LOW-PASS GAUSSIAN NOISE

For a prescribed input power spectrum, the output power spectrum can be obtained by applying the Wiener–Khinchine theorem to the output autocorrelation function.

Assuming an input power spectrum of the form

$$w(f/f_0) = \frac{1}{\sqrt{2\pi} f_0} \exp\left(-\frac{f^2}{2f_0^2}\right), \tag{6}$$

the input autocorrelation function $\phi(\tau) = \frac{1}{2}\exp(-2\pi^2\tau^2 f_0^2)$.

Substituting this expression into (1) and applying the Wiener–Khinchine theorem, we obtain for the normalized output power spectrum

$$\frac{W(f/f_0)}{W(0)} = \frac{1}{W(0)} \sum_{n=1,3,5}^{\infty} \frac{n! C_n^2 \exp\left(-f^2/2nf_0^2\right)}{\sqrt{2\pi n}\, f_0 2^{n-1}} \tag{7}$$

where C_n was calculated previously.

This expression for the normalized output power spectrum was evaluated at various values of fold level a and folding slope m with the aid of a digital

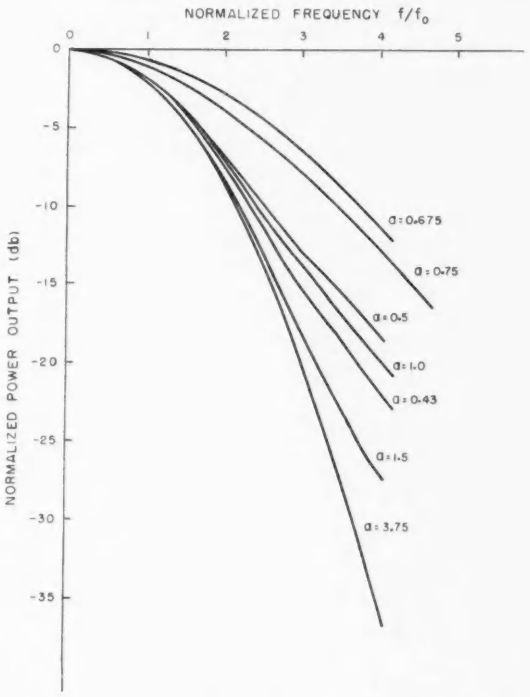

FIG. 4. Normalized output spectrum of symmetrically folded Gaussian noise for various fold levels (unity folding slope).

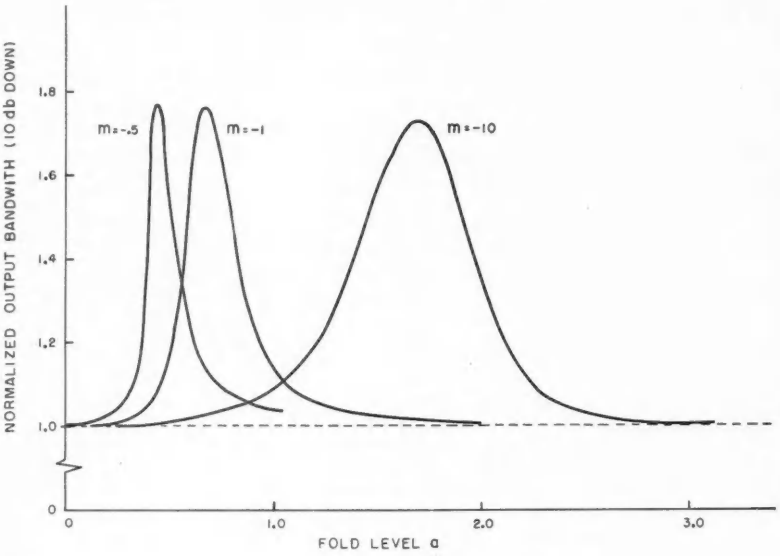
NORMALIZED OUTPUT BANDWITH (10 db DOWN)
1.8
1.6
1.4
1.2
1.0
0
m=-.5
m=-1
m=-10
0
1.0
2.0
3.0
FOLD LEVEL a

FIG. 5.

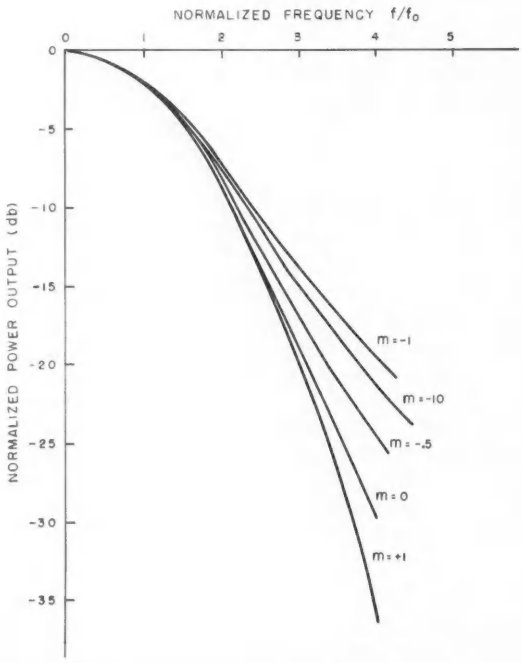
NORMALIZED FREQUENCY f/f0
0
1
2
3
4
5
0
-5
-10
-15
-20
-25
-30
-35
NORMALIZED POWER OUTPUT (db)
m=-1
m=-10
m=-.5
m=0
m=+1

FIG. 6.

computer. A good approximation to the power spectrum was obtained by including intermodulation products as high as the ninth order in the computation. An indication of the error in the computed power spectrum (due to omitting intermodulation products of higher order than the 9th) was obtained by computing the 11th order intermodulation product for two separate cases. In one case, only the sixth decimal place was affected; in the other, the ninth. For all practical purposes these are negligible errors. Typical results of the power spectra obtained appear in Figs. 4 and 6.

The normalized output power spectrum of symmetrically folded Gaussian noise is shown in Fig. 4, for various fold levels when the folding slope is -1. In this figure the curve for $a = 3.75$ approximates the Gaussian noise input spectrum. As the fold level a decreases from 3.75, the ratio of the output spectrum width to the input spectrum width increases until it reaches a maximum when the fold level becomes about 0.675. At this point the output power spectrum is 1.77 times as wide as the input power spectrum. Heavier folding decreases the output spectrum width until at a zero fold level the output spectrum width is again equal to the input spectrum width. This is shown better in Fig. 5 where the normalized output bandwidth (10 db down) is plotted as a function of the fold level for three folding slopes.

The effect of the folding slope on the output spectrum of Gaussian noise symmetrically folded at the r.m.s. input level is shown in Fig. 6.

CONCLUSIONS

Noise uniformly distributed in both amplitude and frequency of level crossings can be generated by symmetrically folding Gaussian noise. The autocorrelation function of such noise has been calculated and used to compute the power spectrum of low-pass Gaussian noise symmetrically folded at various folding levels for several folding slopes.

The results indicate that unlike symmetrically clipped noise a significant widening in the output spectrum width can occur when Gaussian noise is symmetrically folded. In particular, for a unity folding slope the maximum output spectrum width, 1.77 times as wide as the input bandwidth, occurs at a fold level of about 0.675.

ACKNOWLEDGMENTS

The author wishes to express his gratitude to his colleagues at the National Research Council, particularly to Mr. J. H. Craven, who checked some of the mathematics, and to Mr. Bruce Attfield, who programmed the computer.

REFERENCES

Amo, K. 1954. E.R.L. Stanford Tech. Report No. 17.
Baum, R. F. 1957. IRE Trans. **IT-3**, 193.
Bennett, R. R. 1953. Proc. I.R.E. **41**, 1509.
Edson, W. A. 1953. Proc. Natl. Electronics Conf. **9**, 171.
Rice, S. O. 1945. Bell System Tech. J. **24**, 54.
Smith, E. R. 1936. Am. Math. Monthly, **43**, 354.
Thomson, W. E. 1954. Proc. Inst. Elec. Engrs. (London), Monograph No. 106R.

Fig. 5. Normalized output bandwidth as a function of fold level.
Fig. 6. Normalized output spectrum of symmetrically folded Gaussian noise for various folding slopes (unity fold level).

APPENDIX

Proceeding from some of the results of Rice (1945), it can be shown that the average value of the modulus of the slopes of Gaussian noise

$$\overline{S(y)} = \sqrt{\left[8\pi \int_0^\infty f^2 w(f) df\right]}$$

where $w(f)$ = noise power spectrum.

Thus, the average value of the modulus of the slope of Gaussian noise at a particular voltage level is independent of that level. Therefore, when Gaussian noise is passed through a symmetrical folder with a unity folding slope, the average value of the modulus of the slope will remain unchanged.

From elementary considerations, the probability of finding the instantaneous noise voltage in an infinitesimal interval dy at a particular voltage y is

$$p(y)dy \propto \lim_{T\to\infty} \frac{N(y)}{T\overline{S(y)}}$$

where $N(y)$ = number of crossings of y during time T,
$\overline{S(y)}$ = average value of the modulus of the slope during time T.

If, as for Gaussian noise, $\overline{S(y)}$ is independent of y then

$$\lim_{T\to\infty} \frac{N(y)}{T} \propto \overline{S(y)}p(y)dy = Kp(y)dy.$$

THE CONCENTRATION DEPENDENCE OF PARAMAGNETIC RELAXATION IN DILUTE POTASSIUM CHROMI- AND FERRI-CYANIDES AT LIQUID HELIUM TEMPERATURE[1]

A. L. Kipling, P. W. Smith, J. Vanier, and G. A. Woonton

ABSTRACT

Measurements of the spin–spin relaxation time and of the effective, lattice-induced, transition probabilities are reported for magnetically dilute potassium chromicyanide in chemically analyzed concentrations ranging from 0.06 to 1.5%. In these measurements the *c*-axis of the cobalticyanide matrix was parallel to the static magnetic field. All measurements were made at a temperature of 4.2° K. Measurements made at a concentration of 1.5% did not fit into the same pattern as measurements made at lower concentrations, suggesting a change in the dominant mechanism of relaxation. Pulse and saturation measurements have been compared. The effective, lattice-induced transition probability by the pulse method for samples in the lower range of concentration was found to be independent of the concentration and of the transition involved and was found to have a value of

$$W = 65 \pm 7 \text{ sec}^{-1}.$$

The results for potassium ferricyanide were much less reliable and only two concentrations, 0.2 and 0.4%, have been examined. The static magnetic field was parallel to the *b*-axis and the temperature was 4.2° K. The value of W is probably between 1000 and 2000 sec^{-1}.

PARAMAGNETIC RELAXATION

Resonant methods of measurement applied to paramagnetic salts make it possible, as a first approximation, to consider only one pair of energy states, for example state i and state j, out of the manifold available for experiment. When thermal equilibrium exists, these two states are populated by N_i and N_j spins. When the salt is placed in the cavity of a spectrometer and subjected to microwave radiation of frequency ν_0, because of the probability $V(ij)$ that transitions will occur, the states take on an out-of-equilibrium population characterized by N_i' and N_j'.

It is customary in the literature of this subject to make use of a saturation factor $S(ij)$ when discussing the populations of the states. Lloyd and Pake (1954) define the saturation factor and show that its relation to the parameters of the salt and of the radiation is

$$S(ij) = (N_i' - N_j')/(N_i - N_j) = (1 + V(ij)/W(ij))^{-1}, \tag{1a}$$

$$W(ij) = U(ji) + C(ji)^{-1} \sum_{k \neq j} U(jk)C(jk). \tag{1b}$$

The quantity $W(ij)$ is defined as an effective, lattice-induced transition probability. In equation (1*a*), quantities of which $U(ji)$ is typical are lattice-induced, transition probabilities while quantities like $C(ji)$ are the cofactors of a determinant which appears in the Lloyd and Pake derivation. Equation

[1]Manuscript received September 5, 1961.
Contribution from the Eaton Electronics Research Laboratory, Department of Physics, McGill University, Montreal, Que.

(1*a*) makes clear the use of the word effective in connection with $W(ij)$; this quantity depends on lattice-induced, transition probabilities between all states unlike $U(ij)$, which is related to only two of them.

In the literature of nuclear magnetic resonance and sometimes in paramagnetic resonance there is defined a spin–lattice, relaxation time, T_1. Insofar as it is possible to characterize the complex process of relaxation by a single time constant, T_1 is related to W as in equation (1*c*).

$$T_1(ij) = 1/2W(ij). \tag{1c}$$

Andrew (1956, p. 22) has derived the imaginary component of the nuclear magnetic susceptibility. Andrew's method may be applied to the two levels of a paramagnetic salt of effective spin S containing a total of N spins in all states to find an effective susceptibility $\chi''(ij)$. Power P, incident on the coupling hole of the microwave cavity, sets up an alternating magnetic field, $H(\mathrm{rf})$, at the frequency ν_0 at which the spectrometer operates. The selected states are resonant with the radiation when the external static magnetic field has an amplitude $H_0(ij)$ but whatever the amplitude, the probability of a transition is $V(ij)$. In terms of these quantities the imaginary component of the effective susceptibility at a bath temperature T is as follows:

$$\chi''(ij) = N\hbar^2\nu_0 S(ij)\, V(ij)/\pi(2S+1)kT\, H(\mathrm{rf})^2. \tag{2}$$

It is convenient to be able to calculate the radiation-induced transition probability $V(ij)$, from the spin-Hamiltonian of the salt; this has been done for potassium chromicyanide by Chang and Siegman (1959). The first line of equation (3), which follows, is general and shows that the associated matrix element is to be calculated by applying the effective spin-operators to a set of wave functions for which the energy matrix derived from the spin-Hamiltonian is diagonal. Chang and Siegman give tables and graphs for the square of this matrix element which, however, include a factor of 2 as the spectroscopic splitting or g-factor for potassium chromicyanide; for convenience subscripts indicating direction have been omitted from the symbol g. The second line of equation (3) has been adjusted so that if $C(ij)^2$ is the value picked from one of Chang and Siegman's tables, $V(ij)$ has the correct value. In the third line, power P has been substituted for $H(\mathrm{rf})^2$; as indicated, power and the square of the field are related by the parameter K_p, which is mentioned later in connection with equation (8).

$$\begin{aligned} V(ij) &= (1/4\hbar^2)g(H)_{ij}|\langle i|\beta\mathbf{H}.g.\mathbf{S}|j\rangle|^2 \\ &= (1/16)(g\beta/\hbar)^2 g(H)_{ij} H(\mathrm{rf})^2 C(ij)^2 \\ &= (1/16)(g\beta/\hbar)^2 g(H)_{ij} K_p P\, C(ij)^2. \end{aligned} \tag{3}$$

The transition probability $V(ij)$ depends on the static magnetic field H in two different ways. For a given orientation of the salt there is a slow dependence on a field contained in the matrix element itself; this field dependence is taken into account when the matrix element is picked from the tables. Secondly, an explicit dependence appears in the line-shape factor $g(H)_{ij}$. This function

is normalized with respect to frequency and by definition has a maximum value equal to $2T_2(ij)$ where $T_2(ij)$ is the spin–spin relaxation time.

$$\int_0^\infty g(H)dv = 1, \tag{4a}$$

$$g(H_0)_{ij} = 2T_2(ij). \tag{4b}$$

Substitution into equation (2) of the quantities defined in equations (3) and (4) leads to the final expression for $\chi''(ij)$; this expression is general although the form of $V(ij)$ appropriate to Chang and Siegman's values for chromicyanide has been used in defining M, the maximum value of $\chi''(ij)$.

$$\chi''(ij) = (M/2T_2(ij))S(ij)g(H)_{ij}, \tag{5a}$$

$$M = C(ij)^2Nh^2\nu_0(g\beta/\hbar)^2T_2(ij)/8\pi(2S+1)kT. \tag{5b}$$

The object of an experiment in paramagnetic relaxation should be to determine the values of the lattice-induced transition probabilities that appear in equation (1*b*); this objective has not been reached but the effective, lattice-induced transition probabilities $W(ij)$ have been measured. The quantity $W(ij)$ enters the expression for the susceptibility (5*a*) through the saturation factor $S(ij)$. A useful analogy can be established between this subject and that of nuclear magnetic resonance by introducing a power-dependent parameter, σ, of the same general nature as that discussed by Andrew (1956, p. 108).

$$\sigma(ij) = T_2(ij)(g\beta/\hbar)^2K_0P\,C(ij)^2/8W(ij). \tag{6a}$$

In this relation K_0 is the value of K_p, appropriate to an empty cavity. In terms of σ, the expression for the saturation factor becomes:

$$S(ij) = [1+\sigma(ij)(K_p/K_0)g(H)_{ij}/2T_2(ij)]^{-1}. \tag{6b}$$

Feher (1957) has analyzed the response of spectrometers to changes in χ''. Although equation (7*a*), below, is not in his notation, Feher shows that the quality factor, Q_p, of a cavity when a paramagnetic salt in it is absorbing power, is related to the quality factor of an empty cavity, Q_0, in the following way:

$$Q_p = Q_0(1+4\pi\chi''(ij)\eta Q_0)^{-1}. \tag{7a}$$

The instrumental problem is to relate the instantaneous value of Q_p to the deflection of a recorder at the output of the spectrometer subject to the conditions under which the spectrometer is being used. Feher solves the problem with the aid of the assumption that $\chi''(ij)$ is so small that equation (7*a*) can be approximated by the first term of a binomial expansion. During the course of the experiments reported here, it was observed that for many crystals which were used, Feher's approximation was not valid.

It is convenient to characterize the reaction of the crystal on the microwave cavity by a constant, α, defined as follows:

$$\alpha = 4\pi M\eta Q_0. \tag{7b}$$

In terms of α, and the other variables which have been defined, equation (7*a*) can be rewritten:

$$Q_p/Q_0 = (1+\alpha S(ij)g(H)_{ij}/2T_2(ij))^{-1}. \tag{7c}$$

Feher makes use of a coupling constant, β_0, related to the empty cavity; it is now necessary to introduce a variable coupling constant β_p, which is defined in relation to Q_p in the same manner as β_0 is defined in relation to Q_0. Meyer (1955, Appendix) has defined and discussed the constant, K_0, which relates the radio-frequency field in an empty cavity to the incident power. In a more exact analysis it is necessary to recognize that K_p is a variable that depends on Q_p; it is related to the measurable constant K_0 in the following way:

$$K_p/K_0 = (Q_p/Q_0)^2(1+\beta_0)^2(1+\beta_0 Q_p/Q_0)^{-2}. \tag{8}$$

Reference to equations (6*b*), (7*c*), and (8) shows that the exact equation relating Q_p to the measurable constants of the spectrometer and of the crystal is cubic in Q_p. The complexity of the solution for Q_p has made it necessary to seek experimental methods which depend on valid approximations to the exact relations. These experimental methods are explained under the section heading, Saturation Measurements.

SPECIMENS

In these experiments the Cr^{3+} ions of potassium chromicyanide ($K_3Cr(CN)_6$) or the Fe^{3+} ions of potassium ferricyanide ($K_3Fe(CN)_6$) were carried by single crystals of diamagnetic, potassium cobalticyanide; this was arranged by dissolving a paramagnetic salt in water in the desired ratio to the diamagnetic salt. Single crystals whose weight ranged between 40 and 100 milligrams were picked from the solution as the excess water evaporated.

Crystals were selected from each batch and analyzed by the colorimetric method which has been described by Sandell (1959). The following table illustrates the typical relation between the nominal and the measured concentration of paramagnetic ions in the diamagnetic lattice for potassium chromicyanide.

TABLE I

Relation between nominal and measured concentrations. The number of chromium ions is expressed as a percentage of the cobalt ions

Nominal concentration, %	Measured concentration, %
0.1	0.071±0.008
0.5	0.20 ±0.01
1.0	0.44 ±0.07
3.0	1.57
5.0	2.60 ±0.17
	1.55

Opposite the nominal concentration of 5%, there appear two values for the measured concentration. These entries represent the anomalous behavior of one batch of crystals which has not been explained.

The concentrations of iron ions in the diamagnetic lattices have not been determined. It is assumed in what follows that the relation between nominal and measured concentrations for potassium ferricyanide is the same as that given in Table I.

Information on the crystallography of the complex cyanides, on the electronic configurations, and on the constants of the spin-Hamiltonian can be found in a paper by Bowers and Owen (1955) and in the two papers by Baker, Bleaney, and Bowers (1956) and by Bleaney and O'Brien (1956). Tables relating to the energy level structure of potassium chromicyanide have been published by Chang and Siegman (1959) and very useful graphs of energy levels versus the magnitude of the static field for many orientations of the crystal have been published by Butcher (1957). The angular dependence of the paramagnetic resonance spectra of potassium ferricyanide has been calculated for the static magnetic field oriented in the three crystallographic planes by Kipling (1961).

In view of the extensive literature on these salts it is sufficient to say that the Cr^{3+} ions have an effective spin 3/2; there are therefore three transitions associated with single quantum jumps and measurements are reported on all three transitions. The iron ion, Fe^{3+}, in the cyanide environment exhibits an effective spin 1/2 only and there is only one transition to measure and discuss.

The symmetry of the intramolecular field (in fact covalent bonding plays a major role) in these complex cyanides is such that the energy states of the two non-equivalent complexes are superimposed when the static magnetic field vector lies in either the *ac* or *bc* plane of the crystal. This advantage is retained when the static field is oriented along the *c*-axis and with this orientation the resonant frequencies of the various transitions are so widely spaced that there is little danger of the experimental results being confused by the phenomena of cross relaxation that has been discussed at length by Bloembergen, Shapiro, Pershan, and Artman (1959). For these reasons, all results which are reported here on potassium chromicyanide were collected in experiments in which the static field was parallel to the *c*-axis of the crystal.

Since for potassium ferricyanide there exists only one transition, cross relaxation is not a problem and in fact meaningful results can be obtained with any orientation of the static field. Convenience, arising from the required magnitude of the static field for resonance at the frequency of the spectrometers (9400 megacycles/second), dictated that the static field be oriented parallel to the *b*-axis and this orientation has been used in all experiments.

In the case of potassium chromicyanide there is some confusion in the literature concerning the naming of the energy levels. To avoid this confusion in this report, the lowest level is called 1 and the others are numbered in sequence up to 4.

APPARATUS, EXPERIMENTAL CONDITIONS

The spectrometers used in these measurements were similar to those described by Feher (1957); the microwave sources were controlled by Pound stabilizers and operated at a frequency of 9400 megacycles per second. In

order to describe the measurements it is necessary to note two basic modifications to the Feher-type spectrometer: (i) precision, microwave attenuators were added to the spectrometer immediately before and after the magic-T bridge. Compensating adjustments to the two permitted power to the microwave cavity to be varied over a range of 50 decibels, while the power to the balanced mixer that preceded the I.F. preamplifier remained approximately constant; (ii) in some of the measurements, a pair of gyroline, ferrite attenuators in series were interposed between the microwave source (a 2K39 klystron) and the first of the precision attenuators mentioned in (i). A pulse generator was used to supply pulses of current to these attenuators so that their attenuation of 60 decibels could be reduced in a time of 15 microseconds to 2 decibels during the pulse; at the conclusion of the pulse the attenuation returned to its original value in the same time interval. A bypass network, consisting of two directional couplers and an attenuator, permitted a very low level monitor signal to reach the microwave cavity in a manner quite independent of the pulse system.

As in the Feher-type spectrometer a pair of modulation coils were mounted on the pole pieces of the magnet and in saturation experiments (but not in experiments of other types) these coils were supplied with current alternating at a frequency of 200 cycles per second. By this means a small alternating component could be added to the otherwise static magnetic field, H_0, to which the crystal was subjected. In this mode of operation the recorder traced a derivative with respect to field as the static magnetic field was allowed to sweep through resonance.

In addition to the mode of operation described for saturation measurements, two other modes were made possible by the insertion of the gyroline attenuators; in these modes field modulation was not used. When the lineshape factor $g(H)$ and the spin–spin relaxation time T_2 was under investigation, the microwave power to the cavity was amplitude-modulated by pulsing the gyroline attenuators with square waves recurring at the rate of 200 p.p.s. In this mode of operation the resonance line itself was traced by the recorder as the static magnetic field was swept through resonance.

For the purpose of pulse measurements the gyroline attenuators were supplied with square waves of current at the rate of about 16 p.p.s. The output of the I.F. preamplifier passed through a special, main, I.F. amplifier whose gain was much reduced by the same pulse that decreased the attenuation of the gyrolines; the output of this amplifier was direct coupled through a crystal diode to a double beam oscilloscope. The more or less exponential return of $\chi''(ij)$ to its thermal equilibrium value, after the pulse was cut off, was monitored by a steady signal of very low power, supplied through the bypass circuit. The second beam of the oscilloscope was used to display the decay curve of an R-C network, the condenser of which had been charged by the same pulse that had decreased the attenuation of the gyroline. Since manipulation of the controls of the oscilloscope permitted this curve to be superimposed on the curve exhibiting the decay of the saturation of the salt, adjustment of the resistance in the R-C network permitted immediate evaluation of the time constant associated with the value of $W(ij)$. The decay curve of the

R-C network also provided a reference by which it could be decided whether one or more time constants were to be associated with the relaxation process.

Two different spectrometers were used in the experiments. In one of these, the 12-in. magnet that supplied the static field was rotatable and in consequence, errors in orientation made in placing the crystal in the microwave cavity could be compensated by external rotation of the magnet. In the other spectrometer, the 6-in. magnet could not be rotated. To avoid serious errors the crystal was usually cemented to the tuning plunger, which was then inserted in the cavity.

The cavities of both spectrometers were immersed in liquid helium which was boiling at atmospheric pressure. Throughout this report all measurements were made at a temperature of 4.2° K.

SATURATION MEASUREMENTS

Figure 1 illustrates the saturation method of measuring $W(ij)$. Because of the field modulation, the recorder plotted a derivative with respect to the

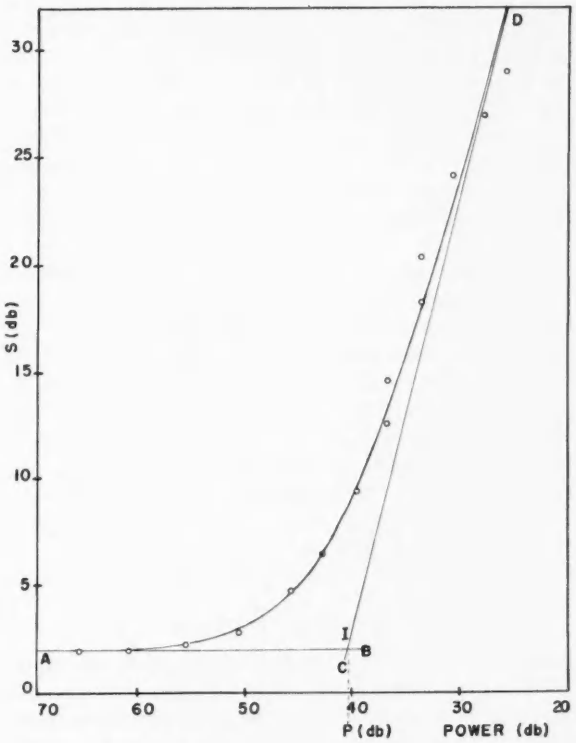

FIG. 1. A typical set of experimental points in a saturation measurement, fitted by a theoretical curve (solid line). The extrapolated linear regions, AB and CD meet at I. The power P_I, used in equation (9), is calculated from the logarithmic power ratio P(db).

field when the static field was allowed to sweep through the resonance line. In many cases a sample of D.P.P.H. was placed in the cavity along with the sample under investigation. The ordinates of Fig. 1 are:

$$S(\text{db}) = 20 \log \left(\frac{\text{max. value of derivative for D.P.P.H.}}{\text{max. value of derivative for sample}} \right).$$

Since D.P.P.H. does not saturate, higher values of the ordinate express increased saturation of the sample. These ordinates are plotted against the power incident on the coupling hole of the cavity, expressed in decibels.

The curve which appears in Fig. 1 is typical of all saturation measurements. On the logarithmic plot, two linear regions always appear, one for the condition $S(ij) \doteqdot 1$, the other for $S(ij) \doteqdot 0$; the approach to a straight line for the latter condition is so slow that theoretical curves are required to establish the correct slope in any set of experiments. In Fig. 1, the two linear regions have been projected and are the straight lines AB and CD; these intersect at I, which provides a unique point on the diagram for determining $W(ij)$.

Andrew (1956, p. 108) provides enough information to determine the theoretical form of the saturation curves that appear in Fig. 1, when it is assumed that the line shape is of the Lorentz form and that the crystal characteristic α, equation (7*b*), is zero; there are two subcases appropriate to whether the saturation factor $S(ij)$ is able to follow the modulation or whether it should be considered a constant. The exact solution when α is not zero is a problem of considerable complexity and has not yet been solved. It is the purpose here to show that measurements based on the unique point of intersection, I, in Fig. 1 can be exact without a complete knowledge of the form of theoretical curves.

In a theoretical derivation, the location of the straight line AB is determined when the power P to the cavity is very small, that is for $\sigma(ij)$, equation (6*a*), approximately zero and $S(ij)$ very nearly unity. These approximations do not make Q_p equal to Q_0 but they do simplify all relations in such a way that the equation of the line AB can be found as a function of α. When the power to the cavity is large, the parameter $\sigma(ij)$ is large and the saturation factor $S(ij)$ approaches zero; in consequence the parameters of the empty cavity Q_0, β_0, and K_0 are excellent approximations for Q_p, β_p, and K_p. The resultant equations are simple enough to permit the determination of the straight line CD and hence to determine P_I, the actual power (not its logarithm) appropriate to a perpendicular dropped from the point I to the axis of abcissae.

The analysis shows that in terms of the power P_I

$$W(ij) = \Lambda(2T_2(ij)\,V(ij)/H_{rf}^2\,g(H)_{ij})\,K_0 P_I. \tag{9}$$

The multiplier Λ is a function of the crystal constant, α, and the cavity coupling constant β_0. Figure 2 represents a graph of the values of Λ plotted against the composite variable $\alpha/(1+\beta_0)$. Four lines appear on the graph corresponding to the four subcases appropriate to a Lorentz or Gaussian model and to $S(ij)$ invariant or variable with modulation.

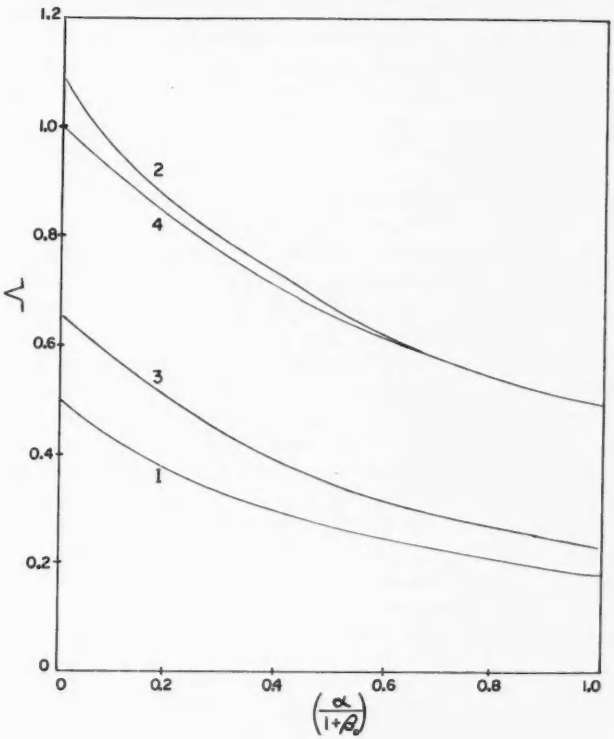

FIG. 2. The multiplier, Λ, from equation (9) plotted as a function of the variable α, equation (7*b*), and β_0 the coupling constant for the empty cavity. The curves are plotted for different models: (1) Gauss, $S(ij)$ invariant; (2) Gauss, $S(ij)$ variable; (3) Lorentz, $S(ij)$ invariant; (4) Lorentz, $S(ij)$ variable.

In order to improve the accuracy of the measurements, experimental points should be fitted by a theoretical curve in order to determine the location of the line AB and the location and particularly the slope of the line CD (see Fig. 1). This has been done with the approximate theoretical curves ($\alpha = 0$) which were available to the authors. It is from the fit and shape of these curves that conclusions have been drawn about whether or not the saturation factor $S(ij)$ was to be regarded as a constant or a variable with modulation.

PULSE MEASUREMENTS

The same argument that has been used in connection with saturation measurements shows that, provided $\sigma(ij)$ is large, the pulse measurements correspond to the decay of saturation. This restriction requires that the decay curve be fitted in its earlier portion for not too many time constants after the termination of the saturating pulse.

All pulse data correspond to a single relaxation time. It is possible that later slow relaxation processes have been missed but since the circuits were operative 15 microseconds after the termination of the saturating pulse, it is unlikely that there were unobserved fast, initial relaxations.

EXPERIMENTAL RESULTS FOR $T_2(ij)$, THE SPIN-SPIN RELAXATION TIME

In line-shape measurements, errors were avoided by picking crystals of such weight, in relation to the concentration of the paramagnetic ions, that there were too few spins to make necessary a correction for the reaction of the spins on the microwave cavity. In all measurements of line shape except one (on a ferricyanide sample) the spectrometer was operated so that the recorder traced line shapes rather than derivatives.

There are available two methods for determining the value of T_2 to be associated with an experimental line. The direct application of the definitions contained in equations (4*a*) and (4*b*) require that the area under the curve be measured with a planimeter; the error in this method may not be negligible if the line exhibits wide wings whose areas are difficult to determine. As a second method, the normalized Lorentz and the normalized Gaussian line shapes may be fitted at (for example) the half-height of the normalized experimental curve. This procedure has the advantage of not requiring a determination of the area under the wings but is approximate since few experimental lines fit the models with precision. The result of both procedures applied to potassium chromicyanide appears in Table II.

TABLE II

Expressions for T_2

Transition	(1–2)	(2–3)	(3–4)
$T_2 = g(H_0)/2$	$2.9C^{-0.55}$	$6.8C^{-0.55}$	$2.9C^{-0.55}$
Lorentz model	$1.9C^{-0.63}$	$5.6C^{-0.63}$	$1.9C^{-0.63}$

Results measured for potassium chromicyanide, when the *c*-axis was parallel to the static magnetic field and the temperature was 4.2° K. The entry expresses $T_2(ij)$ in units of 10^{-4} seconds. The measured magnetic concentration C is to be expressed in per cent and the table is valid for $0.06 \leqslant C \leqslant 1.5$. At the lowest concentration the half-width in magnetic field was $\Delta H(1,2) = \Delta H(3,4) = 10.5$ oersteds; $\Delta H(2,3) = 3.95$ oersteds.

The statements in Table II are to be regarded as predicting a mean value for T_2 appropriate to a concentration C. The average deviation in the experimental results for each of the measured concentrations was ± 2 and in consequence the following statement is typical of the meaning of any entry:

$$T_2(2,3) = (6.8C^{-0.55} \pm 2) \times 10^{-9} \text{ seconds.}$$

Precision is expressed, using average deviation, in this manner in connection with experimental results that appear elsewhere in this report.

It will be observed that results by the two methods overlap in view of the limits set by errors. In the process of fitting the experimental shapes, it was observed that when the concentration was below 1% the experimental shapes

approximated that of Lorentz. The higher concentrations departed from the Lorentz shape but could not be fitted by a Gaussian line.

Bleaney and Ingram (1951) measured the line width of cobalt tutton salt as a function of concentration; they have reported that the line reached an approximately constant width for all nominal concentrations below 0.1% and have suggested that the limiting width is set by the magnetic moment of the protons. It is interesting to note that in Table II there is no indication that a constant width is being approached, probably because of the small magnetic moment associated with the CN radicals.

Castle, Chester, and Wagner (1960) have measured the line widths associated with the (2–3) transition in dilute chromicyanide for measured concentrations ranging from 0.06% to 1.9%. For many of the samples, the line was found to be Lorentzian out to three line widths. The line width increased with concentration even at the lowest concentrations. Evidence in their experiment suggests that the line is broadened inhomogeneously. The line widths of samples of the same concentration but from different sources were different from each other by ratios of more than 2:1. For purposes of comparison, using a Lorentzian model, the authors of the present paper have expressed the results of Castle *et al.* in the same form as that used in Table II; the result is displayed for comparison in Table III.

Swarup (1959) has made a study of the line shapes to be associated with the resonances in dilute chromicyanide. Most of the nominal concentrations are greater than have been considered in the present paper and further an error was made in reporting the measured concentrations which was later corrected; the relation between nominal and measured concentration, after correction, is not the same as the results in Table I of the present paper. Swarup finds $\Delta H(34)$ to be nearly the same as $\Delta H(12)$ and both of these to be somewhat greater than $\Delta H(23)$. Marr and Swarup (1960) report values of $T_2(23)$ for three nominal concentrations of chromicyanide. The present authors have assumed that the nominal and measured concentrations are related as in Table I and on this basis have converted the Marr and Swarup results into the form displayed in Table III.

TABLE III

Comparison of various measurements of $T_2(23)$ for $K_3Cr(CN)_6$

Author	$T_2(23)$ seconds
Castle, Chester, and Wagner	$5.4C^{-0.44}\times10^{-9}$
Marr and Swarup	$7.5C^{-0.43}\times10^{-9}$
KSVW (Lorentz model)	$(5.6C^{-0.63}\pm2)\times10^{-9}$
KSVW ($g(H_0)/2$)	$(6.8C^{-0.55}\pm2)\times10^{-9}$

The measurements by several authors have been converted to comparable form by (KSVW).

In Table IV are listed the measured values of T_2 for ferricyanide; the values were computed from the experimental lines using the Lorentzian approxi-

mation. Values of $T(23)$ for chromicyanide computed from a Lorentz model are given for comparison.

TABLE IV
Values of T_2

Concentration, %	T_2 in units of 10^{-9} seconds	
	$K_3Fe(CN)_6$	$K_3Cr(CN)_6$
0.2	14±1	15±2
0.4	6.2±1	8.6±2

EXPERIMENTAL RESULTS FOR $W(ij)$, THE EFFECTIVE, LATTICE-INDUCED TRANSITION PROBABILITY

Both pulse and saturation measurements of $W(ij)$ have been made on potassium chromicyanide. A very marked change in $W(ij)$ for the higher concentrations suggests the appearance of a new relaxation mechanism; accordingly, the results are reported separately for the range of concentrations 0.49% and less and for a concentration of 1.5%. In the region of lower concentrations, it has not been possible to identify any pattern in the results which would lead to the statement that one transition behaves in a manner different from the others; for this reason all values of $W(ij)$ have been averaged into a single W and the value of this parameter is taken to be representative of all transitions.

Within the precision of the pulse measurements, relaxation in the range of concentrations from 0.061% to 0.49% is characterized by a single time constant and this time constant is independent of concentration. The value of W calculated from the pulse measurements is:

$$W = 65 \pm 7 \text{ sec}^{-1}.$$

In applying saturation analysis to the low concentration measurements, it was necessary to decide on a model line shape and also to decide whether or not, at a modulation frequency of 200 c.p.s., the saturation factor varied with the modulation. Line-shape studies have shown that the best approximation is the Lorentz line. In order to decide the question concerning the saturation factor, experimental results were fitted to theoretical curves and the excellence of fit given a score; the evidence was about two-to-one in favor of a saturation factor, $S(ij)$ invariant at the modulation frequency. Subject to these decisions the value of W was found to be:

$$W = 64\ C^{0.28} \pm 10 \text{ sec}^{-1}.$$

In this relation, C is the measured concentration and the relation is known to apply over the range of concentration expressed by $0.06\% \leqslant C \leqslant 0.49\%$.

There is as yet no explanation for the fact that the pulse measurements yield a value of W which is independent of concentration while the saturation measurements indicate a small but unmistakable dependence on concentration.

The measurements on samples containing 1.5% chromicyanide are summarized in Table V.

There are three reasons why the Lorentz and Gauss assumptions, applied to saturation data, lead to the different values of $W(ij)$ displayed in Table V,

TABLE V

Values of $W(ij)$ for $K_3Cr(CO)_6$

Transition	Pulse measurements	Saturation measurements		
			Dependence of $S(ij)$ on modulation	
		Model	Invariant	Variable
(3–4)	460	Lorentz	240	770
		Gauss	190	970
(2–3)	450	Lorentz	470	1800
		Gauss	380	2000
(1–2)	190	Lorentz	380	1200
		Gauss	270	1200

Values of $W(ij)$ in units of sec^{-1} for potassium chromicyanide in a concentration of 1.5%. The crystals were at a temperature of 4.2° K and were oriented with the c-axis parallel to the static magnetic field. $H(rf)$ was parallel to the b-axis of the crystal; transition probabilities $W(ij)$ correspond to this arrangement. Saturation results have been analyzed subject in turn to each of the four possible ideal assumptions concerning the experiment.

although the differences are not as great as might have been supposed. The greatest difference arises in the value chosen for P_I because of the different shapes of the theoretical curves which were used to fit the experimental data in the manner shown in Fig. 1. Less important are the different values of Λ obtained from Fig. 2 and the different values of T_2 which resulted from fitting the experimental line shapes with either a Lorentz or Gauss model.

The pulse measurements of $W(ij)$ are considered to be the most reliable, partly because no assumptions are required and partly because the measurements are so rapid that instrumental instabilities have little effect on the result. All the results, including the pulse measurements, were repeated on different days; it is believed that there is good justification for reporting that, at a concentration of 1.5%, the (1–2) transition does not respond in the same manner as do the other two.

Comparable data on chromicyanide have been published by Marr and Swarup (1960) and by Castle, Chester, and Wagner (1960). Marr and Swarup have reported that, in nominal concentrations of 0.1% and 0.5%, the spin–lattice relaxation time, T_1, of chromicyanide is a function of the power used in saturating the salt. The authors of the present paper have not been able to repeat this result; $W(ij)$ appears to be independent of the saturating power. Values of W computed from the Marr and Swarup, thermal-equilibrium, spin–lattice relaxation time (which they call T_1°), are all higher than are reported in the present paper and this is particularly true for their nominal concentration of 1.0%.

Castle, Chester, and Wagner (1960) report an increase in the rate and a marked change in the nature of the recovery in passing from a measured concentration of 0.5 to 1.0% Cr^{3+} ion. Values of $1/T_1$ appropriate to 4.2° K can be picked for two concentrations from their Fig. 6: for a concentration of

0.06%, $1/T_1$ is reported to be about 180 and for a concentration of 0.4% to be 200 sec^{-1}, thus indicating a very slow increase in $1/T_1$ with concentration. In the present results, for low concentration W has been found to be 65 sec^{-1}, which yields for comparison a somewhat lower value of 130 sec^{-1} for $1/T_1$.

Potassium ferricyanide relaxes very rapidly; measurements have shown that T_1 for chromicyanide is about 30 times as great as that for ferricyanide. This rapid relaxation has made measurements difficult and has led the writers to be suspicious of the accuracy of the experimental results on this salt. The results in Table VI are to be regarded as order-of-magnitude figures; until further work is reported no great significance should be attached to the fact that W for the higher concentration is smaller than W for the lower concentration. These measurements were made by the saturation method. The fit of the theoretical curves suggests that the saturation factor, S, did not vary with the field modulation.

TABLE VI

Values of W for $K_3Fe(CN)_6$

Concentration, %	Dependence of S on modulation	
	Invariant	Variable
0.2	2200±660	6500±2100
0.44	960±360	3100±1400

Values of W in units of sec^{-1} for potassium ferricyanide. The crystals were at a temperature of 4.2° K and were oriented with the b-axis parallel to the static magnetic field. The direction of $H(rf)$ was parallel to the c-axis of the crystal and the transition probability, V, was calculated for this arrangement. A Lorentz line has been assumed.

Bray, Brown, and Kiel (1960) have reported, briefly, on pulse measurements of T_1 for ferricyanide at temperatures between 2.6 and 4.2° K. The concentration of the sample is not mentioned in their abstract. They suggest that at a temperature of 4.2° K the Raman process is dominant. They find that the relaxation process is characterized by two relaxation times; it is possible that the uncertainties associated with the measurements in Table VI are related to this result of Bray *et al.*

DISCUSSION

The main purpose of this paper has been to report and collate experimental measurements; a second purpose has been to examine the relation between pulse and saturation measurements. The results give support to the idea that in a concentration of 1.5%, the Cr^{3+} ion in a cyanide environment relaxes by way of some mechanism which is not present or at least not dominant when the concentration is 0.5% or less. It would appear that if the results are to be understood, separate theories corresponding to the two different ranges of concentration are required.

It may be supposed that the mechanisms are different in the two ranges of concentration because of differences in the amount of coupling throughout the spin system. For the higher concentrations, the spins constitute one thermo-

dynamic system, the lattice another; relaxation is a co-operative phenomena. For the lower concentrations, to a first approximation, the paramagnetic ions are completely uncoupled from each other; each ion is on its own and relaxes to the lattice as an individual. This idea as it has appeared in the literature has been surveyed by Woonton in a review article to be published (written in the spring of 1960 and containing references only up to that time).

For the lower range of concentrations, Kittel (1958) suggested a form for coupling between the individual spins and the lattice. Mattuck and Strandberg (1960) worked out a detailed analysis of this type of coupling. Shiren and Tucker (1961) have produced experimental evidence which tends to validate the theory. The operator, $\mathscr{H}$, which Mattuck and Strandberg have called the spin–lattice Hamiltonian can be used to yield values of the lattice-induced transition probabilities such as $U(ji)$. Among other terms, the leading term of $\mathscr{H}$ is the anticommutator of the effective spin operators. This leading term applied to the wave functions of ferricyanide yields matrix elements which are identically zero, but this is not true in the case of chromicyanide. From this fact it must be concluded that it is unsafe to attempt to extrapolate the behavior of one salt as an explanation of phenomena related to the other.

The leading term of the Mattuck and Strandberg operator applied to the wave functions of chromicyanide yields very small values for $U(2,3)$, $U(3,2)$, $U(1,4)$, and $U(4,1)$. It had been hoped that differences in the values of $W(ij)$ might appear because of these differences in the U's; it has been shown that within experimental error, the values of the W's are all the same and so no specific statements can be made yet about the U's by the methods reported in this paper. It is now clear that the experiments should have been arranged so that the forbidden transitions could have been measured.

Van Vleck (1960, p. 398) has discussed ideas which apply in the range of higher concentrations: irregularities in the lattice constitute localized centers of very rapid relaxation which form a strong coupling between the lattice and the spin system. Van Vleck explains that by irregularities he means unusual situations for the paramagnetic ions such that an ion experiences an unusual stark splitting or that the ions happen to be in close-spaced groups of three or more, resulting in "exchange pockets". As Van Vleck says, "There is the difficulty of getting enough energy transport from the average atom to one which is a fast relaxer. The intermediary for doing this would have to be dipolar coupling". Van Vleck and others have suggested that the coupling mechanism is cross relaxation as worked out by Bloembergen *et al.* (1959). The experiments of Castle, Chester, and Wagner (1960) reinforce this suggestion. Presumably the region of concentrations over which the mechanism of relaxation changes could be controlled by varying the orientation of the crystal with respect to the static magnet field, thus controlling the onset of strong cross relaxation.

ACKNOWLEDGMENTS

The authors take pleasure in acknowledging the support given to this research by the Defence Research Board, through grant DRB 9512–20, and by the National Research Council, through grant T-127, to one of us (G. A. W.).

Two of us (P. W. S. and J. V.) wish to acknowledge awards from the National Research Council. Prof. G. W. Farnell designed and built the pulse apparatus and suggested the method that has been used in the analysis of saturation data. The authors acknowledge their indebtedness to Prof. J. A. Carruthers, who designed and built the NMR apparatus for field measurements and provided us with specimens. Mrs. Hilary Hayden carried out the chemical analysis of the crystals. Throughout the research, the help in the construction of equipment provided for us by Mr. V. Avarlaid and his assistants has been invaluable.

REFERENCES

ANDREW, E. R. 1956. Nuclear magnetic resonance (Cambridge University Press, London and New York).
BAKER, J. M., BLEANEY, B., and BOWERS, K. D. 1956. Proc. Phys. Soc. London, **69**, 1205.
BLEANEY, B. and INGRAM, D. J. E. 1951. Proc. Roy. Soc. London, A, **208**, 143.
BLEANEY, B. and O'BRIEN, M. C. M. 1956. Proc. Phys. Soc. London, **69**, 1216.
BLOEMBERGEN, N., SHAPIRO, S., PERSHAN, P. S., and ARTMAN, J. O. 1959. Phys. Rev. **114**, 445.
BOWERS, K. D. and OWEN, J. 1955. Repts. Progr. in Phys. **18**, 310.
BRAY, T. M., BROWN, G. C., and KIEL, A. 1961. Bull. Am. Phys. Soc. Ser. II, **6**, 233.
BUTCHER, P. N. 1957. Electron Tube Laboratory, Tech. Rept. No. 155–1, Stanford Electronics Laboratories, Stanford, California.
CASTLE, J. G., CHESTER, P. F., and WAGNER, P. E. 1960. Phys. Rev. **119**, 953.
CHANG, W. S. and SIEGMAN, A. E. 1959. Electron Tube Laboratory Tech. Rept. No. 156–1, Stanford Electronics Laboratories, Stanford, California.
FEHER, G. 1957. Bell System Tech. J. **36**, 449.
KIPLING, A. L. 1961. M.Sc. Thesis, Dept. of Physics, McGill Univ., Montreal. Unpublished.
KITTEL, C. 1958. Phys. Rev. Letters, **1**, 5.
LLOYD, J. P. and PAKE, G. E. 1954. Phys. Rev. **94**, 579.
MARR, G. V. and SWARUP, P. 1960. Can. J. Phys. **38**, 495.
MATTUCK, R. D. and STRANDBERG, M. W. P. 1960. Phys. Rev. **119**, 1204.
MEYER, J. W. 1955. Lincoln Laboratory, Group Report M35–46, Mass. Inst. of Tech.
SANDELL, E. B. 1959. Colorimetric determination of traces of metals (Interscience Publishers Inc., New York).
SHIREN, N. S. and TUCKER, E. B. 1961. Phys. Rev. Letters, **6**, 105.
SWARUP, P. 1959. Can. J. Phys. **37**, 848.
VAN VLECK, J. H. 1960. Quantum electronics, *edited by* C. H. Townes (Columbia Univ. Press, N.Y.).
WOONTON, G. A. 1962. Advances in electronics and electron physics, Vol. XV (Academic Press, New York and London), p. 163. To be published.

ROCKET MEASUREMENTS OF AURORAL RADIO ABSORPTION[1]

W. J. Heikkila and S. R. Penstone

ABSTRACT

Three Black Brant rockets were instrumented by the Radio Physics Laboratory of the Defence Research Board to measure ionospheric radio absorption during ionospheric disturbances. This instrumentation included v.h.f. receivers to measure the strength of cosmic radio noise and of radio signals from the ground during the flight. Geiger counters were provided by the National Research Council of Canada to measure the flux of energetic particles. Results from a flight made at dawn on October 28, 1960, during auroral absorption, indicate that most of the absorption at 22 Mc/s occurred at an altitude between 65 and 90 km, with the most intense absorption occurring in the 70- to 75-km region. This observation is consistent with the observation made by N.R.C. of increasing numbers of electrons with energies greater than 30 kev above about 74 km, both during the ascending and the descending portions of the flight. Assuming large horizontal extent of the absorbing regions, the rocket measurement of 11.5 db of total absorption at 22 Mc/s along an oblique path at 60° from the zenith agrees closely with the 30 Mc/s zenith riometer observation of 3.3 db.

I. INTRODUCTION

For several decades abnormal absorption of high-frequency radio waves has been observed on communication circuits, and by means of ionospheric soundings during so-called radio black-outs. In recent years widespread observations by means of riometers have greatly increased our knowledge of such absorption. This instrument has permitted quantitative observations of the intensity of absorption, because the intensity of v.h.f. cosmic radio noise can be monitored continuously, and decreases below the normal level are a direct measurement of ionospheric absorption. Such riometer observations have permitted classification of absorption events into several distinct types, as indicated by Reid and Collins (1959). Their types II and III, now better known as auroral absorption (AA) and polar-cap absorption (PCA), are of special importance at high latitudes. The PCA events occur only a few times a year even at times of sunspot maximum (Collins *et al.* 1961), but when one occurs, communication circuits are usually disrupted for several days. Energetic protons emitted from solar flares are thought to be the primary agent producing the event. Auroral absorption events are much more frequent, but they are short-lived, with absorption lasting only some minutes or tens of minutes. Energetic electrons are thought to produce this type of ionospheric absorption.

Detailed information on the characteristics of the absorbing regions is difficult or impossible to obtain by means of ground-based equipment. In particular, the height profiles of absorption and the energy spectra of the incident particles are two details that are essential to a good understanding of the absorption events. A program of rocket measurements of ionospheric radio

[1]Manuscript received September 18, 1961.
Contribution from the Radio Physics Laboratory, Defence Research Telecommunications Establishment, Ottawa, Canada.

wave absorption has been undertaken by the Defence Research Telecommunications Establishment (D.R.T.E.), in an attempt to obtain such information by measurements made in the ionosphere.

Three Black Brant I rockets were launched at Fort Churchill, Manitoba (lat. 59° N., long. 94° W.), during October 1960. These were instrumented by D.R.T.E. for radio observations which will be described in this paper, and by the National Research Council for energetic particle observations, which are reported in a companion paper by McDiarmid, Rose, and Budzinski of N.R.C.

The instrumentation was designed primarily for the study of a major PCA event. Unfortunately no suitable event occurred from early in July 1960 to late October while the rockets were being held in readiness at the range. In October it was decided to use the rockets for studies of the more frequent auroral absorption events before the onset of winter would prevent firings from the outdoor launcher. The results of the measurements on ionospheric radio wave absorption obtained on the most successful of the three flights are described in this paper.

II. INSTRUMENTATION

Very high frequency radio receivers were carried in each rocket for the study of ionospheric absorption as a function of height. One of these, at 21.77 Mc/s, was used to measure the signal strength of a modulated c.w. transmission from the ground. Another at 30 Mc/s was of sufficient sensitivity to detect cosmic radio noise. Both receivers were connected through a duplexing network to a pair of folding antennas measuring 117 inches from tip to tip when deployed. A logarithmic detector was used in each receiver, and each detector output was fed to one channel of a multichannel FM–FM telemetry system.

Aspect information was obtained from both solar and magnetic aspect units. An S-band radar beacon was used for tracking. Other auxiliary instrumentation, as well as prototype experimental packages, also were included in the nose cone but will not be described here.

The rocket used was the Black Brant I, a 17 in. diameter single stage solid fuel rocket developed in Canada by the Canadian Armament Research and Development Establishment at Valcartier, Quebec.

III. RESULTS

On October 24 strong geomagnetic activity began with a sudden commencement. This was accompanied by intense aurora, a cosmic-ray Forbush-type decrease, and sporadic auroral absorption. The rocket designated D.R.T.E. 05 was held in readiness for about 10 hours at $X-3$ minutes on the mornings of October 26 to 28. On the third morning the riometers indicated a strong auroral absorption event, and the rocket was fired at 1221 hours U.T. The flight was made just before dawn with the earth's geometrical shadow cutting the descending part of the rocket trajectory at 38-km altitude. Unfortunately, a malfunction of the folded rocket antenna during the upward leg of the flight reduced the receiver sensitivity too much to permit measurements during the

ascent. However, during the flight the power of the ground transmitter was increased to compensate for this loss of sensitivity and absorption data were obtained with the 22 Mc/s system while the rocket was descending through the ionosphere.

Data from two ground-based 30 Mc/s riometers, with antennas directed respectively at the celestial pole and the zenith, are plotted in Fig. 1. The time of the rocket flight is also indicated. The polar riometer (Fig. 1*a*) indicated a fairly steady absorption of almost 3 db. The zenithal riometer (Fig. 1*b*)

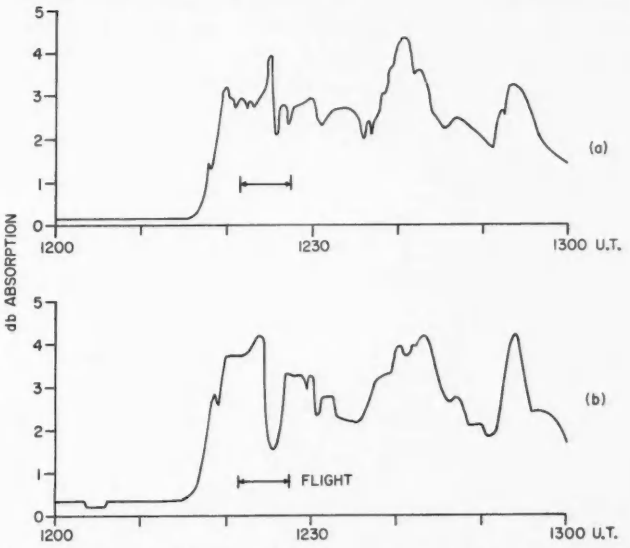

FIG. 1. Absorption records from 30-Mc riometers at Fort Churchill near time of flight. The upper record (*a*) is from a riometer directed at the celestial pole; the lower record (*b*) is from a riometer directed at the zenith. The time of the flight is indicated by the horizontal arrows.

indicated about 3.8 db of absorption at the beginning of the flight, a reduction of at least 2 db for about one minute during the flight, then an increase in absorption to approximately 3.3 db. The direction of the transmission to the rocket on the descent was approximately 60° from the zenith.

While the rocket descended from 90 km to 68 km, the signal strength increased by approximately 11.5 db, after which the receiver ceased to operate. This increase in signal was almost entirely due to the decreasing ionospheric absorption as the rocket penetrated the absorbing region, since corrections for antenna gain variations with orientation, and the inverse square law variation with distance, were negligible during the period of the measurement. When corrected for the obliquity of the transmission, the observed change in signal strength implied a total vertical absorption at 21.77 Mc/s of 5.8 db between 90 km and 68 km. If an inverse square dependence of absorption on

frequency is assumed, this is equivalent to 3.1 db of absorption at 30 Mc/s, again above the 68-km level. This may be compared with the 3.3 db shown by the zenithal riometer, provided that the observed absorbing region was uniform over a sufficiently large area that it covered all the significant portion of the riometer antenna beam, as well as the rocket trajectory, that is, over a region whose dimensions were of the order of 100 km or more.

The height profile of absorption in decibels per kilometer deduced from this data is shown in Fig. 2. The outstanding feature is the thin layer of intense absorption, approaching 1 db per km in the region 73 to 75 km. Below 74 km the absorption falls steadily to 0.2 db per km at 68 km. Below that, the receiver became inoperative, and no estimates of absorption can be made at lower heights.

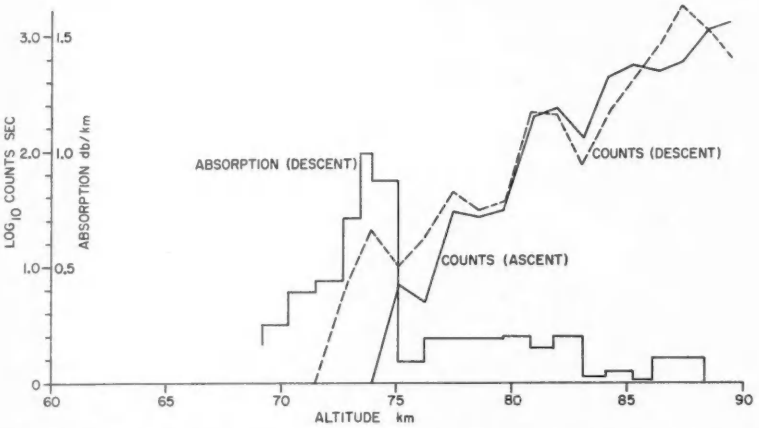

FIG. 2. Vertical absorption profile, measured at 21.77 Mc during the descending portion of the rocket trajectory. Also shown is the counting rate of electrons with energies greater than 30 kev during both the ascent and descent.

Above 75 km there appears to be a sharp decrease in absorption; the values do not exceed 0.2 db per km up to an altitude of 90 km. Above 90 km the absorption was not detectable. The experimental error is generally of the order of 1/8 db per km, but is not constant over the whole region because of departures from a logarithmic law in the receiver output characteristic.

The 30 Mc/s receiver was also affected by the antenna malfunction mentioned above. However, a weak indication of cosmic radio noise was obtained above 88 km, which vanished at lower altitudes, coincident with the initial increase in 21.77 Mc/s signal during the descent.

The counting rate for electrons with energies greater than 30 kev as measured by the N.R.C. equipment is also shown in Fig. 2 for both ascent and descent. The cyclical variation in counting rate is due to the spin of the rocket. The absorption peak at 74 km was undoubtedly due to the secondary electrons produced by the energetic primaries, since the primaries penetrated down to about that height.

Since the flight was made at dawn it is not known whether there was any visible aurora associated with the absorption.

From the measured rate of attenuation it is possible to deduce the values of electron density that would be required to produce this absorption if appropriate values of collision frequency are assumed. Making use of the collision frequencies due to Nicolet (1959), and substituting into the Appleton-Hartree equation the absorption data from Fig. 2, an approximate profile of electron density versus altitude is obtained. This is shown in Fig. 3, where

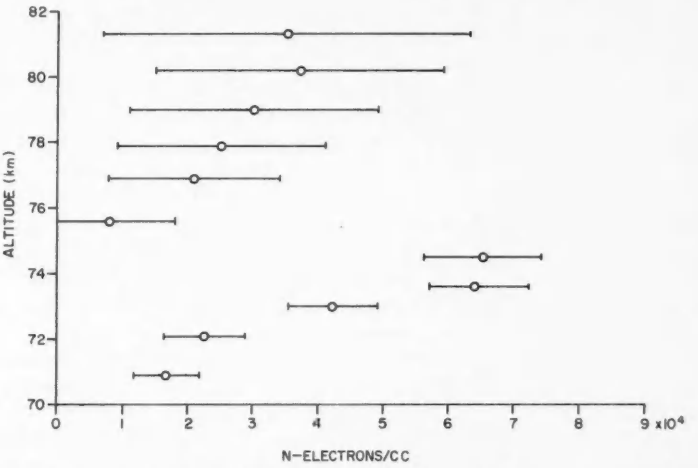

FIG. 3. Electron density profile deduced from the absorption profile, using the Appleton-Hartree equation and assumed values of collision frequency.

the horizontal bars indicate the estimated error in the values. The uncertainties in the computation become very large with increasing altitude, because of the smaller observed absorption, and the decreasing reliability of measurement.

The thin layer of intense ionization between 73 and 75 km is related to the observed sharp peak in the absorption profile shown in Fig. 2, and the deep minimum follows from the weak absorption at 76 km.

IV. DISCUSSION

The failure of the 21.77 Mc/s receiver to operate properly below 68 km leaves the question of the intensity of absorption below that height unanswered, at least directly. However, the total absorption of 3.3 db at 30 Mc/s shown by the zenithal riometer agreed closely with the integrated absorption of 3.1 db at 30 Mc/s inferred from the rocket data above 68 km. This agreement implies that if any appreciable absorption had occurred below this height, then the absorbing region detected in the rocket experiment must have been quite patchy, so as to leave gaps through which the riometer could receive some cosmic radio noise.

The observations made by N.R.C. showed energetic electrons penetrating down to about 74 km. Numerically, the flux at each height was the same during the ascent and the descent, at times when the riometer readings were roughly comparable. The existence of a patchy structure for the strongly absorbing regions, and hence presumably for the local energetic electron clouds, would have required that, by coincidence, the rocket traversed regions of equal intensity on the ascent and the descent, missing regions of lesser or greater intensity.

While these are not conclusive arguments, they do suggest that the region of strong absorption at 70–75 km was a uniform blanket with horizontal dimensions in excess of 100 km. This picture is consistent with that suggested by Chapman and Little (1957). According to their reasoning the incident primary particles may stream along rays aligned with the geomagnetic field lines. As they penetrate lower, they are scattered by collisions, and the stream is spread considerably. The rapid variation of atmospheric density with height, with a scale height of about 6 km, permits particles travelling nearly horizontally to travel much further than particles travelling down. Any intermediate X rays would tend to spread the low level ionization even further, albeit rather thinly. Consequently, the absorption along any ray path through the ionosphere, such as the transmission path to the rocket in this particular case, can be explained as resulting from the total flux of incoming particles over a large region of the upper atmosphere.

We do wish to emphasize that we are not suggesting that no variations in the horizontal plane occur, but only that the scale of such variations must be many tens of kilometers. In fact, comparison of polar and zenithal riometer records, taken at the same station, has shown that at least north to south gradients occur. Even during the present rocket flight a large decrease in absorption overhead was not present to the same degree in the polar direction. This overhead decrease may have been related to the decreased flux of energetic particles detected at the same time in the rocket, which was then located some 100 km to the east of the riometer location, and above 100-km altitude.

The absorption profile we have determined can be explained by an increased electron density, as high as 6×10^4 electrons per cm^3, at 74 km. We feel that this value is an overestimate, since local increases in electron temperature or a significant high-energy tail in the number-energy distribution would result in higher collision frequencies, especially if the collision frequency depends on the electron energy (Crompton *et al.* 1953; Phelps and Pack 1960), and v.h.f. absorption is determined essentially by the product of electron density and collision frequency. These effects would not be likely to alter our conclusion that a thin layer of rather high electron density existed at 73–75 km during this event, although this may not be typical of all AA events. The thinness of this layer is difficult to explain in terms of the ionization by energetic particles (McDiarmid *et al.* 1961). Further rocket experiments will be conducted in this line of investigation.

ACKNOWLEDGMENTS

We wish to express our appreciation to the many individuals and organizations, too numerous to mention individually, whose assistance was essential in the carrying out of this rocket program.

REFERENCES

CHAPMAN, S. and LITTLE, C. G. 1957. J. Atmospheric and Terrest. Phys. **10**, 20.
COLLINS, C., JELLY, D. H., and MATTHEWS, A. G. 1961. Can. J. Phys. **39**, 35.
CROMPTON, R. W. *et al.* 1953. Proc. Roy. Soc. A, **218**, 507.
MCDIARMID, I. B., ROSE, D. C., and BUDZINSKI, E. E. 1961. Can. J. Phys. **39**. This issue.
NICOLET, M. 1959. Phys. Fluids, **2**, 95.
PHELPS, A. V. and PACK, J. L. 1960. Phys. Rev. Letters, **3**, 340.
REID, G. C. and COLLINS, C. 1959. J. Atmospheric and Terrest. Phys. **14**, 63.

POLAR-CAP ABSORPTION FOLLOWING THE SOLAR FLARE OF JULY 16, 1959[1]

SYED ZIAUDDIN[2]

ABSTRACT

The polar-cap absorption event following the solar flare of July 16, 1959, is examined. Short-term recoveries of the cosmic noise level, associated with auroral disturbances, were observed at Saskatoon and Ottawa during the PCA event. It is suggested that these recoveries were due to a magnetic screening mechanism resulting from the interaction of the aurora producing plasma with the geomagnetic field.

I. INTRODUCTION

In polar regions the absorption of radio waves in the ionosphere sometimes increases sharply following a solar flare. These events, which have been called polar-cap absorption (PCA) events because they seem to be confined to geomagnetic latitudes above about 62°, have been studied in some detail (Little and Leinbach 1958; Bailey 1959; Reid and Collins 1959). The usual method of measuring the ionospheric absorption is by means of a riometer which records the strength of extraterrestrial radio waves (cosmic noise). During July 1959, there were three major solar flares and it was noted by Reid and Leinbach (1960) that at least for the second and third flares the PCA events were observed at unusually low latitudes. The event following the flare of July 16, 1959, was observed at Saskatoon (geomagnetic latitude 61°) and the purpose of this paper is to point out some interesting features of this event.

II. THE PCA ONSET AND RECOVERY

The initiating flare of July 16 occurred at 2114 U.T. As is frequently the case with riometer records, it is not possible to determine accurately the time of onset of the PCA event because the solar noise associated with the flare obscured the records until about 2330 U.T. By this time the PCA event appeared to be in progress and the absorption continued to increase sharply until it reached a preliminary maximum between 2338 and 2353 U.T. Essentially the same maximum is shown in the records from Fort Churchill (not shown here), some 1000 kilometers to the north–east of Saskatoon. The main maximum as noticed on the original record was reached about 20 hours after the flare. The progress of the PCA event is shown in Fig. 1 where the absorption is plotted against time over a period of about five days. The constant cosmic noise level for part of the July 17 and 18 is more apparent than real and represents the limit of the dynamic range of the recorder.

[1]Manuscript received August 17, 1961.
Contribution from the Institute of Upper Atmospheric Physics, University of Saskatchewan, Saskatoon, Saskatchewan.
[2]On leave of absence from the University of Mysore, India; now at the National Research Council, Ottawa, Canada.

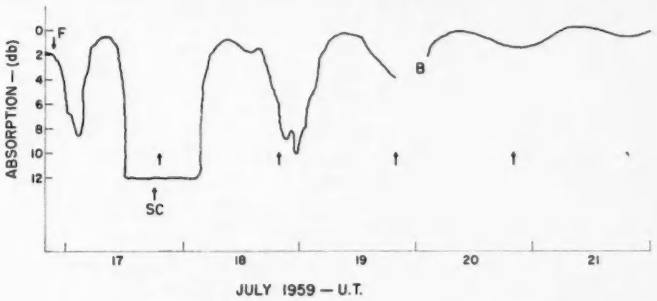

FIG. 1. Diurnal variation of cosmic noise absorption during July 17 to 21, 1959 (smoothed out for auroral absorption and radio noise). Arrows indicate local noon and F the flare associated with the PCA. SC is the sudden commencement and B indicates recorder failure. The constant cosmic noise level for part of July 17 and 18 is more apparent than real and is the limit of the dynamic range of the recorder.

III. TEMPORARY RECOVERIES OF COSMIC NOISE LEVEL DURING THE PCA EVENT

Superimposed on the relatively smooth diurnal variation of absorption during the PCA event are periods of rapidly fluctuating absorption. This behavior (called type II absorption by Reid and Collins) is characteristic of auroral disturbance and may be taken as evidence of the entry into the earth's atmosphere of "auroral" particles by difference in kind, number, or energy). A most interesting feature of the absorption records during the auroral disturbances was the partial recovery, during the early part of the disturbances, of the cosmic noise level. During these recoveries the cosmic noise level reached values well above those to be expected from the normal progress of the PCA event, but well below those to be expected in the absence of a PCA event.

In Fig. 2 are shown the riometer records from Ottawa and Saskatoon for the evening of July 17 (local time). The Saskatoon record was off-scale for most of the period but the occasional recovery is apparent. When there is no superimposed "type II" absorption or radio interference from terrestrial sources or the sun, the cosmic noise level during the progress of a PCA shows a smooth change in cosmic noise level, characteristic of distinct diurnal variation. This enables one to determine the expected level during the period of any superimposed disturbance during a PCA. From the Ottawa record it is seen that the cosmic noise level was above the expected level (indicated by the broken line) between the points B and A. Between A and C the cosmic noise level dips below the expected level for the first time. It is not clear from the record whether the auroral particles first entered the atmosphere during this period or were obscured during the earlier period (BA) by the recovery. In any case the partial recovery and the auroral disturbance seem definitely to be linked. In passing, it may be noted that the "recovery" is not due to interfering signals from distant terrestrial transmitters. Such interfering signals, reflected from auroral ionization, are received occasionally, but are characterized by a spiky record that differs markedly from those of Fig. 2.

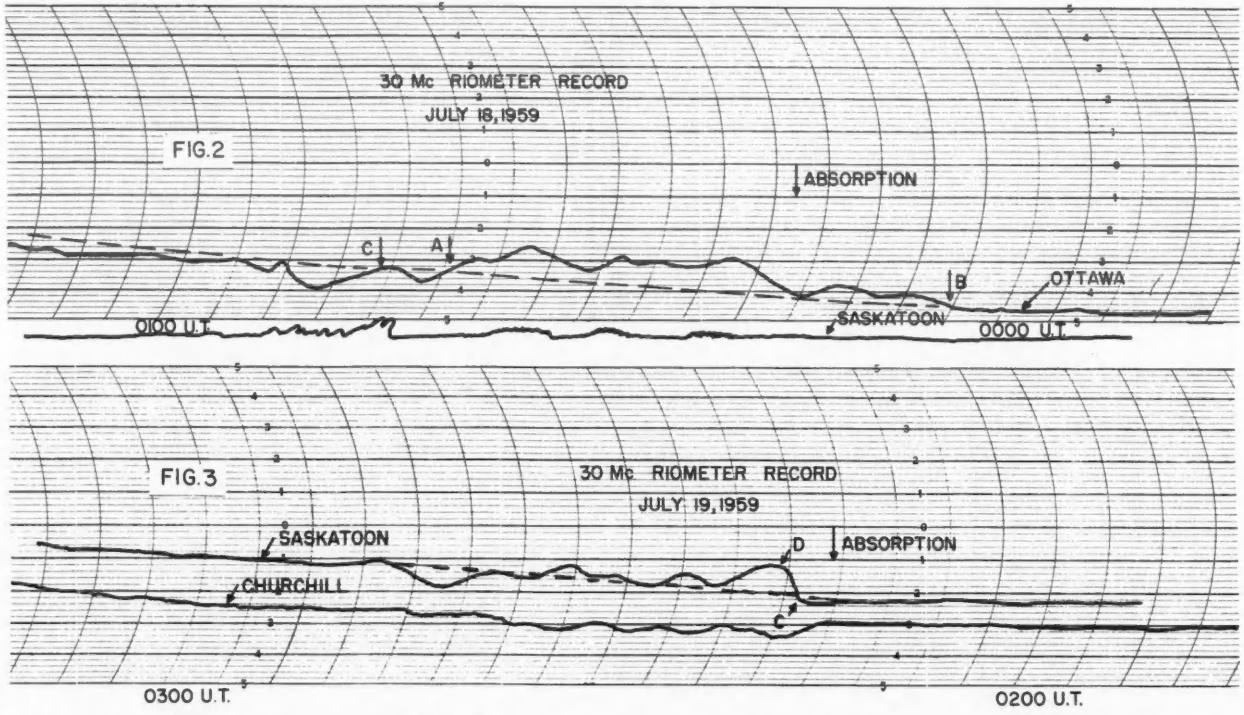

FIG. 2. Cosmic noise records from Saskatoon and Ottawa for July 18, 1959. B indicates the beginning of the increase of cosmic noise level and C the beginning of the auroral type absorption.

FIG. 3. Cosmic noise records from Saskatoon and Churchill for July 19, 1959. C indicates the beginning of the increase of cosmic noise level.

In Fig. 3 the riometer records from Fort Churchill and Saskatoon for a short period of the evening of July 18 are shown. The irregular auroral absorption is nearly coincident in time on the two records. This is typical of major auroral disturbances which are known, from radio studies, to occur simultaneously over large areas. There is some suggestion on the Saskatoon record that the auroral absorption actually started just before the first recovery which began at the point marked C and reached a maximum at D. The Fort Churchill record shows no clear evidence of a recovery.

Yet another recovery, this time during the daylight hours, is shown in Fig. 4. A sudden commencement occurred at the point marked A and the recovery reached its maximum value, both at Ottawa and Saskatoon, near the point marked B. The slight time discrepancy between the two maxima at B is no greater than the possible error in time-keeping between the two stations. For the events shown in Figs. 2 and 4 the Churchill record was off-scale.

Evidently, in all these recoveries, some form of screening of the particles causing the PCA event is involved. At least superficially, the phenomenon is similar to the Forbush decrease of cosmic-ray flux observed at times of greater solar events. The close association in time of the auroral disturbance and the recovery suggests that the screening must occur in the immediate neighborhood of the earth. Certain types of possible interactions between an approaching plasma of auroral particles and the geomagnetic field could lead to the observed recoveries. For example, in the case of the particular event shown in Fig. 3, a recovery was observed at the lower latitude (Saskatoon) but not at a higher latitude station (Fort Churchill). Such a recovery might be caused by a momentary compression of the earth's geomagnetic field. The confinement of the geomagnetic field within a cavity surrounding the earth, due to the presence of an approaching plasma cloud, has been studied by Obayashi and Hakura (1960). They show that the cutoff rigidity of incoming particles is shifted toward higher values as the boundary of the cavity approaches the earth. Table I shows their values of minimum rigidity for solar particles reaching the different latitudes under consideration, under varying degrees of compression of the earth's dipole field cavity.

Assuming that the differential spectrum of particles causing the PCA event does not change very much at the low-energy end and that Saskatoon was close to the lower latitude border of the PCA event, the variation of geomagnetic threshold would reduce the flux density of PCA particles at Saskatoon while the flux would remain nearly unaffected at Fort Churchill.

In the absence of a more complete observational description of the phenomenon it does not seem worth while to speculate further about the precise nature of the interaction between the plasma and the earth's magnetic field. More detailed observations of the kind reported here concerning some future event, combined with contemporaneous satellite information concerning the state of the Van Allen zones, might well lead to a better understanding of the PCA events.

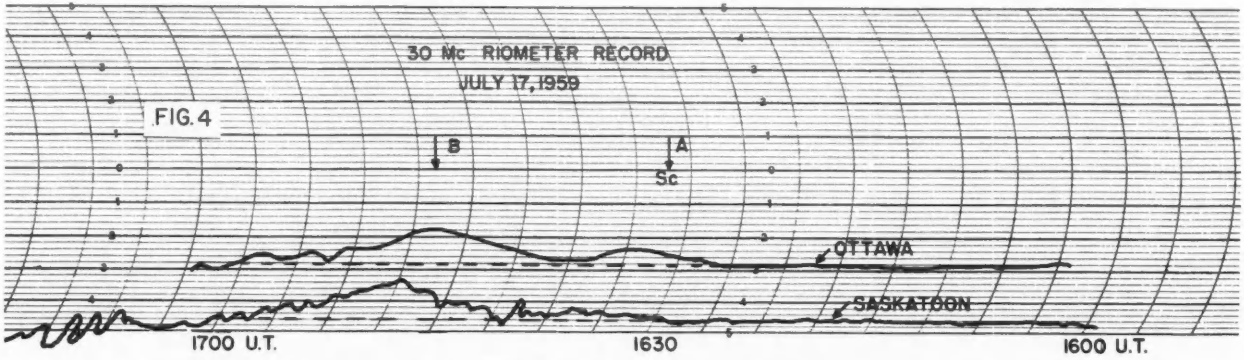

FIG. 4. Cosmic noise records from Ottawa and Saskatoon for July 17, 1959. A marks the sudden commencement and B, the maximum recovery of cosmic noise level.

TABLE I

Minimum particle rigidity required to reach Ottawa, Saskatoon, and Fort Churchill, for different degrees of compression of the earth's dipole cavity. R_0 is the radius of the cavity in terms of the earth's radius a

	Rigidity in units of 10^9 volts		
R_0	Ottawa, geomagnetic latitude 56°.4	Saskatoon, geomagnetic latitude 61°.2	Fort Churchill, geomagnetic latitude 68°.4
∞*	1.38	0.89	0.27
10 a	2.01	1.29	0.80
5 a	3.73	2.09	1.61
3 a	6.00	4.41	2.11
2 a	8.32	6.01	3.59

*Calculated from R (rigidity in volts) = $14.7 \times 10^9 \cos^4 \lambda$ where λ is geomagnetic latitude (Bailey 1957).

ACKNOWLEDGMENTS

Most of the work reported was carried out at the University of Saskatchewan where assistance was received under Defence Research Board Grant 9511-25 and National Research Council Grant T-123. The author is grateful to Professor P. A. Forsyth for very useful suggestions throughout the course of the work. This paper was completed while the author was holder of a postdoctoral fellowship at the National Research Council, Ottawa, where very helpful discussions were held with Dr. D. C. Rose. The cosmic noise data from Fort Churchill and Ottawa were made available through the generosity of Dr. T. R. Hartz and Dr. E. L. Vogan of the Defence Research Telecommunications Establishment.

REFERENCES

BAILEY, D. K. 1957. J. Geophys. Research, **62**, 431.
——— 1959. Proc. I.R.E. **47**, 255.
LITTLE, C. G. and LEINBACH, H. 1958. Proc. I.R.E. **46**, 334.
OBAYASHI, T. and HAKURA, Y. 1960. Space research, *edited by* H. K. KALLMAN BIJL (North-Holland Publishing Co.), p. 665.
REID, G. C. and COLLINS, C. 1959. J. Atmospheric and Terrest. Phys. **14**, 63.
REID, G. C. and LEINBACH, H. 1960. Geophysical Institute, College, Alaska, Report April 1960.

DIRECT MEASUREMENT OF CHARGED PARTICLES ASSOCIATED WITH AURORAL ZONE RADIO ABSORPTION[1]

I. B. McDiarmid, D. C. Rose, and E. Budzinski

ABSTRACT

A rocket experiment to study the charged particles associated with auroral radio absorption is described. A primary electron flux, probably in the form of beams or columns, with a maximum intensity of 2×10^6 particles cm^{-2} sec^{-1} was observed. The integral electron energy spectrum could be represented by exp $(-E/22$ kev) at energies above 30 kev. The angular distribution of the incident electrons was approximately isotropic over the upper hemisphere. Two other types of angular distributions, involving large intensities of upward-moving particles, were observed. The measured electron flux was sufficient to account for the observed radio absorption.

Protons in the energy range greater than 500 kev were recorded with a maximum intensity of 6×10^2 particles cm^{-2} sec^{-1} $sterad^{-1}$. The proton intensity was relatively steady and was not correlated with the electron flux either in space or in time. Most of the protons appeared to enter the atmosphere to the south of Fort Churchill.

I. INTRODUCTION

Charged particle detectors were carried in three Black Brant rockets launched at Fort Churchill (lat. 59° N., long. 94° W.) by the Defence Research Board. The rocket instrumentation was designed to study either polar-cap or auroral absorption events. The larger experiment in the rockets was designed by the Defence Research Board Telecommunications Establishment to measure absorption as a function of frequency and height; the results of this experiment are given in an accompanying paper. The secondary experiments being described here were designed to determine the nature and energy spectrum of the associated charged particles. Initially it was hoped to fire all three rockets, at different times, into the same polar-cap absorption (PCA) event. Unfortunately, no large PCA event occurred from early in July 1960 when the rockets were ready until late in October when the onset of winter made it desirable to either delay launching until spring or change the objective to studies of absorption and particles in much more frequent auroral events. The latter alternative was chosen and the three rockets were launched with varying degrees of success. The results of the measurements on energetic particles from the most successful of the three rockets are described in this report. The rocket was launched about sunrise on October 28, 1960.

II. INSTRUMENTATION

The particle detectors consisted of the following five units. Detector A was an Anton 223 end window Geiger counter located at the end of a cylindrical brass collimator (wall thickness 8 g/cm^2) which looked out through a hole in

[1]Manuscript received September 18, 1961.
Contribution from the Division of Pure Physics, National Research Council, Ottawa, Canada. A preliminary report of this work was presented at the Florence Symposium on Space Research in April 1961.
Issued as N.R.C. No. 6577.

the rocket skin; the half angle of the collimator was 6 degrees while the angle between the collimator and rocket axis was 90 degrees. The solid angle area factor defined by the collimator and counter was 10^{-2} cm^2 sterad for electrons with energies greater than 30 kev and protons greater than 500 kev. Detector B was identical with detector A except that a magnetic field of about 1000 gauss was applied across the collimator in such a way as to exclude electrons with energies less than 1.5 Mev while leaving the proton response the same as for A. These two detectors thus provided low-energy electron and proton counters. Detector C employed five Geiger counters in the form of a tray having an omnidirectional geometric factor of 28.8 cm^2 for protons with energies greater than 25 Mev and electrons greater than 1.8 Mev. The function of this detector was to provide omnidirectional intensity measurements through the atmosphere having reasonable statistical accuracy. Detector D consisted of two Geiger counter trays in the form of a telescope inclined 45 degrees to the rocket axis. The total amount of material between the trays was 8 g/cm^2 and the solid angle area factor was 3.3 cm^2 sterad for protons with energies greater than 90 Mev. The counting rates of each of the above detectors were scaled by various factors and each scaled rate recorded by standard FM–FM telemetry techniques.

Detector E was a NaI scintillation crystal $2\frac{1}{2}$ in. in diameter and $\frac{1}{8}$ in. thick mounted on a Dumont 6363 phototube; crystal and phototube were placed between the two counter trays of detector D. Individual pulse amplitudes from the phototube in coincidence with the counter telescope were converted into pulse length by a keyer circuit and these were transmitted by the telemetry system. The measurable ionization range extended from minimum ionization to about 35 times minimum. The purpose of this detector was to determine proton spectra in the energy range 90–700 Mev and α-particle spectra in the range 0.4–2.8 Bev.

The rocket instrumentation included solar and magnetic aspect indicators from which it was possible to obtain the orientation of detectors A and B as a function of time. Analysis of the aspect data showed that the rocket maintained a nearly constant spin of 0.71 r.p.s. throughout the flight and at the same time the rocket axis precessed about a cone of half angle 23 degrees with a period of about 115 seconds.

Rocket altitude vs. time data was supplied by the Defence Research Telecommunications Establishment; a maximum altitude of about 150 km was reached.

III. RESULTS

On October 24 a sudden commencement occurred followed by a strong magnetic storm which was accompanied by intense aurora at low latitudes and by a cosmic-ray Forbush type decrease. On several occasions during the days following the onset of the storm the Churchill riometer indicated varying degrees of cosmic noise absorption. On October 28 (1221 hours U.T.) after the onset of such an auroral absorption event a Black Brant rocket, designated D.R.T.E. 05, was fired. Figure 1 shows tracings of the Churchill zenithal riometer and magnetogram (horizontal component) records at the time of firing.

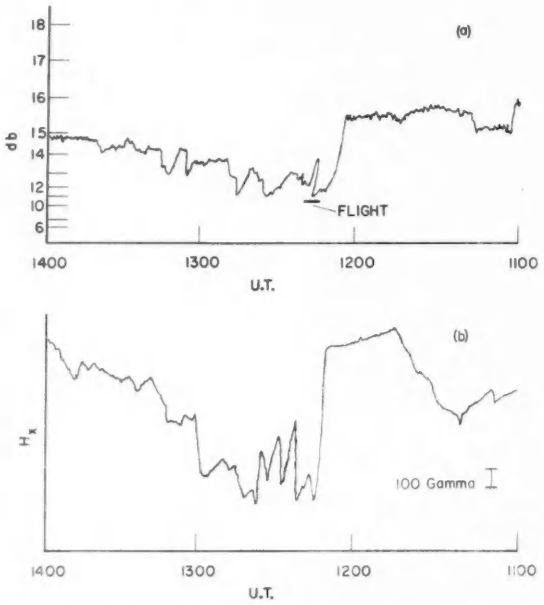

FIG. 1. Churchill riometer and magnetogram records for October 28, 1960.

The riometer indicates absorption of 3.8 db and a recovery of 2 db for about 1 minute during the flight. The magnetogram shows a decrease in the horizontal component of about 800 γ, coincident with the onset of absorption, and a recovery which more or less follows the riometer recovery. The vertical component of the surface field increased by more than 1000 γ and showed large variations during the event.

Throughout the flight the low-energy detectors A and B performed satisfactorily but the high-energy detectors C, D, and E functioned properly only to 100 seconds after launch at which time they stopped; the reason for this failure is not known at present. During the first 100 seconds detectors D and E measured only the normal cosmic-ray background; a background intensity of $0.26 \pm .03$ particles cm^{-2} sec^{-1} $sterad^{-1}$ was obtained of which about 10% was α-particles. The counting rate of detector C (Geiger tray) is shown in Fig. 2 along with the background cosmic-ray rate calculated using the measured background rate given above. The counts in excess of the expected background rate above the Pfotzer maximum and below 80 km are likely due to Bremsstrahlung produced in the atmosphere by primary electrons, this being consistent with the intensity and spectrum of the primary flux given below. The excess counts above 80 km, where the residual atmosphere is small, are probably due to Bremsstrahlung produced in the rocket skin by the primary

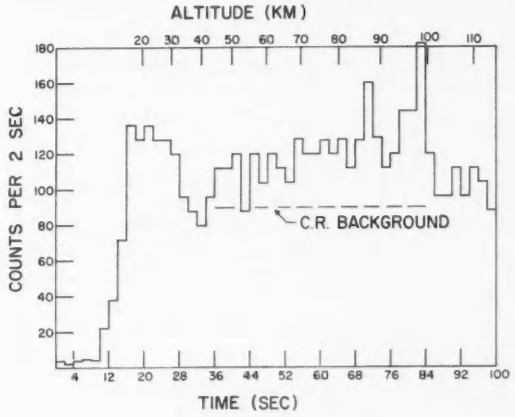

FIG. 2. Counting rate vs. time and altitude for detector C (Geiger tray).

particles. As can be seen in Fig. 3, where the Geiger tray rate is replotted, the two peaks at 87 and 99 km coincide with large fluxes in the low-energy electron counter. In any case the rates observed in detectors C, D, and E show that the particles responsible for the absorption measured by the riometer did not include appreciable fractions of electrons with energies greater than 1.8 Mev or protons with energies greater than 25 Mev.

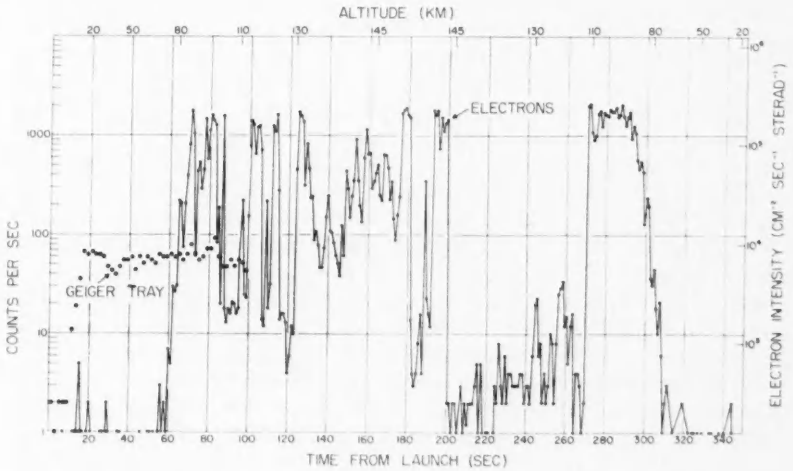

FIG. 3. Counting rate and absolute intensity vs. time and altitude for detector A (Anton 223 no field).

Figures 3 and 9 show the counting rates vs. time and altitude for detectors A (no field) and B (with magnetic field) respectively. The high-energy cosmic-ray background rate for these detectors above the atmosphere is about 0.4 counts/sec. The difference in counting rate of detectors A and B is due to electrons in the energy range 30 kev to 1.5 Mev and, therefore, since the rate in A is large compared to B, Fig. 3 refers essentially to electrons in this energy range. The particles recorded in detector B (Fig. 9) are either protons in the energy range 0.5–25 Mev or heavier particles; here it is assumed that they are protons. This detector is also sensitive to electrons with energies greater than 1.5 Mev but if the observed particles are electrons of this energy then the Geiger tray rate at, say, 90 seconds would be at least two orders of magnitude greater than observed.

Before 200 seconds the electron flux plotted in Fig. 3 shows large and rapid fluctuations. The riometer measurements do not show corresponding variations and this suggests that the electron variations may be due to a spatial structure of the primary flux combined with the horizontal motion of the rocket. The measurements are roughly consistent with a primary flux in the form of beams or columns of particles having widths of the order of 1 kilometer. The riometer measures absorption over relatively large distances and hence would measure only the average effect of such columns. At 200 seconds the electron intensity decreases by approximately three orders of magnitude and remains low for about one minute; this is the time at which the riometer shows a decrease in absorption of 2 db and probably indicates a time variation in the primary flux which occurs over distances covering an appreciable fraction of the riometer acceptance angle. At 270 seconds the electron intensity recovers and remains relatively steady until the rocket begins its descent in the dense atmosphere.

By correlating the counting rate of detector A with the instantaneous orientation of the counter collimator, angular distributions of the electrons have been obtained whenever possible. Due to the spin of the rocket and the inclination of its axis to the magnetic field, detector A scans through a range of magnetic zenith angles (equals particle pitch angle) as well as azimuth angles every revolution; the maximum pitch angle range extends from 40° to 140°. At different times three different types of angular distributions are observed. Within the range of measurement the first of these is isotropic at pitch angles less than 90°, the second has a maximum at pitch angles greater than 90°, and the third is more or less a superposition of these with a minimum about 90°. Figures 4, 5, and 6 show counting rate variations corresponding to these three types of angular distributions. Also shown is the angle between the collimator axis and the magnetic zenith as determined by the magnetic aspect indicator. For times around 286 seconds Fig. 4 corresponds to an isotropic angular distribution at angles less than 90°. These measurements are taken near the end of the flight and the increasing angle corresponds to the rocket beginning to turn over, while the decreasing counting rate is due to atmospheric absorption. Figure 5 corresponds to an angular distribution with a maximum between 100 and 110 degrees; the low counting rate at small pitch

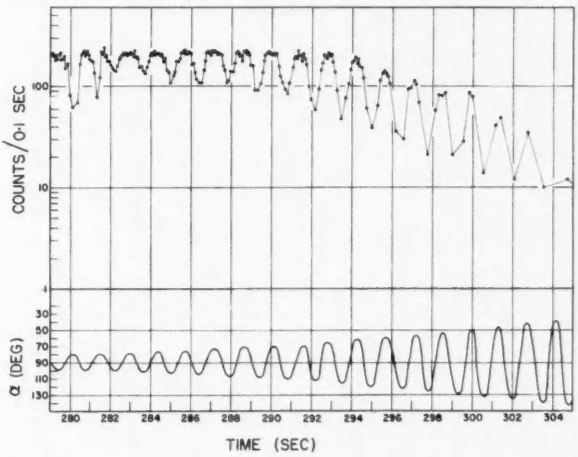

FIG. 4. Counting rate of detector A on an expanded time scale at an altitude of about 96 km on the descent. The lower curve gives the angle between the detector axis and the magnetic zenith.

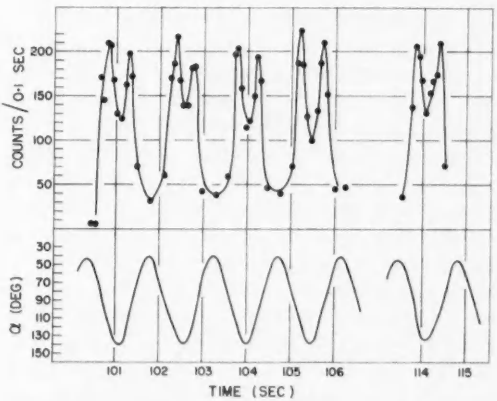

FIG. 5. Detector A counting rate vs. time at an altitude of about 118 km on the ascent. The lower curve gives the angle between the detector axis and the magnetic zenith.

angles is apparent. Figure 6 corresponds to an angular distribution with a minimum near 90°; the counting rate variation here is similar to that of Fig. 5 except that the pronounced minima have been filled in with downward-moving particles. Figure 7 shows angular distributions obtained from the above examples of counting rate variations as a function of orientation: (*a*) refers to a height of about 96 km where multiple scattering is important; at

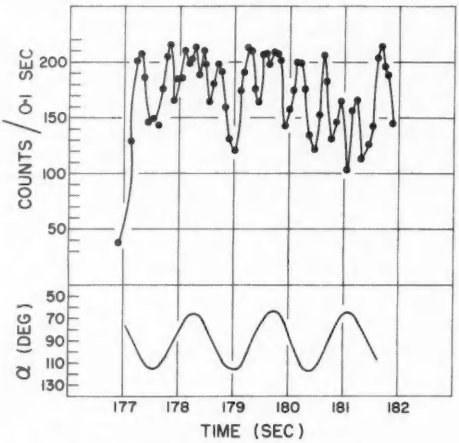

FIG. 6. Detector A counting rate vs. time at an altitude of about 150 km. Also shown is the angle between the detector axis and the magnetic zenith.

higher altitudes where scattering is less important similar angular distributions were observed but these decreased more rapidly at pitch angles near 90°, (*b*) refers to a height of 118 km and has a maximum around 110 degrees indicating an excess of upward-going particles, (*c*) refers to a height of 150 km and shows a minimum around 90°; this distribution could be due to the superposition of distributions similar to those shown in (*a*) and (*b*). At nearly all times when the counting rate was high the angular distribution of the particles could be represented by distributions similar to those shown in Fig. 7 although the type of distribution shown in 7(*a*) was the most common.

A tentative explanation of the angular distributions shown in Fig. 7(*b*) and (*c*) can be given in terms of incoming beams of electrons having a nearly isotropic angular distribution at pitch angles less than 90° and an ionospheric electric field having a small upward component in line with the magnetic field and a relatively larger component at right angles to the field. The upward component of such a field causes the reflection of some of the particles which in the absence of the field would be lost in the atmosphere. This is illustrated in the following numerical example. Suppose particles are observed at a height of 140 km and consider an incoming 40-kev electron with a pitch angle of 80°; normally this particle would be lost in the atmosphere. If, below 140 km, an upward component of an electric field exists of magnitude 5×10^{-4} v/cm, the particle will be reflected at a height of 120 km and when it recrosses the 140-km level it will have a pitch angle of 110°. On the other hand, a particle initially with a pitch angle of, say, 50° would be lost even in the presence of the electric field so that reflected particles with pitch angles of 130° would tend to be absent. Therefore, if the angular distribution of incoming particles is isotropic at small angles and decreases at pitch angles in the neighborhood

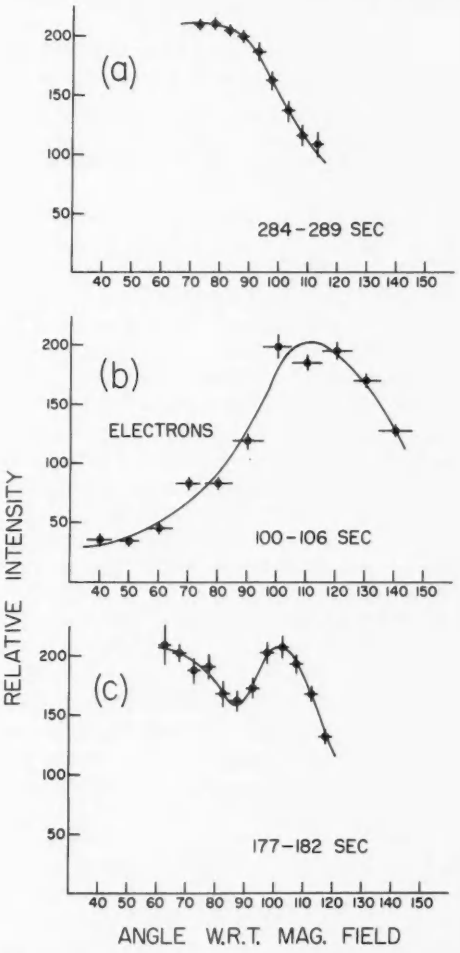

FIG. 7. Pitch angle distributions obtained from the counting rate variations shown in Figs. 4, 5, and 6.

of 80°, we can account for the main features of the distribution shown in Fig. 7(*c*), that is, the minimum at 90° and the near equality of the maximum intensity of the upward- and downward-going particles. Incidentally, the r.m.s. multiple scattering angle of a 40-kev electron penetrating to 120 km is about 12° and to 110 km is about 20° and this will tend to broaden angular distributions considerably. If in addition to the upward component of electric field a horizontal component also exists, a lateral drift of the electrons will

result so that it is possible for the rocket to be outside the incoming beam but still see the reflected particles because of their lateral displacement between crossing the observation level on their downward- and upward-going paths. Consider further the above example taking the horizontal electric field to be 10^{-2} v/cm (admittedly a rather large field but in a direction of relatively low conductivity). This and the earth's field will produce a drift velocity of about 20 km/sec which, in the 5×10^{-3} sec it takes the electron to cross and recross the 140-km level, will cause a lateral displacement of 0.1 km. Therefore, if the incoming beams are sufficiently well defined (Fig. 3 indicates that they are) and depending on the position of the rocket relative to the incoming beam it is possible to see only the reflected particles. Such a mechanism may account for the type of angular distribution shown in Fig. 7(*b*).

If it is assumed that the primary electron flux does not vary appreciably during ascent or descent, then an estimate of the electron energy spectrum can be obtained from air absorption considerations. Only during descent did the flux appear to remain constant; Fig. 4 shows the counting rate during descent and it seems clear that no appreciable intensity changes occurred which were not associated with the rocket motion. Using the intensity peaks shown in Fig. 4 and the Churchill pressure–altitude measurements of Meadows and Townsend (1960) gives the integral energy spectrum points shown in Fig. 8. The expression $\exp(-E/22\text{ kev})$ (approximately an integral Maxwellian distribution at the energies considered) gives a reasonable fit to the measured points while a power law spectrum gives a rather poor fit. The spectrum obtained here is similar in form to those obtained by McIlwain (1960) in visible aurorae and by Walt *et al.* (1960) in the outer Van Allen radiation belt; all are approximately Maxwellian but their KT values differ considerably.

The proton counting rate is shown in Fig. 9 along with the angle between the rocket axis and the earth's field. Note that the high counting rate around 265 seconds occurs at a time when the low-energy electron intensity is very low. The proton counting rate is too low to look at in as much detail as was done for the electrons. However, as can be seen in Fig. 9, the counting rate averaged over several spin rotations does show a correlation with the rocket orientation and from this an approximate magnetic zenith angular distribution can be obtained. An azimuth angle distribution can also be obtained from the solar aspect measurements by taking two intervals, of about 40 seconds each, around the times when the rocket axis was nearly in line with the field and by grouping the counts according to azimuth angle. These intervals correspond to times when the magnetic zenith angle of the detector does not change much during one spin period. Figure 10 shows the approximate angular distributions obtained, a zenith angle distribution with a maximum near 90° and an azimuth angle distribution showing a north–south asymmetry with an excess of particles incident from the south. The statistics here are too poor to be very significant; however, these distributions suggest that the protons enter the atmosphere mainly to the south of Churchill and that a small fraction of the particles are detected due to scattering in the atmosphere. A source of such particles might be the outer Van Allen belt which has a maximum intensity

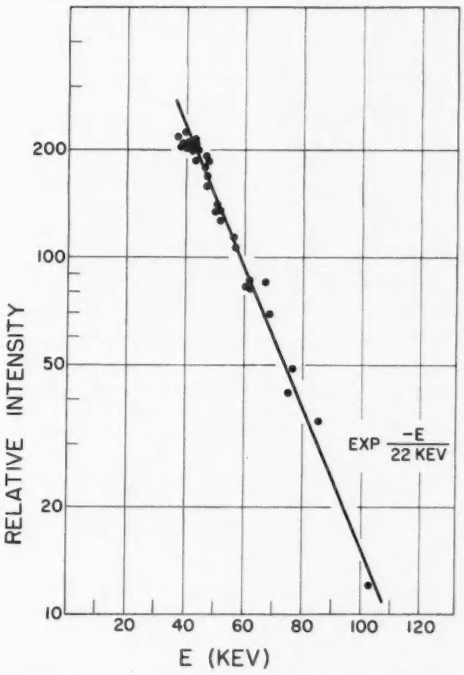

FIG. 8. Integral electron energy spectrum during descent.

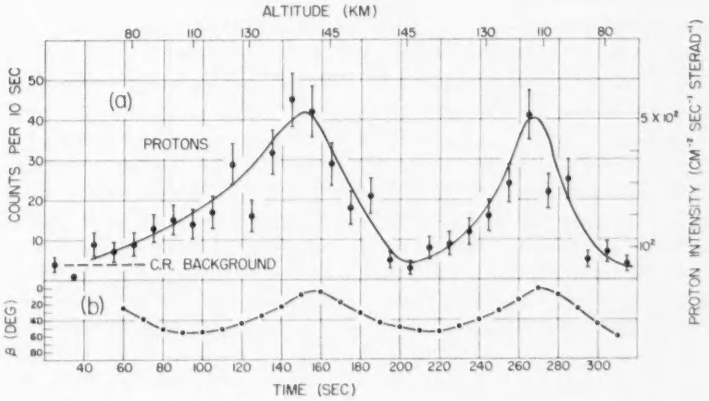

FIG. 9. Counting rate and absolute intensity vs. time and altitude for detector B (Anton 223 with magnetic field). The lower curve gives the angle between the rocket axis and the magnetic zenith.

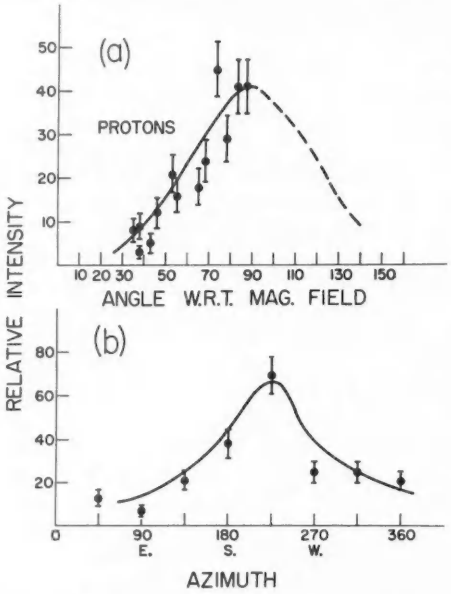

FIG. 10. (*a*) Approximate proton magnetic zenith angle distribution. (*b*) Azimuth angle distribution.

along a line of force which enters the atmosphere well to the south of Churchill. It is also interesting to note that Martyn's (1951) auroral theory predicts that at most times during auroral or magnetic disturbances protons will enter the atmosphere mainly on the southern edge of the auroral zone and that ionospheric electric fields of the order of magnitude of those discussed above will be set up.

Finally, the electron density profile calculated from the particle intensity measurements can be compared with that calculated from the absorption measurements. Figure 11, curve 1, shows electron densities calculated using the rate coefficients given by Crain (1961) and the assumptions that the energetic electron intensity is isotropic over the upper hemisphere (at all altitudes) and has the value measured at a zenith angle of 45° (see Fig. 4) and, secondly, that the measured intensities refer to electrons of 30-kev energy. The results obtained using the latter assumption do not differ significantly from those obtained assuming the primary electron spectrum given in Fig. 8. Curve 2 of Fig. 11 represents the calculated electron densities produced by secondary X rays from the primary electrons while curve 3 represents cosmic-ray produced electron densities given by Crain (1961) for a latitude of 55°. The points shown in Fig. 11 have been calculated from absorption measurements and are those given in the accompanying paper by Heikkila and Penstone. Although the agreement between the electron densities obtained from

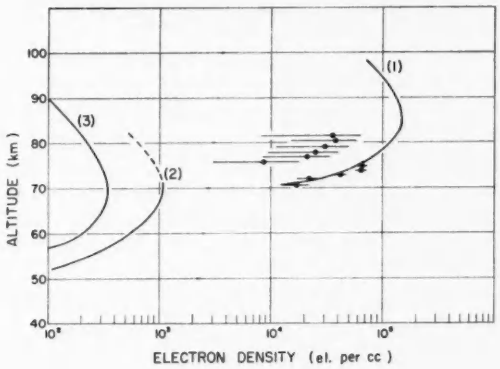

FIG. 11. Electron density vs. altitude. The points are values calculated from absorption measurements. 1 is calculated from the observed electron flux, 2 is due to secondary X rays from the primary electrons, and 3 is calculated from the background cosmic-ray intensity.

the absorption and particle calculations is only fair it seems clear that the measured electron flux is sufficient to produce the observed absorption and at the appropriate heights. It is not expected that the energies of the protons present are sufficient to contribute appreciably to the absorption at altitudes as low as 75 km. If this is generally true then the only difference between auroral events involving radio absorption and those not involving it is the steepness of the associated electron spectrum.

A significant difference between the electron densities calculated from the absorption and particle measurements is the sharp maximum at about 73 km deduced from the absorption measurements. It is difficult to imagine how such a rapid change in electron density with altitude could be produced and it may be that the corresponding sharp increase in absorption should be accounted for by a more rapid variation with altitude of the electron collision frequency possibly associated with the presence of relatively strong electric fields.

IV. DISCUSSION

The main results of this experiment can be summarized as follows:

1. An incident electron flux, probably in the form of beams or columns, was observed. The spectrum of the electrons was approximately Maxwellian and they extended over horizontal distances of at least 100 km (the horizontal distance the rocket travelled).

2. The primary electron angular distribution was approximately isotropic over the upper hemisphere. Two other types of angular distributions, involving upward-moving particles, were observed. These may be accounted for in terms of an ionospheric electric field.

3. The measured electron flux was sufficient to account for the observed radio absorption and at the appropriate heights. Time variations in the primary flux produce corresponding variations in the absorption.

4. A small intensity of protons was observed which probably did not contribute to the absorption. The proton intensity was relatively steady and was not correlated with the electron flux either in space or time. The protons appeared to enter the atmosphere to the south of Churchill.

Many more similar events will have to be studied before any general conclusions can be drawn. Simultaneous rocket and satellite measurements during such events would be very useful in deciding between various possible sources and acceleration mechanisms. It would also be useful to have a more detailed time correlation between the particle flux measurements and high speed magnetograms and riometers. Such measurements are planned for the near future.

ACKNOWLEDGMENTS

We are indebted to the Defence Research Board Telecommunications Establishment for the opportunity of carrying out the measurements reported here. Some of the field operations were carried out by Mr. John Winfield.

REFERENCES

CRAIN, C. M. 1961. J. Geophys. Research, **66**, 1117.
MARTYN, D. F. 1951. Nature, **167**, 92.
MCILWAIN, C. E. 1960. J. Geophys. Research, **65**, 2727.
MEADOWS, E. B. and TOWNSEND, J. W. 1960. Proceedings of the First International Space Science Symposium, p. 175.
WALT, M., CHASE, L. F., CLADIS, J. B., IMHOF, W. L., and KNECHT, D. J. 1960. Proceedings of the First International Space Science Symposium, p. 910.

A PROPOSAL TO USE MICROWAVE CAVITIES TO STUDY THE SURFACE PROPERTIES OF HIGH DENSITY PLASMAS[1]

F. L. Curzon and Roger Howard

ABSTRACT

It is suggested that the resonant properties of a cylindrical microwave cavity containing a highly conducting axial plasma rod could be used to obtain information about the dynamic properties of such a plasma. Two applications of the method are considered: an investigation of electrically exploded wires, and a study of the dynamics of the conventional *z*-pinch during its initial stages.

INTRODUCTION

Microwaves have been used extensively to study the physics of low density plasmas (Allis 1956; Brown 1956). For example, the resonant frequencies of an evacuated microwave cavity are altered when a plasma is introduced into the cavity. This is because of the finite electrical conductivity of such a plasma. The conductivity, in turn, is related to the free electron density, and the electron–ion collision frequency (see, for example, Gilardini 1959). Professor Brown and his co-workers at M.I.T. have developed many elegant methods of using microwave cavities to measure such quantities in low density plasmas.

These quantities may also be measured by determining the propagation constants of microwaves transmitted through plasmas. This method has become very popular in studying plasma confinement in thermonuclear work (Wharton 1961).

In cases where the electron density n_e is high, microwaves of practical frequencies are strongly attenuated by plasmas and there is a practical cutoff density of about $n_e = 10^{13}$ cm^{-3} at frequencies of 30 kMc/s (Wharton 1961). For plasmas where the electron density is greater than this, microwave transmission techniques cannot be readily applied to electron density measurements. However, for such plasmas, the surface reflectivity is high. It therefore seems feasible to study the surface properties of high density plasmas with microwaves.

Again, as with low density plasmas, there are two possible methods of investigation: changes in the resonant frequencies of the cavity containing the plasma, or scattering of free waves. In cases where the surface properties of a high density plasma are of interest, the systems most frequently encountered have axial and radial symmetry. In the *z*-pinch, for example, a high density plasma is formed along the axis of a cylindrical cavity. Similarly, electrically exploded wires, which have been studied extensively by Chase (1959), could also be studied in such a configuration. The resonant frequencies

[1]Manuscript received July 17, 1961.
Contribution from the Department of Physics, University of British Columbia, Vancouver 8, B.C.

of a cavity of this type will be determined primarily by the surface geometry of the axial plasma rod within it, provided the conductivity of the rod is sufficiently high, and that the electron density outside the rod is effectively zero.

In the following paper we have considered the problem of a cylindrical cavity of circular cross section containing an axial rod also of circular cross section. The changes in resonant frequency as the radius of the axial rod is changed are discussed; we also consider the effects of axial variations in this radius for certain cavity modes which are of practical importance.

THEORETICAL DISCUSSION

We have to investigate the characteristic modes of oscillation of concentric cylindrical cavities, and the dependence of the associated resonant frequencies upon the radius of the inner conductor. It is assumed that changes in this radius take place slowly in comparison with the oscillating changes in electric and magnetic fields; a quasi-static approach is then justified. The electric and magnetic field configurations for the modes of oscillation of such a cavity are well known (see, for example, Beringer 1947), and can be categorized either as transverse electric (TE) or transverse magnetic (TM) according as the electric or magnetic field has components only perpendicular to the cylinder axis. The various modes are further designated by suffixes l, m, n which have the following significance:

l is the number of periods of azimuthal variation of electric and magnetic fields,

m is the number of half-periods of radial field variation, and

n is the number of half-periods of field variation along the cylinder axis.

The resonant frequency of a given mode of oscillation is:

$$f = \frac{c}{2\pi}\sqrt{\frac{x_{lm}^2}{R^2}+\frac{n^2\pi^2}{L^2}}. \tag{1}$$

c is the velocity of light; R and L are respectively the radius and length of the cylindrical cavity. The parameter x_{lm} is defined in terms of the radius of the inner conductor, R_1. For a transverse magnetic mode, x_{lm} is the mth root of

$$J_l(x_{lm})N_l(\eta x_{lm}) = J_l(\eta x_{lm})N_l(x_{lm}) \tag{2}$$

in which

$$\eta = R_1/R. \tag{3}$$

For transverse electric modes, x_{lm} is the mth root of

$$J'_l(x_{lm})N'_l(\eta x_{lm}) = J'_l(\eta x_{lm})N'_l(x_{lm}). \tag{4}$$

J_l and N_l are respectively lth order Bessel functions of the first and second kinds; the prime denotes the derived functions.

In order to investigate the dependence of resonant frequency on R_1, it is necessary to know the values of x_{lm} as a function of η. Values have been tabulated by Dwight (1948) and Fig. 1 illustrates their behavior. One can

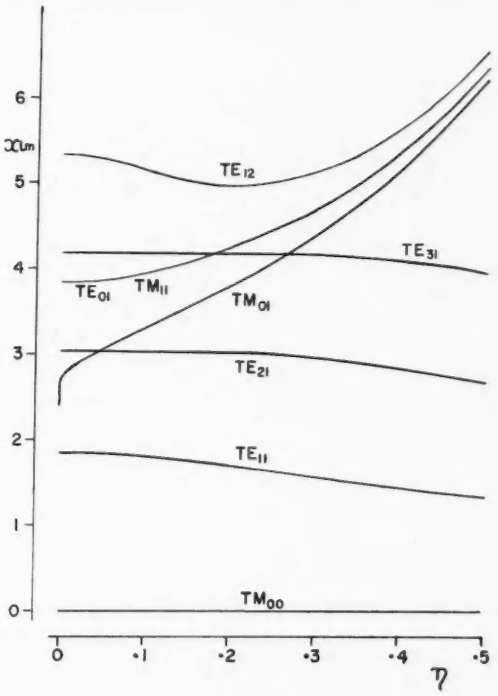

FIG. 1. Plot of some roots of equations (2) and (4) as a function of the diameter ratio η.

compute the resonant frequency for any shape and size of cylindrical cavity from the expression (1); see, for example, Fig. 2, which is a mode chart for a 'square' cylinder ($L = 2R$).

It is proposed to use changes in resonant frequency to measure the radius of the inner conducting surface bounding the cavity. It is therefore obvious that the mode to be used should have as strong a dependence as possible on the parameter η. There are other requirements which stem from experimental considerations; basically these all involve the degeneracy of modes with different oscillating field patterns. If a cavity is excited at a frequency which lies within the resonance bandwidth of two or more modes, the losses, which are not linear in the field strengths, will couple the modes so that power transfer can occur and spurious resonances will be obtained. This is true both for accidentally degenerate modes (e.g. at an intersection on the mode chart) and also for inherently degenerate modes such as TE_{01n} and TM_{11n}. In the latter category occur all modes which have azimuthal variation ($l > 0$); this is because any such mode is, in general, the sum of *two* orthogonal degenerate modes whose $\theta = 0$ axes are at right angles.

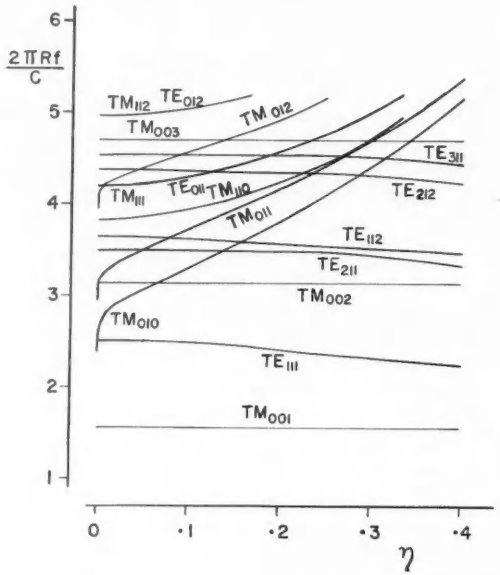

FIG. 2. Plot of frequency (in dimensionless units) against η for the lower resonant modes of a cavity in which $L = 2R$.

Transverse electric modes of oscillation for which $l = 0$ have no radially directed currents associated with them in the conducting end walls; they would therefore be unaffected by an insulating gap between the circular base plates and the outer cylindrical wall. All other modes have associated wall currents which would be directed *across* such a gap and which would in effect encounter an infinite resistance; thus all such modes have very high losses and are effectively inhibited. A cavity constructed with such an insulating gap therefore will sustain only TE_{0mn} modes. These satisfy all the requirements that have been mentioned; their resonant frequencies depend on inner conductor radius; they have no azimuthal dependence, and the mode chart is almost completely free from accidental degeneracies. In the following discussion, which is restricted to TE_{0mn} modes, the effect of change in the inner conductor radius is considered.

Perturbation of the boundaries of a resonant cavity shifts the resonant frequencies, which are then given (Slater 1950) by:

$$f^2 = f_K^2[1 + \iiint (\mathbf{H}_K^2 - \mathbf{E}_K^2) dV]. \tag{5}$$

f_K is the resonant frequency of the unperturbed cavity in its Kth mode; $\mathbf{H}_K$ and $\mathbf{E}_K$ are normalized functions which describe the spatial variation of magnetic and electric fields in this mode of oscillation. The volume integral extends over the volume which has been *removed* from the cavity by the change in its boundaries.

For the TE_{0mn} modes, the functions $\mathbf{H}_K$ and $\mathbf{E}_K$ have the following non-vanishing components (Beringer 1947; Stratton 1941):

$$H_r = \frac{K_3}{AK} Z_0'(K_1 r) \cos K_3 z,$$

$$H_z = \frac{K_1}{AK} Z_0(K_1 r) \sin K_3 z, \tag{6}$$

$$E_\theta = -\frac{1}{A} Z_0'(K_1 r) \sin K_3 z,$$

in which

$$K_1 = x_{0m}/R, \qquad K_3 = n\pi/L, \qquad K^2 = K_1^2 + K_3^2, \tag{7}$$

and

$$Z_0(K_1 r) = J_0(K_1 r) - \frac{J_1(x_{0m})}{N_1(x_{0m})} N_0(K_1 r). \tag{8}$$

A is a normalization constant

$$A^2 = \pi L \int_{R_1}^{R} Z_0^2(K_1 r) r dr. \tag{9}$$

We now proceed to evaluate the change in frequency for a change in the inner conductor radius, in the general case where this change is a function of axial position. Thus we require the integral:

$$\int_{\eta R}^{(\eta+\Delta)R} \int_0^L [\mathbf{H}_K^2 - \mathbf{E}_K^2] 2\pi r dr\, dz. \tag{10}$$

The parameter Δ introduced here is a function of z, and can be defined as the perturbation in η:

$$\Delta = \delta\eta = \frac{\delta R_1(z)}{R}. \tag{11}$$

Now,

$$\mathbf{H}_K^2 - \mathbf{E}_K^2 = \frac{K_3^2}{A^2K^2} Z_0'^2(K_1 r) \cos^2 K_3 z + \frac{K_1^2}{A^2K^2} Z_0^2(K_1 r) \sin^2 K_3 z - \frac{1}{A^2} Z_0'^2(K_1 r) \sin^2 K_3 z \tag{12}$$

$$= \frac{K_1^2}{2A^2K^2} [Z_0^2(K_1 r) - Z_0'^2(K_1 r)] + \frac{1}{2A^2K^2} \cos 2K_3 z [(K_1^2 + 2K_3^2) Z_0'^2(K_1 r) - K_1^2 Z_0^2(K_1 r)].$$

Substituting into the expression (10), the integral over r becomes

$$\frac{\pi}{A^2K^2} \int_{\eta R}^{(\eta+\Delta)R} [K_1^2(Z_0^2(K_1 r) - Z_0'^2(K_1 r)) + \cos 2K_3 z((K_1^2 + 2K_3^2)\, Z_0'^2(K_1 r) - K_1^2 Z_0^2(K_1 r))] r dr. \tag{13}$$

In order to obtain a first-order approximation, the assumption is made that $\Delta(z)$ is small in comparison with η so that the integrand (13) is approximately constant over the range of integration. Since $Z_0'(K_1r)$ is zero at the inner boundary $r = R_1$, the result of integration with respect to r in our approximation is

$$\frac{\pi K_1^2}{AK^2}\eta R^2\Delta(z)Z_0^2(K_1\eta R)[1-\cos 2K_3z]. \tag{14}$$

In order to compute the integral over z, it is necessary to know the explicit form of $\Delta(z)$. However, in general, $\Delta(z)$ can be expanded in a Fourier series:

$$\Delta(z) = \Delta_0+\sum_{s=1}^{\infty}\left[\Delta_s\cos\frac{2\pi sz}{L}+\epsilon_s\sin\frac{2\pi sz}{L}\right] \tag{15}$$

where

$$\Delta_s = \frac{2}{L}\int_0^L\Delta(z)\cos\frac{2\pi sz}{L}\,dz$$

and

$$\epsilon_s = \frac{2}{L}\int_0^L\Delta(z)\sin\frac{2\pi sz}{L}\,dz.$$

The z-integral is now

$$\frac{\pi K_1^2}{A^2K^2}\eta R^2Z_0^2(K_1\eta R)\int_0^L[1-\cos 2K_3z]\left\{\Delta_0+\sum_{s=1}^{\infty}\left[\Delta_s\cos\frac{2\pi sz}{L}+\epsilon_s\sin\frac{2\pi sz}{L}\right]\right\}dz = \frac{\pi K_1^2}{A^2K^2}\eta R^2LZ_0(K_1\eta R)\left[\Delta_0-\frac{1}{2}\Delta_n\right]. \tag{16}$$

This result is a consequence of the definition of K_3, equation (7), and of the orthogonality of the trigonometric functions. The only contributing term in the expansion of $\Delta(z)$ is the *cosine* term for which $s = n$. The expression (16) is the proportional increase in the square of the cavity resonant frequency (see equation (5)). Substituting the expression (9) for the constant A^2, the increase in cavity resonant frequency is given by

$$\frac{\delta f}{f_K} = \frac{K_1^2\eta R^2Z_0^2(K_1\eta R)}{2K^2\int_{R_1}^{R}Z_0^2(K_1r)rdr}\left[\Delta_0-\frac{1}{2}\Delta_n\right]. \tag{17}$$

The expression (17) comprises two terms: the first gives the frequency change resulting from a uniform increase Δ_0R in R_1; the second occurs only if there exists a Fourier cosine component of axial variation of ΔR which is characterized by the same integer n that specifies the oscillating field pattern of the mode in question. Fourier components characterized by an $s \neq n$ have no effect to the order of approximation considered. In experimental investigation it would be convenient to use a cavity whose diameter is small in comparison with its length because the TE_{0mn} modes for different n values would then lie conveniently close together; an investigation of the relative changes in frequency would yield information on the harmonic content of axial variations in R_1. The mean change in R_1 displaces *all* the modes in the

set, while each member of the set is displaced independently by its corresponding Fourier component $\Delta_n R \cos(2\pi nz/L)$ of R_1.

The results, expressed in equation (17), are subject to certain reservations depending on the validity of the assumptions made in the derivation. The most important of these is that there exists, in fact, a cavity of the type described, namely a region of zero conductivity enclosed by highly conducting walls. In practice one would have a spatial variation of conductivity to which our cavity is an approximation; however, the qualitative form of our results should not be changed by a somewhat more realistic viewpoint. The general effect of more gradual spatial variation of conductivity would be to reduce the Q of the cavity. This would result in second-order displacements of the cavity resonant frequencies. Since the frequency shifts produced by changes of the plasma dimensions are of the first order, it should be possible to design experiments in which useful results can be obtained even in relatively low-Q cavities. Of course, if the Q values are too low, mode mixing will occur, leading to difficulties in interpretation of results.

If the changes in R_1 are not small, as assumed, our approximation will, of course, cease to be valid and the dependence of resonant frequencies upon the coefficients Δ_n will become much more complicated. However, in an experiment, one can still take advantage of the simplicity of the first-order results by investigating the initial stages of shifts in resonant frequency which will follow our linear approximation. For small changes in R_1, the over-all volume changes in the cavity will certainly be small enough to justify the use of the perturbation expression (5).

A final point of interest is that if the effects of such changes in cavity dimensions are considered in the context of Slater's formulation of equations of motion for the oscillatory fields (Slater 1950), the equations are exact analogues of those describing small fluctuations in capacitance in a resonant circuit. With suitable frequency relationships, such a system could possibly be utilized as a parametric amplifier of the type discussed by Stevens (1958).

THE *Z*-PINCH

An obvious case where the surface properties of a high density plasma are of importance is the z-pinch (also known as the linear pinch). By studying the emission of neutrons from the linear pinch in deuterium (Anderson, Baker, Colgate, Ise, and Pyle 1957) it has been shown that surface instabilities play an important part in their production. More quantitative data on surface instabilities in z-pinches may be obtained using magnetic probes (Burkhardt, Loveberg, and Philips 1956). These essentially provide information about the current distribution in the pinch. Finally, photographic methods can also be used (Curzon, Folhierski, Latham, and Nation 1960). In particular these have shown that the nature of pinch instabilities is markedly affected by the presence of probes (Latham, Curzon, and Nation 1959). It seems, therefore, that if reliable information concerning the space–time relationships for the pinch surface are to be obtained, virtually the only available method is the photographic one. This suffers from the disadvantage that the return conductor

of the discharge has to be made semitransparent thus reducing its conductivity. As a result, instabilities are damped to a lesser extent than if the return conductor consist of a solid cylinder. A further difficulty of the photographic method is that if instabilities are to be studied continuously, then very expensive high speed motion cameras are required (framing rates in excess of a million per second, and frame exposure times less than 0.2 microsecond). In fact, until now surface instabilities in the z-pinch have only been studied quasi-statistically by means of Kerr cell cameras. Finally, the evaluation of data obtained photographically is an extremely tedious and laborious process and is best avoided if possible. Hence, if a z-pinch system could be designed which conforms to the limitations imposed by the assumptions in the theory given above, the quantitative study of instabilities would be rendered much easier than it is at present.

There should be little difficulty in satisfying most of the conditions except the assumption that the conductivity is zero in the region enclosed by the plasma rod and cavity walls. Gas atoms left behind by the initial contracting current shell can be ionized subsequently, and if the resulting electron density is high enough, severe attenuation of any microwave fields in the vessel occurs. Wharton (1961) gives values of the cutoff electron density, n_{ec}, for microwaves of various frequencies. These indicate that, at 1 kMc/s, electron densities of less than 10^{10} cm^{-3} could be tolerated. Since the resonant frequencies of typical pinch cavities will be somewhat larger than this, 10^{10} cm^{-3} represents a lower limit on the electron density. In order to be sure that the plasma rod itself behaves as a good conductor, its electron density n_{ep} should be at least a thousand times larger than the cutoff density corresponding to the highest microwave frequency to be used in the experiments (say 10 to 20 kMc/s). For a frequency of 10 kMc/s, n_{ep} would be 10^{15} cm^{-3}.

By considering conservation of material and assuming that all gas ions in the pinch are singly ionized it is possible to derive the following simple expressions relating the initial *number* density (n_a) of atoms in the discharge vessel to the number densities of electrons in the pinch (n_{ep}) and outside (n_{eo}).

$$n_{eo} = \frac{\alpha n_a R^2(1-\phi)}{R^2 - R_1^2}, \tag{18}$$

$$n_{ep} = \phi n_a \frac{R^2}{R_1^2}, \tag{19}$$

where α is the degree of ionization in the gas outside the pinch, and ϕ is the fraction of the original gas atoms trapped by the pinch. The other symbols have the same significance as previously in this paper.

Let us consider the parameters in these equations in more detail. Firstly, many experiments have shown that values of $(R/R_1)^2$ greater than 100 are readily achieved (Kolb 1958; Latham, Curzon, and Nation 1959). Hence, assuming $(R/R_1)^2 = 100$, equations (18) and (19) can be reduced to:

$$n_{eo} = \alpha n_a(1-\phi), \tag{20}$$

$$n_{ep} = 100\,\phi n_a. \tag{21}$$

The value of ϕ depends on the mechanism that is responsible for ionizing and trapping atoms in the collapsing current shell. If we assume that collisions between electrons in the current shell and neutral gas atoms are responsible then we can use Phillips' (1959) expression for ϕ:

$$\phi = 1-\exp\left[-\frac{c\bar{\sigma}}{e}\left[\frac{n_a m_a}{2\pi}\right]^{\frac{1}{2}}\right] \tag{22}$$

in which e is the electronic charge, 4.8×10^{-10} e.s.u.; c is the velocity of light, 3×10^{10} cm sec^{-1}; n_a is the number density of neutral atoms; m_a is the mass of such a neutral atom; and $\bar{\sigma}$ is an effective cross section for ionization by electron collision.

Since ϕ depends exponentially on m_a, it is advantageous to use gases of high atomic weight, and for several reasons caesium appears to be a good choice: m_a is 2.21×10^{-23} g, and the best value for $\bar{\sigma}$ is 2.8×10^{-16} cm^2 (von Engel 1956). Substituting this value and the constants given into equation (22) we obtain:

$$\phi = 1-\exp\left[-3.3\times10^{-7}n_a^{1/2}\right]. \tag{23}$$

Typically, n_a is of the order of 3.6×10^{15} cm^{-3} (pressures are approximately equal to 100 μ of mercury). Hence ϕ is of the order of unity. Substituting this value of ϕ in equation (20) leads to the conclusion that the trapping mechanism proposed by Phillips is efficient enough in caesium to reduce the gas density outside the pinch to a level where, even if the untrapped gas were fully ionized, i.e. $\alpha = 1$, the electron density would be too low to attenuate microwaves of the frequency likely to be used in the experiments proposed. Furthermore n_{ep} (equation (21)), under the conditions given, is 3.6×10^{17} cm^{-3}, which is adequate to ensure that the microwave conductivity of the pinch itself is high enough for the theory given to be valid.

The above treatment represents only a crude approximation to the experimental conditions but nevertheless the results are encouraging enough to suggest that it is worth while to pursue the experiment further.

If atoms are, in fact, left behind by the pinch then mechanisms whereby these are ionized have to be considered in more detail before the value of the proposed experiment can be assessed. There are three basic mechanisms: photoionization produced by light emitted by the pinch; collision ionization produced by electrons accelerated in induced electric fields arising from the time-dependent pinch currents; ionization produced by collisions between cold particles outside the pinch with the surface of the pinch itself.

ELECTRICALLY EXPLODED WIRES

In this case the microwave method would be much easier to apply. This is because, in the initial stages, the system conforms almost exactly to the theoretical model. Since the space between the wire and the cavity wall may be evacuated, the tedious conductivity problem associated with the z-pinch does not occur. Bartels, Gansauge, and Bortfeldt (1959) have obtained photographs of electrically exploded wires which show that these, too, behave like the

plasma in z-pinches. They do not show any photographs of instabilities, but these are undoubtedly present.

A further interesting feature of exploding wires which can be studied effectively is the microwave conductivity of molten metals under diverse physical conditions (Chase 1959).

ACKNOWLEDGMENTS

We wish to thank Drs. J. Grindlay and L. G. de Sobrino of this department and Mr. E. L. Lewis of the electrical engineering department for valuable discussions.

We gratefully acknowledge financial support from the President's Committee on Research.

REFERENCES

ALLIS, W. P. 1956. Handbuch der Physik, **21**, 383.
ANDERSON, O. A., BAKER, W. R., COLGATE, S. A., ISE, J., and PYLE, R. V. 1957. Proc. 3rd International Conference on Ionization Phenomena in Gases (Italian Phys. Soc.), 62.
BARTELS, H., GANSAUGE, P., and BORTFELDT, T. 1959. Proc. 4th International Conference on Ionization Phenomena in Gases (Uppsala) (North-Holland Publishing Co.), 1196.
BERINGER, R. 1947. M.I.T. Radiation Laboratory Series (McGraw-Hill Book Co.), **11**, 303.
BROWN, S. C. 1956. Handbuch der Physik, **22**, 531.
BUCHSBAUM, S. J. and BROWN, S. C. 1957. Phys. Rev. **106**, 196.
BURKHARDT, L. C. and LOVEBERG, R. H. 1958. 2nd U.N. Conference on the Peaceful Uses of Atomic Energy, **32**, 29.
BURKHARDT, L. C., LOVEBERG, R. H., and PHILIPS, J. A. 1956. Los Alamos Report LA–2131.
CHASE, W. G. 1959. Phys. Fluids, **2**, 230.
——— 1959. Proc. 4th International Conference on Ionization Phenomena in Gases (Uppsala) (North-Holland Publishing Co.), 1191.
CURZON, F. L., FOLHIERSKI, A., LATHAM, R., and NATION, J. A. 1960. Proc. Roy. Soc. A, **257**, 386.
DESLODGE, E. A., MATTHYSSE, S. W., and MARGENAU, H. 1958. Phys. Rev. **112**, 1437.
DWIGHT, H. B. 1948. J. Math. Phys. **27**, 84.
FÖRSTER, H. and SCHLÜTER, J. 1959. Proc. 4th International Conference on Ionization Phenomena in Gases (Uppsala) (North-Holland Publishing Co.), 867.
GILARDINI, A. 1959. Suppl. Nuovo Cimento, **13**, 132.
KOLB, A. C. 1958. 2nd U.N. Conference on the Peaceful Uses of Atomic Energy, **32**, 328.
LATHAM, R., CURZON, F. L., and NATION, J. A. 1959. Proc. 4th International Conference on Ionization Phenomena in Gases (Uppsala) (North-Holland Publishing Co.), 884.
PERSSON, K. B. 1957. Phys. Rev. **106**, 191.
PHILLIPS, N. J. 1959. Proc. Phys. Soc. **72**, 700.
SLATER, J. C. 1950. Microwave electronics (Van Nostrand Co.).
STEVENS, K. W. H. 1958. J. Electronics and Control, **4**, 275.
STRATTON, J. A. 1941. Electromagnetic theory (McGraw-Hill Book Co.).
VON ENGEL, A. 1956. Handbuch der Physik, **21**, 508.
WHARTON, C. B. 1961. Plasma physics, *edited by* J. E. Drummond (McGraw-Hill Book Co.), 307.

NOTES

OBSERVATIONS OF AURORAL LUMINOSITY FLUCTUATIONS

R. S. Iyengar and G. G. Shepherd

It is apparent to any visual observer of aurora that luminosity fluctuations are often present. The most frequent type suggests a rapid appearance and disappearance of rays in an arc or band, often giving the appearance of waves travelling along the auroral structure. A less frequent type has waves travelling rapidly from the horizon to the zenith. An infrequent type has an isolated arc, or fragment of arc, or patch of aurora pulsating in intensity. Observations of such fluctuations, using photoelectric photometers, have been reported by Penn and Currie (1949), Ashburn (1955), Omholt and Harang (1955), Dzhordzhio (1959), Murcray (1959), Stoffregen and Derblom (1960), Campbell and Rees (1961), and others. Most of the records present a quasi-periodic appearance, with periods ranging from a fraction of a second to several seconds. Some of these observations were made with large fields of view, and some with small fields of view. The interpretation of the two types of observations should be rather different, even though the records look somewhat similar on a casual inspection. A simultaneous comparison of fluctuations as seen with large-field and small-field photometers has yet to be made.

This note reports observations of auroral luminosity fluctuations made with a small-field photometer at Saskatoon (52.1° N., 106.6° W.). Preliminary attempts to estimate the correlation in space and time of the fluctuations have been made.

INSTRUMENTAL

A simple glass objective lens of focal length 330 mm and diameter 128 mm was used. A circular aperture at the focal plane defined the field of view, and a field lens behind it imaged the objective lens on the cathode of a 931-A photomultiplier. A Corning 5850 blue glass filter was used to eliminate the OI 5577 Å radiation, so that the greater part of the light recorded was from the N_2^+ band at 3914 Å. Some of the observations were made with a single angular field of 2°. Many were made with a double-channel system using two circular apertures in the focal plane and two photomultipliers. With this arrangement, light was collected from two fields each 0.55° in size, and separated from each other by 3°. Single-channel recordings were usually made with a Varian G-10 recorder and the double-channel recordings were made with a two-channel Sanborn recorder. Direct-current amplifiers were used between photomultiplier and recorder with no frequency response networks. The photometer unit was held in an altitude–azimuth mount and pointed manually to the desired auroral form with the aid of a telescopic viewfinder.

OBSERVATIONS

Observations were made on 110 nights over a period of 20 months. Most of the records were obtained from the brighter forms, since these generally gave the most pronounced fluctuations. About one-half of the quiet forms observed and about two-thirds of the active forms exhibited fluctuation. These fractions are probably dependent on the observational selection of the operator.

Figure 1 shows examples of single-channel records obtained from a quiet form, an active form, and a pulsating or flaming form. The three records do not display any notable differences, and it is surprising to see such fluctuations in quiet forms. For all records, the impression is one of pulses recurring with some degree of regularity. To obtain an estimate of the spread of recurrence times in different records, the times between successive peaks were measured and histograms plotted of the numbers of recurrences corresponding to the observed recurrence times. Figure 2 shows histograms for fluctuations in a homogeneous arc, a ray band, and for a pulsating or flaming form. They are typical of the majority of aurora for these types. The most frequent recurrence time is between 1 and 5 seconds. Recurrence times in excess of 10 seconds are rare. These values are not inconsistent with the ones reported by observers using wide-field photometers. They are also similar to those reported for magnetic micropulsations. Micropulsation records obtained at Isabella, California, were kindly supplied by Dr. H. Benioff. Occasions were found when micropulsations in California were occurring simultaneously with auroral luminosity fluctuations in Saskatoon. These may have been accidental coincidences, since only a few records were examined, but according to Duffus, Shand, and Wright (1960), micropulsations may occur simultaneously many hundreds of miles apart. Unfortunately micropulsation records of similar time resolution were not available from stations closer to Saskatoon. Histograms of recurrence times for the micropulsations were prepared as for the luminosity fluctuations, and the histogram in Fig. 2(*d*) is for a micropulsation record corresponding to the pulsating auroral record used to construct Fig. 2(*c*). The similarity between the two is striking.

The sharply peaked nature of these distributions suggests that the pulses might not be occurring randomly. To investigate this, autocorrelation curves were calculated for a number of cases, and from them, by digital Fourier transformation, the corresponding power spectra were calculated. Three types of autocorrelation functions resulted. The curves for the first type fall more or less smoothly from a maximum at zero lag time, reaching 50% of maximum at lag times of about 0.5 second, and crossing through zero at about 1.5 seconds. The corresponding power spectra have maxima at 0 c.p.s., falling rapidly to zero by about 1 c.p.s. Small-amplitude shorter-period fluctuations in the autocorrelation function produced small peaks of higher frequency in the power spectra between 2.5 and 5 c.p.s. Statistically, it is doubtful whether these peaks are significant. In support of this, the peaks do not seem to occur at the same frequencies in different records. This type of autocorrelation function was obtained for all types of aurora. The second type of auto-

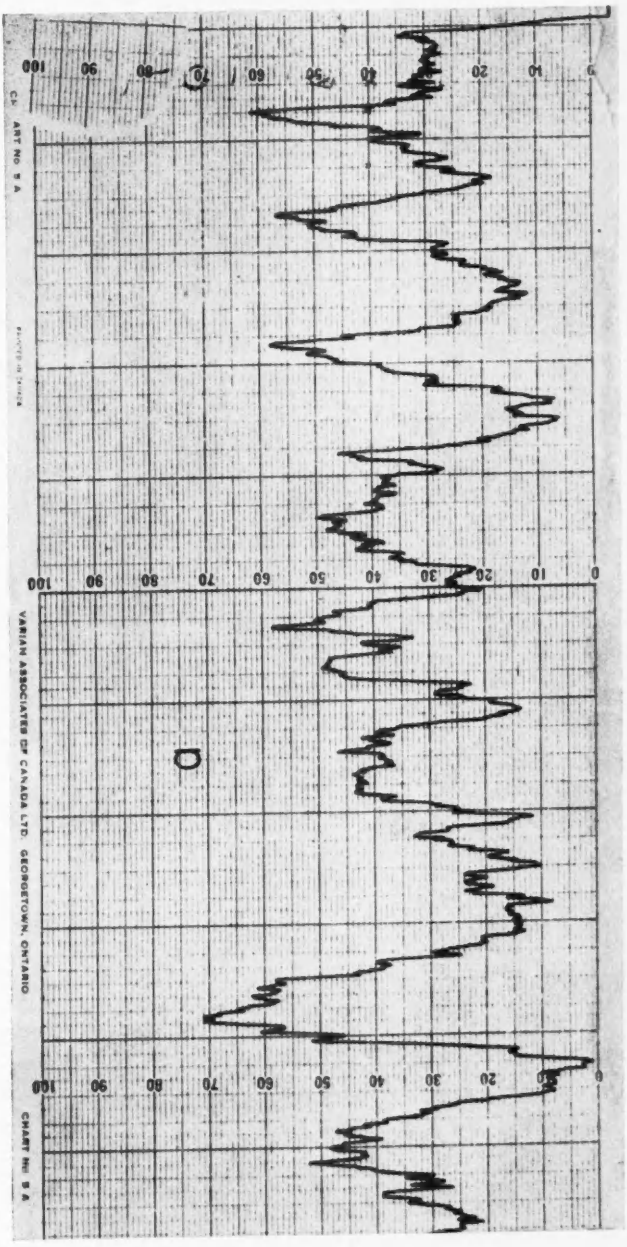
VARIAN ASSOCIATES OF CANADA LTD. GEORGETOWN, ONTARIO
CHART NO. S A

FIG. 1*a*.

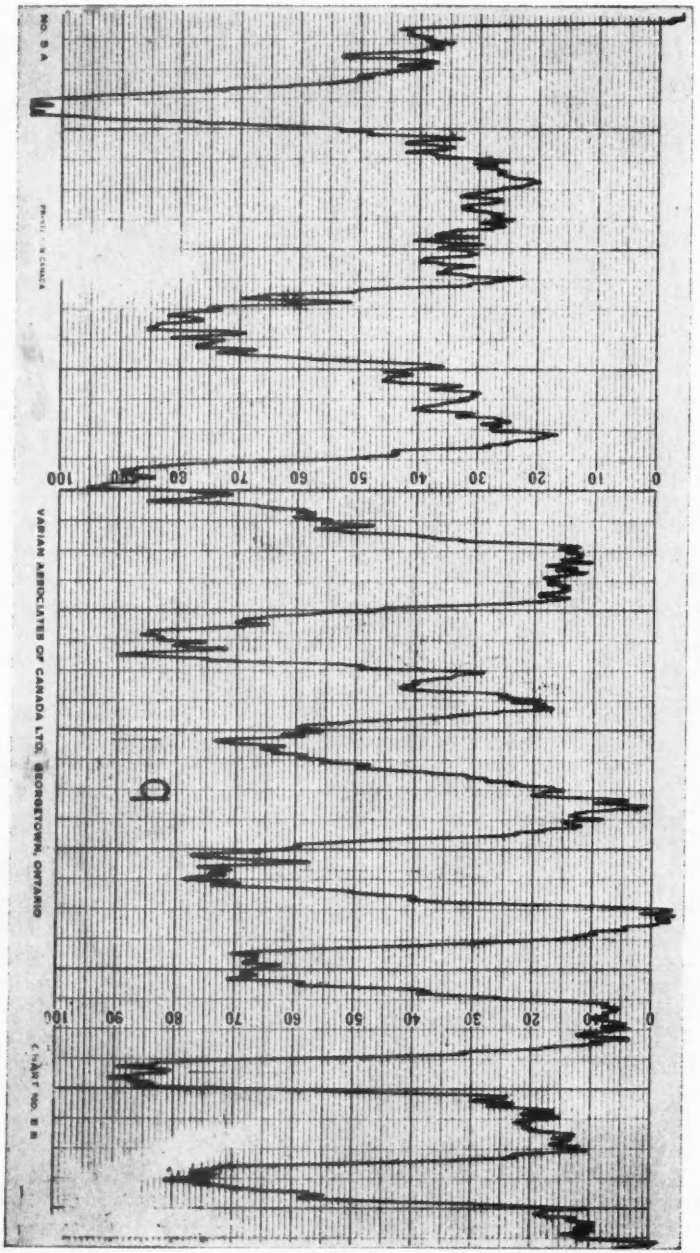
NO. 5 A
VARIAN ASSOCIATES OF CANADA LTD. GEORGETOWN, ONTARIO
b
0 10 20 30 40 50 60 70 80 90 100

FIG. 1*b*.

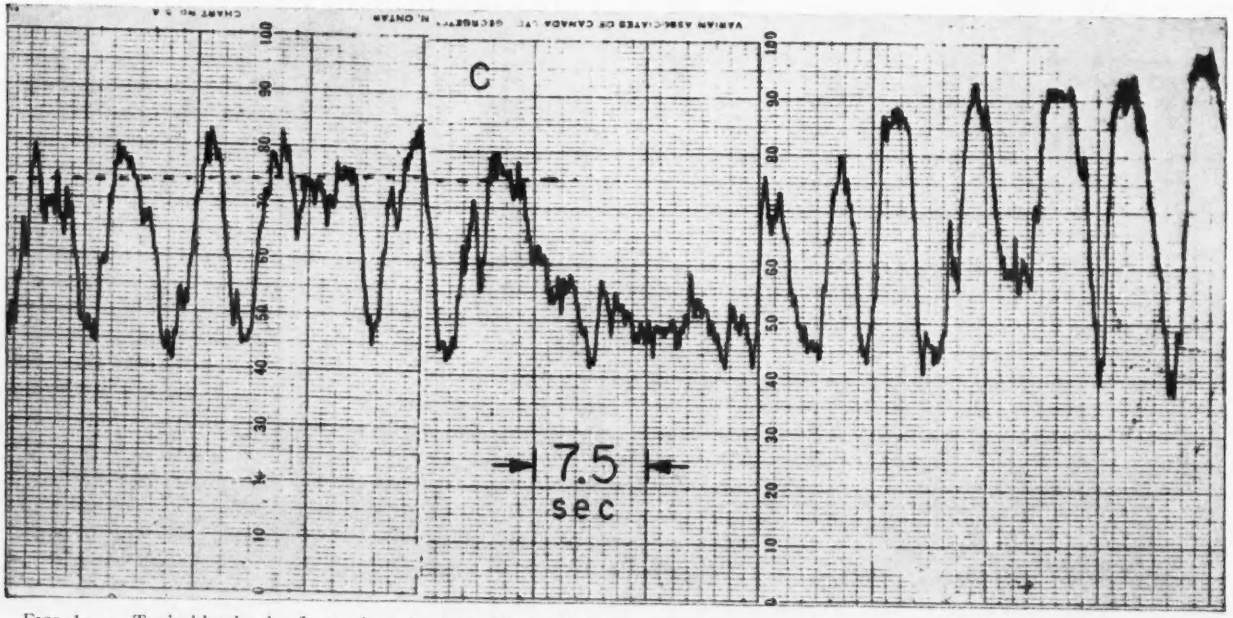

FIGS. 1*a–c*. Typical luminosity fluctuations obtained with the single-channel system using a Varian recorder for (*a*) a homogeneous arc, (*b*) a rayed structure, and (*c*) pulsating aurora. Time increases from right to left.

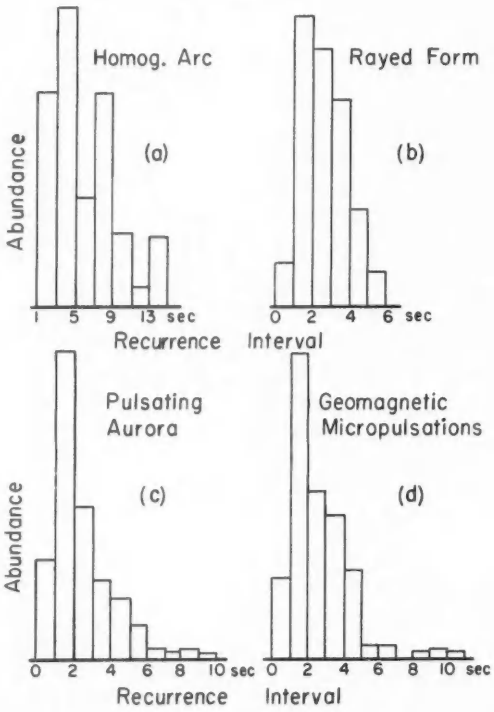

FIG. 2. Histograms of abundance of recurrence interval versus recurrence interval for (*a*) a homogeneous arc, (*b*) a rayed form, (*c*) pulsating aurora, and (*d*) magnetic micropulsations.

correlation function is similar except that the curve falls uniformly towards zero without crossing the axis. An example of this type for a pulsating aurora is shown in Fig. 3(*a*) and the corresponding power spectrum in Fig. 3(*b*). The third, and more striking type of autocorrelation function resembles a damped sinusoid and the result for a pulsating aurora is shown in Fig. 3(*c*). The corresponding power spectrum is shown in Fig. 3(*d*) and has a pronounced peak at 0.2 c.p.s. Only one other analyzed case was so periodic. That was for a homogeneous arc and it gave a peak in the power spectrum at 0.15 c.p.s. On the basis of a small number of cases it thus appears that the fluctuation process is usually random, but not always. Even the random cases are not completely so because some correlation exists over a few seconds.

To get an estimate of the size of the fluctuating volumes the records from the double-photometer system were sorted into three groups by visual inspection. The first group showed detailed correspondence between the features recorded by both channels; the second, correspondence of large-scale features but not in the detailed structure; and the third, no correspondence in any respect. (The term correspondence is used in place of correlation since the

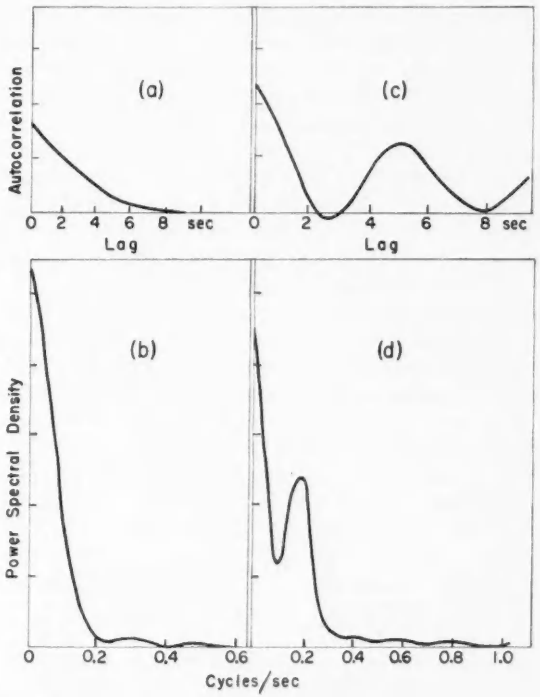

FIG. 3. (*a*) Autocorrelation function for fluctuations from a pulsating aurora. (*b*) Power spectrum corresponding to (*a*). (*c*) Autocorrelation function for fluctuations from a different pulsating aurora. (*d*) Power spectrum corresponding to (*c*).

cross correlations were not calculated.) The number of cases of quiet, rayed, or pulsating aurora in each group was noted. The results, given in Table I, indicate that the best correspondence is for rayed and pulsating forms. The

TABLE I

Correspondence of two-channel signals for different auroral forms

Type of correspondence	Number of observations (%)		
	Quiet forms	Rayed forms	Pulsating forms
Detailed correspondence	26	45	43
General correspondence	37	41	43
No correspondence	37	14	14

quiet forms show poorest correspondence between the signals obtained from the two channels. This suggests that for rayed and pulsating forms the fluctuating volumes are often larger than 3° in angular extent and for quiet forms the fluctuating volumes are more often smaller than this.

CONCLUSIONS

Any conclusions drawn at this stage must necessarily be considered tentative. All types of aurora exhibit fluctuations part of the time. Histograms of the recurrence periods of the fluctuations are sharply peaked for recurrence times of a few seconds. Autocorrelation functions show that the fluctuation pattern is fairly random in most cases, with time correlation extending over only a few seconds. Two cases were remarkably periodic. Observations made with two fields of view 3° apart indicate that for rayed and pulsating forms the fluctuating volume is more often greater than 3°, while for quiet forms it is more often less than 3°. This last conclusion is difficult to reconcile with the occurrence of a periodic fluctuation in a homogeneous arc, since it would imply small, independent, periodically fluctuating volumes. Magnetic micropulsations have been observed occurring in California simultaneously with pulsating aurora in Saskatoon. Histograms of recurrence times for the two are very similar. Much more work needs to be done and is continuing.

The authors wish to thank Dr. P. A. Forsyth for suggesting the problem, Dr. B. W. Currie for many helpful suggestions, and Dr. H. Benioff for supplying the micropulsation records.

ASHBURN, E. V. 1955. J. Geophys. Research, **60**, 205.
CAMPBELL, W. H. and REES, M. H. 1961. J. Geophys. Research, **66**, 41.
DUFFUS, H. J., SHAND, J. A., and WRIGHT, C. S. 1960. Pacific Naval Laboratory Report, **60**, Defence Research Board, Ottawa.
DZHORDZHIO, N. V. 1959. Publ. Acad. Sci. U.S.S.R. **1**, Moscow.
MURCRAY, W. B. 1959. J. Geophys. Research, **64**, 955.
OMHOLT, A. and HARANG, L. 1955. J. Atmospheric and Terrest. Phys. **7**, 247.
PENN, W. D. and CURRIE, B. W. 1949. Can. J. Research, **27A**, 45.
STOFFREGEN, W. and DERBLOM, H. 1960. Nature, **185**, 27.

RECEIVED AUGUST 18, 1961.
INSTITUTE OF UPPER ATMOSPHERIC PHYSICS,
UNIVERSITY OF SASKATCHEWAN,
SASKATOON, SASKATCHEWAN.

SOME NEW OBSERVATIONS ON THE GROWING OF CADMIUM SINGLE CRYSTALS

DORA K. DE GRINBERG

During the growth of Cd single crystals by the Bridgman method some observations were made on the relation between the crystal orientation, the traveling rate of the mold through the furnace, and the nature of the mold.

The single crystals, of a 6 mm diameter, were grown in a vertical furnace. The impurity content was: Pb, 0.0001%; Cu, 0.0001%; Tl, 0.0005%; Zn, 0.001%.

To avoid oxidation of the sample and contamination by the atmosphere, the furnace was first evacuated and then a current of argon circulated through the furnace during heating, traversing, and cooling down of the sample.

The thermal gradient was kept fixed at 15° C/cm, the rate of travel of the sample was changed by means of a gear box.

Two types of molds have been used: (*a*) glass molds prepared from Veridia tubes with 6 mm internal diameter and 2 mm wall thickness; (*b*) graphite molds with 6 mm internal diameter and 20 mm external diameter.

To verify that the crystals obtained were single crystals the following etching was used:

Saturated solution of $CuCl_2$ in H_2O	10 cc,
HCl	5 cc,
HNO_3	1 cc,
H_2O	84 cc.

All the material introduced in the mold was converted into a single crystal, except for a small portion at the tip of the mold, of no more than 5 mm length. The single crystal was nucleated from this polycrystalline portion.

The results obtained when the rate of traveling is changed are given in Table I. It can be seen that for different molds the ranges of rates producing single crystals are shifted. The crystal orientation was measured by X rays.

TABLE I

Mold	Traveling rate (mm/hr)	Result	Length of the single crystal (mm)
Glass	25–60	Single crystal	150–180 (all material)
Glass	60–100	Bi- and tri-crystals	40–60
Glass	>100	Policrystals	10–30
Graphite	15–50	Single crystal	150–180 (all material)
Graphite	50–80	Bi- and tri-crystals	40–60
Graphite	>80	Not tested	Not tested

Several observations can be made on the relationship between the orientation of the basal plane and the traveling rate when the thermal gradient is

fixed. These are shown in Fig. 1 where we have plotted χ versus v, χ being the angle between the crystal axis and the basal plane, and v, the traveling rate through the furnace.

Our results, using the Bridgman method, confirm previous observations on crystals grown by the method of Stöber. In fact, during the growing of single

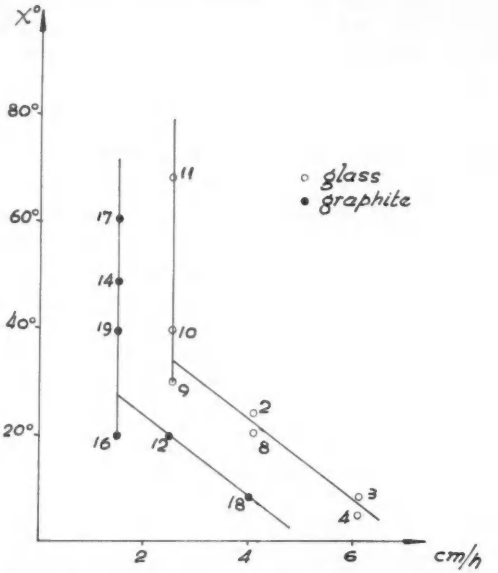

FIG. 1. Curve representing the basal plane orientation as a function of traveling velocity, for two different moulds.

crystals in a fixed thermal gradient, the most compact atomic plane lies parallel to the highest thermal gradient. From the figure, it follows that for decreasing values of v, χ increases linearly until a critical value of v is reached (25 mm/hr for glass molds, 15 mm/hr for graphite molds). At this critical velocity the orientation is at random.

Our interpretation of these results is as follows. For fast growing crystals, the isotherms inside the mold are ellipses elongated in the direction of the mold axis. Therefore, the basal plane is parallel to the major axis of the ellipse. When the rate of traveling slows down the ellipse becomes a circumference; in this case, the orientation of the basal plane with respect to the mold axis will be at random.

By changing the mold (graphite instead of glass), a proof of this interpretation is obtained. The graphite, a better conductor than glass, gives a curve shifted with respect to the curve of the glass mold (Fig. 1), and the direction of this shift is the predicted one. The shape of both curves is the same.

When the orientation of a fixed direction on the basal plane is represented in terms of the rate v, a very interesting fact can be observed. If we plot λ,

angle between the [$1\bar{1}20$] direction (the most compact direction on the basal plane) and the crystal axis, it is found that λ is a linear function of v for $v > 25$ mm/hr. For $v < 25$ mm/hr, λ is distributed at random. These results were obtained with glass molds.

With the graphite molds an irregular distribution is obtained by plotting the angle λ defined above. However, if we take the angle between the [$\bar{2}1\bar{3}0$] direction and the crystal axis we obtain a curve that is identical with the one for [$1\bar{1}20$] for glass but shifted (Fig. 2).

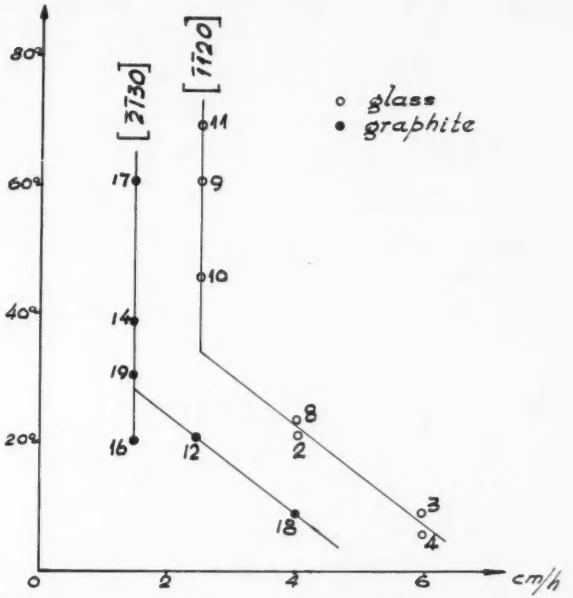

FIG. 2. Curve representing a fixed direction on the basal plane as a function of the traveling rate. [$1\bar{1}20$] direction for glass molds. [$\bar{1}230$] direction for graphite molds.

The [$\bar{2}1\bar{3}0$] direction may result from the simultaneous action of two [1120] directions.

In comparing Figs. 1 and 2 it can be seen that the directions found in both cases follow the same law as that of the basal plane.

These results suggest a marked effect of the anisotropy of the thermal conduction in hexagonal closed packed metals on the orientation of the single crystals.

Thanks are due to the Department of Metallurgy of the Sheffield University, where this work was performed, and to the University of Buenos Aires which made possible the author's stay in Sheffield.

RECEIVED MARCH 6, 1961.
DEPARTMENT OF PHYSICS,
UNIVERSITY OF BUENOS AIRES,
BUENOS AIRES,
ARGENTINA.

Under this heading brief reports of important discoveries in physics may be published. These reports should not exceed 600 words and, for any issue, should be submitted not later than six weeks previous to the first day of the month of issue. No proof will be sent to the authors.

Cyclotron Resonance in Antimony

The tilted-ellipsoidal Fermi surface model proposed by Shoenberg (1952) accounts for cyclotron resonance of electrons in antimony (Datars and Dexter 1961). However, in contrast to the electron model, there have been very limited data pointing to any model for the Fermi surface of holes in antimony. In the investigations with antimony reported in this letter two cyclotron masses, in addition to these resulting from the tilted-ellipsoidal Fermi surface, have been observed. These results suggest the existence of two groups of holes in antimony.

The cyclotron resonance experiments were performed at 1.5° K with a conventional microwave bridge operating at 34.3 kMc/sec and with magnetic fields up to 15 kilo-oersteds. Suitable samples were obtained from a zone-refined antimony crystal supplied by the Consolidated Mining and Smelting Company. Crystal surfaces that contained the binary-bisectrix plane were cleaved, and surfaces that contained the binary-trigonal plane and bisectrix-trigonal plane were cut with a wire saw and electropolished. The resulting plane and shiny surfaces were mounted in turn as part of the end wall of a TE_{111} cylindrical cavity. The magnetic field H was parallel to the sample surface to within 1 degree, and possible electron spin resonance was eliminated by setting the microwave magnetic field along H. Measurements of absorption derivative as a function of magnetic field were taken for many magnetic field directions in the sample surfaces. Cyclotron mass values were determined from the positions of absorption derivative maxima according to the method outlined by Kip (1960).

Figure 1 shows data taken with H along the trigonal axis and parallel to a binary-trigonal sample surface. The signal at 1060 oersteds in Fig. 1 is the superposition of three signals that are separated for other directions of H in the binary-trigonal plane. Since for the trigonal

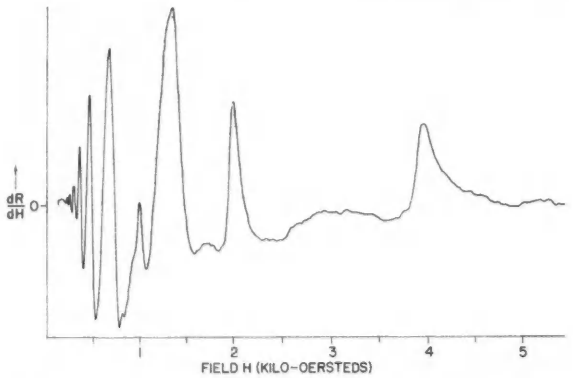

FIG. 1. Cyclotron resonance in antimony at 34.3 kMc/sec and 1.5° K with H parallel to the trigonal axis and to the microwave magnetic field.

direction the tilted ellipsoids are equivalent and signals from each ellipsoid should coincide, the above resonance can reasonably be ascribed to carriers on the tilted-ellipsoidal Fermi surface. The electron mass for the trigonal direction is $(0.088\pm.005)\ m_0$. Further inspection of Fig. 1 shows two Azbel'–Kaner (1958) resonances that are not related to the tilted-ellipsoidal Fermi surface. One resonance at $(0.11\pm.005)\ m_0$ consists of a fundamental resonance at 1340 oersteds and subharmonic resonances at 670, 435, 330, 270, 225, and 190 oersteds. The other resonance is at $(0.32\pm.02)\ m_0$ and has a fundamental resonance at 4000 oersteds with one subharmonic at 2000 oersteds. The carriers $0.088\ m_0$, $0.11\ m_0$, and $0.32\ m_0$ are tentatively identified as electrons, light holes, and heavy holes respectively.

The cyclotron resonance of electrons contains several subharmonics in regions where they do not coincide with the stronger, light-hole resonance and has an $\omega\tau$ of approximately 20. For the heavy-hole resonance, $\omega\tau = 15$. On the other hand, the light-hole resonance with up to six resolved subharmonic resonances has $\omega\tau = 45$. The light hole appears to be a majority carrier in the samples of antimony used in this experiment.

The present experiment supports the theoretical view of Harrison (1960) that the Fermi surface of holes in antimony is probably quite complex. The two masses for a trigonal-directed magnetic field indicate that the hole Fermi surface may consist of two quite distinct parts. While the resonance from the light holes was reasonably isotropic for directions of magnetic field in the three principal crystal planes, a simple model for the light-hole surface such as a spheroid centered about the trigonal axis is not consistent with the data. The resonance which is attributed to heavy holes showed an anisotropy which did not suggest an ellipsoidal model and had a line shape which depended on magnetic field direction. This indicates that there may be a warped surface for the heavy-hole carriers. Work is continuing to clarify the shape of the Fermi surface of antimony.

The author wishes to acknowledge the helpful interest of Professor R. N. Dexter in this work.

AZBEL', M. IA. and KANER, E. A. 1958. J. Phys. Chem. Solids, **6**, 113.
DATARS, W. R. and DEXTER, R. N. 1961. Phys. Rev. **124**, 75.
HARRISON, W. A. 1960. J. Phys. Chem. Solids, **17**, 171.
KIP, A. F. 1960. The fermi surface, *edited by* W. A. Harrison and M. B. Webb (John Wiley & Sons), p. 146ff.
SHOENBERG, D. 1952. Phil. Trans. Roy. Soc. A. **245**, 1.

RECEIVED OCTOBER 2, 1961.
W. R. DATARS
DEFENCE RESEARCH TELECOMMUNICATIONS ESTABLISHMENT,
OTTAWA, ONTARIO.

CONTENTS OF VOLUME 39

Adey, A. W. and **Heikkila, W. J.** Rocket electron density measurements at Fort Churchill, Canada, 219.

Almqvist, E. and **Kuehner, J. A.** Magnetic spectrometer measurements of levels of Ne^{20}, 1246.

Artna, A. and **Johns, M. W.** The decay of Er^{171}, 1817.

Axford, W. I. Note on a mechanism for the vertical transport of ionization in the ionosphere, 1393.

Axford, W. I. and **Hines, C. O.** A unifying theory of high-latitude geophysical phenomena and geomagnetic storms, 1433.

Bachynski, M. P. See French, I.P., 1273; Graf, K. A., 1544.

Baird, K. M. See Hart, K. H., 781.

Baker, K. D. and **Currie, B. W.** An observation of noctilucent clouds in Western Canada, 1515.

Baker, R. G. and **McNeill, K. G.** Angular distribution of fast photoneutrons, 1158.

Balk, P. See Benson, G. C., 1071.

Basinski, S. J. See Bland, J. A., 1040.

Batchelor, R. See Litherland, A. E., 276.

Batthyany, I. and **Demers, P.** Dimensions des grains au cours de la précipitation des émulsions ionographiques, 608.

Bayly, J. G., Duret, M. F., Poulsen, N. B., and **Tomlinson, R. H.** The Xe^{135} yield in thermal fission of Pu^{239}, 1391.

Bell, R. E. See Kavanagh, T. M., 1172.

Belrose, J. S. and **Ross, D. B.** Observations of unusual low-frequency propagation made on 12 November, 1960, 609.

Benson, G. C. and **Balk, P.** Estimation of the effect of surface on the dipolar broadening of magnetic resonance lines in crystals, 1071.

Betts, D. D. The extension of Houston's method with application to Debye Θ_0, 233.

Betts, R. H. See Glentworth, P., 381.

Bhattacharyya, B. K. Dipole-field type magnetic disturbances and auroral activities, 350.

Biloni, H. Substructures and dislocations produced during solidification of aluminum, 1501.

Bishop, R. L. See Magarvey, R. H., 1418.

Bland, J. A. and **Basinski, S. J.** The crystal structure of Bi_2Te_2Se, 1040.

Bland, J. A. and **Flengas, S. N.** The crystal structure of K_2TiCl_6, 941.

Bleakney, H. H. Vacancies and the Kirkendall effect, 947.

Blevis, B. C. See Serson, H. V., 622.

Bloom, M. See Lipsicas, M., 881; Oppenheim, I., 845.

Bloom, M., Lipsicas, M., and **Muller, B. H.** Proton spin–lattice relaxation in polyatomic gases, 1093.

Boivin, A. and **Tremblay, R.** Interféromètre micro-onde à fond cohérent, 393.

Boivin, G. See Lansraux, G., 158.

Bourret, R. C. Turbulent diffusion in two and three dimensions by the random-walk model with memory, 133.

Brand, J. C. D., Callomon, J. H., and **Watson, J. K. G.** The 3820-Å $^1A'' \leftarrow {}^1A'$ transition of propynal, 1508.

Brown, F. See Graham, R. L., 1086.

Brown, F., Graham, R. L., Ewan, G. T., and **Uhler, J.** The conversion electron spectrum from a mass-separated source of Xe^{133}, 779.

Brown, R. F. Effect of two-dimensional mechanical stress on the dielectric properties of poled ceramic barium titanate and lead zirconate titanate, 741.

Buckmaster, H. A. Angular variation of axial spin-Hamiltonian eigenvalues in strong magnetic field, 1073.

Budzinski, E. See McDiarmid, I. B., 1888.

Bukata, R. P. See Standil, S., 229.

Bullock, W. R. and **Hunten, D. M.** Vertical distribution of sodium in the upper atmosphere, 976.

Callomon, J. H. See Brand, J. C. D., 1508.

Cameron, J. A. See King, H. J., 230.

Campbell, C. K. Magnetization nutations in maser oscillation pulses, 1514.

Campbell, W. S. and **Hubert, P. L.** The ionospheric disturbance of November 12 and 16, 1960, 614.

Carette, J.-D. and **Kerwin, L.** Une étude du phosphore rouge par spectrométrie de masse, 1300.

Champness, C. H. Magnetoresistance and Hall effect in oriented single crystal samples of *n*-type indium antimonide, 452.

Investigations on the diffusion of minority carriers from a point on silicon, 754.

Chin, F. K. See Standil, S., 229.
Chrien, R. E. Resonance parameters for the 8-ev level of Sm^{152}, 1193.
Clark, J. W. The role of repulsive cores in the photonuclear effect, 385.
Clark, M. A. The lifetime of the 6.25-kev level in Ta^{181}, 1090.
See also Gove, H. E., 1243; Litherland, A. E., 1249.
Clark, M. A., Gove, H. E., and **Litherland, A. E.** Lifetimes of the low-lying levels in Ne^{20}, 1241.
Clark, M. A. and **Robson, J. M.** A polarized neutron beam produced by Bragg reflection from Co–Fe alloy, 1.
The electron asymmetry in the beta decay of polarized neutrons, 13.
Clarke, E. See Kerwin, L., 1240.
Clarke, R. L. The spectrum of neutrons from the irradiation of uranium by 14-Mev neutrons, 957.
See also Hanna, G. C., 967.
Clement, M. J. Y. and **Ramsay, D. A.** Predissociation in the HNO molecule, 205.
Clifford, C. E. Gamma dose in a hole in a uniformly contaminated plane: contribution by ground penetration, 604.
Cloutier, G. G. See French, I. P., 1273.
Cloutier, J. A. R. Room temperature stabilization of radiation-produced free radicals in barbituric acids, 514.
Cloutier, J. A. R., Flann, B. C., and **Manson, J. M.** Study of the effect of gamma radiation on the molecule of pentobarbital, 1465.
Collings, E. W., Hedgcock, F. T., and **Sakudo, T.** Some remarks on the spectroscopic state of paramagnetic ions in dilute alloys exhibiting resistive anomalies, 1233.
Collins, C., Jelly, D. H., and **Matthews, A. G.** High-frequency radio-wave black-outs at medium and high latitudes during a solar cycle, 35.
Conkie, W. R. An iterative method for neutron transport problems with spherical symmetry, 295.
Connor, R. D. and **MacKenzie, D. R.** Higher-energy gamma rays in the decay of neptunium-239, 1595.
Covington, A. E., Harvey, G. A., and **McNarry, L. R.** The solar noise burst of November 12, 1960, 635.
Currie, B. W. See Baker, K. D., 1515.
Curzon, F. L. and **Howard, R.** A proposal to use microwave cavities to study the surface properties of high density plasmas, 1901.
Daniels, J. M., Giles, J. C., and **LeBlanc, M. A. R.** Nuclear orientation in antiferromagnetic single crystals, 53.
Datars, W. R. Cyclotron resonance in antimony, 1922.
Dawson, D. J. See McNeill, K. G., 1010.
Degen, V. See May, A. D., 1769.
Demers, P. See Batthyany, I., 608.
Dionne, J. G. G. See Wilson, B. G., 935.
Douglas, A. E. and **Hollas, J. M.** The 1600 Å band system of ammonia, 479.
Dowling, J. M. See Norris, T. P., 1220.
Duckworth, H. E. The new unit of atomic mass, 639.
Duret, M. F. See Bayly, J. G., 1391.
Eastwood, H. K. See King, H. J., 230.
Edwards, M. H. and **Woodbury, W. C.** Compressibility of liquid He^4, 1833.
Ewan, G. T. See Brown, F., 779; Graham, R. L., 1086.
Farnell, G. W. Elastic waves in trigonal crystals, 65.
Fejer, J. A. Scattering of radio waves by an ionized gas in thermal equilibrium in the presence of a uniform magnetic field, 716.
The effects of energetic trapped particles on magnetospheric motions and ionospheric currents, 1409.
Ferguson, A. J. See Litherland, A. E., 276, 788.
Ferguson, H. I. S. See Herman, L., 476.
Flann, B. C. See Cloutier, J. A. R., 1465.
Flengas, S. N. See Bland, J. A., 941.
Forsyth, P. A. On the association of radio reflections with optical aurora, 1721.
See Hector, F., 1423; Kelly, P. E., 1535.
Forsyth, P. A. and **Paulson, K. V.** Radio-star scintillations and the auroral zone, 502.
Franck, J. P. and **Martin, D. L.** The superconducting transition temperature of lead, 1320.
French, I. P., Cloutier, G. G., and **Bachynski, M. P.** The absorptivity spectrum of a uniform, anisotropic plasma slab, 1273.
Friedberg, S. A. See Swanson, M. L., 1429.
Fritze, K., Kennett, T. J., and **Prestwich, W. V.** Half life, Q_β value, and γ-ray spectrum of La^{143}, 662.
Gauthier, G. and **Marcoux, J.** Mesure du temps de relaxation d'une vibration de N_2O par une méthode infrarouge, 1130.

Geiger, J. S. See Graham, R. L., 1357.
Ghosh, S. N. and **Srivastava, B. N.** Sensitivity of VG-1A ionization gauge calculated from the probability of ionization of gases, 373.
Giles, J. C. See Daniels, J. M., 53.
Glentworth, P. and **Betts, R. H.** Production of Lu^{178} by the Ta^{181} $(n,\alpha)Lu^{178}$ reaction in the NRX reactor, 381.
Gold, A. V. and **Pearson, W. B.** Phonon drag in lead, 445.
Gopal Rao, M. S. V. and **Ramachandra Rao, B.** Effects of equatorial spread-*F* irregularities on c.w. transmissions, 596.
Gordon, R. D. and **King, G. W.** The emission spectrum of the CCl radical, 252.
Gove, H. E. See Clark, M. A., 1241; Litherland, A. E., 276, 471, 1249.
Gove, H. E., Litherland, A. E., and **Clark, M. A.** Alpha–gamma angular correlations in the reaction $C^{12}(C^{12},\alpha)Ne^{20}$, 1243.
Graf, K. A. and **Bachynski, M. P.** Transmission and reflection of electromagnetic waves at a plasma boundary for arbitrary angles of incidence, 1544.
Graham, R. L. See Brown, F., 779.
Graham, R. L., Brown, F., Ewan, G. T., and **Uhler, J.** The *K-LL* Auger spectrum of $_{55}Cs^{133}$, 1086.
Graham, R. L. and **Geiger, J. S.** The application of a fluxgate magnetometer to an automatic electronic degaussing system, 1357.
Graham, R. L. and **Merritt, J. S.** The *K–LL* Auger spectrum of $_{66}Dy^{161}$, 1058.
Grant, R. F. and **Henry, W. G.** The Knight shift of cadmium in some alloys with group IB and IIB metals, 841.
Gravelle, W. E. See McKay, R. W., 534.
Green, R. E. See Walker, W. H., 1184.
Green, R. E. and **Walker, W. H.** The half-life of Sm^{153}, 1216.
Green, R. M. See McNeill, K. G., 1842.
Griffiths, G. M., Morrow, R. A., Riley, P. J., and **Warren, J. B.** The $T(\alpha,\gamma)Li^7$ reaction, 1397.
de Grinberg, D. K. Some new observations on the growing of cadmium single crystals, 1919.
Gupta, I. C. See Roalsvig, J. P., 643.
Hanna, G. C. and **Clarke, R. L.** Neutron evaporation in the 14-Mev neutron fission of uranium, 967.
Hanna, G. C., Primeau, D. B., and **Tunnicliffe, P. R.** Thermal neutron cross sections and resonance integrals of the reactions $O^{17}(n,\alpha)C^{14}$, $Ar^{36}(n,\alpha)S^{33}$, and $N^{14}(n,p)C^{14}$, 1784.
Hansen, D. R. See Kelly, P. E., 1535.
Hart, K. H. and **Baird, K. M.** On the relation between the old and the new definition of the International Metre, 781.
Hartz, T. R. See Vogan, E. L., 630.
Harvey, G. A. See Covington, A. E., 635.
Haslam, R. N. H. See Roalsvig, J. P., 643.
Hawton, J. J. See Roy, J. C., 1528.
Hector, F. and **Forsyth, P. A.** On the statistical properties of optical and radio aurora, 1423.
Hedgcock, F. T. See Collings, E. W., 1233.
Heikkila, W. J. See Adey, A. W., 219.
Heikkila, W. J. and **Penstone, S. R.** Rocket measurements of auroral radio absorption, 1875.
Henry, W. G. See Grant, R. F., 841.
Herman, L., Ferguson, H. I. S., and **Nicholls, R. W.** Excitation of the first negative system of O_2^+ by a proton beam in air and oxygen, 476.
Herzberg, G. The ionization potential of CH_2, 1511.
Hines, C. O. See Axford, W. I., 1433.
Hollas, J. M. See Douglas, A. E., 479.
Holmes, E. L. See Jubb, J. T., 945.
Holmes, E. L. and **Winegard, W. C.** Effect of solute atoms on grain boundary migration in pure metals, 1223.
Horton, G. K. On the thermal expansion of metals at low temperatures, 263.
Howard, R. See Curzon, F. L., 1901.
Howlett, L. E. The new standard for the Metre, 639.
Hubert, P. L. See Campbell, W. S., 614.
Hunten, D. M. See Bullock, W. R., 976.
Hurd, R. A. A note on the diffraction of a scalar wave by a small circular aperture, 1065.
Iyengar, R. S. and **Shepherd, G. G.** Observations of auroral luminosity fluctuations, 1911.
Jarmain, W. R. See McGregor, A. T., 1215.
Jelly, D. H. See Collins, C., 35.
Johns, J. W. C. The absorption spectrum of BO_2, 1738.

Johns, J. W. C. and **Ramsay, D. A.** The absorption spectrum and dissociation energy of SH, 210.
Johns, M. W. See Artna, A., 1817.
Johnson, E. F. See Scheidegger, A. E., 326.
Jones, G. and **Warren, J. B.** The lifetimes of positrons in metals, 1517.
Jubb, J. T., Holmes, E. L., and **Winegard, W. C.** Concerning the distribution coefficient of gold in lead, 945.
Jursa, A. S. See Tanaka, Y., 1138.
Kaempffer, F. A. Representation of space inversion, time reversal, and particle conjugation in quantum field theory, 22.
The distance correlation between photons in black body radiation, 473.
Kalra, S. N. Frequency measurement of standard frequency transmissions, 228, 380, 477, 637, 778, 956, 1092, 1252.
van Kampen, N. G. A power series expansion of the master equation, 551.
Katzman, J. Changes in the diurnal hour of maximum of the cosmic-ray intensity, 1477.
Kavanagh, T. M. and **Bell, R. E.** Cross sections of (p,pxn) reactions in Au^{197}, 1172.
Kelly, P. E., Hansen, D. R., and **Forsyth, P. A.** The azimuthal distribution of ultra-high frequency radar echoes from aurora, 1535.
Kennett, T. J. See Fritze, K., 662.
Kerwin, L. See Carette, J.-D., 1300.
Kerwin, L., Marmet, P., and **Clarke, E.** The identification of vibrational levels in H_2^+, 1240.
Kidson, G. and **McGurn, J.** Self-diffusion in body-centered cubic zirconium, 1146.
King, G. W. See Gordon, R. D., 252.
King, H. J., Cameron, J. A., Eastwood, H. K., and **Summers-Gill, R. G.** The nuclear spin of indium-115*m*, 230.
Kipling, A. L., Smith, P. W., Vanier, J., and **Woonton, G. A.** The concentration dependence of paramagnetic relaxation in dilute potassium chromi- and ferri-cyanides at liquid helium temperature, 1859.
Koch, J. W. See Van Name, F. W., Jr., 1212.
Kornelsen, R. O. The structure of manganese arsenide between 40° C and 120° C, 1728.
Ksienski, A. Equivalence between continuous and discrete radiating arrays, 335.
Kuehner, J. A. See Almqvist, E., 1246.
Lapointe, S. M. See Rose, D. C., 239.
Lapointe, S. M. and **Rose, D. C.** The effective directional sensitivity of cosmic-ray neutron monitors, 668.
Lansraux, G. and **Boivin, G.** Maximum of the factor of encircled energy, 158.
Laubitz, M. J. Mathematical treatment of a four-component furnace, 951.
On measurement of thermal conductivity at high temperatures, 1029.
LeBlanc, M. A. R. See Daniels, J. M., 53.
Lee, Y. Y. On the temperature dependence of paramagnetic resonance in the case of the Ising model, 1733.
Lipsicas, M. See Bloom, M., 1093.
Lipsicas, M. and **Bloom, M.** Nuclear magnetic resonance measurements in hydrogen gas, 881.
Litherland, A. E. The interpretation of angular distributions and angular correlations from the reaction $C^{12}(C^{12},\alpha\gamma)Ne^{20}$, 1245.
See also Clark, M. A., 1241; Gove, H. E., 1243.
Litherland, A. E., Batchelor, R., Ferguson, A. J., and **Gove, H. E.** Excited states of O^{18} studied by the reaction $H^3(O^{16}_{4+}, p\gamma)O^{18}$, 276.
Litherland, A. E., Clark, M. A., and **Gove, H. E.** A 7.02-Mev level in Ne^{20}, 1249.
Litherland, A. E. and **Ferguson, A. J.** Gamma-ray angular correlations from aligned nuclei produced by nuclear reactions, 788.
Litherland, A. E. and **Gove, H. E.** Linearly polarized gamma rays from nuclear reactions, 471.
Lockwood, G. E. K. Determination of radar auroral heights with the Prince Albert radar, 1725.
Loh, S. C. Uncharged conducting toroidal ring in a uniform electric field, 1495.
McDiarmid, I. B. See Wilson, M. D., 1730.
McDiarmid, I. B., Rose, D. C., and **Budzinski, E.** Direct measurement of charged particles associated with auroral zone radio absorption, 1888.
McEwen, D. J. See Montalbetti, R., 617.
McFarlane, R. A. The finite beam space-charge limited diode as a noise transducer, 568.
Microwave noise in accelerated electron streams, 579.
McGregor, A. T., Nicholls, R. W., and **Jarmain, W. R.** Franck–Condon factors and *r*-centroids for some bands of the SiO $A^1\Pi$–$X^1\Sigma^+$ band system, 1215.
McGuire, J. H. An absolute thermal radiation calorimeter, 1583.
McGurn, J. See Kidson, G., 1146.

McIntosh, B. A. Analysis of a type of rough-trail meteor echo, 437.
McKay, R. W. and **Gravelle, W. E.** The Hall effect and resistivity of tellurium, 534.
MacKenzie, D. R. See Connor, R. D., 1595.
McLaren, E. H. and **Weinberg, F.** Zn:Tl phase diagram at very low thallium concentrations, 588.
McLay, A. B. See Pieczonka, W. A., 145.
McNamara, A. G. Auroral radar observations at 48 Mc/s during the period of the 12 November, 1960, solar event, 625.
McMillan, M. and **Opechowski, W.** The temperature dependence of the shape of paramagnetic resonance lines. Part II, 1369.
McNarry, L. R. See Covington, A. E., 635.
McNeill, K. G. See Baker, R. G., 1158.
McNeill, K. G. and **Green, R. M.** Scintillation spectra from thick sources, 1842.
McNeill, K. G. and **Prentice, J. D.** The 1.2-Mev beta decay of I^{128}, 1080.
McNeill, K. G., Trojan, O. A. D., and **Dawson, D. J.** Gamma-active fall-out in Ontario 1958–60, 1010.
McPherson, R. See Taylor, H. W., 1235.
Magarvey, R. H. and **Bishop, R. L.** Transition ranges for three-dimensional wakes, 1418.
Manson, J. M. See Cloutier, J. A. R., 1465.
Marcoux, J. See Gauthier, G., 1130.
Marmet, P. See Kerwin, L., 1240.
Martin, D. L. Specific heat anomalies associated with the resistance-minimum phenomena in magnesium–manganese alloys, 1385.
The electronic specific heat of lithium–magnesium alloys, 1388.
See also Franck, J. P., 1320.
Matthews, A. G. See Collins, C., 35.
May, A. D., Degen, V., Stryland, J. C., and **Welsh, H. L.** The Raman effect in gaseous hydrogen at high pressures, 1769.
Maynard, L. A. Propagation of meteor burst signals during the polar disturbance of November 12–16, 1960, 628.
Merritt, J. S. See Graham, R. L., 1058.
Millar, R. F. Scattering by a grating. I, 81.
Scattering by a grating. II, 104.
Montalbetti, R. and **McEwen, D. J.** Hydrogen emissions during the period November 9–16, 1960, 617.
Moorcroft, D. R. Models of auroral ionization. Part I. Auroral ionization models and their radio-reflection characteristics, 677.
Models of auroral ionization. Part II. Applications to radio observations of aurora, 695.
Morrow, R. A. See Griffiths, G. M., 1397.
Muller, B. H. See Bloom, M., 1093.
Mulliken, R. S. See Verma, R. D., 908.
Namioka, T. See Tanaka, Y., 1138.
Needler, G. T. and **Opechowski, W.** On the nuclear spin relaxation in hydrogen gas, 870.
Niblett, E. R. Geomagnetic variations between November 12 and November 16, 1960, 619.
Nicholls, R. W. See Herman, L., 476; McGregor, A. T., 1215.
Nilson, J. A. See Shepherd, G. G., 1807.
Nilson, W. G. The effect of quenching and neutron irradiation on internal friction of aluminum – 5% magnesium alloy, 119.
Niven, C. D. The electrical conductivity of gelatin film humidified with heavy water vapor, 657.
A psychrometer table for heavy water humidities, 825.
The friction of heated bismuth, 1264.
Norris, T. P. and **Dowling, J. M.** Calculation of the ν_2 and inversion energy levels for ammonia and some of its isotopically substituted species, 1220.
Noxon, J. F. Observation of the $(b^1\Sigma_g^+ - a^1\Delta_g)$ transition in O_2, 1110.
Noxon, J. F. and **Vallance Jones, A.** A balloon-borne spectrometer for study of the airglow beyond 2.0 μ, 1120.
Olafson, R. A., Thomas, M. A., and **Welsh, H. L.** The Raman spectrum of methane-d_4, 419.
Oleksiuk, L. W. See Storey, R. S., 917.
Opechowski, W. See McMillan, M., 1369; Needler, G. T., 870.
Oppenheim, I. and **Bloom, M.** Nuclear spin relaxation in gases and liquids. I. Correlation functions, 845.
Owyang, G. H. Theory and design of a coaxial supporting bead made of composite dielectrics, 926.
Paulson, K. V. See Forsyth, P. A., 502; Shepherd, G. G., 1807.

Pearson, W. B. See Gold, A. V., 445.
Pearson, W. B. and **Templeton, I. M.** The effect of dissolved iron on the thermoelectricity of silver at very low temperatures, 1084.
Penstone, S. R. See Heikkila, W. J., 1875.
Petch, H. E. See Pieczonka, W. A., 145.
Pieczonka, W. A., Petch, H. E., and **McLay, A. B.** An electron spin resonance study of manganese impurity in brucite, 145.
Poll, J. D. and **Van Kranendonk, J.** Theory of translational absorption in gases, 189.
Poulsen, N. B. See Bayly, J. G., 1391.
Prentice, J. D. See McNeill, K. G., 1080.
Prescott, J. R. and **Rupaal, A. S.** The specific fluorescence of plastic scintillator NE102, 221.
Prestwich, W. V. See Fritze, K., 662.
Primeau, D. B. See Hanna, G. C., 1784.
Raghavacharyulu, I. V. V. Representations of space groups, 830.
Normal modes of vibrations of crystals, 1704.
Ramachandra Rao, B. See Gopal Rao, M.S.V., 596.
Ramsay, D. A. See Clement, M. J. Y., 205; Johns, J. W. C., 210.
Rastall, P. Mach's principle and scalar theories of gravitation, 218.
Riley, P. J. See Griffiths, G. M., 1397.
Roalsvig, J. P., Gupta, I. C., and **Haslam, R. N. H.** Photoneutron reactions in C^{12} and O^{16}, 643.
Roberts, P. H. On Bourret's hypothesis concerning turbulent diffusion, 1291.
Robson, J. M. See Clark, M. A., 1, 13.
Rose, D. C. See Lapointe, S. M., 668; McDiarmid, I. B., 1888.
Rose, D. C. and **Lapointe, S. M.** Asymmetry in the recovery from a very deep Forbush-type decrease in cosmic-ray intensity, 239.
Ross, D. B. See Belrose, J. S., 609.
Ross, R. A. The effect of an explosion in a compressible fluid under gravity, 1330.
Roy, J. C. On the production of Be^7, Mg^{28}, and Ni^{66} in the slow neutron fission of U^{235}, 315.
Roy, J. C. and **Hawton, J. J.** The $B^{10}(\alpha,n)N^{13}$ and $B^{10}(t,2n)C^{11}$ reactions in a nuclear reactor, 1528.
Rupaal, A. S. See Prescott, J. R., 221.
Sakudo, T. See Collings, E. W., 1233.
Scheidegger, A. E. Dynamic similarity of instabilities of displacement fronts in porous media, 1253.
On the statistical properties of some transport equations, 1573.
Scheidegger, A. E. and **Johnson, E. F.** The statistical behavior of instabilities in displacement processes in porous media, 326.
Serson, H. V. and **Blevis, B. C.** Observations of auroral ionization during the period November 11–16, 1960, 622.
Shepertycki, T. H. The autocorrelation function of symmetrically folded Gaussian noise, 1851.
Shepherd, G. G. See Iyengar, R. S., 1911.
Shepherd, G. G., Paulson, K. V., and **Nilson, J. A.** Stereo-projection systems for auroral height measurements, 1807.
Shepherd, L. T. and **Skarsgard, H. M.** Radio-frequency breakdown controlled by drift of electrons in an inhomogeneous magnetic field, 983.
Shkarofsky, I. P. Values of the transport coefficients in a plasma for any degree of ionization based on a Maxwellian distribution, 1619.
Skarsgard, H. M. See Shepherd, L. T., 983.
Smith, A. W. and **Williams, G. W.** Strain in crystals of yttrium iron garnet, 768.
Smith, P. W. See Kipling, A. L., 1859.
Srivastava, B. N. See Ghosh, S. N., 373.
Standil, S., Bukata, R. P., and **Chin, F. K.** The sudden increase in the photon component of cosmic radiation on May 4, 1960, 229.
Stevenson, R. Typical failures in pulsed field magnet coils, 367.
Storey, R. S. and **Oleksiuk, L. W.** Low-lying energy levels in Cl-35, 917.
Stryland, J. C. See May, A. D., 1769.
Summers-Gill, R. G. See King, H. J., 230.
Sundaram, S. Potential energy constants, rotational distortion constants, and thermodynamic properties of stibine, 370.
Swanson, M. L. and **Friedberg, S. A.** The electrical resistivity of Mn_3ZnC between 4.2° and 630° K, 1429.
Tanaka, Y., Namioka, T., and **Jursa, A. S.** New emission bands of N_2^+, $^2\Pi_g - A\,^2\Pi_u$, 1138.
Tang, C. L. High-frequency diffraction by a sphere, 1486.
Taylor, H. W. and **McPherson, R.** Directional correlation of the 769–609 kev gamma-ray cascade in Po^{214}, 1235.
Templeton, I. M. See Pearson, W. B., 1084.

Terentiuk, F. See Wilson, B. G., 935.
Thomas, M. A. See Olafson, R. A., 419.
Tomlinson, R. H. See Bayly, J. G., 1391.
Tremblay, R. Déphaseur micro-onde à prismes diélectriques, 409.
See also Boivin, A., 393.
Trojan, O. A. D. See McNeill, K. G., 1010.
Tudge, A. P. Studies in chromatographic transport. I. A simplified theory, 1600.
Studies in chromatographic transport. II. The effect of adsorption isotherm shape, 1611.
Tunnicliffe, P. R. See Hanna, G. C., 1784.
Uhler, J. See Brown, F., 779; Graham, R. L., 1086.
Vallance Jones, A. See Noxon, J. F., 1120.
Van Kranendonk, J. General formula for the second virial coefficient, 1563.
See also Poll, J. D., 189.
Van Name, F. W., Jr. and **Koch, J. W.** Angular correlation of beta–gamma coincidences in the Compton effect, 1212.
Vanier, J. See Kipling, A. L., 1859.
Venables, H. A. Maxwell's equations and matrix elements in quantum electrodynamics, 141.
Representations of the unitary group and wave functions, 510.
Verma, R. D. New spectrum of CF^+, 1377.
Verma, R. D. and **Mulliken, R. S.** A $^1\Sigma^- - {}^3\Pi_r$ spectrum of SiO, 908.
Villeneuve, A. T. Application of Fourier transforms to antenna pattern synthesis, 1347.
Vogan, E. L. and **Hartz, T. R.** Ionospheric absorption on November 12, 1960, 630.
Volkoff, G. M. A note on some properties of Hamiltonians involving spin matrices for half-integral values of I, 1226.
Wait, J. R. The electromagnetic fields of a horizontal dipole in the presence of a conducting half-space, 1017.
Walker, W. H. See Green, R. E., 1216.
Walker, W. H. and **Green, R. E.** The ratio of the resonance integral to the thermal neutron cross section for Sm^{152}, 1184.
Warren, J. B. See Griffiths, G. M., 1397; Jones, G., 1517.
Watanabe, T. Waves in a rarefied ionized gas propagated transverse to an external magnetic field, 1044.
Alfvén waves in partially ionized gases, 1197.
Watson, J. K. G. See Brand, J. C. D., 1508.
Weinberg, F. See McLaren, E. H., 588.
Welsh, H. L. See May, A. D., 1769; Olafson, R. A., 419.
Weston, V. H. The pressure pulse produced by a large explosion in the atmosphere, 993.
Williams, G. W. See Smith, A. W., 768.
Williams, W. E. Refraction and diffraction of pulses, 272.
Wilson, B. G., Dionne, J. G. G., and **Terentiuk, F.** Variations in solar time of extensive air showers, 935.
Wilson, M. D. and **McDiarmid, I. B.** Transition curves in lead for μ-meson induced showers, 1730.
Winegard, W. C. See Holmes, E. L., 1223; Jubb, J. T., 945.
Wirt, T. M. See Zingery, W. L., 1384.
Wolfson, J. L. Structure of the line at 2892 gauss cm in the conversion electron spectrum of the active deposit of RdTh, 468.
The K internal conversion coefficient of the 412-kev transition in Hg^{198}, 773.
Woodbury, W. C. See Edwards, M. H., 1833.
Woods, A. D. B. Inelastic scattering of neutrons from rotating liquid helium II, 1082.
Woonton, G. A. See Kipling, A. L., 1859.
Ziauddin, S. Polar-cap absorption following the solar flare of July 16, 1959, 1882.
Zingery, W. L. and **Wirt, T. M.** The reversible temperature coefficient of remanence of a Pt–Co permanent magnet, 1384.

NOTES TO CONTRIBUTORS

Canadian Journal of Physics

MANUSCRIPTS

General.—Manuscripts, in English or French, should be typewritten, double spaced, on paper 8½×11 in. **The original and one copy are to be submitted.** Tables and captions for the figures should be placed at the end of the manuscript. Every sheet of the manuscript should be numbered. Style, arrangement, spelling, and abbreviations should conform to the usage of recent numbers of this journal. Greek letters or unusual signs should be written plainly or explained by marginal notes. Characters to be set in boldface type should be indicated by a wavy line below each character. Superscripts and subscripts must be legible and carefully placed. Manuscripts and illustrations should be carefully checked before they are submitted. Authors will be charged for unnecessary deviations from the usual format and for changes made in the proof that are considered excessive or unnecessary.

Abstract.—An abstract of not more than about 200 words, indicating the scope of the work and the principal findings, is required, except in Notes.

References.—References should be listed **alphabetically by authors' names,** unnumbered, and typed after the text. The form of the citations should be that used in current issues of this journal; in references to papers in periodicals, titles should not be given and only initial page numbers are required. The names of periodicals should be abbreviated in the form given in the most recent *List of Periodicals Abstracted by Chemical Abstracts.* All citations should be checked with the original articles and each one referred to in the text by the authors' names and the year.

Tables.—Tables should be numbered in roman numerals and each table referred to in the text. Titles should always be given but should be brief; column headings should be brief and descriptive matter in the tables confined to a minimum. Vertical rules should not be used. Numerous small tables should be avoided.

ILLUSTRATIONS

General.—All figures (including each figure of the plates) should be numbered consecutively from 1 up, in arabic numerals, and each figure referred to in the text. The author's name, title of the paper, and figure number should be written in the lower left corner of the sheets on which the illustrations appear. Captions should not be written on the illustrations.

Line drawings.—Drawings should be carefully made with India ink on white drawing paper, blue tracing linen, or co-ordinate paper ruled in blue only; any co-ordinate lines that are to appear in the reproduction should be ruled in black ink. Paper ruled in green, yellow, or red should not be used. All lines must be of sufficient thickness to reproduce well. Decimal points, periods, and stippled dots must be solid black circles large enough to be reduced if necessary. Letters and numerals should be neatly made, preferably with a stencil (**do NOT use typewriting**) and be of such size that the smallest lettering will be not less than 1 mm high when the figure is reduced to a suitable size. Many drawings are made too large; originals should not be more than 2 or 3 times the size of the desired reproduction. Whenever possible two or more drawings should be grouped to reduce the number of cuts required. In such groups of drawings, or in large drawings, full use of the space available should be made; the ratio of height to width should conform to that of a journal page (4¾×7¼ in.), but allowance must be made for the captions. **The original drawings and one set of clear copies (e.g. small photographs) are to be submitted.**

Photographs.—Prints should be made on glossy paper, with strong contrasts. They should be trimmed so that essential features only are shown and mounted carefully, with rubber cement, on white cardboard, with no space between those arranged in groups. In mounting, full use of the space available should be made. **Photographs are to be submitted in duplicate;** if they are to be reproduced in groups one set should be mounted, the duplicate set unmounted.

REPRINTS

A total of 100 reprints of each paper, without covers, are supplied free. Additional reprints, with or without covers, may be purchased at the time of publication.

Charges for reprints are based on the number of printed pages, which may be calculated approximately by multiplying by 0.6 the number of manuscript pages (double-spaced typewritten sheets, 8½×11 in.) and including the space occupied by illustrations. Prices and instructions for ordering reprints are sent out with the galley proof.

Contents

Y. Y. Lee—On the temperature dependence of paramagnetic resonance in the case of the Ising model - - - - - - - - - - - - - - - - - - 1733

J. W. C. Johns—The absorption spectrum of BO_2 - - - - - - - - - 1738

A. D. May, V. Degen, J. C. Stryland, and H. L. Welsh—The Raman effect in gaseous hydrogen at high pressures - - - - - - - - - - - - 1769

G. C. Hanna, D. B. Primeau, and P. R. Tunnicliffe—Thermal neutron cross sections and resonance integrals of the reactions $O^{17}(n,\alpha)C^{14}$, $Ar^{36}(n,\alpha)S^{33}$, and $N^{14}(n,p)C^{14}$ - 1784

G. G. Shepherd, K. V. Paulson, and J. A. Nilson—Stereo-projection systems for auroral height measurements - - - - - - - - - - - - 1807

A. Artna and M. W. Johns—The decay of Er^{171} - - - - - - - - - - 1817

M. H. Edwards and W. C. Woodbury—Compressibility of liquid He^4 - - - 1833

K. G. McNeill and R. M. Green—Scintillation spectra from thick sources - - 1842

T. H. Shepertycki—The autocorrelation function of symmetrically folded Gaussian noise - 1851

A. L. Kipling, P. W. Smith, J. Vanier, and G. A. Woonton—The concentration dependence of paramagnetic relaxation in dilute potassium chromi- and ferri-cyanides at liquid helium temperature - - - - - - - - - - 1859

W. J. Heikkila and S. R. Penstone—Rocket measurements of auroral radio absorption - 1875

Syed Ziauddin—Polar-cap absorption following the solar flare of July 16, 1959 1882

I. B. McDiarmid, D. C. Rose, and E. Budzinski—Direct measurement of charged particles associated with auroral zone radio absorption - - - 1888

F. L. Curzon and Roger Howard—A proposal to use microwave cavities to study the surface properties of high density plasmas - - - - - - - - 1901

Notes:

R. S. Iyengar and G. G. Shepherd—Observations of auroral luminosity fluctuations - 1911

Dora K. de Grinberg—Some new observations on the growing of cadmium single crystals - 1919

Letters to the Editor:

W. R. Datars—Cyclotron resonance in antimony - - - - - - - - - 1922

Contents of Volume 39 - 1925

Printed in Canada *by* University of Toronto Press